Doctoral theses at NTNU, 2021:38

Marco Sauermoser

Non-equilibrium thermodynamics and nature-inspired chemical engineering applied to PEM fuel cells

Doctoral thesis

NTNU
Norwegian University of Science and Technology
Thesis for the Degree of
Philosophiae Doctor
Faculty of Natural Sciences
Department of Chemistry

NTNU
Norwegian University of
Science and Technology

Marco Sauermoser

Non-equilibrium thermodynamics and nature-inspired chemical engineering applied to PEM fuel cells

Thesis for the Degree of Philosophiae Doctor

Trondheim, February 2021

Norwegian University of Science and Technology
Faculty of Natural Sciences
Department of Chemistry

NTNU
Norwegian University of
Science and Technology

NTNU
Norwegian University of Science and Technology

Thesis for the Degree of Philosophiae Doctor

Faculty of Natural Sciences
Department of Chemistry

ISBN 978-82-326-5749-0 (printed ver.)
ISBN 978-82-326-4752-1 (electronic ver.)
ISSN 1503-8181 (printed ver.)
ISSN 2703-8084 (online ver.)

Doctoral theses at NTNU, 2021:38

Printed by NTNU Grafisk senter

Das schwere Leben ist am leichtesten
zu ertragen, wenn man sich
schwere Aufgaben stellt.

Peter Rosegger

Acknowledgments

I was always told that if you enjoy doing something, time passes quickly. Doing my PhD is a perfect example of this. More than three years have already passed since I moved to Trondheim, and it feels like I arrived here yesterday. For the great time I had and am still having here, I would like to thank several people.

First of all, I need to thank my supervisors Signe Kjelstrup and Bruno G. Pollet. Without them, my thesis, but also, my personal development would not have been the same. Whenever I had doubts or was stuck on something, I could always ask for help, and I got supported no matter what. Thank you, Signe, for being my scientific role model. I have never seen anyone who was as passionate about research as her. Whenever I got new results, she celebrated them in the same way as I did, which always raised the moral. I have never seen her in a bad mood and the saying "There are no stupid questions" really applied to her. I think no one can explain a complicated topic such as non-equilibrium thermodynamics better than her. The talks I had with Bruno were always very inspiring, and his connections and knowledge of fuel cells were always precious to me. He always cheered me up and made sure that I knew my values. Without Bruno, the fuel cell would not be running correctly even now. Natalya also played a big role in my PhD thesis by supporting me with her knowledge and giving me the possibility to do a short research stay at the Warsaw University of Technology. A big thank you goes out to Fredrik for spending countless hours together with me in the laboratory and who was a massive help while getting the fuel cell up and running.

PoreLab also deserves its own paragraph. Not only did PoreLab provide the funding for my PhD thesis, but additionally offered a work environment where someone like me can thrive and develop himself. Due to the interdisciplinary research focus of PoreLab, it was possible to broaden my horizon even further with lots of talks and discussions on different subjects.

But I also have to thank my future wife, Mari. Without her, the transition

from Austria to Norway would have never been as comfortable. She lifted me up when I was down during difficult times, and I could always resort to her if something was on my mind. For this, I love you. I also need to thank my parents. Without their education, support and love throughout my whole life, I could not have become the person I am now.

Life is not only mandated by work. Social activities are also equally important, which is where friends come into play. When you move away from your home, you really see who your best friends are. Thank you for the endless of hours talking and chatting over various platforms on the internet, which made me feel like I was still in Austria. Especially Patrick, who helped me through a hard time during my sick leave by motivating me to not just stay in bed till noon with our daily coffee meetings at sharp 8:40 in the morning. I also always highly appreciated the yearly visits from you and Joel. Thank you Thomas for countless times you have cheered me up and made me laugh, and of course for the many hours we played together in online games.

Moving to a new country bears a lot of difficulties. One of them is the lack of people you know. However, I met amazing people at the Department of Chemistry, PoreLab and in my Norwegian classes, who I can call friends now. Thank you all for letting me feel at home in Trondheim. Thank you for all the activities we did together, such as pizza or dinner nights, parties, lønningspils or climbing sessions. Thank you Eivind and Olav for having some great adventures during our stays at conferences in New Orleans, Boulder and Valencia.

Summary

The first objective of this thesis is to discover potentials for the optimisation of the performance of polymer electrolyte membrane (PEM) fuel cells by using new designs for the flow field plates (FFP) based on nature-inspired chemical engineering. The second objective is to give a detailed understanding of the processes and effects, mostly heat-related ones, inside a PEM fuel cell.

To have a better understanding of how to develop new flow field designs, we reviewed the current state of FFP development for PEM fuel cells. We looked at serpentine, parallel, interdigitated, mesh type or their mixtures, furthermore, 2D circular and 3D tubular geometries, porous, fractal, and biomimetic flow fields and how they performed compared to the serpentine pattern which is in most cases the industry standard right now. The advantages and disadvantages of each design were investigated. A well-optimised FFP gives uniform gas distribution, low pressure drop for transport, and sufficient rib area to provide high electronic conductivity while also preventing water flooding and providing sufficient membrane hydration. The big challenge is that often the demands are sometimes contradictory. Therefore, we recommended that future optimisation of FFPs should be based on the minimisation of entropy production, thus offering the possibility of multi-criteria optimisation methods.

Using nature-inspired chemical engineering for the development of a new flow field design to improve the PEM fuel cell performance is, as discussed, the first objective of this thesis. A tree-like structure approach was chosen. However, before we implemented them into experiments, we wanted to understand the pattern itself better. The promise of using them was that they uniformly distribute reactants across the active area of the PEM fuel cell. Such a pattern, scaled by the so-called Murray's law, was recently tested and showed an increase in performance compared to a standard serpentine pattern. Therefore, we investigated the impact of width scaling factor and channel width on the entropy production of the system. The width scaling factor described the reduction of channel width with changing branching

generation level. Analytical calculations and 3D CFD simulations were used to calculate the entropy production due to viscous dissipation, meaning the heat generated due to frictional losses, along the channels. Results indicated that an increase in width scaling factor decreased the entropy production and that the one from Murray's law did not yield the lowest entropy production. Furthermore, we showed that the analytic equations delivered a pressure drop which was within a few percents of the 3D CFD simulation results. This work opens up new strategies and approaches for the optimisation of tree-like flow field patterns.

Based on the theoretical work performed on the tree-like patterns, we designed a new two-layer FFP, which used such a pattern as an inlet and outlet for the reacting gases and water. The patterns were milled in high-quality graphite plates by CNC machining. Three different flow field designs, which differed in their width scaling factors in the inlet and outlet plate, were tested on the cathode side of the PEM fuel cell and compared against the standard 1-channel serpentine pattern. Tests included a performance, electrochemical impedance spectroscopy (EIS) and a three-hour hold test at 70%, 60% and 50% relative humidity at both the anode and cathode. The experimental setup consisted of a Biologic FCT-50s PEM fuel cell test station and a combination of the balticFuelCell qCF FC25/100 V1.1 LC support frame and the balticFuelCells cellFixture cF25/100 HT Gr.V1.3 fuel cell housing. We showed that the design with a width scaling factor of 0.917 at the inlet and 0.925 at the outlet plate delivered a peak power density which was within 11% (a 0.08 W/cm^2 difference) of the serpentine pattern at 70% relative humidity. Other designs showed a reduction of the power density of up to 37% (a 0.26 W/cm^2 difference). Cell voltages during the hold test experiments were stable when the relative humidity was reduced to 60% and 50% for all presented designs. It was also found that a reduction in the viscous dissipation in the flow pattern was not directly linked to an increase in PEM fuel cell performance. It was argued that water accumulation, together with a slight increase in single fuel cell resistance, were the main reasons for the reduced power density compared to the serpentine pattern. To further improve the PEM fuel cell performance, we recommended reducing the number of branching generation levels and width scaling factor for both the inlet and outlet plate but also using gas diffusion layers (GDL) with better hydrophobic properties.

As initially described in this summary, the second objective of this thesis is to have a better understanding of the processes within the PEM fuel cell. We developed a model to calculate the concentration, temperature, heat

flux and electrical potential profiles in 1D within the PEM fuel cell based on non-equilibrium thermodynamics (NET) including all available coupling terms, which are commonly neglected. For this, we divided the PEM fuel cell into three homogeneous layers, connected by two planar Gibbs interfaces which acted as cathode and anode. NET allowed for a consistency check by comparing the difference between the entropy flux through the system and the calculated total entropy production. We found out that coupling terms such as Peltier and Soret effects played a significant role in calculating the profiles. The presented polarisation curves showed a non-linear area at higher current densities. Contrary to expectations, this non-linearity was not caused by mass transport limitations, but due to varying membrane resistance.

The next step was to improve further the presented NET model for a PEM fuel cell. This was done by changing the algorithm of the model to a multi-point boundary value problem approach. Furthermore, the equations for calculating the cathode GDL profiles were extended to include all coupling terms. Again, a consistency check was performed to see any weaknesses in the model. For all domains besides the cathode backing, the error was within 10%. We showed that the commonly neglected Dufour effect/thermal diffusion and the Peltier/Seebeck coefficient had significant contributions to the water and heat flux in the system. The Dufour effect, for example, could introduce a temperature change of up to 9 K at the anode and cathode. By applying a temperature difference of 5 K to the boundaries of the system, we were able to show that the system was susceptible to temperature changes as the heat flux could change up to 44%. Having a 5 K lower temperature at the cathode side increased the performance between 1 mV and 3 mV at a current density of 13500 A/m^2. Additionally, while having a cooler cathode side, the temperature and heat flux were more uniform in the PEM fuel cell.

Contents

Chapter 1

Introduction

1.1 Main objectives and motivation

According to the 2030 climate and energy framework of the European Commission [1], the key targets for 2030 are the reduction of greenhouse gas emissions by at least 40%, an increase of renewable energy by at least 32% and an improvement of energy efficiency of at least 32.5%. By reaching these goals, it will enable the EU to move towards the climate-neutral economy [1]. Therefore, a transition towards renewable energy in the near future is crucial, not only in the EU but also worldwide, to reach these goals. Norway is an excellent example of such a future transition. Only zero-emission vehicles for passenger cars and vans should be sold by 2025. Furthermore, busses for public transport in cities should use zero-emission drives or biogas by 2025 [2]. One of the energy sources for zero-emission vehicles is the polymer electrolyte membrane (PEM) fuel cell, which converts hydrogen and oxygen in contact of a catalyst (Pt - platinum) into energy, with the only by-product being pure water. However, efficiencies still need to be significantly improved. Different organisations, *e.g.* the US Department of Energy (US DOE) or the New Energy and Industrial Technology Development Organization (NEDO), set several technological and cost targets for PEM fuel cells which should be reached in order to achieve the global goals of clean and zero-emission energy transition and reduction of CO_2 emissions. The US DOE, for example, stated a target cost of US$40/kW with an efficiency of 65% peak power and a maximum total platinum (Pt) loading of 0.125 mg/cm^2 for 500,000 systems per year [3]. High technology targets had also been set by NEDO [4]. According to NEDO, a cell voltage of 0.85 V at 4.4 A/cm^2 and 1.1 V at 0.2 A/cm^2 should be reached until 2040. In order to reach such set targets, the PEM fuel cell needs to be optimised further, but also better understood,

especially at component level. A discussion of these targets was presented by Pollet *et al.* [5].

Fuel cell optimisation can be performed on the component level as well as on the operating parameters. To identify the full potential of optimisation, one has to understand all the processes inside the PEM fuel cell, such as heat effects and media transport through the porous and non-porous components. Especially the flow field plate (FFP) has a great potential due to its contribution of around 60% to the overall mass and 40% of the overall PEM fuel cell cost [6]. A large amount of new flow field (FF) designs and variations of already known ones have been introduced and studied in great detail over the last years. Therefore, a review of the current state of the art of FF designs was conducted to have a practical overview of development directions. This review can be found in Chapter 2. Optimisation of the FF is quite complex, as there are several factors to be accounted for, such as the electric resistance, the water management, the thermal resistance and the gas distribution. Within all the newly introduced FF designs, one of the most promising approaches is the use of nature-inspired chemical engineering to design biomimetic flow field patterns such as lung-, tree- or plant-like patterns [7–12].

The main inspiration for this thesis came from the work of Kjelstrup *et al.* [13]. Results showed that if a tree-like channel structure, based on the bronchial tree of a human lung, was used in the FFP, a as uniform as possible gas and water transport in and out of the PEM fuel cell could be achieved. The improved transport properties could enable the removal of the gas diffusion layer (GDL), which would lead to an avoidance of mass-transfer limitations. In combination with the tailoring of the catalyst layer (CL) with macroporous columns, the performance of a PEM fuel cell should increase. The optimisation of the CL and FFP was based on the principle of minimum entropy production in non-equilibrium thermodynamics. Zlotorowicz *et al.* [14] later showed an increase in PEM fuel cell performance by using micrometer-sized pores in the CL.

Nature has shown us many times, that biological processes are highly optimised, *e.g.* optimal gas delivery in a human lung [15]. Another example is the geometry of a reindeer's nose which is optimised to be able to breathe in cold air with a minimal energy input [16]. Therefore, researchers have striven to understand biological systems and have used the gained knowledge within nature-inspired chemical engineering (NICE) to optimise, for example, chemical reactors [17]. As objectives vary between nature and human-made

applications or processes [18], it is crucial to fully understand the designs coming from nature and tweak them according to their intended use, *e.g.* for FF design.

We pursued this approach, and so the first objective of this thesis is to have a better insight into nature-inspired flow field patterns in order to improve the performance of PEM fuel cells. This can be done either in theory, with numerical simulations or with experiments. On the one hand, it is essential to know how specific design decisions impact, for example, pressure drops in the FFP, as there is a complex interplay between channel geometry, pressure drop and water removal in PEM fuel cells, as shown in studies of the serpentine pattern by Choi *et al.* [19]. On the other hand, new FF designs need to be experimentally validated and compared to industry standards.

As discussed, optimising the PEM fuel cell requires a detailed understanding of the various processes within the PEM fuel cell. For example, heat effects can change the temperature distribution significantly, which can lead to a performance in- or decrease [20, 21]. Higher temperatures could eliminate water problems caused by the flooding of pores, but could also lead to dehydration of the PEM, which in turn increases the PEM fuel cell resistance. Therefore, the second objective of this thesis is to model the PEM fuel cell with non-equilibrium thermodynamics to investigate a variety of profiles and effects within, such as heat effects or temperature distributions. The focus was mainly on specific coupling terms, like the Dufour or Peltier heat, which are often neglected in current research.

The most important components in the PEM fuel cell will be described in the next section (Section 1.2), to have a better comprehension of the presented papers in this thesis. An introduction to non-equilibrium thermodynamics follows (Section 1.3), which will show the derivations of the equations used in Chapter 5 and 6. Section 1.4 will give a brief summary of nature-inspired chemical engineering and its applications in research.

1.2 Fuel cell technology

PEM fuel cells use pure hydrogen and either pure oxygen or an oxygen mixture to create electricity. Water is produced as the only by-product during the electrochemical reactions. The different components of a single cell PEM fuel cell can be seen in Fig. 1.1.

Component 1 is the polymer electrolyte membrane (PEM), which is a

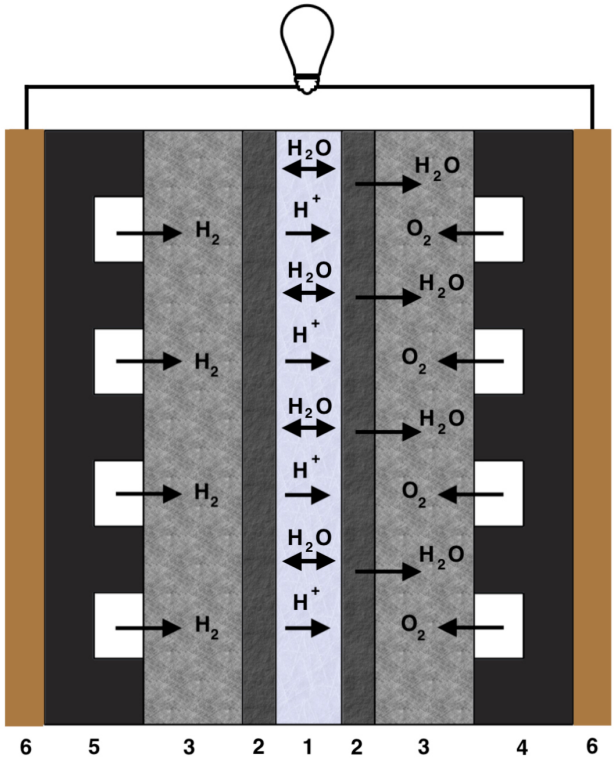

Figure 1.1: Schematic picture of the PEM fuel cell. The layer thickness is given in parenthesis. For abbreviations, see text. 1-PEM (∼50–150 μm), 2-CL (∼10–20 μm), 3-GDL (∼200–300 μm), 4-cathode FFP (∼1 mm), 5-anode FFP (∼1 mm), and 6-CCP.

proton exchange membrane (proton conductive material). The most popular type of PEM is made of perfluorinated polymers, *e.g.* Nafion. Sulfonic acid chains ($SO_3^-H^+$) are responsible for its proton conductive behaviour [22]. The properties of such membranes are often heavily dependent on the water content, which makes humidification a vital process. For example, a decrease in PEM humidity results in an increase in cell resistance, which decreases the performance and, in the worst case, can lead to the damaging of the membrane. Due to this water dependency, PEM membranes are often restricted to a cell temperature below 100°C. As Fig. 1.1 indicates, water is moving in the membrane in both directions, dictated by back-diffusion due to lower water concentrations on the anode side and by electro-osmotic drag linked to the flux of protons through the membrane.

Component 2 is the catalyst layer (CL). Usually, it contains finely dispersed graphite particles, which sit on both sides of the membrane. On these particles, the catalyst is attached, which is commonly Pt. The catalyst layer acts as a porous electrode where the following electrochemical reactions take place. On the anode side:

$$\frac{1}{2}\mathrm{H}_2 \rightarrow \mathrm{H}^+ + e^- \tag{1.1}$$

On the cathode side:

$$\frac{1}{4}\mathrm{O}_2 + \mathrm{H}^+ + e^- \rightarrow \frac{1}{2}\mathrm{H}_2\mathrm{O} \tag{1.2}$$

The CL serves two purposes [22]:

1. Deliver and collect the electrons from the PEM fuel cell.
2. Deliver and collect the reactants and products from the electrochemical reactions.

The CL requires, therefore, high electric conductivity, high gas permeability, high corrosion resistance, efficient water removal, and good mechanical properties [22]. All these requirements need to be fulfilled while keeping the cost of the CL low.

Component 3 is the so-called gas diffusion layer (GDL) or porous transport layer (PTL), which acts as a diffusion media for the gases. There are two common groups of GDLs, woven (carbon paper) and non-woven (carbon cloth). Carbon paper has a lower cost, however, often produces lower power densities (in $\mathrm{W/cm^2}$) in the PEM fuel cell than carbon cloth [23]. Both types consist of carbon fibres in different shapes and sizes. The properties of the GDL change, due to its fibrous structure, with the applied compression on the fuel cell. Higher compression reduces the pore space, which creates less area for the gases and the liquid water to flow through (lower gas permeability), but on the other hand, decreases the ohmic resistance due to higher contact areas within the PTL. To enhance the water removal in the PEM fuel cell, materials, such as PTFE, are often added to the GDL to increase its hydrophobicity. Some GDLs also have a microporous layer (MPL) included, which has a different pore size than the rest of the GDL, to improve the water management further[24]. A MPL usually consists of carbon black powder mixed with PTFE [23].

Component 1, 2 (both anode and cathode) and 3 together are called membrane electrode assembly (MEA) or 5-layer MEA.

Components 4 and 5 are the flow field plates (FFP) for the cathode and anode, respectively. They act as the gas distribution system in the fuel cell. The FFP consists of flow channels which can have a variety of different geometries. The discussion of the advantages and disadvantages of these geometries can be found in Chapter 2. The FFP needs to have certain abilities to ensure good PEM fuel cell performance, such as:

- Uniform flow distribution
- Low ohmic resistance
- Proper water management
- Low pressure drop to reduce parasitic losses (impacts efficiency of auxiliary equipment)
- Good scalability

The problem with these requirements is that often a compromise has to be made. For example, lowering the pressure drop to increase the overall efficiency of the PEM fuel cell, including auxiliary equipment (*e.g.* gas supply system) can often lead to a worsening of the water management. A higher pressure drop, on the other hand, causes a better removal of the water droplets from the channel [25]. The ohmic resistance of the FFP is based on the material resistance itself and the contact resistance, which is influenced by the contact area with the GDL. A low channel to land width ratio decreases the contact resistance due to an increase in the contact area, however, also decreases the pressure drop [26] and the fuel consumption [27].

Component 6 is the current collector plate (CCP) and is used to connect the load cables with the PEM fuel cell. The CCP should have low ohmic resistance.

1.3 Non-equilibrium thermodynamics

This section gives a short introduction to non-equilibrium thermodynamics (NET) and how to approach the modelling of PEM fuel cells. A more thorough explanation can be found in the books from Kjelstrup *et al.* [28, 29]. As discussed in the previous chapters, to increase the efficiency of PEM fuel

cells, it is possible to optimise the operating conditions. However, to find the optimum, a deep understanding of the local mechanisms inside the PEM fuel cell is crucial. Especially heat effects and changes in temperatures can have a significant influence on the PEM fuel cell performance [20, 21]. These heat effects have several contributions, *e.g.* from the Peltier or Dufour effect. One way to model these effects is to use NET.

With this method, it is possible to calculate the lost work w_{lost} (given by Eq. 1.3), which is the difference between the actual work w and the ideal work w_{ideal} [29]. w_{ideal} is the work of a system for a completely reversible process.

$$w_{lost} = T_0 \frac{dS_{irr}}{dt} = T_0 \int \sigma dV \tag{1.3}$$

where T_0 is the temperature of the surroundings in K, $\frac{dS_{irr}}{dt}$ is the total entropy production of the system in W/K, σ is the local entropy production per m^3 in W/(K m^3) and V is the volume of the system in m^3. Knowing the lost work, the second law efficiency, which is also called the thermodynamic efficiency, is calculated as follows:

$$\eta_{II} = \frac{w_{ideal}}{w} = 1 - \frac{w_{lost}}{w} \tag{1.4}$$

NET is not only important for calculating the second law efficiency in a system. By looking at the entropy production, we can also derive the flux-force relationships used for modelling the processes. The next sections show how the equations are derived starting with the entropy production. They will later be utilized for the modelling of PEM fuel cells.

1.3.1 The Fuel Cell Model

The following derivations and equations are based on the work from Kjelstrup *et al.* [28]. Our work focuses on the modelling of the process in one dimension (1D). Therefore equations will be derived for the x-direction. The starting point is the description of the local entropy production σ, shown by Eq. 1.5, which gives the general expression for the flux-force relationships.

$$\sigma = \sum_i J_i X_i \geq 0 \tag{1.5}$$

where J_i is flux of transport phenomena i and X_i is the driving force of transport phenomena i. In a fuel cell, we have transport of heat, mass and electric charge, therefore Eq. 1.5 can be rewritten as:

$$\sigma = J_q' \left(\frac{d}{dx} \frac{1}{T} \right) + \sum_{j=1}^{n} J_j \left(-\frac{1}{T} \frac{d\mu_{j,T}}{dx} \right) + j \left(-\frac{1}{T} \frac{d\phi}{dx} \right) \tag{1.6}$$

where J'_q is the measurable heat flux in J/(m^2 s), T is the temperature in K, J_j is the mass flux of component j in mol/(m^2 s), n is the number of different components in the system, $\mu_{j,T}$ is the chemical potential at constant temperature in J/mol, j is the charge flux, further referred to as current density (current divided by the surface area) in A/m^2, and ϕ is the electric potential in V. In the next step, the fluxes are defined. NET assumes that there is a linear relationship between the fluxes and their according forces:

$$J_i = \sum_{k=1}^{m} L_{ik} X_k \tag{1.7}$$

where m is the number of independent fluxes in the system and L_{ik} is the Onsager conductivity coefficient, which is a phenomenological coefficient. With the help of Eq. 1.7, the equations for the different fluxes given in Eq. 1.6 can be defined:

$$J'_q = L_{qq}\frac{d}{dx}\left(\frac{1}{T}\right) + \sum_{j=1}^{n} L_{q\mu_j}\left(-\frac{1}{T}\frac{d\mu_{j,T}}{dx}\right) + L_{q\phi}\left(-\frac{1}{T}\frac{d\phi}{dx}\right) \tag{1.8}$$

$$J_j = L_{\mu_j q}\frac{d}{dx}\left(\frac{1}{T}\right) + \sum_{k=1}^{n} L_{\mu_j\mu_k}\left(-\frac{1}{T}\frac{d\mu_{k,T}}{dx}\right) + L_{\mu_j\phi}\left(-\frac{1}{T}\frac{d\phi}{dx}\right) \tag{1.9}$$

$$j = L_{\phi q}\frac{d}{dx}\left(\frac{1}{T}\right) + \sum_{j=1}^{n} L_{\phi\mu_j}\left(-\frac{1}{T}\frac{d\mu_{j,T}}{dx}\right) + L_{\phi\phi}\left(-\frac{1}{T}\frac{d\phi}{dx}\right) \tag{1.10}$$

The Onsager symmetry relations state, that the off-diagonal terms are symmetric, meaning that $L_{i,k} = L_{k,i}$ where $i \neq k$. These Equations (Eq. 1.8 to 1.10) will be modified by introducing familiar transport coefficients. Each modelled layer will be discussed in detail in the next sections.

Anode and cathode PTL

The anode and cathode PTL are considered to be homogenous layers, and more than one component is present. To simplify the approach, we introduce the interdiffusion flux J_D, which can be derived by introducing the Gibbs-Duhem equation (Eq. 1.11). Below, the derivation of the interdiffusion flux for the anode PTL is shown.

$$x_w d\mu_{w,T} + x_{\mathrm{H_2}} d\mu_{\mathrm{H_2},T} = 0 \tag{1.11}$$

Considering only the mass fluxes in Eq. 1.6, where the components are water (w) and hydrogen (H_2), we can use Eq. 1.11 to express one chemical potential

by the other.

$$-J_w\frac{1}{T}\frac{d\mu_{w,T}}{dx}-J_{\mathrm{H_2}}\frac{1}{T}\frac{d\mu_{\mathrm{H_2},T}}{dx}=-\frac{1}{T}\left(J_w\frac{d\mu_{w,T}}{dx}-J_{\mathrm{H_2}}\frac{x_w}{x_{\mathrm{H_2}}}\frac{d\mu_{w,T}}{dx}\right) \quad (1.12)$$

After some rearrangements, we receive the following expression for the mass fluxes which uses the interdiffusion flux J_D instead of J_w and $J_{\mathrm{H_2}}$:

$$\left(\frac{J_w}{x_w}-\frac{J_{\mathrm{H_2}}}{x_{\mathrm{H_2}}}\right)x_w\frac{1}{T}\frac{d\mu_{w,T}}{dx}=J_D\frac{1}{T}\frac{d\mu_{w,T}}{dx} \quad (1.13)$$

In the cathode PTL, we have oxygen (O_2), nitrogen (N_2) and water. As we assume that nitrogen is inert, we neglect it in the following equations. For the cathode PTL, the interdiffusion flux J_D is as follows:

$$J_D=\left(\frac{J_w}{x_w}-\frac{J_{\mathrm{O_2}}}{x_{\mathrm{O_2}}}\right)x_w \quad (1.14)$$

By using J_D, we can reduce the number of components j to 1 in Eq. 1.9, thus reducing the number of Onsager conductivity coefficients. As the next step, we eliminate the electric potential gradient in the flux equations by inserting Eq. 1.10 into Eq. 1.8 and 1.9. With this, we introduce a new set of flux equations:

$$J_q'=l_{qq}\left(\frac{d}{dx}\frac{1}{T}\right)-l_{q\mu}\frac{1}{T}\frac{d\mu_{j,T}}{dx}+\frac{L_{q\phi}}{L_{\phi\phi}}j \quad (1.15)$$

$$J_D=l_{\mu q}\frac{d}{dx}\left(\frac{1}{T}\right)-l_{\mu\mu}\frac{1}{T}\frac{d\mu_{w,T}}{dx}+\frac{L_{\mu\phi}}{L_{\phi\phi}}j \quad (1.16)$$

$$j=L_{\phi q}\frac{d}{dx}\left(\frac{1}{T}\right)-L_{\phi\mu}\frac{1}{T}\frac{d\mu_{w,T}}{dx}-L_{\phi\phi}\frac{1}{T}\frac{d\phi}{dx} \quad (1.17)$$

where, for better readability, we write $l_{\mu_w\mu_w}$ as $l_{\mu\mu}$.

The newly introduced coefficients l_{ik} can be linked to the phenomenological coefficients:

$$l_{ik}=L_{ik}-\frac{L_{\phi k}L_{i\phi}}{L_{\phi\phi}} \quad (1.18)$$

Now, the coefficients l_{ik} and L_{ik} need to be related to parameters and properties which are well known from theory and experiments, such as the transference or Peltier coefficient or the heat of transfer:

$$t_D\equiv\left(\frac{J_D}{j/F}\right)_{d\mu_T=0,dT=0}=F\frac{L_{\mu\phi}}{L_{\phi\phi}} \quad (1.19)$$

where t_D is the transference coefficient and F is the Faraday constant (96485 C/mol).

$$\pi \equiv \left(\frac{J'_q}{j/F}\right)_{d\mu_T=0,dT=0} = F\frac{L_{q\phi}}{L_{\phi\phi}} \tag{1.20}$$

where π is the Peltier coefficient in J.

$$q^* \equiv \left(\frac{J'_q}{J_D}\right)_{j=0,dT=0} = \frac{l_{q\mu}}{l_{\mu\mu}} \tag{1.21}$$

where q^* is the heat of transfer in J/mol.

Eq. 1.19 to 1.21 are then introduced into Eq. 1.15 to 1.17. The main transport coefficients (Eq. 1.22 to 1.24) can then be identified as:

$$\lambda = \frac{l_{qq}}{T^2} - (q^*)^2\,\frac{l_{\mu\mu}}{T^2} \tag{1.22}$$

where λ is the thermal conductivity of the homogenous phase in W/(K m).

$$D_{ij} = l_{\mu\mu}\frac{R}{x_w} \tag{1.23}$$

where D_{ij} is the concentration corrected diffusivity coefficient (binary diffusivity of the two components multiplied by the total concentration in the homogenous phase, which is assumed to be constant) of component i in component j in mol/(m s) and R is the gas constant in J/(K mol). In the anode PTL it is $D_{w\mathrm{H_2}}$ and in the cathode PTL it is $D_{w\mathrm{O_2}}$.

$$r = \frac{T}{L_{\phi\phi}} \tag{1.24}$$

where r is the electrical resistance of the homogenous phase in Ohm m.

It is often better to calculate the concentration- or molar fraction profiles of a component, instead of the chemical potential profile, as it is easier to interpret the results of the PEM fuel cell model. Therefore, we can additionally introduce the equation for the chemical potential of water (Eq. 1.25) into Eq. 1.16.

$$\mu_{w,T} = \mu^0_{w,T} + RT\ln\left(\frac{x_w}{x^*_w}\right) \tag{1.25}$$

where μ^0_T is the chemical potential at constant temperature and standard conditions in J/mol, and x^*_w is the molar fraction at saturation. The last

steps result in the final equations, which can be used for the modelling of the homogeneous anode and cathode PTL layers:

$$J'_q = -\lambda \frac{dT}{dx} + q^* \left(J_D - t_D \frac{j}{F} \right) + \pi \frac{j}{F} \tag{1.26}$$

$$J_D = -\frac{q^* D_{ij} x_w}{RT^2} \frac{dT}{dx} - D_{ij} \frac{dx_w}{dx} + t_D \frac{j}{F} \tag{1.27}$$

$$j = -\frac{\pi}{TFr} \frac{dT}{dx} - \frac{t_D RT}{F x_w r} \frac{dx_w}{dx} - \frac{1}{r} \frac{d\phi}{dx} \tag{1.28}$$

Proton exchange membrane

The same procedure as for the anode or cathode PTL is applied to derive the equations for the membrane. Parameters and variables used in this section are corresponding to the membrane layer of the model. There are three major differences:

1. The only moving component in the membrane is water. Therefore, J_D is not required, and only J_w is used instead. The membrane gives the frame of reference.

2. In the membrane, the solution is in the liquid state and it is not an ideal solution.

3. For calculations of membrane properties, the consensus is to use the water activity a_w instead of x_w (see, for example, Weber and Newman [30] or Springer *et al.* [31]). Therefore, the equations have to be slightly modified, which is discussed in this section.

Based on points 2 and 3 above, we introduce the water activity $a_w = p_w / p_w^*$ and the water content $\lambda = c_w M / \rho$ in mol water per mole membrane ionic side, where p_w is the partial pressure of the liquid water in the membrane in atm, p_w^* is the standard pressure in atm, c_w is the concentration of liquid water mol/m^3, M is the molar mass of the polymer in the membrane in kg/mol, and ρ is the membrane dry density in kg/m^3.

Eq. 1.26 stays the same, but Eq. 1.27 and 1.28 need to be adjusted. The equation for the water content λ is inserted into Eq. 1.27, followed by using the expression $d\lambda/dx = (d\lambda/da_w)\,(da_w/dx)$:

$$J_w = -\frac{q^* D_w \lambda \rho}{RT^2 M} \frac{dT}{dx} - \frac{D_w \rho}{M} \frac{d\lambda}{da_w} \frac{da_w}{dx} + t_w j / F \tag{1.29}$$

where D_w is the self-diffusion coefficient of water in m^2/s. $d\lambda/da_w$ can be calculated by using experimental expressions such as the one from Springer *et al.* [31] or Weber and Newman [30]. To receive the third flux equation for the membrane, the charge flux (Eq. 1.30), we use $\mu_{w,T} = \mu^0_{w,T} + RT \ln a_w$ instead of Eq. 1.25 to modify Eq. 1.17.

$$j = -\frac{\pi}{TFr}\frac{dT}{dx} - \frac{t_w RT}{Fa_w r}\frac{da_w}{dx} - \frac{1}{r}\frac{d\phi}{dx} \tag{1.30}$$

Anode and cathode

The anode and the cathode are seen as surfaces in Gibbs' sense. They are not homogenous phases. This changes the approach of deriving the equations for the modelling. The thermodynamic properties of the surface are defined by using the Gibbs excess properties, as described by Bedeaux *et al.* [32] and Albano and Bedeaux [33]. The main point in this approach is that the surface is seen as a discrete phase. This allows calculating the differences between the left and right side of the surface, removing the need for solving a differential equation. Across the surfaces, both on the anode and cathode, we assume water equilibrium, meaning that the chemical potential difference between both sides is zero. As shown in [28], the general equations for the electrodes are as follows:

$$\Delta_{\mathrm{i,s}}T = -\frac{1}{\lambda^{\mathrm{s,i}}}\left[J_q'^{\mathrm{i}} - q^{*,\mathrm{i}}\left(J_w^{\mathrm{i}} - t_w^{\mathrm{i}}\frac{j}{F}\right) - \pi^{\mathrm{i}}\frac{j}{F}\right] \tag{1.31}$$

$$\Delta_{\mathrm{s,o}}T = -\frac{1}{\lambda^{\mathrm{s,o}}}\left[J_q'^{\mathrm{o}} - q^{*,\mathrm{o}}\left(J_w^{\mathrm{o}} - t_w^{\mathrm{o}}\frac{j}{F}\right) - \pi^{\mathrm{o}}\frac{j}{F}\right] \tag{1.32}$$

$$\Delta_{\mathrm{i,o}}\phi = -\eta - \frac{\Delta_n G^{\mathrm{s}}}{F} - \frac{\pi^{\mathrm{i}}}{T^{\mathrm{s,i}}F}\Delta_{\mathrm{i,s}}T - \frac{\pi^{\mathrm{o}}}{T^{\mathrm{s,o}}F}\Delta_{\mathrm{s,o}}T - r^{\mathrm{s}}j \tag{1.33}$$

where η is the electrode overpotential in V and $\Delta_n G^s$ is the Gibbs free energy of either the anode or cathode in J/mol. The super- or subscripts i mean the input of the surface, o the output and s the surface itself. Subscripts used for Δ describe that the value of the first subscript is subtracted from the value of the second subscript. The jump of the heat flux can be calculated by using the energy balance of the surface. For the anode, this is defined as:

$$J_q'^{\mathrm{i}} + j\phi^{\mathrm{i}} + \sum_{k=1}^{N^{\mathrm{i}}} J_k^{\mathrm{i}} H_k^{\mathrm{i}} = J_q'^{\mathrm{o}} + j\phi^{\mathrm{o}} + \sum_{k=1}^{N^{\mathrm{o}}} J_k^{\mathrm{o}} H_k^{\mathrm{o}} \tag{1.34}$$

where N^{i} and N^{o} are the number of components on the inlet and outlet side, respectively, of the surface and H_k is the molar enthalpy of component k on either the inlet or outlet side, respectively, of the surface in J/mol.

1.4 Nature-inspired chemical engineering

Nature-inspired chemical engineering (NICE) is the use of biological or nature-inspired tools or systems to improve different processes. This approach looks at how nature optimised specific features, for example, in animals or plants. Kjelstrup and Magnanelli gave an extensive overview of how NICE can be used for the optimisation in the process industry [34]. The special issue edited by Coppens *et al.* [35] provides several papers on the topic of NICE.

It is important to note, that NICE does not mean mimicking or imitating natural features. Designs originated in nature are not blindly taken but carefully and scientifically analysed, and the gathered information is then used for human-made processes and applications [36]. One reason for this is that objectives often differ between nature and human-made applications. Therefore, an optimum in nature is not automatically the best case [18], which can be seen in Chapter 3.

If this approach is connected with the previously introduced NET, one can conclude that natural systems often minimise their entropy production by having a uniform entropy production distribution. An example of this is the human lung, as shown by Gheorghiu *et al.* [15]. The human lung is built like a self-similar fractal system, where the dimensions at the bronchial level are scaled in a way to achieve constant pressure drop along the flow channels. This leads to minimum entropy production and a uniform entropy production distribution. Furthermore, a uniform flow distribution is achieved.

Another example is the reindeer nose, which is optimised to allow the reindeer to breathe in cold air with the lowest amount of energy needs. Magnanelli *et al.* [17] showed that using the information of the geometry of the reindeer's nose can be used to improve the performance of chemical reactors by adapting the geometry of the reactor. The new geometry led to reduction of entropy production of around 16%.

1.5 Thesis outline

This thesis is organised as a collection of papers, where each chapter from Chapter 2 to 6 represents one of them. The content of the different chapters is summarised as follows:

Chapter 2 gives an overview of the current state of the design and optimisation of FFPs in PEM fuel cells. Well established FF designs are reviewed and compared to newly developed ones. We look at the different approaches for

optimisation for each design and identify the advantages and disadvantages. Furthermore, we provide an outlook on how the development of new designs and the improvement of already used ones should continue.

In Chapter 3 and 4, the focus is on the first objective of this thesis, namely the improvement of flow fields for the use in PEM fuel cells. First, we discuss a numerical framework on how to analyse biomimetic flow patterns such as tree-like structures in Chapter 3. The scaling of the tree-like pattern is described. A set of equations is developed to calculate the viscous dissipation and entropy production in the flow channels and compare the results for different width scaling factors. Here, the viscous dissipation is the generation of heat due to frictional losses in a flow system. The width scaling factor describes the reduction of channel width with the change of branching generation level. Computational fluid dynamics (CFD) simulations are done in OpenFOAM to support the results from the analytic equations and provide further insight into the viscous dissipation in 3D. Additionally, the uniformity of the flow is investigated, and Peclet numbers at the outlets of the tree-like patterns are analysed to see if this can be used for the optimisation of the patterns.

Based on the work presented in Chapter 3, we present new designs for flow field plates in Chapter 4, which are machined in high-quality graphite plates by CNC milling. The objective is to identify how the scaling factor of such tree-like patterns on the cathode flow field impacts the performance of PEM fuel cells. Performance, electrochemical impedance spectroscopy and hold test experiments at 70%, 60% and 50% relative humidity are conducted to study the different new designs. Results are compared to an industry-standard serpentine pattern, and we give recommendations for future improvements of these presented designs.

Chapter 5 discusses the approach on how to model the fuel cell with NET. General assumptions and equations are described. A consistency check based on the difference between entropy balance and the calculated entropy production is implemented to discover weaknesses in the assumptions and models. The concentration, temperature, heat flux and potential profiles are calculated and plotted for varying current densities. Based on these results, we analyse the contributions to the heat and water flux in the different layers and investigate the importance of the exchange current density (j_0).

In Chapter 6 we present an improved model and code based on the work carried out in Chapter 5. The new approach uses a multi-point boundary value problem algorithm, which increases the stability of the code. As the

main objective, we investigate heat effects inside the PEM fuel cell while looking in detail at the various contributions to them. Furthermore, we analyse how changing the temperature at the boundaries impacts the system and if this can be used to improve the performance of a PEM fuel cell.

At the end of the thesis, in Chapter 7, a summary of the presented work and an outlook to the future development on the models and presented designs are given.

1.6 List of publications

Papers 1-5 listed in this section are included as Chapters 2-6 in the thesis. Papers 1,2,4, and 5 have been published in international peer-reviewed journals. Paper 3 has been submitted for publication.

Paper 1. M. Sauermoser, N. Kizilova, B. G. Pollet and S. Kjelstrup *"Flow Field Patterns for Proton Exchange Membrane Fuel Cells"* Front. Energy Res. (2020), 8:13.

Paper 2. M. Sauermoser, S. Kjelstrup, N. Kizilova, B. G. Pollet, and E. G. Flekkøy *"Seeking minimum entropy production for a tree-like flow-field in a fuel cell"* Phys. Chem. Chem. Phys. (2020), 22:6993-7003.

Paper 3. M. Sauermoser, B. G. Pollet, S. Kjelstrup and N. Kizilova *"Scaling factors for channel width variations in tree-like flow field patterns for polymer electrolyte membrane fuel cells - An experimental study"* Submitted to J. Power Sources Advances.

Paper 4. M. Sauermoser, G. Fossati, N. Kizilova, and S. Kjelstrup *"Modelling Electrochemical Cells with Porous Electrodes. The Proton Exchange Membrane Fuel Cell"* ECS Transactions (2019), 92(8):279-292.

Paper 5. M. Sauermoser, S. Kjelstrup and B. G. Pollet *"The impact of Peltier and Dufour coefficients on heat fluxes and temperature profiles in the polymer electrolyte fuel cells"* J. Electrochem. Soc. (2020), 167(14):144503.

During his PhD, the author of this thesis has contributed to the computations used in the following paper, which has not been included in this thesis:

Paper 6. N. Kizilova, M. Sauermoser, S. Kjelstrup, and B. G. Pollet *"Fractal-Like Flow-Fields with Minimum Entropy Production for Polymer Electrolyte Membrane Fuel Cells"* Entropy (2020), 22(2):176.

1.6.1 Author contributions

The work in Paper 1 was initiated as a part of the PhD project of Marco Sauermoser. Natalya Kizilova made the first draft, with substantial input, writing efforts, and discussions from Marco Sauermoser, Natalya Kizilova, Bruno G. Pollet, and Signe Kjelstrup.

The work in Paper 2 was based on the initial description of tree-like structures from Eirik G. Flekkøy. Marco Sauermoser created the software code for evaluating the tree-like flow field in MATLAB based on the theory developed in cooperation with Signe Kjelstrup and Natalya Kizilova. Simulations in OpenFOAM were conducted by Marco Sauermoser with support and input from Natalya Kizilova. Marco Sauermoser made a first draft of the manuscript, with input, comments and discussions from Bruno G. Pollet, Signe Kjelstrup, Natalya Kizilova and Eirik G. Flekkøy.

Marco Sauermoser developed the idea of the experimental comparison of tree-like flow field patterns for Paper 3 in cooperation with Bruno G. Pollet, Signe Kjelstrup and Natalya Kizilova. Marco Sauermoser conducted the experiments with support from Bruno G. Pollet. Marco Sauermoser wrote the first draft of the manuscript with input, comments and discussions from Bruno G. Pollet, Signe Kjelstrup and Natalya Kizilova.

The scope of the simulations for Paper 4 was developed by Marco Sauermoser, Signe Kjelstrup and Giulio Fossati. The code for the model was developed by Marco Sauermoser and Giulio Fossati, based on the theory from Signe Kjelstrup. Signe Kjelstrup wrote the first draft of the manuscript, which was then refined with the simulation results and input from Marco Sauermoser, Giulio Fossati and Natalya Kizilova.

The idea for Paper 5 came from Marco Sauermoser with support from Signe Kjelstrup. Marco Sauermoser developed the code for the simulations. Marco Sauermoser wrote the first draft of the manuscript with input, comments and discussions from Signe Kjelstrup and Bruno G. Pollet.

Chapter 2

Flow Field Patterns for Proton Exchange Membrane Fuel Cells

Marco Sauermoser[1], Natalya Kizilova[2,3,1], Bruno G. Pollet[4] and Signe Kjelstrup[1]

1. PoreLab, Department of Chemistry,
Norwegian University of Science and Technology, NTNU,
NO-7491 Trondheim, Norway

2. Warsaw University of Technology,
Institute of Aviation and Applied Mechanics,
PL-00-665 Warsaw, Poland

3. Department of Applied Mathematics,
V.N. Karazin Kharkov National University,
UA-61022 Kharkiv, Ukraine

4. Department of Energy and Process Engineering,
Norwegian University of Science and Technology, NTNU,
NO-7491 Trondheim, Norway

This chapter was published in
Front. Energy Res. (2020), 8:13

Abstract

Flow field designs for the bipolar plates of the proton exchange membrane fuel cell are reviewed; including the serpentine, parallel, interdigitated, mesh type or their mixtures, furthermore 2D circular and 3D tubular geometries, porous, fractal, and biomimetic flow fields. The advantages/disadvantages and tendencies from field optimizations are discussed. The performance of each flow field design is compared to the conventional serpentine flow field. Good flow field plates give uniform gas distributions, low pressure drop for transport, and sufficient rib area to provide high electronic conductivity. A good field should also prevent water condensation, remove water efficiently, and provide sufficiently high moisture content in the membrane. The demands on design are sometimes contradictory. Future work should aim for a flow field geometry and topology that produces uniform gas delivery at a low pressure drop, and at the same time has an optimal channel shape for better water removal. It is concluded that for an area-filling gas distributor, the developments should aim to find a flow field in accordance with minimum entropy production, making an emphasis on multi-criteria optimization methods.

2.1 Introduction

The rising demands for energy have led to over-consumption of available fossil fuel sources, air pollution, and climate warming. Currently, the necessity for renewable green energy has driven the development toward new energy technologies like solar, wind, tide, geothermal energy, and fuel cells (FC). The proton exchange membrane fuel cell (PEMFC) converts chemical energy into electrical energy and water. The heart of the PEMFC is the Membrane Electrode Assembly (MEA). This is composed of a proton conducting polymeric membrane (PEM) sandwiched between anode and cathode catalyst layers (CL) as well as gas diffusion layers (GDL), see Figure 2.1. The following electrochemical reactions occur in the anode, in the membrane and in the cathode layers:

$$\text{Anode}: \frac{1}{2}\mathrm{H_2} \rightarrow \mathrm{H^+}(a) + e^- \tag{2.1}$$

$$\text{Membrane: } \mathrm{H^+}(a) + t_w\mathrm{H_2O}(a) \rightarrow \mathrm{H^+}(c) + t_w\mathrm{H_2O}(c) \tag{2.2}$$

$$\text{Cathode}: \frac{1}{4}\mathrm{O_2} + \mathrm{H^+} + e^- \rightarrow \frac{1}{2}\mathrm{H_2O} \tag{2.3}$$

The very first FC was designed in 1842 by W.R. Grove and named by him as gaseous voltaic battery [37]. The term "fuel cell" was coined later, in 1889, by the chemists L. Mond and C. Langer. A breakthrough in FC development are connected with the introduction of a sulphonated polystyrene (SP) ion-exchange membrane as the electrolyte by W. T. Grubb in 1955, and by

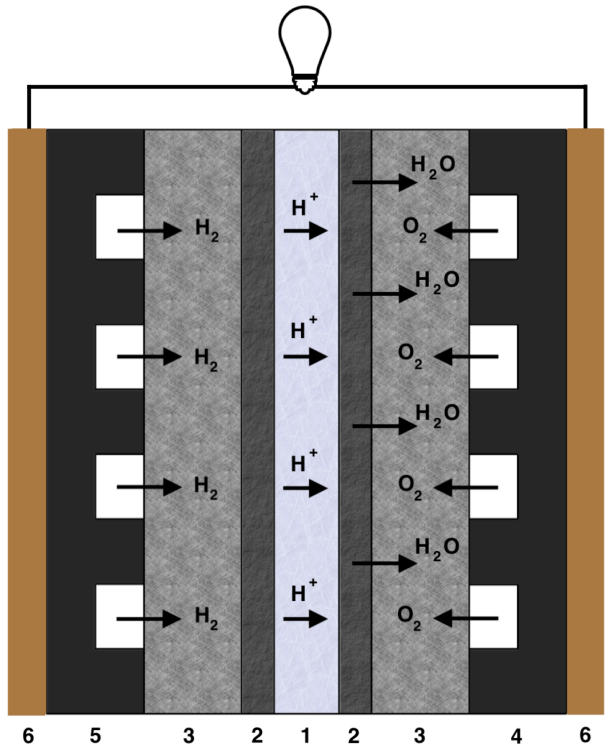

Figure 2.1: Schematic picture of the PEMFC. The layer thickness is given in parenthesis. For abbreviations, see text. 1-PEM (∼50–150 μm), 2-CL (∼10–20 μm), 3-GDL (∼200–300 μm), 4-cathode FFP (∼1 mm), 5-anode FFP (∼1 mm), and 6-CCP.

platinum deposition onto the membrane by L. Niedrach in 1958. In 1966 the SP membrane was replaced by Nafion ionomer that is in use nowadays.

The MEA itself is sandwiched between two flow field plates in a single cell or between two bipolar plates in a PEMFC stack. The flow field plate (FFP) is an important component of the cell as it supplies fuel (hydrogen, H_2), and oxidant (air, O_2) to the MEA, removes water, and collects electrons produced. It also provides mechanical support for the MEA (Figure 2.1). The FFP has several roles, for example, it separates gases between the half cells and neighboring cells in a stack; it provides an electronic conducting medium between the anode and cathode; it possesses a specific flow field design containing channels allowing even distribution of the reaction gases; it provides a solid structure for the MEA, and it facilitates water and heat

management [6].

The FFPs are fabricated from porous/non-porous graphite, coated/non-coated metal, polymer-carbon or polymer-metal composites [6, 38]. The FFP material must be physically durable, electronically and thermally conductive, chemically inert, gas impermeable, easy to manufacture, and have low-cost [25]. The graphite plates are brittle and must be manufactured rather thick to meet the durability requirements, which in turn increases their weight and cost. Metal plates can be machined very thin, but many metals are subject to corrosion when exposed to oxygen and water at high temperatures. Also, graphite is unstable and spontaneously exfoliated with respect to chemical oxidation [39].

Power losses in the FC depend greatly on the current density and the gas transport to the electrodes [13, 14]. Losses are evaluated from the polarization curve. This is also used when someone speaks of the FC efficiency. It can be distinguished between direct and indirect losses. The direct losses are connected to the electric circuit and consist of resistance losses due to the chemical reaction (overpotentials) and ohmic resistances in the circuit. The indirect ones are connected with changes in concentration at the catalytic site, due to rate-limiting diffusion of reactants to the catalyst. Liquid water clogging the pores, will contribute to diffusional losses. Mass transport limitations can seriously affect the PEMFC performance [40–43]. The main role of the FFP is to prevent this type of loss, while keeping the electric and thermal conductivity high. A poor flow-field design can lead to non-uniform reactant distribution in the cell, water condensation in the cathode FFP and clogging of channels with water films and/or drops [44, 45]. The clogging develops gradually via the (i) single-phase flow with stray water droplets, followed by (ii) droplet flow with stable droplets, (iii) film flow with continual films of the walls and stable droplets, and finally (iv) slug flow with high water accumulation [46].

The PEMFC performance can also be hampered by a high local operating temperature, water management, and need for high density of catalyst. The main challenge in the development of PEMFC for automotive applications is to reduce the overall costs of the FC stack [42, 47]. In their latest report, the US Department of Energy (April 25, 2018) announced a target price of US$40/kW for 500,000 systems per year, including 80 kW automobiles and 160 kW trucks [3]. The FFP comprises $> 60\%$ of the weight and 30% of the total cost of the FC stack [5, 26, 48]. A good design of the FFP can thus improve the overall PEMFC stack performance in terms of costs as much as

50% [49].

The Japanese NEDO's Technology Development Roadmap 2017 [4] has as goal for 2040 to achieve a cell voltage of 0.85 V at 4.4 A/cm^2 and 1.1 V at 0.2 A/cm^2. According to Suzuki *et al.* [50] these targets are within reach if all parts of the FC can be optimized beyond the state-of-the-art. Especially materials innovations are needed because the target operating temperature is 120°C.

Performance targets set within Europe differ from application to application (for example for use in electric cars, in trains, etc.) [51]. There is a big focus on parameters like catalyst loading, system costs, durability and general cell volumetric power, and less focus on the performance curve alone as described in [4]. The system's cost goal for 2030 is set at €40/kW for light electric vehicles, given a power density of minimum 2 W/cm^2.

China has likewise created a Roadmap for Energy Saving and New Energy Vehicles [52]. The stated goal is focused more on the cost of FC stacks in vehicles, than on the performance in terms of power density. The power density goal of a stack is set at 4 kW/L for 2030, which is much lower than the one from the NEDO's Technology Development Roadmap 2017 (6 kW/L). The cost goal however is below the one set in the current DOE target (around US$22/kW in 2030).

A comparison between what is available on the market and the progress beyond the state of the art in research is given by Gittleman *et al.* [53] and Wang *et al.* [54].

There is now consensus in the literature that the following properties are important for good FC performance [55–62]. The flow field must:

1. Uniformly deliver well-dispersed gases to the whole catalytic layers at the cathode and the anode;
2. Have sufficient rib area to electronic conductivity;
3. Ensure transport of oxygen gas with a small pressure drop across the FFP;
4. Provide simple and effective liquid water removal to prevent water flooding;
5. Supply oxygen to the catalytic layer at a speed sufficient to meet demands of the cathode.

In this review, the most central flow field designs that have been proposed in the literature, will be discussed with respect to their performance on points 1-5. The most important criterion is that of uniformity in the gas distribution to and inside the GDL and in the catalytic layers. If this can be achieved with a small pressure drop, also the energy dissipation in the flow field becomes favorable. The designs are in the end compared with respect to these criteria in Table 2.1. The review is limited to flow field plate patterns only. Materials, design, and optimum combinations of the MEA and flow field plate are separate important problems and issues for other reviews. The geometry of the bipolar plates is essential in yet another context. They may allow for weight reductions through thickness variations. This counts in disfavor of graphite as a FFP, as this material must be thick to avoid gas leakage and damage of the plate which must be pressed to GDL in a stack. Song *et al.* gives an overview about materials which can be used to create thin FFPs [63].

The present review focuses on low temperature PEMFCs. For studies on the flow field pattern in high temperature PEMFCs, it can be referred to Taccani and Zuliani [64]. Hamilton and Pollet [6] and Asri *et al.* [65] gave a good overview of the different materials and coatings being used in fuel cells, including material suitability, and performance analysis.

2.2 Conventional designs and their modifications

The four most common FFP designs are schematically shown in Figure 2.2. They include serpentine, parallel, pin-type, and interdigitated flow fields that are referred as conventional designs. Their advantages and disadvantages have been thoroughly studied [48]. Great efforts have been devoted to design and explore flow fields that solve the flooding, current distribution, and pressure drop problems [19, 66]. Besides these conventional FFPs, there are mixed designs, circular, tubular (3D), cascade (or pyramid), fractal, and biomimetic flow fields [25, 67]. It has been shown that variations in the FFP design cause differences in peak power density; up to 300% difference between equivalent systems [68]. The serpentine flow field is still regarded as the most popular choice, because of its performance, robustness, reliability, and an acceptable pressure drop [69–71]. For this reason, all the other flow fields shall be compared with the serpentine pattern.

2.2.1 Serpentine design

The traditional serpentine design (Figures 2.2a, c) has a single continuous channel covering the whole area of the FFP. A single inlet is connected to a

Table 2.1: Advantages and disadvantages of various designs tested in the proton exchange membrane FC.

Property tested/ Design	Serp.	Parallel	Mesh-type	Inter-digitated	Channel improv. (L/W)	Non-planar	Porous-type	Fractal-type	Bio-mimetic
Uniform gas distribution	-	-	-	+	+		-	+	+
Electrical conductivity					+				
Pressure drop	-	+			+/-		-	-	+
Water removal	+	-	-	+	+		-	-	
Diffusion limitations	-		-	+	+				

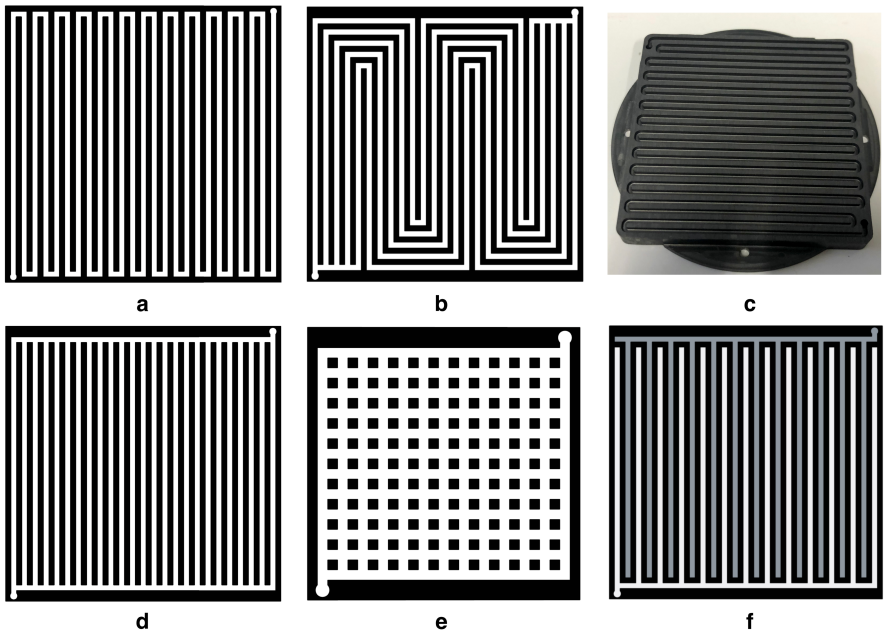

Figure 2.2: Schematic pictures of conventional FFP designs: 1-channel serpentine (a), 5-channel serpentine (b), parallel (d), pin-type (e), interdigitated (f), and a photo of the 1-channel serpentine with 50 x 50 mm FFP (c); the inlet channels are marked in white the outlet ones are in gray.

single outlet. The reactant gases move everywhere from the FFP through porous GDL via under-rib paths. The serpentine design has emerged as an industry standard because of its robust performance and ability to reproduce results [72]. It is used as a reference design, to assess any improved or new designs of FFP. Though water accumulates in the downstream channels, and there are short bends [71, 73, 74], the serpentine topology reduces the risk of flooding in the channel because liquid water can be pushed out. A gas exposed to a relatively high-pressure drop will accomplish this [25, 49]. The column for the serpentine design in Table 2.1 has therefore a plus for water removal. The serpentine flow field is suitable for both small and large active membrane areas [49, 75–78]. This is because it provides good under-rib convection in the GDL due to the relatively high local pressure drop between consecutive channels [49, 75–79]. It also provides a stable performance due to its good mass transfer and reactant distribution capabilities across the flow channels [19, 57]. Furthermore, it gives a relatively smooth temperature distribution. The disadvantages of the serpentine designs are a high resistivity to flow

due to the long narrow channel and presence of short bended channel paths [71, 72, 80, 81]. At low current densities, water can be accumulated below the ribs of the FFP, while at higher current densities this can also happen in the channels (Figures 2.2a, b). Serpentine flow channels for the reactant gas streams and coolant flows produce a low-temperature region near the channel inlet, and a high-temperature region near the outlet [74]. The problem of high-pressure drops has been partially solved using a smaller-sized PEMFC and by optimization of the channel and base dimensions (see below) [49, 75–78]. There is often a non-uniform reactant distribution in the GDL due to reactant depletion along the channel [49, 75–78]. A partial solution to these disadvantages was obtained by multi-path serpentine geometries (Figure 2.2b) and smaller sized PEMFC. For instance, for commercial FFPs with dimensions 50 x 50 mm, the design is based on five parallel channels of width $W = 1$ mm and depth $D = 1$ mm each, see Figure 2.2b. In this design the gas moved in a serpentine manner through 5 parallel paths from the inlet to the outlet at the corners of the FFP (round holes in FFP) making 4-5 turns only. In comparison to the single channel serpentine, this design has channels with 4-5 times shorter lengths and therefore, smaller pressure-drop governing the flow; better water removal from the channels; more uniform gas distribution and, in that way, higher performance. Location of the inlet/outlet and the type of their connection to the parallel channels also influences the FC performance [82].

The disadvantages of such designs remain similar to those for the single channel serpentine [25, 49, 75–79]:

1. Non-uniform reactant distribution in the GDL due to reactant depletion in the short bends and along the channels;

2. A relatively high pressure drop across long length, parallel channels, and in the short bends when the flow gets rotated at 180°.

During the last 15 years there have been many attempts to improve the FFP design and obtain more uniform distributions of reactants and better water removal at reasonable low pressure drops. The relative efficiency of the single-and multi-channel serpentine geometry depends upon their detailed shape and the flow regime. The shape is determined by the W and D of the channels and the distance between them (rib or base, B). In the single-serpentine design sub-rib convection presents under all ribs because of the pressure difference between them. Therefore, the sub-rib convection

significantly influences the FC performance especially when the O_2 supply or membrane moisture content is limited, and the influence almost does not depend on the aspect ratio ($AR = D/W$) [83]. In the multi-pass serpentine FFP the sub-rib convection between the parallel channels is lower due to small pressure differences. At operating voltages < 0.7 V, the reduced channel $AR < 1$ increased the reactant inlet flow velocity, enhanced liquid water removal, and promoted O_2-transport to the GDL. For both designs, the cathode pressure drops increase as the channel AR decreases. They also found that the low external and internal heat transfer coefficients increased the temperature inside the PEMFC and led to too strong sub-rib convection. The combination of high temperature and sub-rib convection may cause PEM dry-out and rapid decrease in the PEMFC performance [83].

Different numbers of the parallel channels in the serpentine design have been studied. For commercial FFPs, with 200 cm^2 reactive area, the 26-channel serpentine flow field gave the best performance and the lowest "pumping power" because the channels became reasonably short and the bends were longer compared to the single channel design [84]. The multi-path geometry decreased the risks of water accumulation and decreased the pressure drop. Two types of interconnections of the 26 channels of W x $D = 0.9$ mm x 0.55 mm, and $B = 0.9$ mm have been studied. It was shown that the shorter path resulted in a more uniform temperature and current distribution and less condensed liquid water accumulation than in the longer path. The 13-channel serpentine FFP geometry has as advantage of its overall performance in comparison with the 26-channel, 6-and 3-channel, due to smaller differences in PEM hydration. The membrane water content and its uniformity are key factors for a low ohmic membrane resistance [84].

Serpentine geometry with tapered, constricted, stepped, and asymmetric channels exhibited [49]: (i) improved performance under low cell voltage, (ii) improved mass transport, and (iii) improved water removal. However, these geometries exhibit high pressure drops and are vulnerable for flooding in the downstream channels and short bends [71, 73, 74].

The mixed serpentine designs like split with mirror or double-mirror locations were aimed at an intensification of mixing of the reactants at every turn of the channels. The advantages are [49, 85] as follows: (i) high uniform reactant distribution, and (ii) lower pressure drop in comparison to the single channel serpentine. The disadvantages are the same as for single and multiple-path serpentine geometries. The mirror-serpentine designs have been recommended for large active MEA areas, because the flow field can be

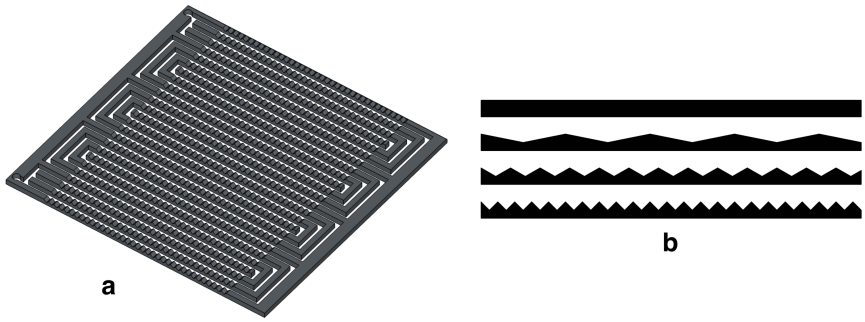

Figure 2.3: 3-channel serpentine FFP with waved channels (a). A cross-sectional view is shown in (b) [sketched after [86]].

split into smaller independent flow-field cells with their own inlets and outlets. That lead to: (i) a decrease in the pressure drop, and (ii) a more uniform reactant distribution in comparison to the non-split serpentine design over the entire MEA area.

Waved channels for the serpentine design (Figures 2.3a, b) were found to be better for reactant transport and water removal because they allow a variation in the local flow along the waved walls [86]. The 3D CFD computations revealed that slopes of 30 and 45° were more efficient than slopes 0 and 15°. The finding was confirmed experimentally. Since the slope 45° exhibited a higher hydraulic resistivity, the value 30° was recommended for the cathode FFP. A summary of results on the serpentine flow fields is shown in the first column of Table 2.1. The minuses are due to liquid water that tends to accumulate in the short bends of the serpentine channels, and the relatively high and variable pressure drop that can cause uneven gas diffusion from the FFP into the GDL. The design is favorable with respect to water removal.

2.2.2 Parallel design

The parallel design, first patented by Pollegri and Spaziante [87], has multiple parallel paths from the inlet to the outlet without bends (Figure 2.2d) in order to decrease the hydraulic resistivity of the flow-field. It was found that this geometry reduced the pressure needed to maintain a constant flow rate at the inlet [88, 89]. This feature can be beneficial for the entropy production rate, but low pressure at the outlet side may not be able to push out the condensed water. Therefore, water droplets appeared, grew and finally blocked the flow-field channels. This led to a non-uniform distribution

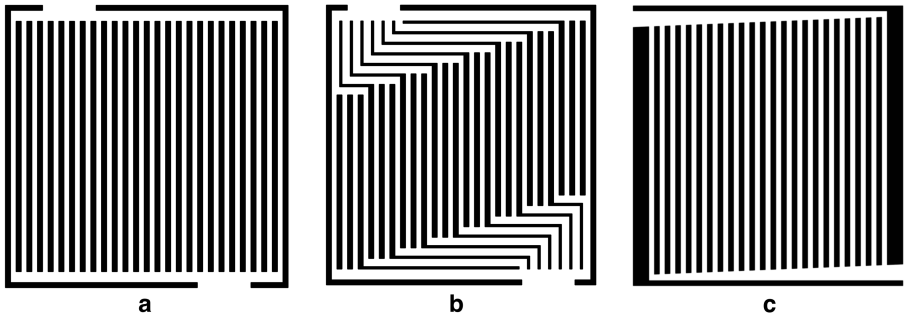

Figure 2.4: Examples of modifications of the parallel design: one multi-path inlet/outlet (a), several multi-paths (b) and inlets/outlets of a constant width with a gradually decreasing inlet channel (c).

of reactant gases and temperatures, which again reduced the life of the system and the overall performance. Parallel designs usually demonstrate the lowest overall performance among the conventional designs [49, 78, 90–93]. Results for these designs are summarized in Table 2.1, column two. Some modifications of the parallel design are shown in Figures 2.4a-c. Several variations including one multi-path (Figure 2.4a), two narrow and two multi-tube (Figure 2.4b) inlets and outlets with different widths of the transverse and longitudinal channels have recently been proposed [94]. The increased width of the outlet channels created a larger pressure drop at the distal ends of the channels, pushing out water. CFD simulations showed that the proposed designs yielded a more uniform flow distribution, as well as gradual pressure reduction from the inlets to outlets, both increase the PEMFC performance. The single inlet/outlet design generated more uniform reactant distribution than the double inlet/outlet designs.

The parallel design with gradually decreasing inlet channel width (Figure 2.4c) gives high flow rates through the secondary channels in the mid portion of the FFP. Thus, in this design ∼60-70% of the flow passed through the initial 80% of total flow-field area [95]. The smoother branching angles of the secondary channels produced lower hydraulic resistivity and therefore smaller energy dissipation. The central location of the outlet provided a better flow distribution compared to conventional parallel channel flow field.

So-called Z-shape designs with the parallel channels located in the Z-shape (Figure 2.4b) have some advantages over the parallel ones (cf. Table 2.1): (i) lower pressure drops, (ii) uniform distribution of single-phase and two-phase

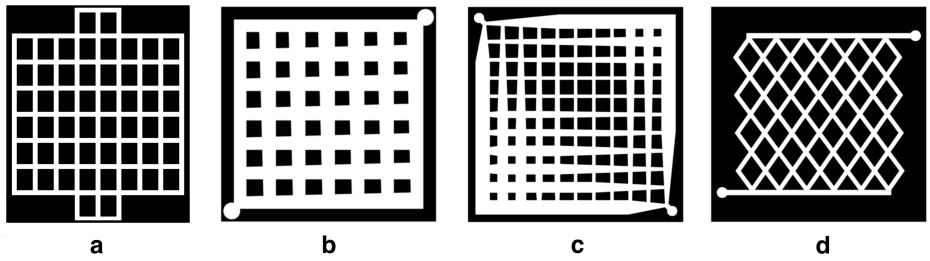

Figure 2.5: Sketches of mesh-type design modifications: with additional areas helping the gas coalesce with water droplets, from [49] (a), with gradually increasing/decreasing, from [100] (b) and optimized, from [98] (c) channel widths, and intersectant geometry, from [90] (d).

flow and absence of plugs, (iii) lower parasitic power for the air supply system; and (iv) higher overall efficiency [96].

2.2.3 Mesh-type design

Mesh-type (pin- or grid-type) designs are composed by two orthogonal sets of parallel channels (Figure 2.2e) allowing two-directional flows [61, 78, 97, 98]. Such designs provide a much lower pressure drop than the serpentine design, since the water accumulation at the cathode FFP becomes lower than in the parallel designs, meaning that the number of droplets blocking an individual channel are reduced [25]. The main advantage of the mesh-type design in comparison to the serpentine and other conventional designs, is the low pressure drop, due to a relatively low hydrodynamic resistivity of the interconnected channels. The disadvantage is an uneven flow distribution and appearance of stagnant areas (see Table 2.1). The disadvantages can be related to the presence of a variety of different routes for flow from the inlet to the outlet. The routes located close to the diagonal of the FFP have the lowest resistivity and, thus, the highest flow rate. This altogether leads to [49, 61, 78, 97, 98] (i) inhomogeneous reactant distribution when the corners far from the inlet and outlet remain almost without reactant, (ii) inhomogeneous condensed water removal, (iii) inhomogeneous current density distribution, (iv) low PEMFC power efficiency (power density values are much lower than in the serpentine designs for the same flow regimes [99]). A prolonged PEMFC operation with mesh-type FFP at high flow rates can lead to complete flooding of the FFP. To overcome the problem, the designs have been modified with additional areas outside the active area, to help the gas coalesce with water droplets (Figure 2.5a) [49]. Using smoothly varying channel widths (Figure 2.5b) [25, 100], and gradually decreasing channel

widths (Figure 2.5c) [98] the problem was overcome. Assuming Poiseuille flow with uniform reactant consumption in each node of the mesh, the optimal widths of the nodes for the minimal flow variations in the nodes over all the system were computed. It was shown this geometry could increase the PEMFC performance by ∼10%.

Recently a non-rectangular intersectant geometry (Figure 2.5d) has been tested based on a theoretical model and on the experimental setup for a metallic FFP [101, 102]. The optimal dimensions and porosity per unit length were determined as 0.6 x 0.3 mm and 0.5, respectively. The intersectant design at the optimal operating parameters, 300 ml/min for the hydrogen flow, 500 ml/min for the air flow, and at operating temperature of 80°C, exhibited better performance than the standard single channel serpentine design (see Table 2.1).

2.2.4 Interdigitated designs

Interdigitated flow-field geometries do not have a continuous path from the inlet to the outlet, so the channels have dead-ends (Figure 2.2f) [103]. Such designs are aimed at forcing gas flow delivery through the GDL to the reaction sites in the MEA and remove water more efficiently [25]. It was shown that generally, interdigitated designs performed better than parallel designs, but worse than serpentine ones [68, 103]. The corresponding differences depended on flow conditions [104]. Interdigitated designs seem to be able to manage water removal better than parallel designs, without the excessively large pressure drops proper to serpentine designs [67].

The advantages of the interdigitated design [49, 75, 77, 78, 90, 92] are as follows: (i) efficient water removal due to forced under-rib convection in the GDL (high pressure drop), and (ii) high performance at high current densities when water production is significant. The disadvantages are: (i) this type of FFP has the highest resistivity and pressure drop among all designs due to disconnected channels, (ii) the PEMFC performance is strongly determined by GDL properties, (iii) possible long-term damage to the GDL and MEA from excessive convective forces (see Table 2.1). Some modified interdigitated designs with varying (both decreasing and increasing) widths of the parallel channels from central to lateral ones with two (Figures 2.6a, b) and three (Figure 2.6c) inlets and different number of parallel channels may be beneficial, due to their reduced pressure drop and improved current distribution compared to conventional interdigitated design (Figure 2.2f). Variation of the widths, depths and rib width values within wide ranges, reveals designs with lowest pressure drops and highest performance [105].

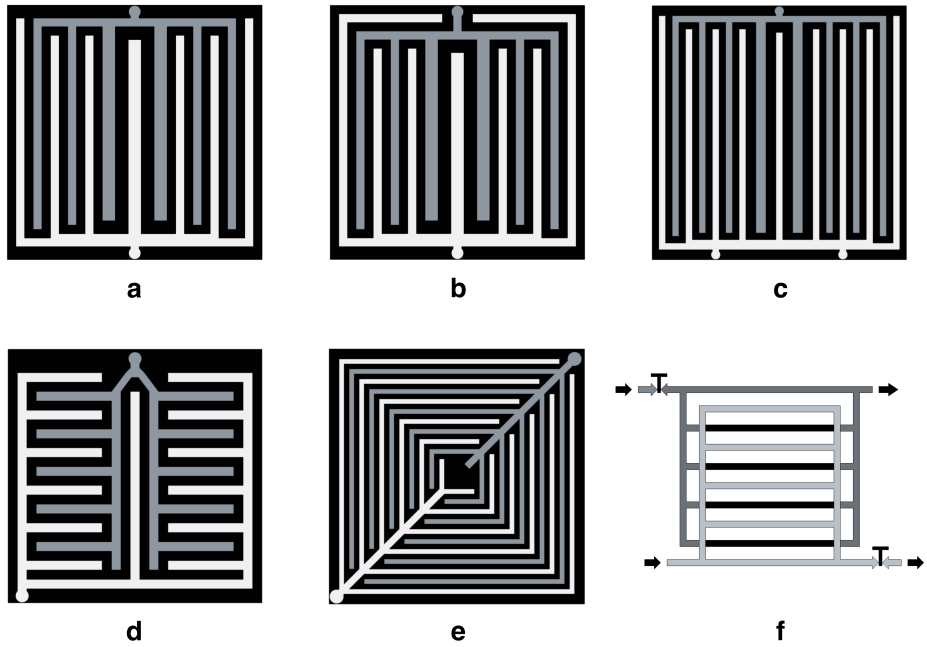

Figure 2.6: Sketches of modifications of interdigitated designs: with two inlets (a) and perimeter channels (b), with three inlets (c) from [105], non-fractal lung-type (d) and leaf-type (e) from [81], switched parallel-interdigitated type (f) from [106].

Two interdigitated designs (Figures 2.6d, e) are biologically inspired. They mimic the lung (Figure 2.6d) and the plant leaf flow conduction systems (Figure 2.6e) [81]. 3D numerical computations revealed that both designs can produce up to 30% more in peak power density in comparison with conventional interdigitated (Figure 2.2f) and single-channel serpentine (Figure 2.2a) designs, with the same dimensions of the channels and bases. It was shown by CFD simulations and experiments at operating temperatures T = 65-75°C, 2 atm back-pressure, and 100% relative humidity (RH), that the leaf design (Figure 2.6e) performed better than the lung-type design (Figure 2.6d). A comparative experimental study of different combinations of 5-channel serpentine, lung-based (Figure 2.6d), and leaf-based (Figure 2.6e) designs showed that the lung-based structure displayed the lowest performance under all tested operating conditions [77].

The synthetic design (Figure 2.6f) can be switched from classical parallel to interdigitated and vice versa by closing/opening of the taps (T) [106]. It was shown by experiments that the parallel flow field regime produced higher

system power and lower water at lower current densities. At high current densities, when water production was significant, the interdigitated design was more efficient for water removal and higher performance of the FC.

In principle, one could use different designs for the anode and cathode FFPs. Combinations of serpentine (S) and interdigitated (I) FFP designs S-S, S-I, and I-S for the anode and cathode, respectively, have been tested [78]. It was found that the best performance could be achieved when the serpentine FFP was used at the anode and the interdigitated FFP at the cathode. The highest reactant uniformity in the catalyst layer (CL) was observed in the S-S and S-I configurations.

2.3 Improvement of the channel geometries

2.3.1 Variations in dimensions of the channels and ribs

High impact of the 3D-nature of gas and water channels in the FFP system on the FC efficiency has been confirmed by experiments and numerical simulations. In the 3-channel serpentine FFP the decrease in the channel depth from $D = 1.0$-0.3 mm linearly increased the FC performance due to lower water accumulation in the channels confirmed by experiments on a transparent FFP [107]. The decreased channel depth leads to an increase in the linear velocity of the reactants and products at the same flow rate that, in turn, improves water removal.

The ratios between W, L, and B have also a great effect on the reactants flows, pressure drop, water removal, mechanical stiffness, temperature distribution, as well as on the electrical conductivity [108, 109]. It is recalled that the flow channels are used for water and heat removal, reactants delivery and distribution to/in GDL and CL. The space between the flow channels is used for heat/mass transfer, electric current collection, and transmission. Different strategies to improve the water/heat management and PEMFC efficiency by changing the channel path length, rib width B, and rib/channel width ratio B/W have been proposed [61, 84, 110].

An experimental study of the flow interactions in the adjacent micro-channels, revealed that under-rib convection has an essential effect on the PEMFC performance arising from the local electricity collection under either the inlet channel or the rib areas [111]. The rib areas possessed the highest current density when sufficient pressure differences were applied to the FFP. The inlet channel always exhibited a higher current density than the outlet channel, possibly due to its higher gas concentration. The existence of an

optimal pressure drop in the flow field was documented, when the current density under the inlet channel and the rib areas reached its maximum. The 3D CFD computational results showed that significant temperature gradients exist within the PEMFC, with temperature differences of several degrees within the MEA [112]. This was explained by charge transport under the collector plates. A major impact on the current distribution as well as the predicted limiting currents was also seen. The 6- and 10-channel serpentine flow fields with different combinations of the channel dimensions $W = 0.5$ and 0.9 mm, $D = 0.5$ and 1 mm, $B = 0.5$ and 0.8 mm have been studied with isothermal two-phase 3D models [113]. It was shown that the PEMFC performance can be increased by using narrower channels and smaller cross sections [113, 114]. At low current densities when water starts to accumulate in the GDL at under-rib regions, the under-rib convection plays a more important role for water removal, than the pressure drop does. At high currents, water starts to accumulate in the channels and the pressure drop becomes more important for water removal and promotion of the oxygen transport to the catalyst layer.

Some of the proposed designs have led to a higher pressure drop [115], lower PEM hydration and conductivity, ineffective heat and water management [84]. The general conclusion is that wider ribs and shorter and narrower channels improve the reactant distribution in the GDL [61, 84]. Nevertheless, the influence of the L/W ratios on the flow parameters and FC performance revealed some contradictions [26, 61, 84]. For instance, the ratio $L/W > 1$ is favorable for:

- Mechanical support of flow field for PEM and GDL;
- High membrane water content;
- Good electrical conductivity;
- Fast heat transfer from the membrane;
- Uniform current distribution in MEA;
- Uniform temperature distribution in MEA;
- Better PEMFC performance at high current densities;

while the ratio $L/W < 1$ is favorable for:

- Lower pressure drop across the flow fields;
- Larger contact area between the reactants and the GDL;
- Better water removal from the GDL;
- Lower total cell voltage losses.

Additionally, the width/rib (W/B) ratio influences the same main features of the PEMFC efficiency and make the problem of the FFP optimization even more ambiguous. In [116], the importance of the width of the ribs was demonstrated, and the best performance of the PEMFC was detected for $W/B = 0.25/0.25$ mm value within the limits $B = 0.25$-1 mm. FFPs with shallow channels exhibited higher performance than the deep ones. The reason for this was that shallower channels have a higher-pressure difference between adjacent channels than deeper channels, leading to an increase in O_2 transport due to higher under-rib convection [117]. The forced gas delivery led to better performance when the FFP had tapered channels [118].

For some channel designs, the reactants were removed too quickly from the CL, leading to appearance of dead zones with low energy production [78]. In conclusion it can be said that multi-criteria optimization approaches are important for design improvements. Some designs for optimal pressure drop and cooling efficiency have been discussed in Alizadeh *et al.* [119].

Similar conclusions have been derived in the experimental study of 44 cm^2 graphite cathode plates with four single serpentine geometries of 1 mm channel depth and various widths of 0.5, 1, 1.5, and 2 mm [120]. The number or the parallel paths were 43, 31, 27, and 23, accordingly. It was found that the cell performance always increased with a decrease in the rib width and an increase in the inlet flow rates in the channels when the provided pumping power was not taken into consideration. However, when pumping power was accounted for, the net power density reached a maximum at different combinations of rib widths and reactant flow rates depending on the cell voltage.

Numerical simulations revealed that a maximum current density $j = 1.04$ A/cm^2 could be achieved at $B/W = 0.25/0.25$, but the anode/cathode pressure drop in this case became very high ($\sim$15/92 Pa (anode/cathode) for 25 mm channel length) [26]. A low pressure drop along anode/cathode channel $\Delta p \sim 2/6$ Pa was reached at $B/W = 0.25/2.0$, but in this case the current density was only 0.79 A/cm^2 and the ohmic resistance was very high.

Therefore, an intermediate value $B/W = 1.0/1.0$ mm was proposed as an optimal one, giving the current density 0.9 A/cm^2, and the anode/cathode pressure drop of $\Delta p \sim 3/11$ Pa [26]. The ohmic losses from the interfacial contact between the FFP and GDL increased monotonously with the B/W ratio, while the loss due to diffusion in the GDL remained negligible. The impact of the FFP on the polarization curve rapidly decreases at $B/W < 0.2$ and slowly decreases at $B/W > 0.2$. As a result, the total voltage loss is at its minimum at $0.4 < B/W < 0.6$.

2.3.2 Variations in cross-sectional shape

Variations in the geometry of the serpentine design and the shape of the channels have been studied theoretically and experimentally. Circular [108, 121], annular [122], semi-circle [27], trapezoidal [123], and triangle [124] cross-sectional shapes of the channel have been proposed and tested.

Numerical computations on the FFP with dimensions 40 x 40 mm with 20 channels of the same $W = 1.5$ mm and square, triangle, and semicircle cross-sections in a serpentine design have been carried out [27]. It was shown for the same inlet flow rates, that the pressure drop was lower in the rectangular shape and higher in the semi-circle channels. Hydrogen consumption was 84.8% in the rectangular, 92.5% in triangular, and 92.9% in the semi-circular channels, *i.e.*, the latter was more efficient. O_2-consumption was maximal at $D = 1.5$ mm, *i.e.*, in the quadratic cross-sections. Therefore, simultaneous demands for minimum pressure drop and high H_2-consumption are contradictory. A two-criterion optimization approach could determine optimal WxD dimensions and cross-section shape. The problem formulation in Kumar and Reddy [27] is incorrect because the chosen cross-sections (square WxD = 1 x 1 mm, equilateral triangle $W = 1$ mm, and semicircle $D = 0.5$ mm) possess different hydraulic resistivity and lateral surfaces for the mass and heat exchange.

The rectangular and triangular shapes of the same width and cross-sectional area were compared in experiments [124]. Both cathode and anode FFPs had the 5-channel serpentine design with four short bends (Figure 2.2c), and the anode plate was turned at an angle of $\pi/2$ cathode plate. It was found that the condensed water was mostly trapped in the two corners adjacent to the GDL; therefore, the channels with triangular geometry retain less water than rectangular channels. When the GDL with lower in-plane gas permeability was used, a smaller amount of the retained water was detected.

With a 3D non-isothermal model of the flow-field, using a genetic algorithm

to study the optimization of channel configuration, it was found that the trapezoidal shape was better than the square shape 1 x 1 mm with the same cross sectional area [125]. The optimal dimensions ($W = 1.3$ mm, $D = 1.1$, and bottom width 0.89) increased the productivity of the PEMFC by 10.92% at an operating cell voltage of 0.4 V.

2.3.3 Additional improvement measures

The channels could also be modified by an additional slant up or down related to the plane of the FFP. The down-slanted (at the angle of 20°) parallel channels in the 5-channel serpentine design of the anode FFP increased the PEMFC performance [126]. The down-slanted channels increased water back diffusion from the cathode to anode, decreased the concentration of condensed water in the anode GDL and CL, leading to PEM hydration and higher PEMFC performance especially in the medium current region. The same modifications of the cathode FFP led to intense water draining from the cathode side leading to PEM dehydration and reduction in the PEMFC performance. The up slanted anode or/and cathode channels induced flooding and low performance. Similar results have been obtained on the 35° slanted channels [110].

2.4 Mixed and non-planar designs

There are many experimental and theoretical studies of different modifications of conventional designs, including different numbers [71, 127], and dimensions [27, 128–130] of inlets, outlets, and channels, smoothed corners, and other improvements. Mixed designs are based upon combinations of two or more of the convenient designs like parallel-serpentine, mirror-serpentine, serially linked serpentine [49], spiral-serpentine [131], split-serpentine [72], and others. Some of them managed to enhance under-rib convection, improve water removal, and FC performance noticeably [72]. Several tubular designs presented by the usual sandwich-type FC composition (Figure 2.1) rolled into a cylindrical [122, 132] or conical shapes have also been proposed [121]. The cone geometry was estimated as more efficient in comparison to the cylindrical one with the same design (serpentine or parallel) of the flow-field.

2.5 Circular geometry of FFP

Other less common approaches include radial (Figures 2.7a-c) [133, 134] and spiral (Figure 2.7d) [135] designs for circular FFPs and PEMFCs. A radial flow-field design was developed for a circular, tablet-type PEMFC.

The reactants enter the flow-field through a tube in the middle of the circular region (Figures 2.7a-c) and move through the radial channels to the perimeter. In some of these designs (Figures 2.7a, b) [136], radial channels are linked by circular ones that are used to keep the pressure drop even across the channel length. The number of the radial channels could be different. A numerical analysis of three radial flow configurations with 4, 8, and 12 radial channels revealed that the 4-channel model had the best performance, i.e., the highest current density production at the lowest pressure drop along the channel length [133]. The best gas velocity range 0.03 m/s $< v <$ 0.04 m/s allowed fast flow without any stagnation and flooding at reasonable low pressure drops. In other designs, the inlet and outlet channels are not connected (Figure 2.7c). This mixed radial interdigitated design provides additional smoothing of the reactant- and temperature distributions, due to intensified mixing in the space between the two systems of the interdigitated inlet and outlet channels. The short paths of the radial designs provide very low resistance and, thus, pressure drop. Due to the same reason, the water removal is better, and a higher mass-transport, current density, and better performance can be obtained [49, 133, 134]. A better performance was achieved even when the pressure drop was kept twice as low as that in the square FC with the serpentine FFP [134], leading to the assessments in Table 2.1.

The radial flow-field design is still under development and not well-documented by experiments. There are disadvantages connected with the presence of the distributed system of outlets at the perimeter. This increases system complexity especially when the PEMFC is integrated into a full stack. That may also produce instability, if one or several outlets become clogged by condensed water [134]. In dry air with radial flow-fields, the PEM is susceptible to drying. The problem can be solved by humidification of in the environment. Large ohmic losses are also among the disadvantages of the radial design.

Spiral flow field geometry has also been developed for the circular region [135, 137], but the relatively long spiral channels need higher pressure than the parallel or synthetic designs do. An improved design with multiple concentric spirals (Figure 2.7d) decreases the hydraulic resistivity of the channels by decreasing their lengths. CFD computations on spiral designs with 1-8 channels, showed that the model with 4 spirals exhibited more uniform distributions of reactants and current density, larger power generated, and relatively small pressure drops [135]. The model with 8 spirals demonstrated the worst performance.

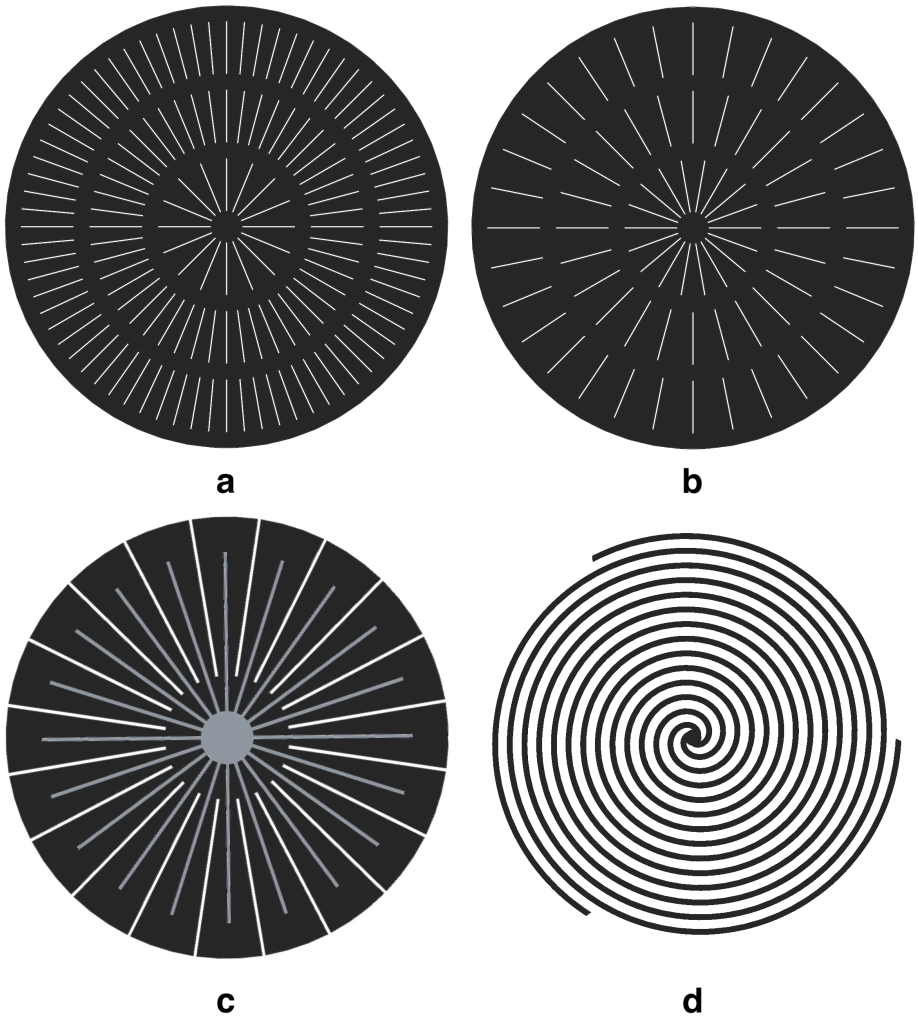

Figure 2.7: Sketches of radial designs: with 16-48-72 (a) and 18-24-32 (b) radial and 2 circular channels, with 20 pairs of radial interdigitated channels (c), from [134], and 3-channel spiral design (d), from [135].

2.6 Porous type FFP

The porous materials provide better drainage of the condensed water that is advantageous at high current densities [138, 139], and more uniform reactant gas distribution compared to the FFPs with channels [88]. The foams, meshes and fibrous porous materials have been tested as candidates for the FFP [131, 140].

Metal meshes and foams are easy to manufacture; they provide a uniform flow distribution over the MEA and even distribution of the current density, but they are vulnerable for corrosion and need special anti-corrosion and hydrophobic coating that is not such stable and durable like titanium and graphite [25]. Unlike the foams, meshed materials have a regular porous structure with single or dual porosity and are easier for manufacturing, while in the foams identical porosity properties are difficult for reproduction. Due to their plane construction the meshes have a better controllable contact area with GDL than the foams. Meshed FFP demonstrated good performance at limited current ranges. Smaller pores lead to more uniform reactant distributions but higher hydraulic resistivity and water accumulation. Therefore, the optimal design satisfying the main performance criteria for the FCs (see section 2.1) is difficult for elaboration due to numerous disadvantages [49, 78, 141, 142]. The flow resistance could be decreased by optimizing the porosity of materials. Thus, the highly porous material with ∼85% porosity and double peak in the pore diameter distribution with maxima at d ∼150 and ∼30 μm exhibited the smallest gas diffusion resistance at a high current density operation among other materials [139].

2.7 Fractal type design

The first multichannel fractal design of the PEM and direct methanol FCs was proposed in 2004 [80] (Figures 2.8a, b). It was based on a combination of fractal distributing and parallel delivering channels. A combination of fractal distributing and serpentine delivering channels has also been tested [143]. By a fractal approach, it is meant that the diameters and lengths of the channels of the consecutive generations are related by the scaling laws

$$\frac{d_{j+1}}{d_j} = a, \frac{L_{j+1}}{L_j} = b \tag{2.4}$$

where a and b are constants for self-similar scaling. The algorithm that generates the structure is designed to fill in a given area of rectangular shape (Figures 2.8a, b), Z-shape or other shapes. The diameter ratios in the

junctions were not determined in Tüber *et al.* [80]. Under some operating conditions with low water condensation, the PEMFC with fractal structure FFP (Figures 2.8a, b) exhibited better performance than the serpentine (Figure 2.2a) and parallel (Figure 2.2d) designs, mainly due to the lower hydraulic resistivity of the fractal structure [80, 144]. Anyway, the fractal system was found to be vulnerable for blockage of the channels by water, leading to non-uniform reactant distribution. Therefore, the PEMFC performance with fractal channels was higher than the conventional parallel design, but lower than the conventional serpentine design [80], cf. Table 2.1. A uniform gas delivery to the MEA active area could be achieved with a binary tree fractal with branching angle $\alpha = \pi$ (Figure 2.8c). Rectangle channels in such designs can easily be engraved in a graphite plate. Designs with different number of generations with N = 16-64 outlets, have been studied theoretically and experimentally [11, 146, 147].

The dimensions of the channels were computed based on the optimization approach

$$\dot{W} \rightarrow \min, V = \text{const} \tag{2.5}$$

where $\dot{W}$ is the viscous dissipation and V is the volume. Such design corresponds to minimum entropy production at isothermal conditions [13, 148]. Due to asymmetry of the streamlines at the branching and rather short lengths of the tubes, the resulting flow in the multiple outlets will not be uniform. The flow non-uniformity has been estimated by the parameters:

$$q = \sqrt{\frac{1}{N-1}\sum_{n=1}^{N}\left(\frac{Q_j}{Q_{avr}} - 1\right)^2} \text{ and } \theta = \frac{Q_{max}}{Q_{min}} \tag{2.6}$$

where Q_j are flow rates in the n=1,...,N outlets, Q_{max}, Q_{min}, Q_{avr} are the maximum, minimum and average values of the flow rate.

In the model with N = 16 outlets, presented in Figure 2.8c, q increased from 0.001 to 0.055 and θ increased from 1.003 to 1.014 when the Reynolds (Re) number increased from Re = 150 to 650 [147]. In the model with N = 64 outlets, q increased from 0.0002 to 0.0013 and θ increased from 1.002 to 1.007. Therefore, the model with N = 64 outlets produced a more uniform flow distribution at the lowest pressure drop and energy dissipation. The fractal system with 256 outlets was found to have the highest uniformity of the flow and consequently the current distribution [147], but the overall PEMFC performance was lower than in the convenient parallel design [78, 85, 146, 149].

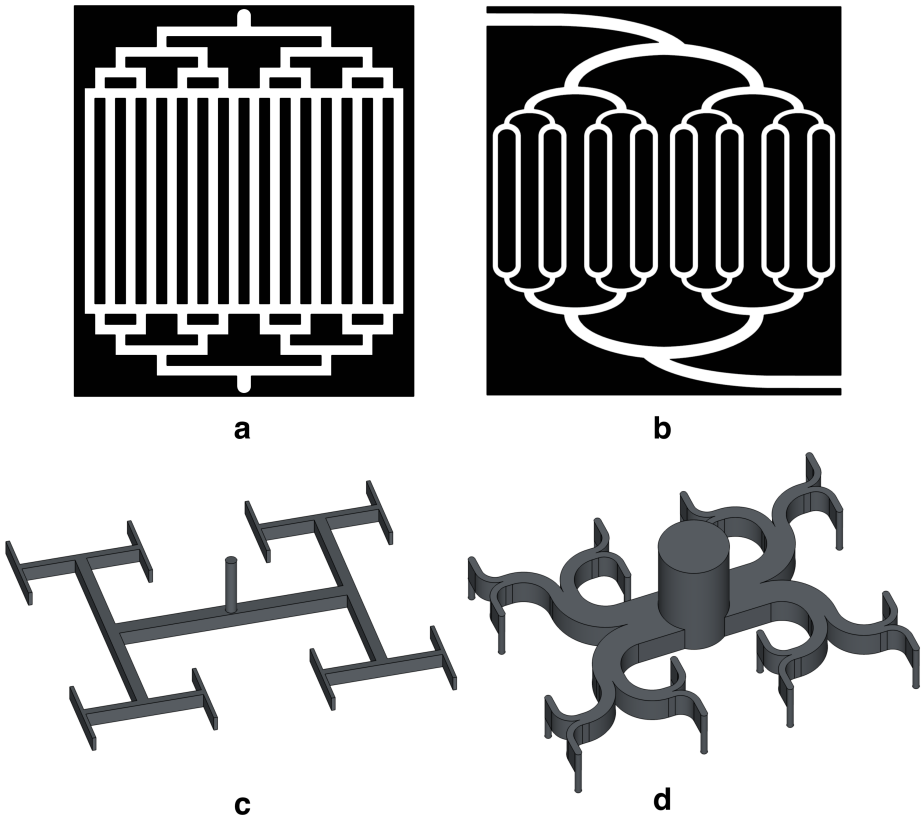

Figure 2.8: Sketches of the fractal type designs for FFP: open channels fractal+parallel with sharp (a) and smoothed (b) angles from [80], and closed channels fractal tree with sharp (c) and smoothed (d) branching angles, from [145].

The angles in the bifurcations can be smoothed, and in that way a more efficient fluid distribution system (Figure 2.8d) can be obtained. It was shown by Lattice Boltzmann simulations that the optimized distributor has between 15.9 and 25.1% lower pressure drop than one with sharp angles (Figure 2.8c) [150]. The fractal-type flow fields composed by n parallel plates with a network of interconnecting channels are called "pyramidal" [146, 151]. In the case $n = 3$ the FFP is presented by three parallel plates with one tubular inlet, planar tree-like fractal system and tubular outlets. Similar 3D binary trees with sharp and smoothed branching angles have been tested [145]. Such structures are not good for PEMFCs because the thickness of the graphite layers increases both weight and cost of the FC.

At higher Re numbers the non-uniformity increased, and when Re increased from 1,020 to 2,247, q increased from 0.050 to 0.069 and θ increased from 1.170 to 1.252 [146]. However, the disadvantages of the fractal design are as follows: (i) vulnerability for blocking one or two outlets by liquid water. This makes the gas flow and generated current non-uniform; (ii) large widths of the first generations of the channels are unfavorable for the under-rib convection (see Variations in dimensions of the channels and ribs), and this decreases the FC performance; and (iii) manufacturability problems are essential for the smallest channels.

2.8 Bio-mimetic designs for FFP

During the last decade, novel types of FFP designs, inspired by nature and mimicking the structure of biological transport networks, have been elaborated [9, 25, 80, 81, 98, 147, 152]. The idea has been that the FFP in PEMFC should mimic the transport function that can be seen in blood vessels, bronchial airways, and fluid conducting vessels in plants. These biological structures deliver fluids, gases or their mixtures to porous structures (tissues, lungs, wood, or GDL), and uniformly distribute them over a given volume. Over time on Earth, optimal structures and systems in plants and animals have evolved, including fluid delivery systems that are constructed as branched networks; each conducting element with diameter do is split into k daughter elements with diameters d_1,....,d_k satisfying the relationship:

$$d_0^\gamma = d_1^\gamma + d_2^\gamma + \ldots + d_k^\gamma \tag{2.7}$$

Murray derived the relationship (Eq. 2.7) from the optimization problem (Eq. 2.5) in the case of binary trees $k = 2$ and obtained $\gamma = 3$ [153]. This relationship is widely used as the most popular biomimetic optimization rule [154–156]. According to (Eq. 2.7), in a symmetrical branching, the fractal

scaling coefficient $a = k^{-1/\gamma}$; and for binary trees $a \approx 0.8$. The branching angles φ_1, φ_2 in an optimal bifurcation are also related to the diameters [157].

Numerous statistics on the geometric construction of natural transport networks have shown that they comply with principles of minimum work, minimum energy dissipation or minimum entropy production. For asymmetric bifurcations (Eq. 2.5), gives the values that correspond perfectly to the geometry of the respiratory systems [158]. Fractal-type geometries (Figures 2.8a, b) have therefore been designed using the Murray's scaling factor a = 0.8 [25]. It was shown that the pressure drop needed for gas delivery and distribution over the GDL surface was negligibly small in comparison to the conventional designs. Murray's law-based design has been used for power-law fluid flows in microfluidic fractal systems with Y-junctions of tubes with rectangular cross-sections and constant depth. A similar approach was proposed to deal with suspensions of micro- and nanoparticles in rigid and compliant ducts [159–161]. An improved intersectant design (Figure 2.5d) with the cross-sectional angles computed according to Murray's formula (Eq. 2.7) was studied by CFD and validated experimentally [101]. The design showed better performance, more uniform distribution of reactants and better water removal. Therefore, the biomimetic design based on the Murray's rules for dimensions and branching angles of the channels in the FFP, can be successfully used for performance improvement of the PEMFC.

2.8.1 Constructual theory-based designs

The constructal law was formulated by Bejan as a self-standing physical law that explained existing designs in natural transport systems as a result of evolutionary optimization. According to the law, evolution has aimed for minimum entropy production, which under certain conditions is equivalent to minimum flow resistance, minimum weight, or uniform maximum stresses at constant volume [154].

The constructal law was used for shape-optimization of the traditional serpentine design [49], (see section Variations in Dimensions of the Channels and Ribs, Figure 2.3d). A non-planar layered design of channels with scaled width $a_1 = w_{j+1}/w_j$, base $a_2 = b_{j+1}/b_j$, and length $a3 = L_{j+1}/L_j$ was studied for constant PEMFC membrane area of the PEMFC and constant width and base of the inlet channel [151]. Flow in channels of rectangular cross-section was considered, and the target design was determined from the condition of minimum hydraulic resistance. The optimal scaling coefficients were computed for different number of channels in the branching, and inlet

velocity in the parent channel. The computed values $a_1 = 0.8151$-0.8422 and $a_2 = 0.7892$-0.7936 were surprisingly close to Murray's scaling factor for binary trees of tubes with circular cross-sections. It was shown for different inlet velocities $v_0 = 10$, 20, 30, 40, and 50 m/s, that the tree network system provided 12, 26, 51, 114, and 485% higher maximum net power densities, respectively, in comparison to the conventional FFP designs.

2.8.2 Lung-shaped designs

The fractal structure of human bronchi and lower airways provides uniform distribution of O_2 to and CO_2 from a given volume. It has been shown that they conform with Murray's law [15]. The structure provides also a good balance between the convection and diffusion driven flows in the larger and smaller airways [162]. An interdigitated design resembling the respiratory system with main bronchi branched into the secondary airways (Figure 2.6d), but without the fractal scaling, was proposed and compared to the serpentine, interdigitated and leaf-inspired (Figure 2.6e) designs [81], see section 2.2.4. Relative to the studied configurations, this design displayed the lowest performance under all tested operating conditions [77]. A multi-plate layered design for the FFP inspired by the lung geometry was recently developed [7]. The larger branches of the fractal tree were scaled according to (Eq. 2.7), with $\varphi_1 = \varphi_2 = \pi/2$. The flow field plate was then 3D printed via Direct Metal Laser Sintering. The size of the outlet channels was based on the Peclet number $Pe = 1$, considered as a necessary and sufficient condition for efficient convective and diffusive transport [162]. The advantages of the 3D lung-inspired design compared to the serpentine design [7] were: (i) low pressure drop (minimum entropy production); (ii) uniform reactant distribution for both low and high temperatures; (iii) high electrocatalyst stability; (iv) easy scalability. The disadvantage was that the design is more vulnerable for flooding than serpentine design [10].

2.8.3 Plant leaf-based designs

The plant leaf-type designs are mostly based upon leaf-like patterns with bifurcations and trifurcations of the secondary channels going from the parent channel at some branching angles proper to plant leaves. Since the structure has to fill in a square, rectangle or circular area, the angles follow the geometry of the MEA. Patterns resembling the pinnate venation of plant leaves with one or two (Figure 2.9a) consequent branches at two different angles have been modeled using CFD [11]. This structure resembles two flow fields of the parallel type with a common straight inlet tube. By changing the branching angle from $\pi/2$ to an acute angle, the viscous dissipation

in the system decreases. When the branching angles are combined with Murray's law for the diameters, Equation 2.7, and branching angles [157], the energy dissipation is minimal [155, 157]. In the design presented in Figure 2.9a, the first and second branching angles have been taken as $\alpha = 37, 74°$. These are the most frequently found in leaf venations [11]. The resulting current density values were in some cases 10 orders of magnitude larger than the ones detected in a serpentine flow field at the same flow conditions (6,900 A/m^2 at the entrance and 2,200 A/m^2 at the exit), but the gas and current density distributions were highly non-uniform. A leaf-like structure of channels (Figure 2.9a) [9] was designed, paying attention to mechanical properties of graphite. Since the material is very hard, but fragile, the diameters of the channels cannot be too wide because one must avoid weakening of the FFP. The 3D CFD simulations showed that such a design provided more uniform mass- and velocity-distributions along the channels than those in the conventional parallel and serpentine designs. The power density was also higher than in the parallel and serpentine FFP, up to 56 and 26%, respectively [9]. The leaf-based design was reported to need ∼15% less material in comparison to conventional designs, namely with masses of 3.50 g for leaf-based, 3.83 g for parallel, and 4.06 g for serpentine designs. Three branching angles (30, 45, and 60°) were tested and the angle 45° provided the most uniform reactant distribution. When the angle was 30°, the fluid flow between lands was blocked, and most of the flow moved throughout the sides of the cell. When the angle was 60°, most of the flow passed between lands and a very small portion was transferred across the sides or penetrated into the GDL.

A leaf-inspired square-filling FFP design with two inlets and interdigitated parallel channels of constant width and depth was studied in Kloess *et al.* [81], see section 2.2.4. Similar structures, resembling parallel channels of constant dimensions and decreasing width of the inlet channels (Figures 2.9b, c) were studied [77]. The width of the tapered parent channel was computed from Murray's law for the hydraulic diameters $D_h = 2WD/(W + D)$ of the rectangle channels with dimensions WxD ($k = 3$). Experiments on different combinations of designs L1 (Figure 2.9b), L2 (Figure 2.9c), lung inspired LI and 5-channel serpentine S on a direct methanol FC (DMFC) at 70°C as anode and cathode FFPs demonstrated that: (i) the S-L2 configuration had the highest performance (peak power density for the S-L2 888 W/m^2 while S-S configuration produced only 824 W/m^2); (ii) the L1, L2, and LI designs showed their highest performance when used on the cathode side; and (iii) the performance depended upon the reactants flow rates and was the highest for $Q = 3.9$ ml/min methanol and $Q = 1.2$ ml/min O_2 flow rates.

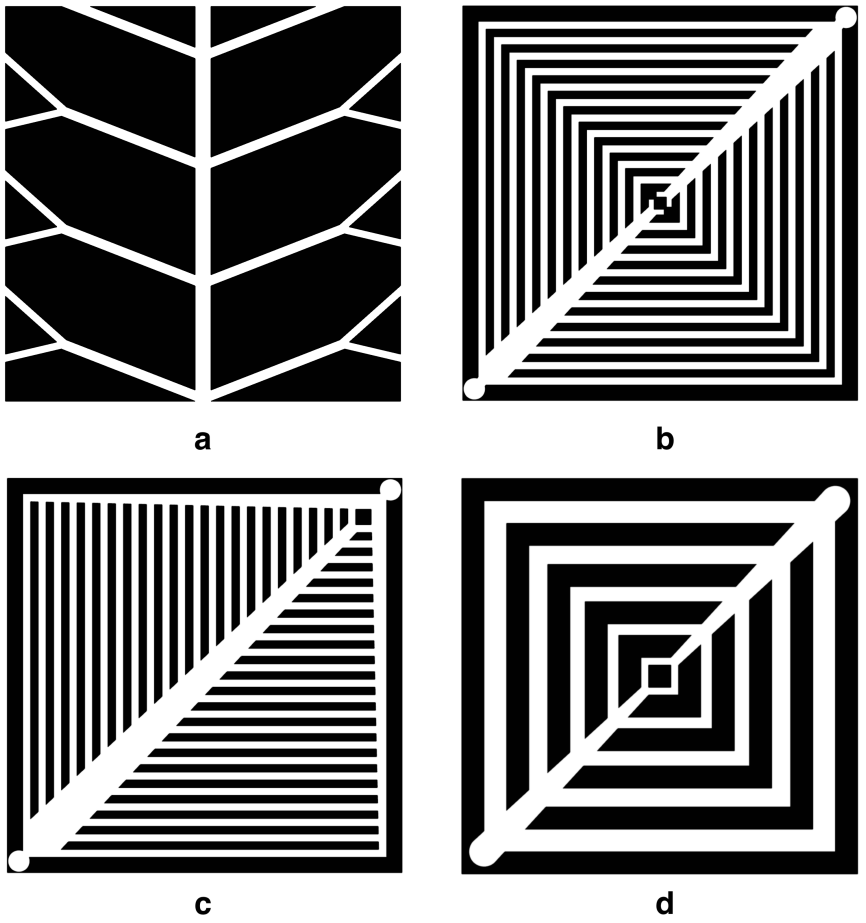

Figure 2.9: Sketches of leaf-inspired FFP designs: pinnate venation with two branching angles (a) (from [11]), parallel with two (b) and three (c) tapered channels, and with gradually decreased widths of the side branching channels (d) (from [77]).

The variation of the L1 design with gradually decreasing widths of the parallel channels according to Murray's law at each consecutive branching, had much lower pressure drop and better performance than a standard parallel design [25, 163]. Anyway, the flooding detected in the bioinspired FFPs was worse than in triple-serpentine designs. The design in Figure 2.9b resembles the multi-serpentine FFP with only one turn in each corner of the square FFP. The inlet and outlet for the gases are located at opposite corners of the FFP. The design presented in Figure 2.9c had a lower pressure drop, better current density distribution and higher power density output than the corresponding interdigitated designs. It also exhibited better performance at high temperatures [77], although poor water removal and flooding of the outlet channels was observed. The oblique margins of the FFP with parallel design provide better removal of liquid water and prevent flooding, even with channels of constant dimensions and without side margins. The design in Figure 2.9c with the diameters of channels corresponding to Murray's law (Eq. 2.7), could also be completed by periodic semi-cylindrical obstacles at the bottom of the daughter channels in order to increase the diffusion into the GDL and reduce the concentration overpotentials, especially at high current densities (see also Figure 2.3). Experimental measurements confirmed that the waved-type bottom had a better performance (by 42.1% at 0.4 V operating voltage) compared to the serpentine design [85]. When additional parallel channels were added to the leaf-based design in Figure 2.9c, the obtained biomimetic mesh-type flow field exhibited more uniform gas distribution, a higher gas consumption ratio, generated less ohmic heat, but had a larger amount of condensed water near the outlet of the system [12].

Two leaf-based designs correspond to the plant leaves with a palmate venation system that at the inlet of the transport system (i.e., from the leaf petiole) divides into 3, 5, 7, or more main channels which have branches of the 2nd and 3rd order. A counter-flow system of channels is located along the perimeter of the MEA and can be connected or interdigitated to the inflow system of channels. It was demonstrated that such designs provide further uniform gas distribution across the GDL and higher PEMFC performance in comparison to the conventional serpentine FFP design, due to a more uniform pressure and velocity distribution within the flow channels. This allows a more homogeneous diffusion of reactants onto the MEA active area [9, 12, 78, 81, 152]. It was detected, that interdigitated designs with >2 generations, need a relatively high pressure drop between adjacent branches to ensure better uniformity of the gas distributions without 'dead zones' between the branches. The design gave the worst performance when it was

used for both anode and cathode FFPs [78].

When the dimensions of the channels in the branches corresponded to Murray's law (Eq. 2.7), the PEMFC performance was ∼20-25% higher than the two serpentine and interdigitated designs due to the higher reactant transport through the FFP [152]. The difference between experimental and theoretical results was <10% for most of the current densities. The bio-inspired flow field geometries provide therefore a more uniform concentration, pressure and velocity distribution into the CL, and therefore higher power densities than the conventional flow fields. The interdigitated FFP designs were able to manage liquid water more efficiently due to the use of under-rib convection [152]. Nevertheless, the reactant distribution in this design was less uniform than in the fractal-type FFP.

2.9 Discussion

Since the first FCs were designed to enhance conditions for reactions (Eq. 2.1-2.3), all their components including material parameters, geometry, design of FFP and cooling systems, have been subject to continuous modifications, all aiming at better performance at lower weight and cost. The first serpentine (Figure 2.2a) design of the FFP remains the 'golden standard' for comparative studies of new design proposals. It produces, however, highly non-uniform reactant distributions partially smoothed by GDL. It needs a high pressure drop, transporting the flow through the long channel with high hydraulic resistivity, but is not so vulnerable for water flooding, due to the high pressure drop which is washing out the condensed water. Different conventional designs like parallel, interdigitated, and pin-type (Figures 2.2d, e) possess significantly lower hydraulic resistivity and, thus, smaller entropy production, but do not provide a uniform reactant distribution and demonstrate bad water removal abilities (Table 2.1).

During the last decade considerable efforts have been applied to modify the existing FFP, and elaborate novel FFP designs in order to improve the FC efficiency. Based on the presented literature review, the following tendencies can be reported:

- Mixed convenient designs (serpentine-parallel, pin-parallel, parallel-interdigitated, etc.) for better performance; especially the 5-channel parallel-serpentine one remains the most popular ones among those accepted for commercial FCs;

- Multiplication of convenient designs (serial-serpentine, mirror-serpentine, split-serpentine, spiral-serpentine, etc.) produce more uniform gas delivery and lower hydraulic resistivity;
- Modifications of the width/length-, width/depth-, and width/base-ratios of the open channels can be used for better under-rib forced convection, reactant mixing, distribution and liquid water removal;
- Cross-sectional shape optimization (trapezoidal, triangle, semi-circular, etc.) may hamper water accumulation at the walls. Waved bottoms of the channels give better water removal;
- Channel tapering may lead to uniformity of the hydraulic resistance of the consecutive channels;
- Smoothing of the sharp corners is favorable for lower hydraulic resistivity and viscous dissipation; Additional pathways/loops are useful for alternative flow directions in the case of water accumulation and occlusion of the main channel(s);
- Z-shape arrangement of the parallel channels provides efficient water removal into the vacant areas;
- Different 2D (rectangle, circular) and 3D tubular (cylindrical, conic) geometries for the non-planar FCs;
- Fractal trees with open sides connected to the GDL are favorable for lower hydraulic resistance and more uniform flow distribution;
- Fractal trees with closed sides of the channels provide perfect uniform reactant delivery to the GDL through the open outlets only;
- Biomimetic designs based on the nature-inspired geometries (lung-types, plant leaf-types) including Murray's law (Eq. 2.7) and optimal branching angles, are promising for lower hydraulic resistance and uniform flow distribution.

The proposed design modifications have been tested by different means: experimental, semi-analytical, numerical, and CFD computations, and the benefits of the novel designs have been reported as increases in some integral parameters and the overall FC efficiency. Unfortunately, there is no consensus on the set of parameters determining the most successful design of the FFP, as one can see in Table 2.1. Moreover, the same ratios W/D, W/L, W/B

could be beneficial for some of the accepted demands for good FC efficiency, like uniform current density and temperature distribution in the MEA, low pressure drop across the flow field, low FC voltage losses, good water removal (see section 2.1), but non-beneficial to others (see section 2.3.1). This implies that design modifications can lead to an increase in the FC efficiency, but that the optimal design in the meaning of Eq. 2.5 has not been reached yet. Very probably, a multi-criteria optimization approach must be used to reach such a state; an optimal design with a reasonably low pressure drop at high contact area, high membrane water content, high water removal from GDL as well as other contradictory demands (see section 2.3.1).

Combinations of beneficial designs like 5-channel serpentine (Figure 2.2b) or leaf-based (Figure 2.9c) plus local improvements with cross-sectional shapes (trapezoidal [125]), or waved bottoms with smooth obstacles (Figure 2.3 [77, 79]), have proven to be promising for PEMFC applications. Such waved channel systems have demonstrated a high efficiency for cooling systems of FC stacks [164]. Even though improvements in each type of design have been reported (the data on rise in % in FC efficiency is given in this review), a combination of successful designs does not imply any cumulative effect on the efficiency and must be studied separately.

The open channel fractal-type (Figures 2.8a, b and others) and leaf-type (Figures 2.9a-d and others) designs for the FFP are all designs that improve flow uniformity. When the dimensions of the side branches and branching angles are computed from Murray's rules [153, 157], a noticeable decrease in the hydraulic resistivity, pressure drop and viscous dissipation can be found. Since Murray's law (Eq. 2.7) follows from the optimization formulation (Eq. 2.5), the obtained fractal trees possess minimal energy dissipation at a given fixed volume of the tree. For the FFPs with constant channel depth this means that a fixed cumulative surface area of the FFP, in contact with the GDL, collects current. Since the formulation (Eq. 2.5) also applies to a tree with fixed energy dissipation and minimum volume, the design also provides a FFP with minimum ohmic resistance.

The fractal-type design with closed channels (Figures 2.8c, d and others) is the only construction that provides a perfect uniform gas delivery to GDL and distributed water removal system with equal cumulative hydraulic resistivity of all water pathways from the open outlets to the inlet [165]. The open channel design of the cathode FFP serves to transport both oxygen and water. This has to take place in different pathways, however. With closed channels, one may develop separate flow fields for gas delivery and water

collection, each pathway optimized for its purpose. Additional improvements of fractal designs can be achieved, by introduction of the solutions confirmed for non-fractal geometries. These include:

- Shape optimization of channels for less water condensation and better water removal (like trapezoidal cross-sections and waved walls);
- Variation in the number of generations in the fractal tree according to optimal rib/land ratio for under-rib convection and Peclet number $Pe \sim 1$ at the flow outlets to the GDL;
- Smoothing of the bifurcation angles for lower energy expenses;
- Design of additional pathways as side connections between the channels, as reserve pathways for gas flows in the case of rapid occlusion of the main pathway(s) by condensed water;
- Optimal scaling of the channel widths in the generations according to minimum energy dissipation from viscous, thermal, chemical, and ohmic sources.

In addition, one may use different optimization criteria for gas delivery and water removal channels on the anode and cathode sides, to achieve optimization of single-phase and multi-phase flows, respectively, to increase the FC efficiency.

2.10 Conclusions

1. From this detailed literature review, it can be concluded that the most efficient design for the FFPs of a FC has not yet been found, in spite of great efforts to modify serpentine and other conventional designs, mixing them or developing entirely new designs.
2. Demands deemed as necessary for best FC performance are sometimes contradictory, say with respect to channel widths and lengths, distances between them and direct contact with GDL (lands). Therefore, a whole list of criteria for FC optimization must be considered, making it into a multi-criteria optimization problem. Rather than optimizing a single hydraulic resistance, a pressure drop, or a uniform distribution, one should develop multi-optimization strategies.

3. As objective function for multi-criteria FFP design optimization, the entropy production or energy dissipation serves as a good objective function, because it includes all sources of the energy dissipation in the complex multi-physics system. Its applicability to describe best engineered performance in transport systems like lungs, blood vessels and conducting systems of plant leaves, has been reported.

Author contributions

The work was initiated as a part of the Ph.D. project of MS. NK made a first draft, with substantial input, writing efforts, and discussions from MS, NK, BP, and SK.

Funding

MS and SK are grateful to the Center of Excellence Funding Scheme of the Research Council of Norway (RCN), Project No. 262644 PoreLab. NK is grateful to the HighEff Center for Environmental-friendly Energy Research, RCN Project No. 257632/E20.

Conflict of interest

The authors declare that the research was conducted in the absence of any commercial or financial relationships that could be construed as a potential conflict of interest.

Chapter 3

Seeking minimum entropy production for a tree-like flow-field in a fuel cell

Marco Sauermoser[1], Signe Kjelstrup[1], Natalya Kizilova[2,3,1], Bruno G. Pollet[4], and Eirik G. Flekkøy[1]

1. PoreLab, Department of Chemistry,
Norwegian University of Science and Technology, NTNU,
NO-7491 Trondheim, Norway

2. Warsaw University of Technology,
Institute of Aviation and Applied Mechanics,
PL-00-665 Warsaw, Poland

3. Department of Applied Mathematics,
V.N. Karazin Kharkov National University,
UA-61022 Kharkiv, Ukraine

4. Department of Energy and Process Engineering,
Norwegian University of Science and Technology, NTNU,
NO-7491 Trondheim, Norway

This chapter was published in
Phys. Chem. Chem. Phys. (2020), 22:6993-7003

Abstract

Common for tree-shaped space-filling flow-field plates in polymer electrolyte fuel cells is their ability to distribute reactants uniformly across the membrane area, thereby avoiding excess concentration polarization or entropy production at the electrodes. Such a flow field, as predicted by Murray's law, was recently shown experimentally to perform better than serpentine or parallel flow fields. We document that a tree-shaped flow field can also perform better than Murray's law, as measured with the system's entropy production. The width and width scaling parameters of tree-shaped flow-field channels were varied, and the resulting Peclet number at the channel outlets was computed. We show using 3D hydrodynamic calculations that pressure drops and channel flows can be accounted for within a few percent, for most of the investigated geometries, by a quasi-1D model. The model gives lower energy dissipation than of Murray's law. The results open up for new strategies for fuel delivery to fuel cells and other catalytic systems.

3.1 Introduction

Since the start of polymer electrolyte membrane fuel cell (PEMFC) research [166], serpentine flow fields have been commonly used to supply reactants (oxygen and hydrogen) to the cell's catalytic layers in the membrane electrode assembly (MEA). The serpentine field is in use [6, 85, 167] also in industry, but it has become increasingly clear that other flow fields perform better, in terms of a better polarization curve and lower operational costs [168, 169]. The distance from the polarization curve to the value of the reversible potential of the cell expresses the energy dissipated as heat or the entropy production times the temperature of the fuel cell [170]. The losses, which vary with the current density, are much larger at the electrodes and in the membrane, than in the porous transport layers (PTLs) [28]. However, the losses in the PTLs will have an impact on the cell's overpotentials via the gas concentration at the catalyst. A flow field, that can deliver reactants at uniform conditions to the cell's active membrane area is therefore beneficial. An optimal field can thus be characterized by a uniform entropy production. Among numerous replacement proposals, it has been argued that bio-inspired fractal-type flow fields would be beneficial, because they are developed for energy-efficient biofluid delivery, meaning uniform delivery of fluids to animal and plant tissues [155, 171]. Recent experimental evidence confirms their superiority in this respect for the PEMFC. Trogadas *et al.* [7] used a 3D lung-inspired tree perpendicular to the PEMFC membrane, which supplied the active area with a uniform gas mixture from above. The flow field was better

than a serpentine flow field in terms of its polarization curve. The property of equipartition of entropy production has been connected with minimum energy dissipation in various process equipment (for an overview, see [29]). This altogether has led us to speculate that fractal-like (or self-similar) patterns with constant scaling parameters could be beneficial as distributors of gases in the PEMFC [13]. Perfect equipartition can be obtained using scaling parameters obtained with the method of Gheorghiu *et al.* [15] and Trogadas *et al.* [7], but in reality, there are often boundary- or material conditions that do not allow us to reach the ideal limit. Additional constraints or variables are therefore interesting. We shall study such here, comparing the outcome all the time to the performance of Murray's law for volume or area-filling conditions [172], see Appendix A. This condition is also close to the practical condition facing a fuel cell designer. Murray [172] used a volume-filling condition as constraint for flow in tree-shaped structures, and obtained as an outcome of the optimization his famous scaling law, saying that the diameters of the branches from one generation to the next were scaling as Equation 3.1 shows.

$$d_0^3 = \sum_{j=1}^{n} d_j^3 \tag{3.1}$$

where d_0 is the diameter of the parent branch, d_j are the diameters of the n daughter branches belonging to the next generation level.

Equation 3.1 characterises the fluid delivery system for which the total entropy production by viscous dissipation is minimum, given the total volume available to flow [172]. An optimization problem with minimum total volume at a given entropy production, has, however, the exact same solution. Both formulations are beneficial to use in flow-field plate design. Minimum total volume at constant channel depth means maximum gas-land contact area and, therefore, smaller total electric resistance of current collectors (smaller Ohmic losses). In this sense, it is logical to start considering the flow field alone.

Gheorghiu *et al.* [15] studied airflows in the bronchial tree of humans and used as constraint that the volume flow through each generation of branches was constant. They found that minimum entropy production corresponded to a constant pressure drop across each branch. In their case; minimum entropy production could be understood as equipartition of entropy production (uniformly distributed entropy production).

The geometric design principle of Murray [172] was seen a manifestation of

equipartition of entropy production [15]. The constraints used by Gheorghiu *et al.* and Murray were *not* the same, however. In the first case, no restriction was placed on geometry, while in Murray's case the volume-filling geometry compatible with minimum work was of primary interest.

From studies of Nature, we know, however, that a decrease in the entropy production in one a part of a complex system will be beneficial for the overall efficiency. This was confirmed by an enormously high number of studies of fluid delivery systems in Nature (in plants, animals, sponges, fungi, etc.). They were shown to have minimum energy loss (entropy generation), independent of other functions [155, 171]. Therefore, we shall assume that an approach to minimize the viscous dissipation in the flow field could also be beneficial for PEMFC, in spite of non-constant temperatures across the cell and other types of dissipation. This hypothesis needs, of course, to be checked by experiments and/ or more detailed multiphysics CFD computations, but a successful starting geometry could well come from the simplest base.

There are presently few quantitative reports on bio-inspired designs [7, 13, 25], and the present work attempts to change this situation, contributing to analytic and numerical studies of biomimetic designs of the flow fields in PEMFC. The problem is challenging, as the transport of oxygen can be severely hindered by water formation in the catalytic layers and water clogging in the porous transport layer (PTL). In addition, the heat production at the cathode can shift the ratio of water vapor to liquid [28].

But in this context, a tree-like structure for supply of gases may offer advantages. Trogadas *et al.* [7] used a 3D lung-inspired tree perpendicular to the PEMFC membrane, supplying the active area with the same gas mixture from above. We shall use a "flat" tree, or a quasi-3D tree that is parallel to the membrane, see Figure 3.1 as in the original proposal of Kjelstrup *et al.* [13]. The inlet is set at the symmetry line of the area close to its perimeter (Branch 0.1 in Figure 3.1), while the outlets are (only) at the ends of all the branches of the last generation (here 4 generations are shown). Both types of trees will, by construction, deliver gas at (nearly) uniform conditions to the membrane active area. The "flat" tree may also be embedded into the end-plates of the cell, and possibly help us avoid the PTL all together. There is a possibility to construct parallel outlet channels for water, with a similar structure operating in the reverse direction.

These potential options have motivated this first study of a flat tree-like flow field. We are concerned with a gas inlet distributor where hydrodynamic flows take place in a plane, with a certain channel depth and width. The

Peclet number will be used to assess how far we are from the diffusional regime. The model applies so far to the anode side of the PEMFC, where hydrogen and water vapour flow in the same direction, and where there is negligible water condensation. In order to use it for the cathode, we need to introduce two-phase flow of water and gas with the possibility for water clogging the pores in an outlet system with the same shape. This problem will be postponed, however. The paper is organized as follows. We describe first (Section 3.2) the quasi 3-dimensional (3D) tree-shaped flow field pattern, with a finite number of branches, to set a practical stage for the investigation. Afterwards we define the equations which describe the system in use. The 3D system describing the flow in the fractal flow-field is solved numerically, while a simplified 1D representation of the same is solved analytically. The flow fields are studied under flow and boundary conditions typical for PEM fuel cells. The impact of geometry is pointed out. In our study, we find that there are other geometries than those given by Murray, that have a smaller energy dissipation. We proceed to explain the benefits / disadvantages of various case studies, followed by a discussion of results. We believe that our systematic use of the entropy production as a tool to observe the performance of a flow field, is new in the context of fuel cells.

3.2 System

The flow field of a fuel cell should preferably deliver gas at uniform conditions all over the 2D catalytic layer. This motivated our choice of a tree-like structure where each branch always splits into 2 sub-branches. The cross-section of the branch is rectangular or squared. Such patterns, which are in the focus here, can be characterized by geometric series. The system can be designed to fill the space available, be it a certain volume or, in the quasi-3D case, an area.

The uniform supply of a fluid to the catalyst is the first essential requirement of an optimal PEMFC [13]. A working quasi-3D flow field needs inlet- and outlet-patterns. Only one pattern leads to dead-end flow channels. However, we shall now look at the inlet pattern only for the sake of simplification, where only the branches in the last generation are connected with the gas diffusion layer. The situation shares similarities with an interdigitated flow field design, where the flow needs to go through the gas diffusion layer before the gases and water are able to leave the fuel cell.

The outlet pattern can be machined onto a new plate, making it a 2-layer flow field plate. Machining can be done with conventional milling methods

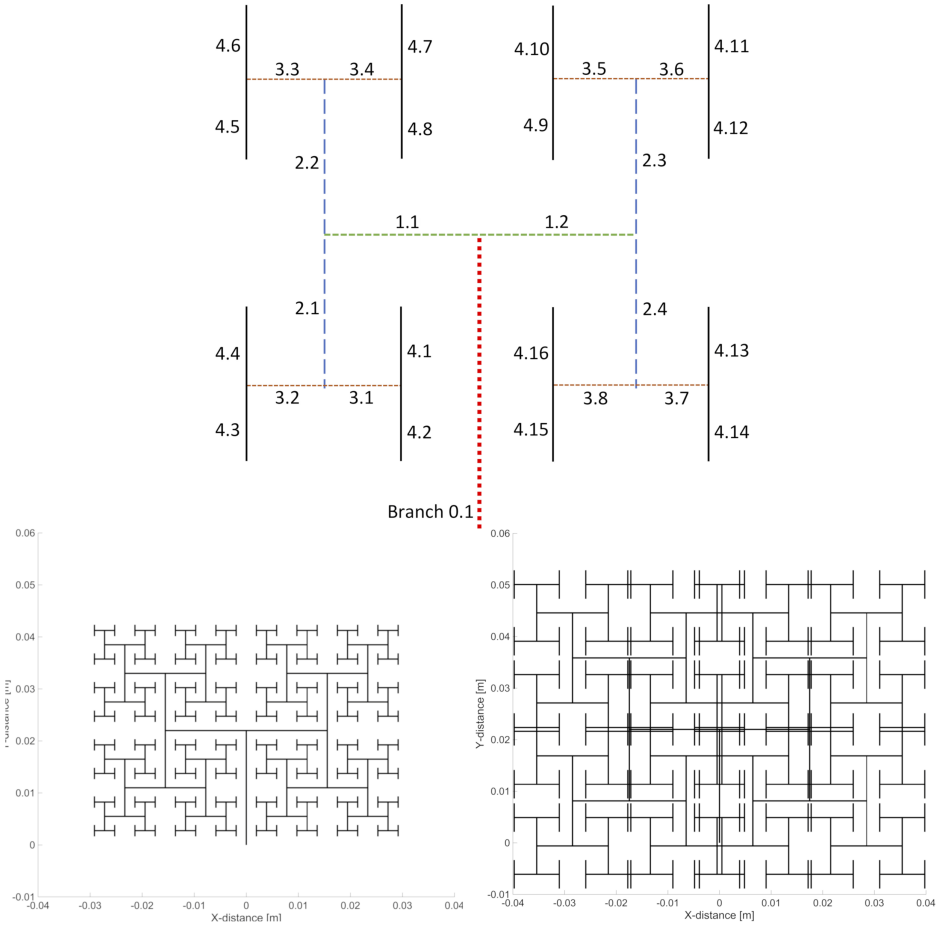

Figure 3.1: Top: Schematic picture of the tree-shaped flow field in a layer parallel to the membrane. The picture shows the numbering of branches i and generation levels j from the inlet 0 to the outlet. When the gas outlet is restricted to the ends of the branched tree, gas is delivered at similar conditions. Bottom: Self similar fractal-like pattern with k-parameter 2 (left) and 3 (right).

since we propose to use a 2D channel structure with constant channel depth. Constant depth allows an easy milling process and reduces pressure loss effects from an otherwise stepwise decrease of channel depth. Any 3D printing will, therefore, not be needed. The branches of the last generation of the inlet pattern will be on the second plate, where the outlet pattern eventually will be encarved. One advantage of this type of flow field plate is the modularity, meaning that the outlet pattern can be easily changed independently of the inlet pattern. The first generation of both inlet and outlet patterns will need to be connected with the fuel inlet and gas outlet of the fuel cell, and this can be done by a straight channel.

Take the symbol l_0 for the length of the first branch which is not yet split (level 0). When N_j is the sum of the number of branches at level j, the ratio N_j/N_{j+1} is therefore 1/2. The parameter j_f is defined as the generation level number of the last generation. In the first step we are looking at a self-similar system, meaning that the length, $l_{j,i}$, and width $w_{j,i}$, of each branch i at generation level j is scaled down by the same factor, k and respectively a. Widths and lengths have the unit m.

The numbering of branches was illustrated in Fig. 3.1. We show in Appendix 1 how the length scaling parameter can be derived for volume-filling or area-filling conditions. The branch length will scale as:

$$l_{j,i} = \frac{1}{2^{j/k}} l_0 \tag{3.2}$$

with $k = 3$ for volume-filling constraints, and $k = 2$ for area-filling constraints. The width scales according to a geometric series, cf. Equation 3.3.

$$w_{j,i} = a^j w_0 \tag{3.3}$$

where a is the dimensionless diameter scaling parameter and w_0 is the width in the first branch of generation level 0. Another and quite common way to scale the diameter or width in biological flow systems is to use Murray's Law [172] (Equation 3.4):

$$d_{j,i} = \frac{1}{2^{j/3}} d_0 \tag{3.4}$$

where d_0 is the diameter of the first branch (generation level 0) in m and $d_{j,i}$ is the diameter of the branch at generation level j in m. The flow rate $Q_{j,i}$ of each branch can be calculated with following equation:

$$Q_{j,i} = \frac{1}{2^j} Q_0 \tag{3.5}$$

Table 3.1: Lengths chosen to give a pattern that fills a 25 cm^2 active fuel cell membrane area.

Generation level j	Length [mm]
0	24
1	12
2	12
3	6
4	6

where Q_0 is the flow rate in the first branch of generation level 0 in $m^3\ s^{-1}$.

For the case of a rectangular-shaped (quasi-3D) flow channel, we chose to replace d_0 and $d_{j,i}$ with w_0 and $w_{j,i}$. From Equation 3.4, we calculated a value for a, which is $0.5^{1/3} \approx 0.79$. This value will be used for all calculations where we refer to Murray's law. The $k-$value has an impact on how the pattern fills out the free space in the plane. We shall study values where $2 < k < 3$ in connection with Murray's law for width-scaling cases. The endpoint values have clear geometric interpretations. The shape of other fractal-like patterns will also be investigated; changing the k-parameter from 2 up to 3.

Figure 3.1 (bottom two figures) shows the space-filling ability of such a tree as a function of the k-parameter (the width was not scaled in this figure). The number of generations in the tree was set to 9 for visual purposes, which means that $j_f = 8$. Values below k=2 created patterns that did not fill the space. Values of $k > 2.2$ create cross-overs. This means that the pattern will turn out to be problematic in a manufacturing process, that uses 3D techniques like 3D printing. The analysis (Fig. 3.1) of the length scaling parameter k demonstrated the biggest disadvantage of this way to scale the pattern: This always results in a rectangular area. The PEMFC area, to be investigated, was however a square. Therefore, we set the branch length at a predefined value, constant for all cases, when we asked for the space filling pattern. The only parameter to be scaled was then the width of the rectangular channel. Table 3.1 shows the length of the different generation levels which were used in the calculations (j_f set to 4), chosen in such a way that we obtain an area-filling pattern for a 25 cm^2 active fuel cell membrane area.

3.3 Theory

The "flat" tree flow-field will be modelled in several ways. In the most precise manner, we consider all three dimensions of each channel, and compute the flow field in the full network of branches. The entropy production due to viscous dissipation at isothermal conditions in the 3D case is:

$$\left(\frac{dS_{irr}}{dt}\right)_{j,i} = \int_{V_{j,i}} -\frac{1}{T}\Pi : \nabla \mathbf{v} dV \tag{3.6}$$

Here $\left(\frac{dS_{irr}}{dt}\right)_{j,i}$ is the entropy production of branch i at generation level j in J s^{-1} K^{-1}, Π is the viscous stress tensor in Pa, $V_{i,j}$ is the volume of branch i at generation level j in m^3, and $\mathbf{v}$ is the barycentric velocity in m/s. The total entropy production is the sum of the entropy production of all branches:

$$\frac{dS_{irr}}{dt} = \sum_{j,i}\left(\frac{dS_{irr}}{dt}\right)_{j,i} \tag{3.7}$$

For the 1D tree, the expression for the entropy production simplifies. For one branch, the driving force is minus the pressure drop across the branch divided by the temperature. This gives:

$$\left(\frac{dS_{irr}}{dt}\right)_{j,i} = -Q_{j,i}\frac{\Delta p_{j,i}}{T} \tag{3.8}$$

Here $Q_{j,i}$ is the volume flow rate in m^3 s^{-1} in the branch i at level j , $\Delta p_{j,i}$ the pressure drop across the branch i at level j from the outlet to inlet in Pa and T the temperature of the system in K. The entropy production of one generation level is calculated with

$$\left(\frac{dS_{irr}}{dt}\right)_{j} = -\sum_{i=1}^{N_j} Q_{j,i}\frac{\Delta p_{j,i}}{T} \tag{3.9}$$

where $\Delta p_{j,i}$ is the pressure drop in the branch i at level j in Pa and N_j is the number of branches at generation level j, which is 2^j. The total entropy production (TEP) is then simply the sum of the values obtained from Equation 3.9 over all generation levels in the fractal-like pattern.

$$\frac{dS_{irr}}{dt} = \sum_{j=0}^{j_f}\left(\frac{dS_{irr}}{dt}\right)_{j} \tag{3.10}$$

Here j_f is the maximum number of generation levels in the tree-shaped pattern. To compare different geometries, the specific entropy production $\frac{dS^*_{irr}}{dt}$ in J m^{-1} s^{-1} K^{-1} is introduced:

$$\left(\frac{dS^*_{irr}}{dt}\right)_{j,i} = \left(\frac{dS_{irr}}{dt}\right)_{j,i} w_{j,i}^{-1} \tag{3.11}$$

The total specific entropy production (TSEP) is then again the sum of the specific entropy production of each branch in the flow system:

$$\frac{dS^*_{irr}}{dt} = \sum_{j,i} \left(\frac{dS^*_{irr}}{dt}\right)_{j,i} \tag{3.12}$$

We introduce the assumption of Poiseuille flow for cylindrical flow channels [7, 15] and obtain:

$$\Delta p_{j,i} = -\frac{128 \mu l_{j,i}}{\pi d_{j,i}^4} Q_{j,i} \tag{3.13}$$

where μ is the dynamic viscosity of the fluid in Pa·s. We shall compare two expressions for the diameter in Equation 3.13. In the first case (Case Dh) we used the common hydraulic diameter ($d_{j,i} = D_{j,i}$) [173]:

$$D_{j,i} = \frac{2 w_{j,i} h_{j,i}}{w_{j,i} + h_{j,i}} \tag{3.14}$$

In the second case (Case Equivalent A) we used the diameter of a cylindrical cross-section, which gives the same area as the rectangular or squared channel, leading to:

$$d_{j,i} = \sqrt{\frac{4}{\pi} w_{j,i} h_{j,i}} \tag{3.15}$$

In addition to the use of Hagen-Poiseuille flow for the cylindrical flow channel, combined with with the first two cases, we also used the analytical solution of Hagen-Poiseuille flow for a rectangular channel [173] (Case Rectangular):

$$\begin{aligned} \Delta p_{j,i} = &- Q_{j,i} \frac{12 \mu l_{j,i}}{h_{j,i}^3 w_{j,i}} \\ &\left[1 - \sum_{n=0}^{\infty} \frac{192}{(2n+1)^5 \pi^5} \frac{h_{j,i}}{w_{j,i}} \tanh\left(\frac{2n+1}{2} \frac{\pi w_{j,i}}{h_{j,i}}\right)\right]^{-1} \end{aligned} \tag{3.16}$$

The total pressure drop along the tree branches, Δp, is the sum of the pressure drops across the generations j. See Figure 3.1 for branch notation.

$$\Delta p = \sum_{j=0}^{j_f} \Delta p_{j,i} \tag{3.17}$$

3.4 Methods

3.4.1 Case studies

Table 3.2 shows a summary of the conducted studies on the chosen tree-shaped pattern. To start, we studied the variation in the entropy production with flow rate, and the impact of the pressure drop calculation method (Study 1 in Table 3.2), followed by an analysis of Murray's Law and the impact of it on the entropy production (Study 2). We studied the impact of geometry and scaling properties on the TEP (Eq. 3.9) and TSEP (Eq. 3.12) to answer the question: Is Murray's Law is the most efficient way to scale the pattern in terms of entropy production?

All three cases described in section 3.3 were used and compared to each other (Study 3). It was of interest to see how the pressure varied along the branches for different scaling parameters. The 1D calculations of the pressure drop in the tree-shaped pattern (with Equations given in section 3.3) do not include entrance length effects or the flow retardation at the T-junctions, thus promoting the 3D calculations. (Studies 4, 5, 6).

Due to branching, the flow inside the channels can become asymmetric (see [146, 147]), and this may cause an undesirable nonuniform flow distribution over the PEMFC. Therefore we computed the outlet flow rate from the last generation and compared them to each other, in order to see if we were able to reproduce the results of Ramos *et al.* [147], and to prove that tree-shaped patterns deliver the fuels uniformly (Study 4).

To answer how well the simple 1D method can capture a more advanced result, we performed 3D simulations. We examined the pressure drop prediction of the 1D model and evaluated its impact on the entropy production (Study 5 and 6). Finally (Study 7) we computed the Peclet number (cf. Equation 3.18) at the outlet of the last branch. The Peclet number defines the ratio between convective and diffusive flow. A Peclet number lower than one means that diffusion dominates the flow. We have:

$$Pe = \frac{Lv}{D} \tag{3.18}$$

where L is the characteristic length in m, v is the flow velocity in m/s and D is the diffusion coefficient of gas relative to the wall in m/s^2. A Peclet number of smaller than 1 in the last branch helps provide uniform distribution of the fluids to the catalyst [162].

Table 3.2: List of conducted case studies.

Study	Investigation	Variables	Method
1	Q_0 & Δp calculation method dependency on TEP & TSEP	Q_0, Δp calculation method, w_0	1D
2	Murray's Law and entropy production	a, w_0	1D
3	1D Δp	a, Δp calculation method	1D
4	Flow rate distribution	a, w_0	3D
5	3D TEP & TSEP	a, w_0, Q_0	3D
6	a, Comparison of 1D & 3D Δp	a, Δp calculation method, 3D Δp	3D, 1D
7	Peclet number	L, w_0, a, Q_0	1D

3.4.2 Computational methods

1D-calculations

The 1D calculations were done using equations 3.6 to 3.17 in section 3.3. The equations were solved in MATLAB R2019a for various w_0 and scaling parameters a. We used pure oxygen as a flow medium. The temperature was set at 353 K, a common temperature in fuel cell experiments. The system was assumed to be isothermal working at a constant flow rate condition [7]. The flow rates, which can be seen in Table 3.3, were calculated using Faraday's law. The fuel cell active area was 25 cm^2, the density of oxygen was 1.09 kg/m^3, the stoichiometric coefficient was 3, and a molar mass of 36 g/mol. The flow pattern outlet has atmospheric pressure and the inlet pressure is then calculated with the pressure drop along the branches. The viscosity of oxygen at the given operating conditions was calculated with Sutherland's formula and resulted in 2.1×10^{-5} Pas. To investigate the impact of the channel width, the channel depth was kept constant at 1 mm.

3D-calculations

The 3D calculations were done using OpenFoam 4.1. The simpleFoam solver was used to solve Navier-Stoke's equation for isothermal, incompressible, single-phase and steady-state flow. Meshes of the tree-shaped patterns were created in Ansys Workbench with a fully hexahedral mesh. Models for five different widths (1, 1.5, 2, 2.5 and 5 mm) and 3 different width scaling

Table 3.3: Flow rates at inlet of branch in generation 0 used in the computations.

Current density [A/m^2]	Flow rate [m^3/s]
10000	5.7104×10^{-6}
5000	2.8552×10^{-6}
1000	5.7104×10^{-7}
100	5.7104×10^{-8}

parameters (0.79, which was scaling according to Murray's law, 0.9 and 1) were created and computed for the same 4 flow rates (Table 3.3) which were used in the 1D calculations. The same viscosity and temperature as in the 1D studies were used. To reduce computational time, the tree-shaped pattern was split in half, with the symmetry plane being at the axisymmetric line of generation 0. Afterwards the pressure drop was evaluated and the specific entropy production computed in ParaView-5.6.0. The entropy production was computed from equation 3.6.

3.5 Results and discussion

3.5.1 TEP dependence on flow rate and total pressure difference

The results for TEP and TSEP (Study 1) are shown in Figure 3.2 as a function of channel width, for the flow rates corresponded to the current density of 10^4 and 100 A/m^2, and the three ways to compute the pressure drop. The value of a was kept constant (0.79). The pressure drop was calculated using the hydraulic diameter (full line), the analytic solution of Hagen-Poiseuille flow for a rectangular channel (broken line) and the same for an equivalent cross-sectional area (dotted line). We saw an expected impact of the flow rate. An increase or decrease in the rate led to an increase or respectively decrease in the TEP and TSEP. The variation between the flows was large, four orders of magnitude for the values chosen, since the entropy production is scaled with the flow to the power of 2. Figure 3.2 shows furthermore the change of TEP and TSEP with different ways to compute the pressure drop. Generally speaking, the use of the hydraulic diameter gave the highest entropy production (pressure drop values), whereas the method which uses a diameter calculated from the equivalent cross-sectional area gave the lowest values. The difference between the choice of areas was not large, however, considering the variation in the gas flow rates.

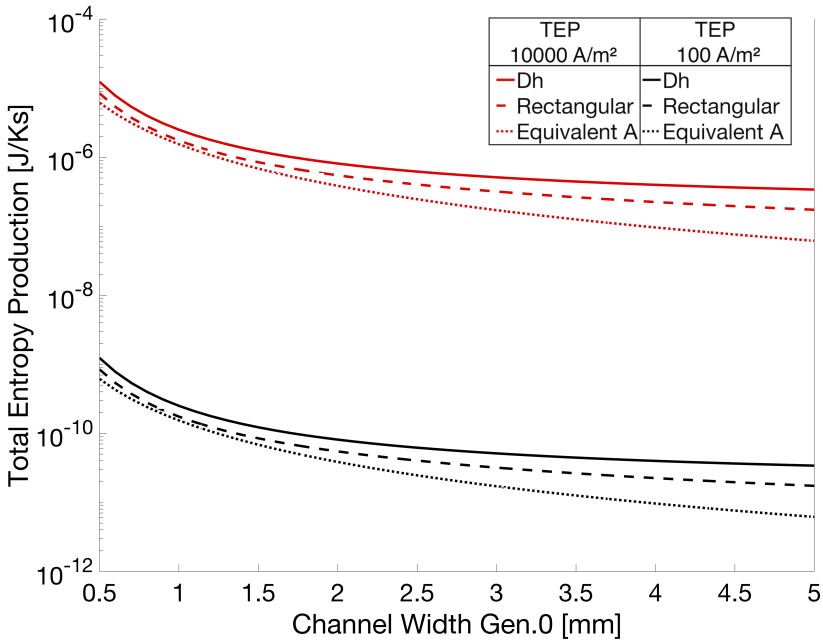

Figure 3.2: TEP as a function of channel width for a =0.79, at a flow rate equivalent to current densities of 10000 A/m^2 (upper region in graph) and 100 A/m^2 (lower region in graph). The pressure drop was calculated with the three different cases, namely Case Dh (full line), Case Equivalent A (dotted line) and Case Rectangular (broken line).

The width of the channels (Figure 3.2 showed the channel width of generation 0 in mm) had a big impact on TEP (and TSEP), especially at the initial increase of w_0. The higher the w_0 was, the lower was the decrease in entropy production. This could be explained by a much lower pressure drop at higher channel widths (at constant channel depth). The results will be compared to full hydrodynamic 3D simulations below.

3.5.2 Murray's Law and entropy production

The impact of the width scaling parameter a on TEP and TSEP (Study 2) is shown in Figure 3.3. The figure shows the TEP and TSEP as a function of the width of generation 0 for different values of a, at a flow rate which corresponds to 10000 A/m^2, where the pressure drop was calculated with the hydraulic diameter Dh. We saw that the value of a obtained from Murray's Law (a =0.79), did not give the lowest total entropy production (total specific entropy production), independent of the way we computed the pressure drop

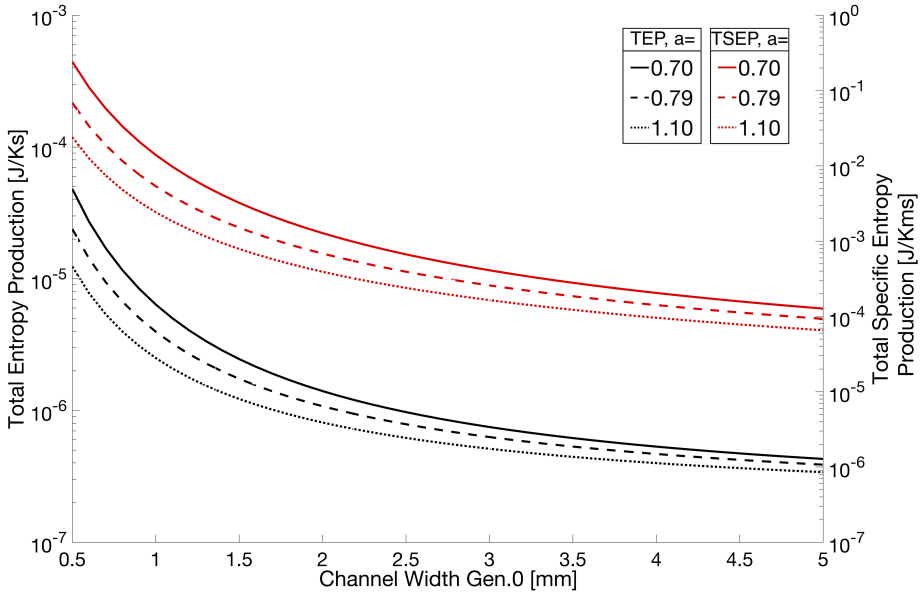

Figure 3.3: TEP and TSEP as a function of channel width for different values of a. The flow rate was equivalent to a current density of 10000 A/m^2. The pressure drop was calculated with Case Dh.

and the flow rate. An increase in a led to a decrease of the entropy production values. This was caused by the faster decline in pressure drop with a higher a, see Figure 3.4 (Study 3). If a >0.79 (Figure 3.4 bottom left) the pressure along the branches became a convex function, whereas if a <0.79 (Figure 3.4 top left) the pressure dropped in a concave way. Using Murray's Law led (Figure 3.4 top right) to a close-to-linear pressure variation. The same effects could also be found for a variation in w_0. Gheorghiu *et al.* [15] described, that if the pattern is scaled with Murray's Law, a constant pressure drop leads to the minimum total entropy production. This was no longer the case here because we were setting the lengths manually to obtain a square area-filling pattern, contrary to the work of Gheorghiu *et al.* where the lengths were scaled with the assumption of a volume filling pattern (k =3).

3.5.3 Flow rate distribution

As a consistency check, the overall outlet flow rate (summed flow rates at each branch outlet in the fourth generation) was compared to the set inlet flow rate (Study 4). The deviation was maximum 0.45% and minimum 0.19%. The differences were caused by numerical errors and we assumed that the

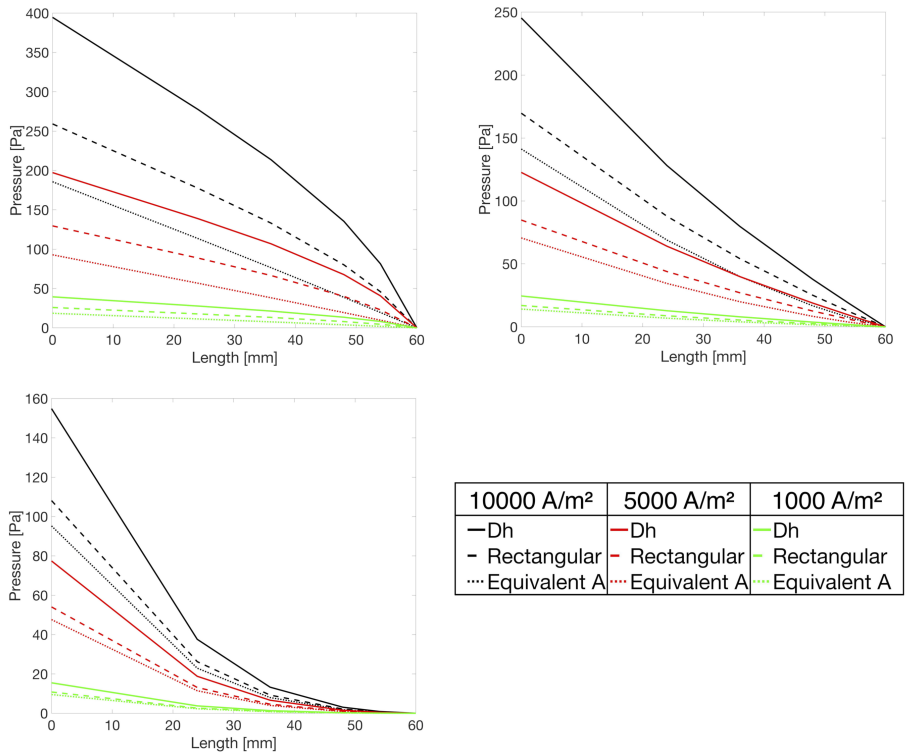

Figure 3.4: Pressure along the branches of different generation levels at a flow rates equivalent to current densities of 10000 A/m^2 (black lines), 5000 A/m^2 (red lines) and 1000 A/m^2 (green lines) for a =0.7 (top left), a =0.79 (top right) and a =1.1 (bottom left) and w_0=1 mm, where the pressure drop was calculated Case Dh (full line), Case Equivalent A (dotted line) and Case Rectangular (broken line).

results are therefore acceptable. The results for the analysis of the outlet flow rates can be found in Table 3.4. Furthermore, Figure 3.5 shows the asymmetric effects caused by the branching in the tree-shaped pattern. As it can be seen, the difference was in most cases negligible, except for the cases with w_0 =5 mm, a =0.9 and a = 1. For the case of a = 0.9, differences up to 2.5% could be seen, but only at flow rates equivalent to 10^4 A/m^2. The explanation could be the asymmetry in the system: The branches did not have enough time to fully develop the hydrodynamic flow, leading to an asymmetric flow. For the case of a =1, variations up to 8% could be seen even at lower flow rates, making this geometry less suitable for the use in fuel cells due to non-uniform fuel distribution. Also Fan *et al.* [146] documented non-uniform flow rates, and proposed that a good flow distribution could be

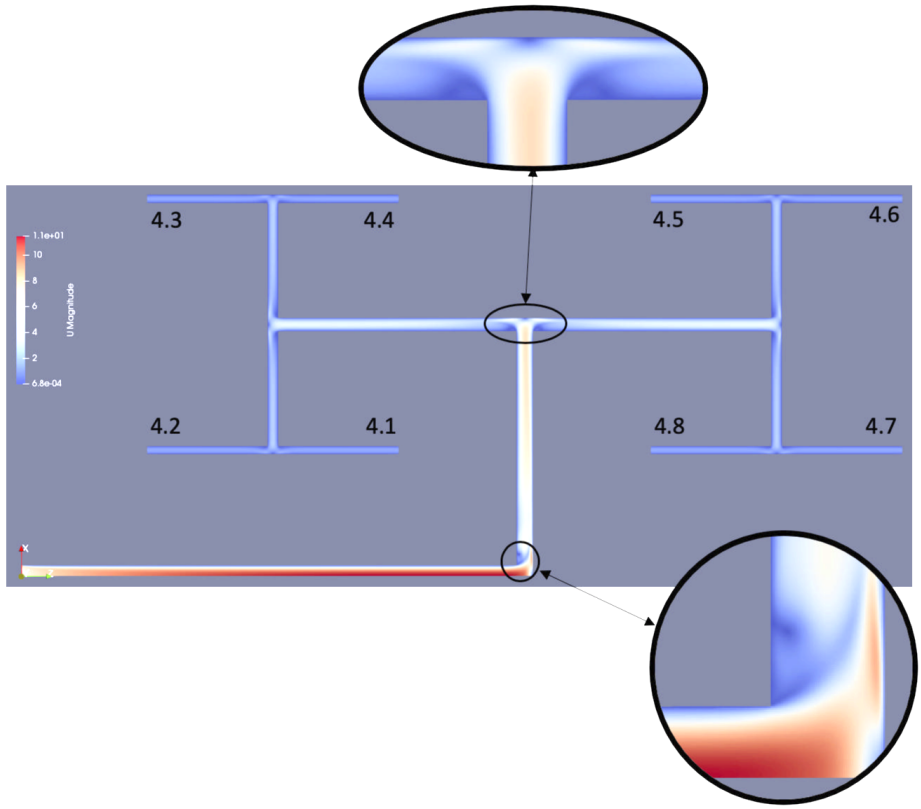

Figure 3.5: Flow velocity distribution in the geometry with w_0 =1 mm, a =0.79, at a flow rate equivalent to 10000 A/m^2.

achieved at certain flow rates. In their study however, only one geometry was analysed. Ramos *et al.* [147] also worked on this type of investigation with similar results.

3.5.4 TEP and TSEP from 3D calculations

The results of the TEP and TSEP computations are shown in Figure 3.6 (Study 5). The same conclusion could be drawn from this, as we did in the 1D calculations. An increase in a and w_0 led to a lower TEP and TSEP. Scaling the width according to Murray's Law did not give the minimum entropy production. A quantitative comparison between the 3D and 1D results showed, that the entropy production values, both TEP and TSEP, were in the same order of magnitude. The maximum difference between the 1D and 3D calculations was dependent on the pressure drop calculation

Table 3.4: Maximum differences in % between the highest flow rate at the outlet of the branches in the fourth generation and the actual flow rate at those outlets. Numerical errors in the numbers were within 0.5%.

	10000 A/m^2	5000 A/m^2	1000 A/m^2	100 A/m^2
w_0 =1 mm, a =0.79	0.02	0.03	0.04	0.08
w_0 =1 mm, a =0.9	0.11	0.20	0.27	0.53
w_0 =1 mm, a =1	0.23	0.36	0.62	0.84
w_0 =1.5 mm, a =0.79	0.03	0.01	0.01	0.01
w_0 =1.5 mm, a =0.9	0.16	0.09	0.14	0.36
w_0 =1.5 mm, a =1	0.37	0.14	0.17	0.46
w_0 =2 mm, a =0.79	0.24	0.17	0.31	0.59
w_0 =2 mm, a =0.9	0.29	0.03	0.04	0.09
w_0 =2 mm, a =1	0.77	0.10	0.04	0.09
w_0 =2.5 mm, a =0.79	0.20	0.02	0.03	0.06
w_0 =2.5 mm, a =0.9	0.61	0.06	0.07	0.14
w_0 =2.5 mm, a =1	0.75	0.11	0.18	0.34
w_0 =5 mm, a =0.79	0.28	0.14	0.40	0.53
w_0 =5 mm, a =0.9	2.54	0.41	0.70	0.90
w_0 =5 mm, a =1	3.78	3.82	7.77	8.53

method. For the most suitable one, we had a maximum deviation of around 10%, whereas the worst one gave differences up to 61%. This emphasized the importance of the selection of the pressure drop calculation method. Also, the same trends could be observed.

3.5.5 1D- and 3D pressure drop calculations compared

The pressure, plotted along the center of the flow channels, for the 1 mm and 2.5 mm geometries at different width scaling parameters and a flow rate equivalent to 10^4 A/m^2 is presented in Figure 3.7. Here the 3D results are compared to the ones from the 1D calculations (Study 6). Again there was a lower entropy production at higher a values than the one given by Murray's law, which could be explained by looking at the pressure drop (Figure 3.7). The pressure drop was nearly linear with a =0.79, whereas there was a non-linear pressure drop with higher scaling parameters, leading to a higher gradient. In this sense, we reproduced the results of Gheorghiu *et al.* [15].

The pressure peaks appear only in the 3D simulations, which have a continu-

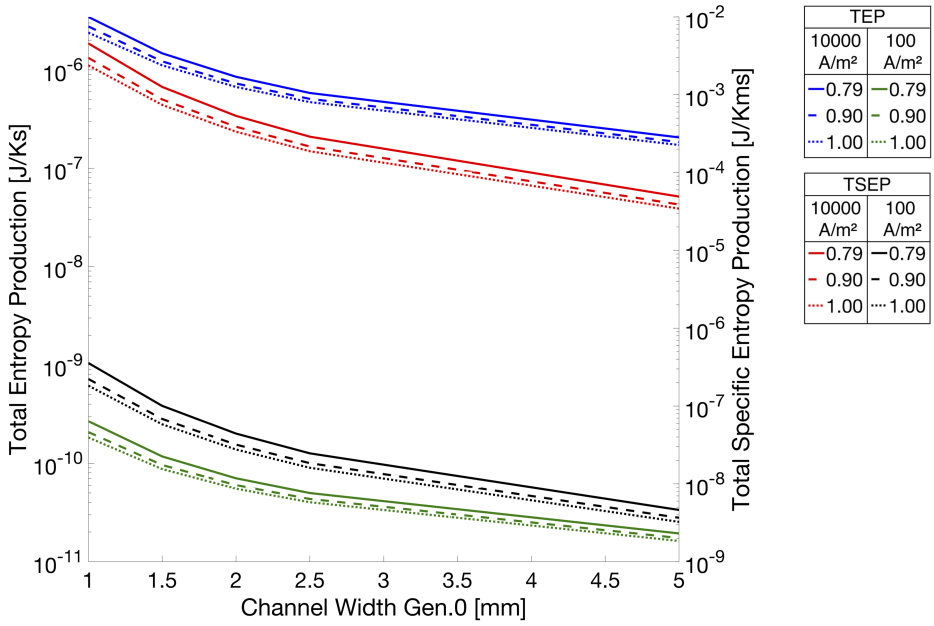

Figure 3.6: TEP and TSEP as a function of channel width for all simulated geometries for flow rates equivalent to current densities of 10000 and 1000 A/m^2 for a =0.79 (solid lines), a =0.90 (dashed lines) and a =1.00 (dotted lines). The two sets of three lines at the top are the TEP and respectively TSEP for 10000 A/m^2, whereas the lower two sets of three lines are the TSEP and respectively TEP for 100 A/m^2.

ously connected flow channel. The peaks are due to the branching. In the bifurcations, flow is hampered and that increases their hydraulic resistance and, therefore, produces higher pressure drops to maintain the constant flow rate. 1D calculations based upon analytic equations do not produce such peaks. Figure 3.7 gives a comparison of this branching effect on the pressure drop. The pressure peaks may be computed from the 1D model if the known approximate hydraulic formulas for the inlet flows, and flows in curved or T-shaped geometries, are used. Since CFD computations are quite fast and reliable, we have not reproduced the distributions with pressure peaks in the 1D models with approximate formulas.

However, except for the first 2 branches, there was only a negligible pressure drop added to the system from this branching. Even though, Ramos *et al.* [147] used a slightly different geometry than here, the pressure drop values computed in the 3D simulations were of the same order of magnitude.

The use of the hydraulic diameter overestimated the pressure drop in all simulated geometries. For the w_0 =1 mm geometry, the pressure drop in generation 0 and 1 could be well estimated with the analytic solution of Hagen-Poiseuille for rectangular channels. However, the results started to deviate at higher generation levels. For the other geometries (*e.g.* Figure 3.7 bottom), the most accurate way to estimate the pressure drop in higher generation levels was the method of equivalent cross-sectional area. However, the interesting part is, that even though the pressure drop of the branches itself deviated from the method using the analytic solution, the overall pressure drop of the complete pattern (pressure at x =0) was quite accurate up to a width of the generation 0 of 2 mm. It seemed that the more rectangular a channel got, the more difficult it was to estimate the pressure drop in the channels with 1D calculations.

3.5.6 Peclet number

As discussed in 3.4.1, the Peclet number (Equation 3.18) could be used as some form of design criterion for the channel geometries (Study 7). Trogadas *et al.* [7] approached this problem by looking at the number of generation levels needed to achieve a Peclet number lower than one, using the thickness of the PTL as characteristic length. In our case, we have a different approach. We were looking at two different characteristic lengths. One was the hydraulic diameter of a rectangular channel, the other one was the width of the last branch. By doing so we were able to find the Peclet number directly at the outlet of the flow pattern, independent of the thickness of the PTL. It was then possible to conclude on the status of the flow at the end of the tree-shaped pattern. The Peclet number at the last branch (here generation 4) was calculated for both mentioned characteristic lengths, varying width between 1 to 5 mm, a width scaling parameter a of 0.79, 0.9 and 1, and a current density between 10 A/m^2 and 10^4 A/m^2. We chose a diffusivity coefficient of 3.5×10^{-5} ms^{-2} for oxygen in water vapour according to Trogadas *et al.* [7] The results can be seen in Figure 3.8. The graphs illustrate the following points: Both characteristic lengths give nearly the same results. At the last branch, the surface plot showing the Peclet number showed non-linear behavior, but neither the width of the channel nor the width scaling parameter had any significant influence on the Peclet number. The biggest impact came from the flow rate. For the case where the Peclet number was calculated with the width of the last branch as characteristic length, the Peclet number was influenced by neither the width scaling parameter nor the width itself. This was due to the fact that the widths in Eq. 3.18 cancelled each other out (if $L = w_{4,i}$). It only depended

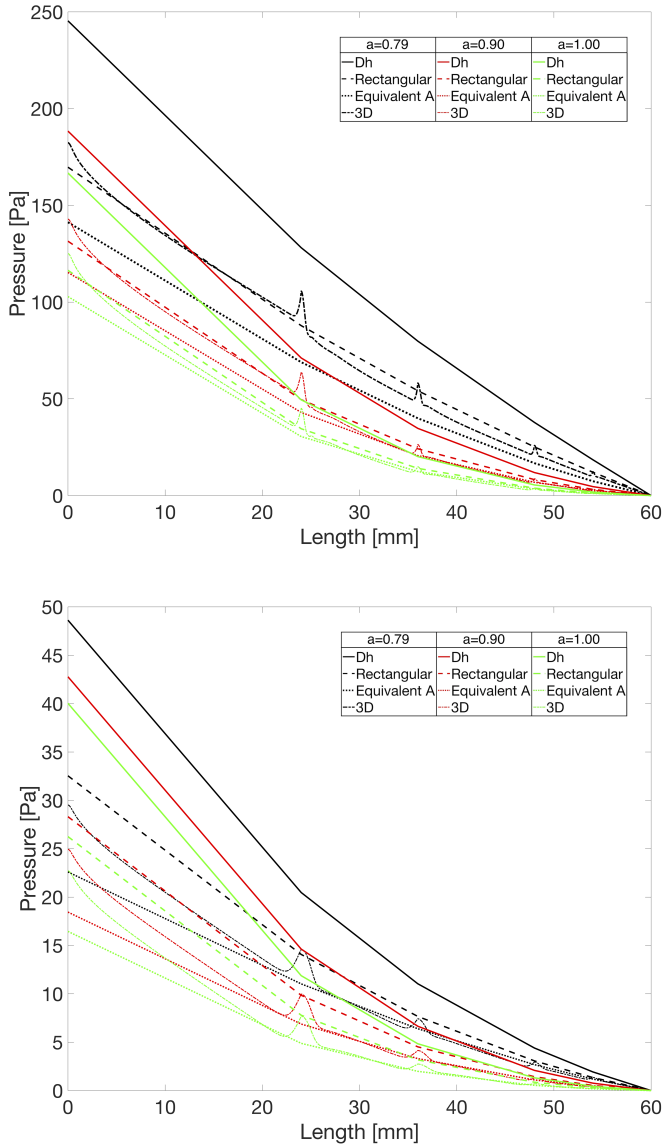

Figure 3.7: Pressure plotted along the centerline of the channels for different a parameters, at a flow rate equivalent to a current density of 10000 A/m^2, the pressure drop calculated with the three different cases and for the geometry with w_0 =1 mm (top) and w_0 =2.5 mm (bottom).

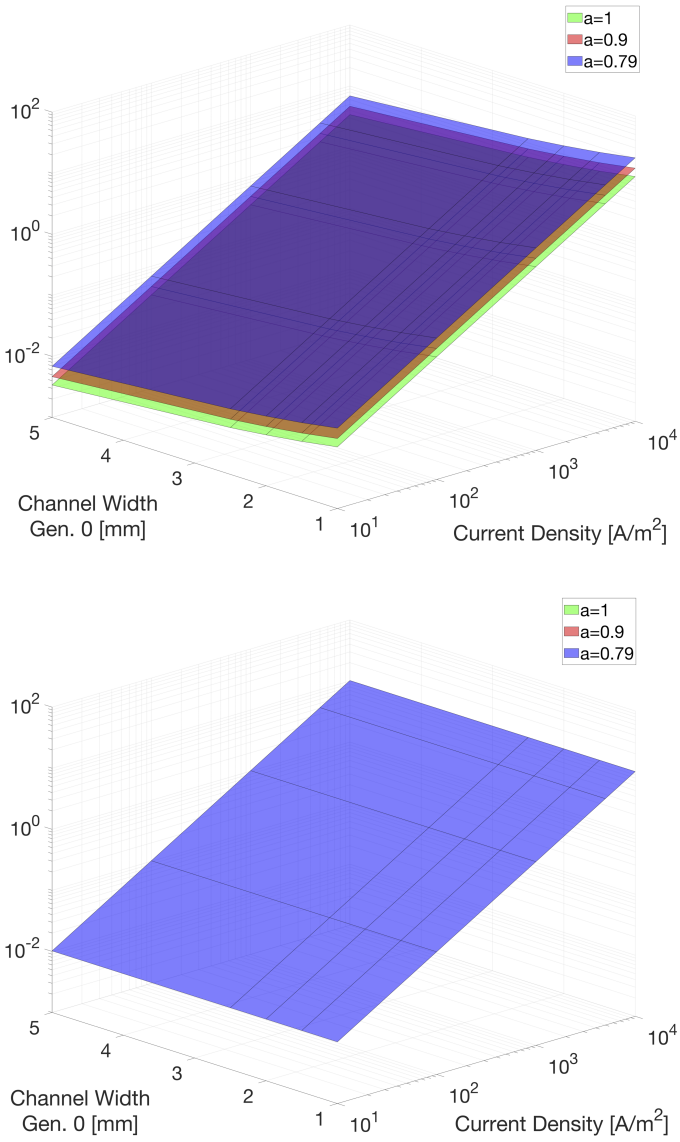

Figure 3.8: Peclet number plotted over different flow rates equivalent to a certain current density in A/m^2 and channel width of generation 0 for different width scaling parameter a. Top: Calculated with the hydraulic diameter D_h as characteristic length L. Bottom: Calculated with w_0 as characteristic length L.

on the depth of the channel, which was constant in our case.

This means that it will be difficult to use the Peclet number as a design criterion for the dimension/shape of the flow pattern. The huge influence of the flow rate, within a typical regime of flow variation, prevented this. It was still possible to use the Peclet number of a given channel width and width-scaling parameter to find a current density range, where the Peclet number was smaller than 1. This will then enable us to obtain a diffusion dominated flow at the last branches. An increased number of generations will make the condition more likely.

3.6 Discussion

We know already from the experiments of Trogadas *et al.* [7] that the tree-shaped field gives a better PEMFC performance than serpentine fields. The present flow field gave also uniform distribution of reactants, but at an entropy production that was lower than the one in the field predicted by Murray. The entropy production was reduced from branch to branch. The work was pointing at further improvements, in terms of geometric choices, and possibilities to keep the Peclet number at a reasonably low value.

We have seen that much of the 3D behaviour could be captured in a simpler quasi-1D model. This has the interesting aspect, that a model of the total cell obtains a good quasi 1D representation. A simplified, but realistic fuel cell model can, therefore, be obtained, by combining the present 1D tree calculation with 1D calculations, see *e.g.* [28, 174]. This allows for simple tests of, say, the impact of boundary conditions. The value of the flow rate is more important for the concrete result than any approximation used to compute the hydraulic diameter. The pattern used by Trogadas *et al.* [7] was similar to ours; as it was also inspired by a natural design (the lung). While their design was a 3D design, perpendicular to the MEA ours had the flow-field tree in-plane with the MEA. Our design can be machined with conventional milling techniques, where the outlet branches are located on a different layer. This may facilitate production and lead to decreased production costs for the flow field plates.

A quasi-3D pattern allows for an easy adjustment of the area filling property, through an increase of the generation levels. The pressure drop, as shown in Figure 3.4, will not increase significantly when the generation level increases, due to the ever-decreasing gradient when $a > 0.79$. This creates room for the adjustment of generation levels and area filling properties. The pattern of Trogadas *et al.* [7] does not have this flexibility.

The computed pressure drop across our flow field could be compared to measured results for the conventional serpentine or parallel patterns. In order to do so, we used the results from 3D simulations of Su *et al.* [175]. With similar operating conditions as ours, we found that our tree-shaped field had a lower pressure drop than the serpentine field. Depending on the chosen width scaling parameter a, the difference could be as big as one order of magnitude. It has to be noted, however, that the pressure drop across the tree-shaped pattern will slightly increase if a more space-filling pattern is used. On the other hand, the pressure drop was bigger than the one across simulated parallel pattern (up to 1 order of magnitude). To see the full impact on the performance of our flow field on the fuel cell, experiments need to be conducted, and compared to industry-standard flow field patterns. Another point of interest in connection with the tree-shaped pattern is the use of different branching rules. For example, different branching angles or number of branches per generation level (*e.g.* 4 instead of 2, to create some form of "H" branching) can be introduced. Effects on the uniformity of fuel and entropy production need to be investigated and compared with the presented flow field. The fractal FFP has been designed for uniform distribution of reactant gases over the PEM, with a constant density of outlet channels. This implies that the TEP in a FC can be lowered by optimizing the flow field alone. The entropy production of other origins can be considered as a separate optimization problem. This separation of problems was performed already in the original article of Kjelstrup *et al.* [13], which also Cho *et al.* [10] draw inspiration from. The optimal catalytic layer did not depend (much) on the flow field geometry, at least when the water accumulation had no impact on the hydraulic resistivity. According to Cho *et al.* [10] the multilayer 3D FFP may lead to high water accumulation. Thick 3D FFPs are not beneficial for FC because of their high mass and cost. The present fractal flow field can be milled into the flow field plate of standard thickness and hopefully give an essentially lighter and cheaper alternative.

In the complete fuel cell system, there are many other different sources of entropy production. These sources and values for different current densities can be found in the paper of Sauermoser *et al.* [174] which describes the 1D modelling of a PEMFC with non-equilibrium thermodynamics. A general aspect of the above study should finally be pointed out. The flow field evaluated here is by no means restricted to the PEMFC. Also, other fuel cells may benefit from a similar structure. Supply systems like this are common in nature, and may thus have more applications also in technology, say in catalysis.

3.7 Conclusion and perspectives

We have documented a tree-shaped flow field based on Murray's law's constraints, but with different geometric variables, for the supply of gases to a PEMFC membrane. The gases were delivered at the membrane at uniform conditions, but with smaller entropy production than Murray's tree. Entropy production was based on viscous dissipation only. A quasi-1D model was used and found to represent a 3D model within a maximum deviation of 10% for the most suitable pressure drop calculation method and most flow magnitudes relevant to the PEMFC. This applied when the channel cross-section was rectangular, not circular. Flow channels which had a high width to depth ratio, produce a small asymmetric behaviour, which explained the deviations.

We have thus established a basis for a 1D analysis of the whole single cell PEMFC, to be expanded to non-isothermal conditions in the future. 3D computations are time-consuming and can only be conducted for a restricted number of geometries. The 1D results give an opportunity for fast quantitative estimations on different fractal-type geometries.

The main difference between this design and that of Trogadas *et al.* is that Trogadas *et al.* used a 3D structure, whereas we propose a two-layer flow field plate with 2D patterns of constant channel depth. We hope that the new design may help reduce the weight and costs of the flow field plate. Experimental proof beyond that offered by Trogadas *et al.* [7] remains to be obtained. Additional sources of entropy production from thermal, electrical and chemical sources, are there. Preliminary studies indicate that the present design allows us to optimize these sources independently of the flow field optimization. [174]

Conflicts of interest

There are no conflicts of interest to declare.

Acknowledgments

We gratefully acknowledge the support from NTNU in Trondheim and the Research Council of Norway through its Centre of Excellence funding scheme with Project No. 262644 (PoreLab). The simulations were performed on resources provided by UNINETT Sigma2 - the National Infrastructure for High Performance Computing and Data Storage in Norway.

3.A Filling properties of self-similar networks

West *et al.* [176] required that the spherical volume around one branch was equal to the sum of the volumes of all spheres around the sub-branches. This is expressed in equation 3.A.1. The conditions follow from the need to accommodate the entire volume flow in the network [176]. Each sphere has as diameter the length of the corresponding branch.

$$\sum_{i=1}^{N_j} V_{spherical,i,j} = \sum_{i=1}^{N_{j+1}} V_{spherical,i,j+1} = V_{spherical} \tag{3.A.1}$$

Here $V_{spherical,i,j}$ is the spherical volume around one branch i at level j and $V_{spherical}$ is a volume around the branch at level 0, which is constant.

$$\frac{4}{3}\pi \left(\frac{l_{i,j}}{2}\right)^3 N_j = \frac{4}{3}\pi \left(\frac{l_{i,j+1}}{2}\right)^3 N_{j+1} \tag{3.A.2}$$

Rearrangements lead to Equation 3.A.3:

$$\left(\frac{l_{i,j+1}}{l_{i,j}}\right)^3 = \frac{N_j}{N_{j+1}} \tag{3.A.3}$$

Due to the premise used here, that each branch splits into two branches, the ratio between N_j and N_{j+1} equals 1/2. After reformulating Equation 3.A.3, the length scales as follows:

$$l_{i,j} = \left(\frac{1}{2}\right)^{j/3} l_0 = \frac{1}{2^{j/3}} l_0 \tag{3.A.4}$$

Equation 3.A.4 is similar to Equation 3.2, apart from the length scaling parameter k of 3. It is easy to show that the relation changes when the constraint changes. For constant occupation in terms of areas we obtain

$$l_{i,j} = \left(\frac{1}{2}\right)^{j/3} l_0 = \frac{1}{2^{j/2}} l_0 \tag{3.A.5}$$

Any value for k between constraints given by the 3 or 2-dimensions, imply a particular space-filling structure. When $k = 2$, the flow field is optimized to deliver the media to a (quasi-) two-dimensional area. For $k = 3$ it is optimised for a 3-dimensional one.

Chapter 4

Scaling factors for channel width variations in tree-like flow field patterns for polymer electrolyte membrane fuel cells - An experimental study

Marco Sauermoser[1], Bruno G. Pollet[2], Signe Kjelstrup[1] and Natalya Kizilova[3,1]

1. PoreLab, Department of Chemistry,
Norwegian University of Science and Technology, NTNU,
NO-7491 Trondheim, Norway

2. Department of Energy and Process Engineering,
Norwegian University of Science and Technology, NTNU,
NO-7491 Trondheim, Norway

3. Warsaw University of Technology,
Institute of Aviation and Applied Mechanics,
PL-00-665 Warsaw, Poland

This chapter was submitted to
J. Power Sources Advances

Abstract

Numerical simulations have shown that the width scaling parameters of tree-like patterns in flow field (FF) plates used in polymer electrolyte membrane fuel cells (PEMFC) reduces the viscous dissipation in the FF channels. In this study, experimental investigations were conducted on a 2-layer FF plate possessing a tree-like FF pattern which was CNC milled on high-quality graphite. Three FF designs of different width scaling parameters were employed. I-V curves, power curves and impedance spectra were generated at 70%, 60% and 50% relative humidity (25 cm^2 active area), and compared to those obtained from a conventional 1-channel serpentine FF. It was found that the FF design, with a width scaling factor of 0.917 in the inlet and 0.925 in the outlet pattern, exhibited the best peak power out of the three designs (11% - 0.08 W/cm^2 difference to serpentine FF). Results showed that reducing the viscous dissipation in the flow pattern was not directly linked to a PEMFC performance increase. It was found that water accumulation, together with a slight increase in single PEMFC resistance, were the main reasons for the reduced power density. As further improvements, a reduction of the number of branching generation levels and width scaling factor were recommended.

4.1 Introduction

Polymer electrolyte membrane fuel cell (PEMFC) systems already contribute to the rapidly growing transition from a fossil fuel-based to a green and renewable energy-based society. A PEMFC is an electrochemical device that uses oxygen and hydrogen in the presence of a catalyst to produce power and water only. A PEMFC stack consists of a series of single cells in which membrane electrode assemblies (MEA) are sandwiched between flow field plates or bipolar plates. A MEA contains the proton exchange membrane, the catalyst layers (electrodes) and the gas diffusion layers (GDL). However, the cost and efficiency of PEMFC systems still need to be greatly improved for full commercial deployment. Several bodies of authority and organisations have released technological targets for fuel cell stacks and systems [3, 4, 51]. A discussion of these targets has been presented by Pollet *et al.* [5]. One of these targets is, for example, US Department of Energy's cost target of US$40/kW with an efficiency of 65% at peak power and with 12.5 g of platinum (Pt) for 500,000 systems per year, including 80 kW automobiles and 160 kW trucks [3]. The Japanese NEDO's Technology Development Roadmap 2017 has also set high technological targets for PEMFC performance [4]. For example, cell voltages of 0.85 V at 4.4 A/cm^2 and 1.1 V at 0.2 A/cm^2 by 2040 are targeted. Such cell voltages can only be reached when all components are optimised in the PEMFC stack, and therefore innovative solutions for current problems

need to be proposed and implemented. In Europe, the performance targets focus more on the reduction of the catalyst loading, the system cost and the improvement on durability and general cell volumetric power [51].

In this context, one important target is the optimisation of the flow field plate (FFP), with the important role to (i) evenly distribute the gas at the surface of the electrodes' catalytic layers, (ii) provide good electronic conductivity and (iii) a rigid structural integrity on the MEA. The FFP usually has a specially designed flow field design made of channels to supply the oxygen and hydrogen on both sides of the MEA [6]. It contributes ∼60% of the overall mass and represents ∼30% of the overall cost of a PEMFC [48]. There are many different ways to design an efficient FFP, however, there is always a compromise in the design, such as having a low pressure drop and at the same time reducing the capabilities of transporting water out of the flow field (see [177] for a recent review). Among the most promising ones are the tree-like or biomimetic flow field patterns, which offer an uniform flow distribution and a desirable change from convective to diffusional flow over the length of the channels; accomplished by the step-wise decrease in channel size [165]. Kjelstrup *et al.* [13] showed that the reactants need to be distributed uniformly to minimise the entropy production in the PEM fuel cell. If the reactants are not supplied uniformly, it could cause severe and permanent damage to the PEM fuel cell catalyst layer due to fuel starvation [178]. Another advantage of the uniform distribution is that the catalyst utilisation is maximised [7].

Already in 2002, Morgan Fuel Cell Ltd (no longer trading) developed and patented a high-performance flow field pattern called Biomimetic^{TM}. This pattern was inspired by animal lungs and plant tissues [179]. Since then, several various approaches have emerged using this type of patterns. Ozden *et al.* [77] studied different configurations such as variations of leaf- or lung-based designs for the use in direct methanol fuel cells (DMFC). However, these designs turned out to yield the lowest performance when compared to other flow field designs at all operating fuel cell conditions. Behrou *et al.* proposed a topology optimization approach for the biomimetic leaf-type FFP based upon maximisation of both output power and homogeneity of the current density distribution [180]. Trogadas *et al.* presented a lung-inspired flow field pattern, which was 3D printed [7]. They compared different designs with three, four or five branching generation levels of H-formed branches and found that the one with four generations delivered the highest performance. To lower the cost of production, Bethapudi *et al.* [8] proposed a novel flow field design manufacturing process, adopting a layer-wise printed circuit board

(PCB) structure approach. Experiments showed a more stable operation than standard serpentine flow fields with an increase in performance while running the PEMFC with air and at low relative humidity (RH). The design with four generations of H-formed branches was implemented.

To date, there have been a few numerical investigations on other biomimetic patterns. Gheorghiu *et al.* [15] showed that the human lung conforms with Murray's Law and distributes oxygen and carbon dioxide uniformly. Duhn *et al.* elaborated a complex shape inlet and outlet channels for the parallel FFP for solid oxide fuel cells (SOFC) which provided high uniform reactant distribution between the parallel channels [181]. Hou *et al.* [162] investigated how the flow changed from convective to diffusional flow. When it comes to the design of a lung-like or tree-like pattern, the scaling was mostly set to conform with Murray's Law [7, 8].

Sauermoser *et al.* [165] recently showed that a change in the width scaling factor (the rate of reduction of the channel width with changing branching generations) away from that of Murray's could have a significant impact on the viscous dissipation. Viscous dissipation is the heat generated due to frictional losses in a flow system. An increase in the width scaling factor showed a reduction in pressure drop along the channels, thus reducing the viscous dissipation. This, in turns, decreased the overall entropy production, which should be beneficial for the PEMFC performance. Therefore, in this work, we investigated the effect of varying this scaling factor experimentally, by changing the flow field channel width, and how it impacted the PEMFC performance. To do this, we ran experiments using pure oxygen, to eliminate issues with fuel/gas starvation effects or gradients under partial pressure conditions. The other objective of this study was to design a flow field, which could be simply machined using traditional CNC milling techniques, capturing still the essential advantage of the tree-like flow field; the homogenous distribution of reactants and products at small viscous dissipation.

In the first section, a brief summary of the theory around the width scaling factors for tree-like flow field patterns (while keeping the cell active area constant) is given, followed by an in-depth description of the newly designed flow fields. In the following section, the experimental setup is described in which different tests are shown. Next, we present the results of the experimental tests performed with the newly designed flow field patterns. The findings are compared to those obtained using an industry-standard single-channel serpentine pattern. We also discuss the impact of the scaling factor on the PEMFC performance. In conclusion, we provide an outlook on

future developments of FF designs which could lead to improved PEMFC performance.

4.2 Theory

Tree-like patterns can be characterised by the following parameters, when the channel depths are constant:

1. The width of the channel in the first generation, w_0
2. The depth of the channel, d
3. The maximum number of generations, j_{max}
4. The width scaling parameter, a

In the tree-like pattern, we start to number channels at branching generation level $j = 0$. In addition to the points above, one needs to describe how the length of the channels changes. There are two possibilities for this: a) Either the lengths are scaled, like the channel width, or b) manually set to a certain value. In our case, we used the latter option, to allow us to serve a square area with feed points. By scaling the length, only a rectangular area could be uniformly filled [165]. The channel width was therefore scaled using the following equation for the inlet (i) and outlet plates (o) (see next section):

$$w_{j,\mathrm{i}} = w_{0,\mathrm{i}} a_{\mathrm{i}}^{j} \tag{4.1}$$

$$w_{j,\mathrm{o}} = w_{0,\mathrm{o}} a_{\mathrm{o}}^{j} \tag{4.2}$$

where $w_{j,\mathrm{i}}$ and $w_{j,\mathrm{o}}$ are the channel widths at generation j for the inlet and the outlet plate, respectively, and $w_{0,\mathrm{i}}$ and $w_{0,\mathrm{o}}$ are the channel widths of generation 0 for the inlet and outlet plate, respectively. As already described in the Introduction, our previous work has shown [165], that the entropy production from viscous dissipation (see Eq. 4.3) reduces when the width scaling parameter a is increased. In a 1D-system, as used in this section, the viscous dissipation is calculated based upon the pressure drop along the channels, as seen in Eq. 4.3.

$$\frac{dS_{irr}}{dt} = -\sum_{j=0}^{j_{max}} \sum_{i=1}^{N_j} Q_{j,i} \frac{\Delta p_{j,i}}{T}, \tag{4.3}$$

where $\frac{dS_{irr}}{dt}$ is the total entropy production of the system in J s^{-1} K^{-1}, i is the i-th branch of branching generation level j, N_j is the maximum number

Table 4.1: Parameters of three tree-like flow fields, for the inlet (i) and outlet plates (o). Listed are the width of generation 0, channel depth and generation numbers of the inlet (a_i, $w_{0,\mathrm{i}}$, d_i, $j_{max,\mathrm{i}}$) and the outlet (a_o, $w_{0,\mathrm{o}}$, d_o, $j_{max,\mathrm{o}}$). Widths and depths are given in mm.

Design	a_i	a_o	$\frac{w_{0,\mathrm{i}}}{d_\mathrm{i}}$	$\frac{w_{0,\mathrm{o}}}{d_\mathrm{o}}$	$j_{max,\mathrm{i}}$	$j_{max,\mathrm{o}}$
1	0.917	0.925	1	0.8	8	6
2	0.917	1	1	0.8	8	6
3	1	1	1	0.8	8	6

of branches at branching generation level j, $Q_{j,i}$ is the volumetric flow rate of branch i in branching generation level j in m^2/s, $\Delta p_{j,i}$ is the pressure drop along branch i in branching generation level j in Pa and T is the uniform temperature of the system. An increase in a leads to larger channels and a lower overall pressure drop along the channels. This decreases the overall entropy production of the system.

In order to avoid having unfeasible or non-machinable patterns, a should be capped at one. Otherwise, the channel width would increase at each branching generation level j. The reason for this is that branches will overlap at a certain point. For the patterns presented below, Equation 4.1 and 4.2 was used to calculate the channel widths in the inlet and outlet plate, respectively. As mentioned already, the lengths were set manually.

4.3 Experimental

4.3.1 Tree-like flow field plates

Tree-like flow field patterns were CNC milled in Schunk FU4369 graphite plates by HySA Systems Competence Centre, University of the Western Cape, South Africa. As previously mentioned, the scope of this study was to design a FFP, machinable with conventional CNC milling techniques. The flow field had, therefore, an inlet and an outlet plate clamped together by the fuel cell support frame. Three different designs were machined with width-scaling parameters for the patterns in the inlet and outlet plates as shown in Table 4.1. The table also shows other important parameters, such as the channel width and depth. The sealing of the two FF plates was accomplished by compressing them together with the help of the fuel cell support frame, which also acted as the seal to the environment. The channel lengths were manually set with the aim to achieve a good coverage of the 25

cm^2 active cell area, cf. Section 4.2. The length of generation 1 and 2 was set at 12 mm. After this, the length was set for branching generation level 3 and 4 at 6 mm. This trend, namely reducing the length of the channels by 50% every second branching generation level, was kept until the last generation. The length was always measured from one midpoint of the intersections of two branching generation levels to the next one. For branching generation level 0, the length could only be 23.95 mm, because it needed to be connected to the inlet or outlet hole of the flow field plate, determined by the fuel cell housing. The thickness of the inlet plate was 3 mm and of the outlet plate 2 mm.

The scaling parameters at the inlet and outlet plate (0.917 and 0.925) were given by limitations of the CNC milling. The smallest cutter was able to mill 0.5 mm. Therefore the scaling parameter was adjusted so that the branch in the last generation had a channel width of 0.5 mm. The maximum number of branching generations j_{max} also contained generation 0. Therefore the absolute number of branching generations was $j_{max}+1$. From the overall nine branching generations of the inlet plate, the last one made the connection to the outlet plate. With this, the connection to the inner layers of the PEMFC's gas diffusion layer (GDL) and membrane electrode assembly (MEA) was obtained. Small rectangular holes connected the two plates with the same width as the branch of the last branching generation of the inlet plate and the width of the previous branching generation. For Design 1 and 2, this means 0.5 mm x 0.55 mm, and for Design 3, 1 mm x 1 mm. Figure 4.1a shows Design 3 assembled in the balticFuelCells housing, while Figure 4.2 shows drawings of the inlet (Fig. 4.2a) and outlet (Fig. 4.2b) plate of Design 3. In addition, Figure 4.1b displays a rendered model of the assembled flow field plate of Design 1, to see how the inlet and outlet plate are aligned. The ears included at the inlet plate (Fig. 4.2a) are used to connect the plate to the fuel cell housing.

4.3.2 Setup

A Biologic FCT-50s test station was used in combination with a balticFuelCells qCF FC25/100 V1.1 LC support frame and a balticFuelCells cellFixture cF25/100 HT Gr. V1.3 fuel cell housing. The single cell PEMFC had an active area of 25 cm^2. The setup was controlled with the software delivered with the FCT-50s. LabVIEW 2019 was used to read the measurements of two thermocouples, which measured the temperatures at the anode and cathode flow fields. The temperature of the fuel cell housing was controlled with a Grant LT Ecocool 100 thermostatic bath, which was connected to the anode

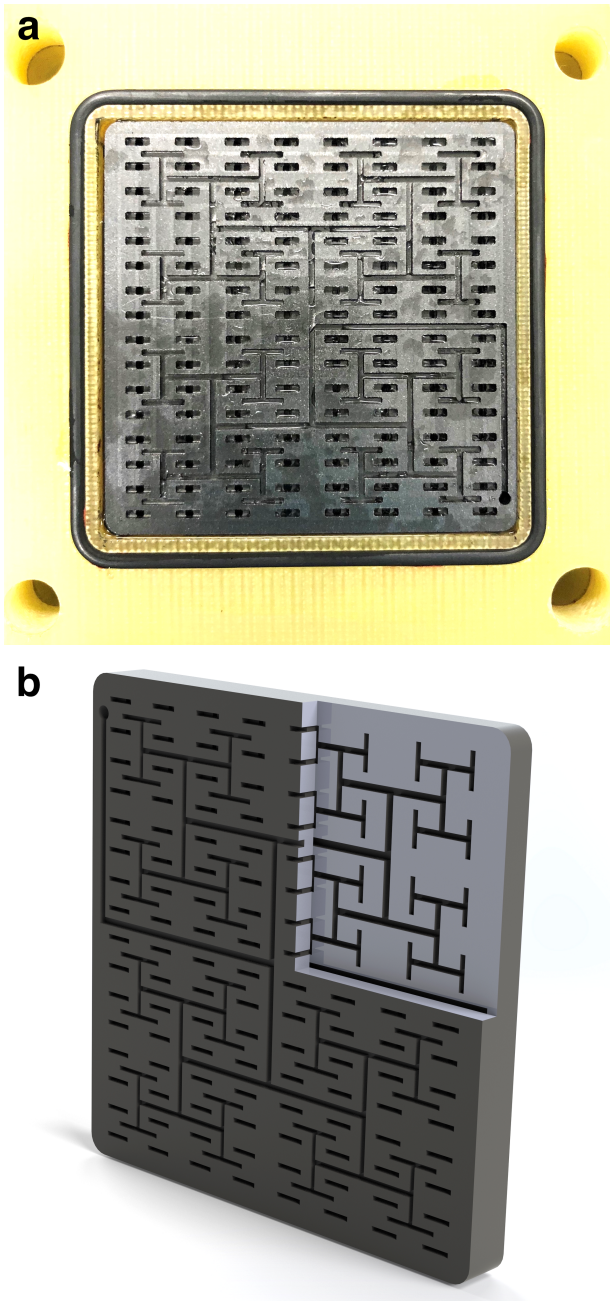

Figure 4.1: Design 3 assembled in the balticFuelCell housing after experiments (a) and render of the assembled flow field plate (Design 1) (b).

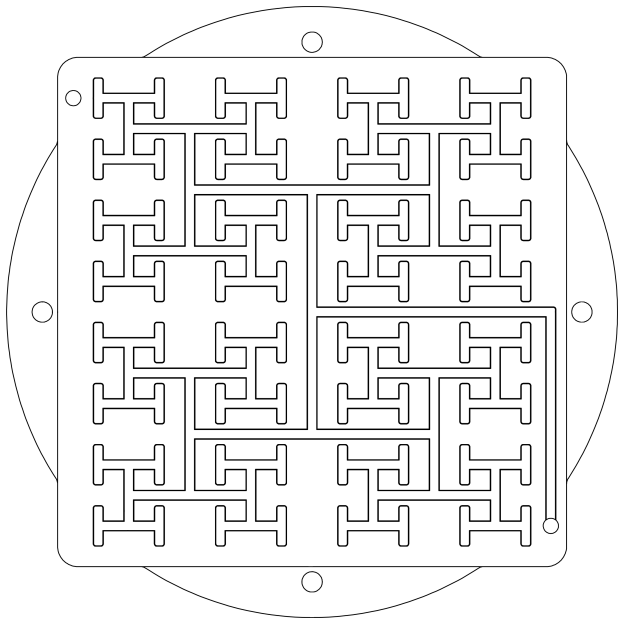

(a)

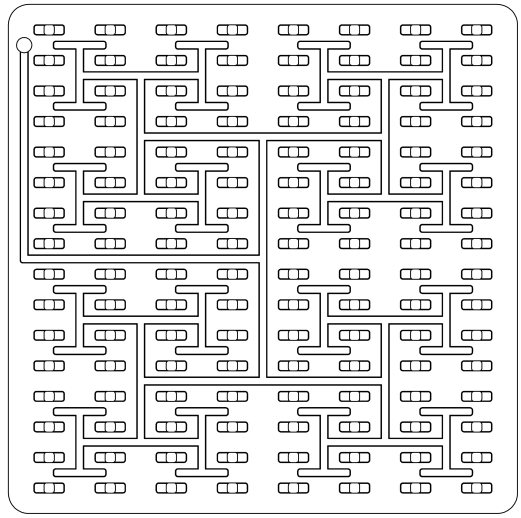

(b)

Figure 4.2: Drawings of the inlet (a) and outlet (b) plates of Design 3.

Table 4.2: Accuracy and resolution information of equipment used in the experiments.

Equipment	Manufacturer	Accuracy	Resolution
FCT-50s	Biologic	Current: 0.5% Voltage: <0.1% Frequency: 1%	Current: 4 mA Voltage: 76 μV
VPPM-6	FESTO	Pressure: 2%	-
NI 9211	National Instruments	Temperature: 0.07 °C	-
NI USB-6215	National Instruments	Voltage: 2690 μV	Voltage: 91.6 μV
LT ecocool 100	Grant	Temperature stability: ± 0.05 °C	-

and cathode side of the qCF FC25/100 fuel cell support frame. The relative humidity (RH) was calculated based on the cell and humidifier temperature, and the gas properties within the Biologic test station software's integrated humidity calculator. The compression of the single-cell was regulated with air, where the pressure was controlled by a FESTO VPPM-6 electrical pressure regulating valve, which was connected to a National Instruments NI USB-6215 for voltage input. This was connected to the LabVIEW software, where the compression was set and measured. A set of two 1 m long 16 mm^2 copper cables were used as load cables. The cell voltage of the PEMFC was measured with a set of two additional high-ohmic sense cables, which were in direct contact with the FFP. Cell temperatures were measured with K-type thermocouples at the anode and cathode flow field plates. The thermocouples were connected to a National instrument Ni 9211. Table 4.2 gives an overview of the accuracies and resolutions of the equipment used in the experiments. The reference flow field plate, which was made by balticFuelCells, had a 1-channel serpentine flow field pattern with a channel width and depth of 0.8 mm and a land width of 0.96 mm, milled in graphite with a density of $\geq$1.85 g/cm^3 and a specific resistance of <12 $\mu\Omega$m (through-plane). The reference flow field was always used on the anode side, also in the tests of Designs 1-3. The Designs 1-3 were thus tested as cathode flow fields only.

The 5-layer MEA consisted of the following parts: The anode and cathode side consisted of a Sigracet S28BC GDL, a cathode and anode with Pt on advanced carbon with a loading of 0.3 mg Pt/cm^2 and 0.1 mg Pt/cm^2

respectively, and a Nafion 212® membrane with a thickness of 50.8 μm. The MEA was purchased completely assembled (hot pressed) from balticFuelCells. Each experiment used the same 5-layer MEA.

Pure oxygen (99.999%) and hydrogen (99.999%) were purchased from Linde and used as PEMFC gases. Using pure oxygen reduces the effects of concentration gradients inside the GDL and facilitates the interpretation of the width scaling analysis. This helped us avoid the effects of concentration gradients of the gases inside the gas diffusion layer and facilitates the interpretation. For all experiments using the four types of FF designs, an overpressure of 0.5 bar was set and kept constant.

Each newly assembled PEMFC single cell was subjected to the same break-in procedure, which took overall 20 hours. The single cell temperature was kept constant at 80°C, the gas lines for both the anode and cathode were heated at 83°C. At first, the humidifier temperature was set to 75°C, which was then reduced to 72°C after 10 hours. The current was slowly ramped up to 35 A, held for 11 hours and then reduced to 30 A for the rest of the break-in procedure, to avoid a cell voltage drop below 0.4 V. The fuel cell was run in stoichiometric mode with a stoichiometric factor of 2 for hydrogen and 6 for pure oxygen. A minimum flow of 200 ml/min for hydrogen and 300 ml/min for oxygen was set.

Each of the following experiments was carried out without a shut-down of the PEMFC. The order of the tests was as follows: Directly after the break-in, the performance test at 70% RH was started. After that, electrochemical impedance spectroscopy (EIS) test was performed, followed by the 3-hour hold test. The RH was changed, and then the next performance test was started, with the other two tests following. The same order was then kept for the last RH.

4.3.3 Performance test

The performance test procedure followed the European guidelines [182] for testing of automotive MEAs and PEMFCs (see Table 4.A.1). The performances of the three new FF designs were measured, and the corresponding I-V and power curves at the three different relative humidities (70%, 60% and 50%) were generated. The cell temperature was kept constant at approximately 80°C. The humidifier temperatures were set at 72°C, 68°C and 64°C. The temperature of the heated gas lines, both for the oxygen and hydrogen, was set at 83°C for all RH settings. Stoichiometric flow settings were used, with a stoichiometric factor of 2 for hydrogen and 6 for oxygen. Gas flow

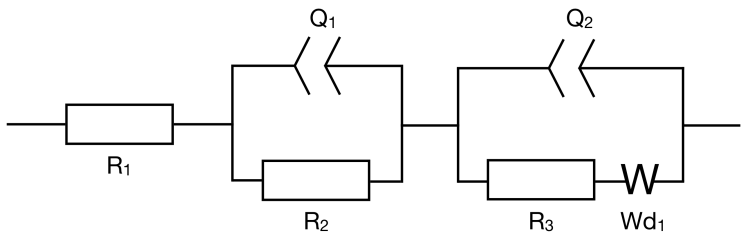

Figure 4.3: Modified Randles circuit from Dhirde *et al.* [183] used for the circuit fitting where R_i is an ohmic resistor, Q_i is a constant phase element and Wd_1 is a Warburg convective diffusion element.

rates had a minimum value of 200 ml/min for hydrogen and 300 ml/min for oxygen. If the cell voltage had not equilibrated itself, the current was kept constant, until it stayed the same within a certain tolerance for 30 seconds. The cell voltage measurements were then averaged over the last 30 seconds of each current step.

4.3.4 Electrochemical impedance spectroscopy test

Three different currents, 7.5 A, 15 A and 22.5 A, were used during the EIS procedure for each RH and flow field pattern employed. An amplitude around the mentioned base values of ± 5% was set. The frequency was decreased from 10 kHz to 0.1 Hz. A minimum flow of 84 ml/min for hydrogen and 126 ml/min for oxygen, with a stoichiometric factor of 2 for hydrogen and 6 for oxygen was used. The cell temperature was set at 80°C, the line temperature at 83°C and the humidifier temperature between 72°C and 64°C, according to the RH (see Section 4.3.3). Before each of the three currents was tested, the fuel cell was equilibrated for 2 min. The data was then analysed with the EC lab, followed by a circuit fitting procedure performed in MATLAB 2019.

Circuit fitting

Circuit fitting was performed in MATLAB with the help of the open-source code from Dellis [184]. To allow for a better comparison of the fitted parameters, upper and lower boundaries were set within the MATLAB code. A modified Randles circuit (see Fig. 4.3), taken from Dhirde *et al.* [183] was used for the curve fitting. R_1 represents the ohmic resistance of the fuel cell in Ohm (Ω). The first parallel loop describes the process at the anode, whereas the second one describes the equivalent at the cathode. A constant phase element (CPE) was used in the curve fitting because the semi-circles were depressed at high frequencies [185]. The CPE uses two parameters,

namely a time constant Q in F cm^2 s$^{\alpha-1}$ and an exponent of phase angle α. The R_2 and R_3 are charge transfer resistances at the anode and cathode, respectively, in Ω. Additionally, a Warburg (W) convective diffusion element was used, where we had a diffusion resistance R_d in Ω and a time constant τ_d in s.

Because we have several elements with two parameters in the circuit, a pseudo capacitance C^p and a diffusion impedance Z_d was calculated with the equations below (Eq. 4.4 and 4.5). This allowed for an easier comparison of the values between the different EIS tests.

$$C_i^p = \frac{(Q_i R_{i+1})^{1/\alpha_i}}{R_{i+1}} \tag{4.4}$$

$$Z_d = R_d \frac{\tanh\sqrt{\tau_d j\omega}}{\sqrt{\tau_d j\omega}} \tag{4.5}$$

where i can be either 1 or 2, depending on the parallel loop, ω is the angular frequency in 1/s, and j is the imaginary unit. After calculating Z_d, the absolute value $|Z_d|$ was taken for comparison.

4.3.5 Hold test

During the hold test, which was started right after the EIS test, a current of 20 A was applied and held for 3 hours. The cell temperature was kept at 80°C, the line temperature at 83°C and the humidifier temperature between 72°C and 64°C, depending upon the RH (see Section 4.3.3). The same settings regarding gas flow rates as in the EIS test procedure were used.

4.4 Results and discussion

The results of the three tests carried out on the four flow field plates setups will be are reported in the same order as described above.

4.4.1 Performance tests

Figure 4.4 shows the results of the performance tests for all four flow fields and three RH values. The standard deviation was on average ± 0.3 mV, with a maximum of 4 mV, which occurred at the last current step of Design 3. It can be observed from the I-V and power curves that the serpentine pattern had the best performance, independent of RH. Additionally, higher current densities could be reached with the serpentine pattern than Design 1 to 3. The tree-like flow field plate designs, however, were in the best case,

able to achieve a maximum power density, only 11% (0.08 W/cm^2) lower than the reference one. In the worst case, a reduction of 37% (0.26 W/cm^2) was observed. Between 0 A/cm^2 and 0.6 A/cm^2, all tree-like patterns had a higher cell voltage which was stable throughout all current steps in this range.

Among the new flow field designs, Design 1 had the best performance, especially at 70% RH. The pattern with no width scaling (a_i=a_o=1) was clearly worse. The performance tests for Design 3 for all three RH values were interrupted at 1.2 A/m^2, because the cell voltage did not reach a steady-state.

4.4.2 Electrochemical impedance spectrum tests

Figures 4.5 and 4.6 shows the results of the EIS tests for all FF setups and RH values, in the form of Nyquist plots. Data appeared to be regular with only a few outliers. At first glance, an immediate difference could be seen between the results of the serpentine FFP (Fig. 4.5a) and the three new designs (4.5b, 4.6a and 4.6b). Tree-like FFs have a distinct second semi-circle at lower frequencies at all currents and RH values. The serpentine FF (Fig. 4.5a) has only a very small one at high currents (22.5 A). When looking at the first semi-circle, at higher frequencies, it can be observed that the size (radius) of it, is relatively constant at 7.5 A for all FF designs. The same applies to 15 A. At 22.5 A, however, a significant increase in radius for both Design 2 (Fig. 4.6a) and 3 (Fig. 4.6b) at all RH values is observed. For Design 1 (Fig. 4.5b), only the test at 70% RH exhibits a comparable size.

This could help explain the performance drop at lower RH settings during the performance tests. When changing the relative humidity, the shape of the EIS curves did not significantly change for the serpentine pattern. However, for the tree-like patterns, in some cases, large deviations were observed compared to the serpentine pattern. Another point is that the intersection of the measurements with the real axis, occurs at a higher value for Designs 1 and 3, compared to the serpentine pattern. The intersection gives an estimate of the cell resistance. This is further discussed in the next section.

Circuit fitting

Figures 4.7a to 4.7f shows the result of the circuit fitting for all four FF design setups and three RH settings. On average, a R^2 value of 0.986 was achieved with the curve fitting.

As already mentioned above, the Nyquist plots for Designs 1 (Fig. 4.5b) and

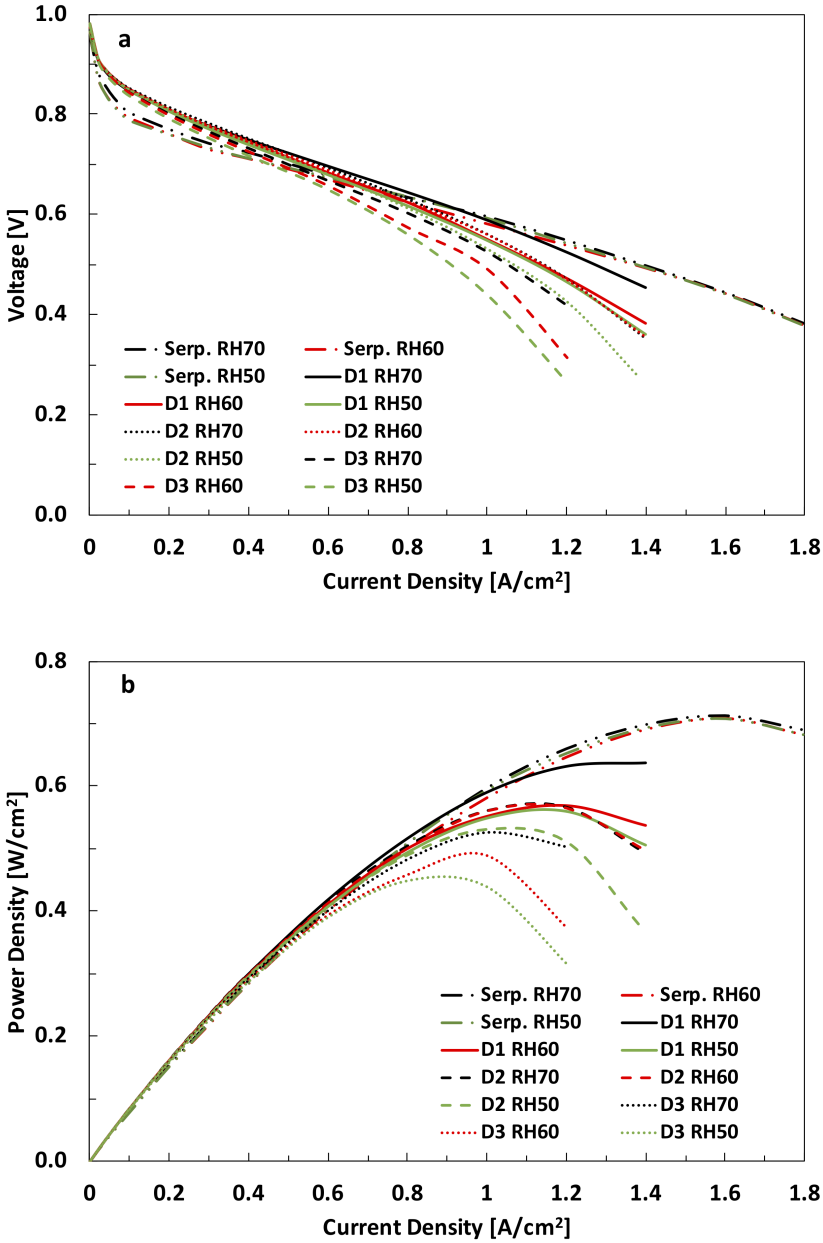

Figure 4.4: I-V curves (a) and power curves (b) for all four flow field plate setups at 70%, 60%, and 50% RH.

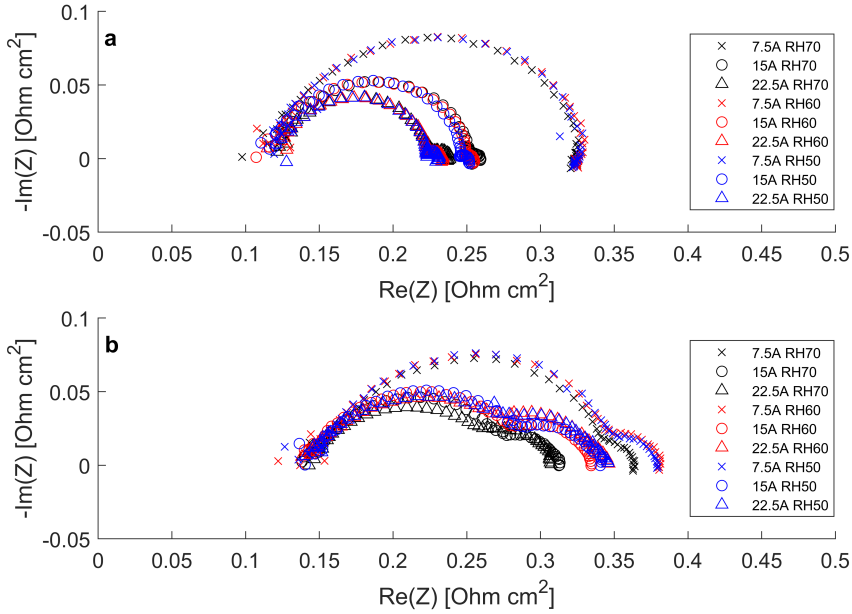

Figure 4.5: Nyquist plots of the EIS tests for serpentine pattern (a) and Design 1 (b) at 7.5 A, 15 A, and 22.5 A and 50%, 60%, and 70% RH.

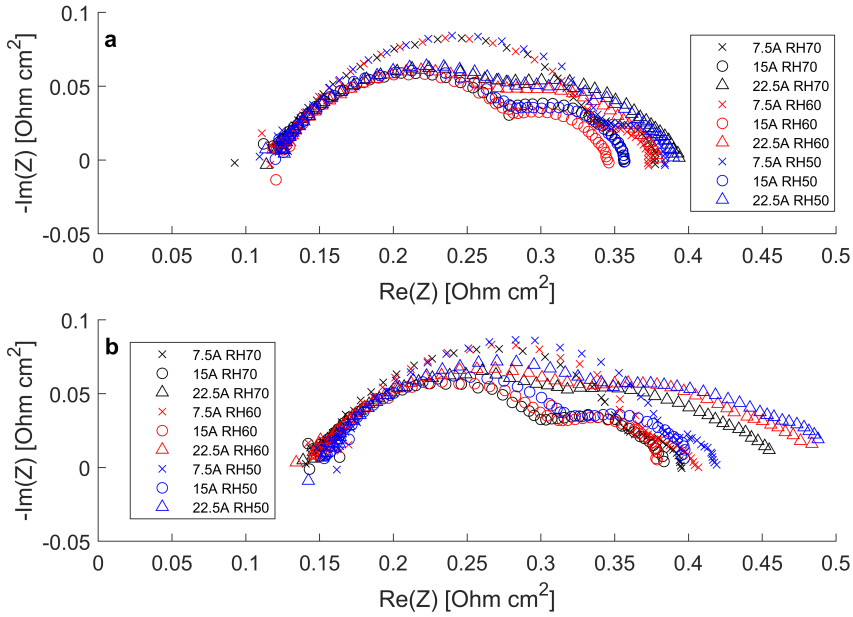

Figure 4.6: Nyquist plots of the EIS tests for Design 2 (a) and Design 3 (b) at 7.5 A, 15 A, and 22.5 A and 50%, 60%, and 70% RH.

3 (Fig. 4.6b) showed an intersection with the real axis at a higher value than the serpentine pattern (Fig. 4.5a) did. The same variation was observed in the fitted parameter R_1 (Fig. 4.7a) *i.e.* the ohmic resistance of the PEMFC. The pattern with a scaling factor of 1 for both inlet and outlet plate (Design 3), had wider channels, and therefore an increased channel/width ratio compared to Design 1. This results in a slightly higher resistance of the flow field plate and to a smaller contact area with the GDL leading to a higher contact resistance.

Design 2, however, showed ohmic resistances similar to the serpentine pattern. This variation was counter-intuitive, because of the scaling factor of 1 at the outlet, instead of 0.925 in Design 1. This was not a curve-fitting issue, as evident from the Nyquist plot. One reason for this behaviour could be that the two plates of the tree-like flow field plate (inlet and outlet plate) had a better contact (lower contact resistance) in Design 2 than 1. It is known that the contact resistance depends upon the machining tolerances of the surface. The ohmic resistances of the patterns are further discussed in Section 4.4.5. Because the intersections of all curves with the real axis are situated near the same position, we can assume that the membrane was hydrated properly, even at lower relative humidity values. Problems that are allocated to water must therefore be connected to water removal from the catalyst layer.

R_2 is the charge transfer resistance at the anode (Fig. 4.7b). Results show that the new FF designs showed on average an increase between 70% (Design 1) and 200% (Design 2). This was not expected, as the same flow field plate, which had a serpentine pattern, was used for the anode during the experiments of all four setups. This finding suggests that the cathode flow fields had a detrimental effect on the anode.

R_3 (Fig. 4.7c), which is the charge transfer resistance at the cathode, on the other hand, behaved differently. Design 1 showed a similar R_3, to that of the serpentine FFP on the cathode. On average, Design 2 had a 10% lower R_3, whereas Design 3 had a 44% higher R_3. Both, however, exhibited a large increase in R_3 at 22.5 A. This could be indicative of water flooding in the catalyst layer, according to Fouquet *et al.* [185], especially because the resistance should decrease with an increase in current due to the fact that as the overpotential increases at higher current densities, the charge transfer resistance decreases [186]. Another reason for the variation in R_3 are uncertainties in the curve fit. Therefore, it is interesting to look at the pseudo capacitance C_1^p (Fig. 4.7e) and C_2^p (Fig. 4.7f), because it incorporates Q_i, α_i and R_{i+1} in the parallel loops. The values for C_1^p (Fig. 4.7e) of Designs

1 and 2 are found to be similar to the one from the serpentine pattern. Design 3 shows values which are several orders of magnitude higher at 22.5 A, which is in agreement with the poor performance of the FF for this design. The C_2^p-values (Fig. 4.7f) are generally a little higher for the tree-like FF compared to the serpentine reference, again in good agreement with the lower performance of these.

The absolute Warburg diffusion impedance $|Z_d|$, gives an estimate of the mass transport resistances in the PEMFC. At high frequencies, the oxygen molecules do not need to move far, thus decreasing the impedance [186]. Therefore, we primarily looked at the results at 0.1 Hz, the lowest tested frequency (Fig. 4.7d). It was observed that the tree-like pattern had an order of magnitude higher Warburg impedance compared to the reference one. According to Fouquet *et al.* [185], the Warburg diffusion resistance changes significantly, when flooding occurs in the catalyst layer. This leads to an increase in $|Z_d|$, and agrees with our observations.

Direct comparison with EIS data from Trogadas *et al.* [7] or Bethapudi *et al.* [8] is rather difficult due to the different operating parameters. However, results from Bethapudi *et al.* [8] showed that the biomimetic patterns exhibited no distinct second semi-circle, with lower charge and mass transfer resistances. This was contributed to the uniform reactant and water distribution. In contrast, the serpentine pattern had one starting at 600 mA/cm^2, indicating no substantial mass transfer limitations, even though air was used on the cathode. Again, this shows that our designs, despite the uniform reactant distribution of tree-like patterns, had restrictions regarding fuel transport to the catalyst. These restrictions are assumed to be caused by water flooding, as discussed above.

4.4.3 Hold tests

The objective of the hold test was to study the long-term performance of the new FFP designs. Results are shown in Fig. 4.8 for the serpentine pattern (black), Design 1 (red), Design 2 (green) and Design 3 (blue) at 70% (Fig. 4.8a), 60% (Fig. 4.8b), and 50% (Fig. 4.8c) RH. The tests were immediately performed after the EIS test. Generally said, and as expected, an improvement of cell voltage stability with a decrease of RH, was observed. At 70% RH, all four flow field plate setups showed cell voltage drops and unstable behaviours. Especially Design 2 had voltage drops of more than 0.2 V. Another interesting fact was that Design 2 had a sudden drop in cell voltage either at the start or at the end of the test. Design 3 showed no significant cell voltage drops. However, the cell voltage constantly decreased

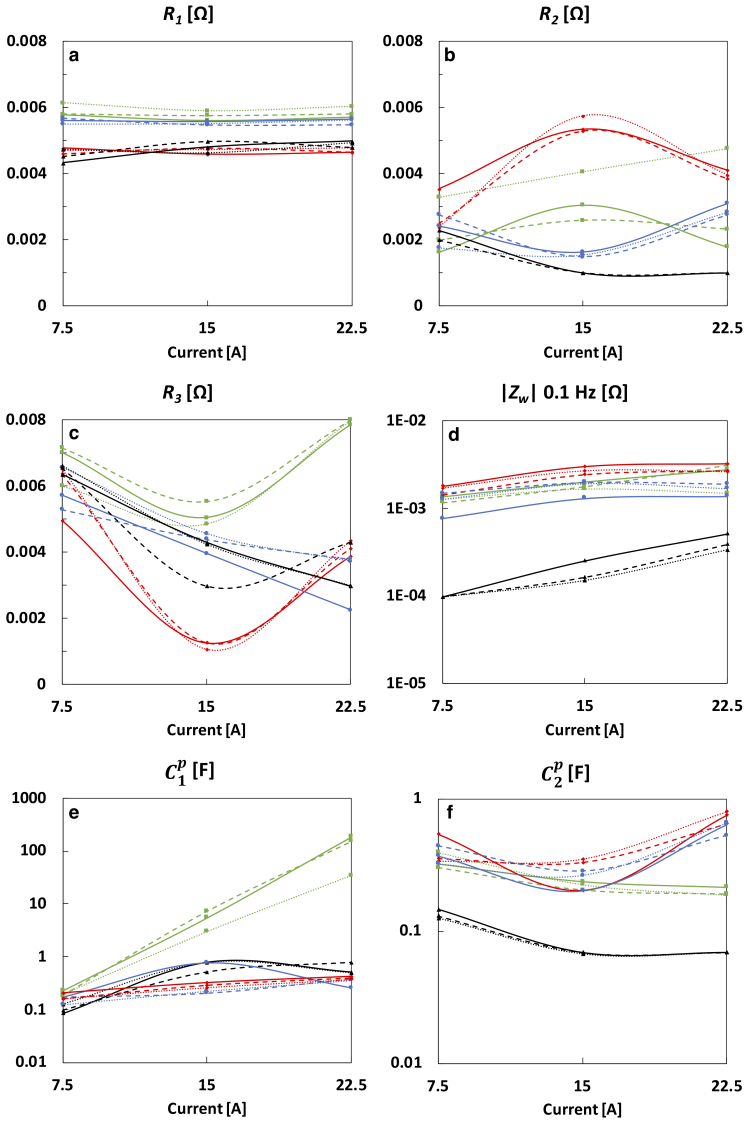

Figure 4.7: Results of the circuit fitting using the modified Randles circuit for the serpentine pattern (black), Design 1 (blue), Design 2 (red), and Design 3 (green) at 70% (solid line), 60% (dashed line), and 50% (dotted line) relative humidity. R_1 (a) is the ohmic resistance of the cell, R_2 (b) is the charge transfer resistance of the anode, R_3 (c) is the charge transfer resistance of the cathode, $|Z_d|$ (d) is the absolute Warburg diffusion impedance calculated with Eq. 4.5 at 0.1 Hz, C_1^p (e) and C_2^p (f) are the pseudo capacitances of the anode and cathode respectively calculated with Eq. 4.4.

over the course of the 3-hour experiment at all three RH settings. Design 1 was the most stable tree-like pattern, at 50% even better than the serpentine FF.

This is a promising new result, with respect to the future development of this particular type of flow field.

4.4.4 Influence of relative humidity

As documented in Section 4.4.1, it can be observed that the tree-like FFs in the best case (Design 1, 70% RH) may come within 11% to the performance of the serpentine flow field. The promise of the presented tree-like FFPs is their uniform flow distribution [165]. Supplying fuels in a uniform way helps avoiding local concentration gradients and, therefore, additional overpotential losses. Even though the gases were evenly distributed, and pure oxygen was used on the cathode side, to reduce mass transfer limitations caused by low oxygen partial pressures, the Warburg diffusion impedance (Fig. 4.7d) of the tree-like designs was one order of magnitude higher than with the serpentine flow field. Therefore, a resistance against the gas transport to the catalyst layer must have been created, for example by a water blockage of pores inside the GDL [187]. Such blocks are known to decrease the reaction rate at the electrodes [188]. Cho *et al.* [10] showed already that lung-like flow fields, which are similar to the presented designs, have problems with the water removal in the small branches of the pattern due to limited convection.

The hold tests at 50% and 60% RH (Fig. 4.8b and c) did not show any sharp cell voltage drops, meaning that the water accumulation was very steady over time as no sudden blockage of channels and the followed drop of cell voltage occurred. The general weakness of tree-like patterns is said to be their water management [7], caused by the low flow rate in the branches at high generation numbers. The higher pressure drop in Design 1 compared to Design 2 (∼6% higher) and 3 (∼9% higher), seems beneficial for the water transport out of the PEMFC, reflecting its better performance at all RH values. The pressure drops were calculated with the hydraulic diameter approach as discussed in [165].

It could also be seen that changing the RH, had no significant impact on the results of the performance (Fig. 4.4) and EIS (Fig. 4.5 and 4.6) test performed with the serpentine flow field. As the intersection with the real axis of the Nyquist plot does not change with RH, proper membrane hydration can be therefore assumed. This can also be said about presented tree-like flow fields. However, the higher charge transfer resistances (Fig. 4.7b and c), pseudo

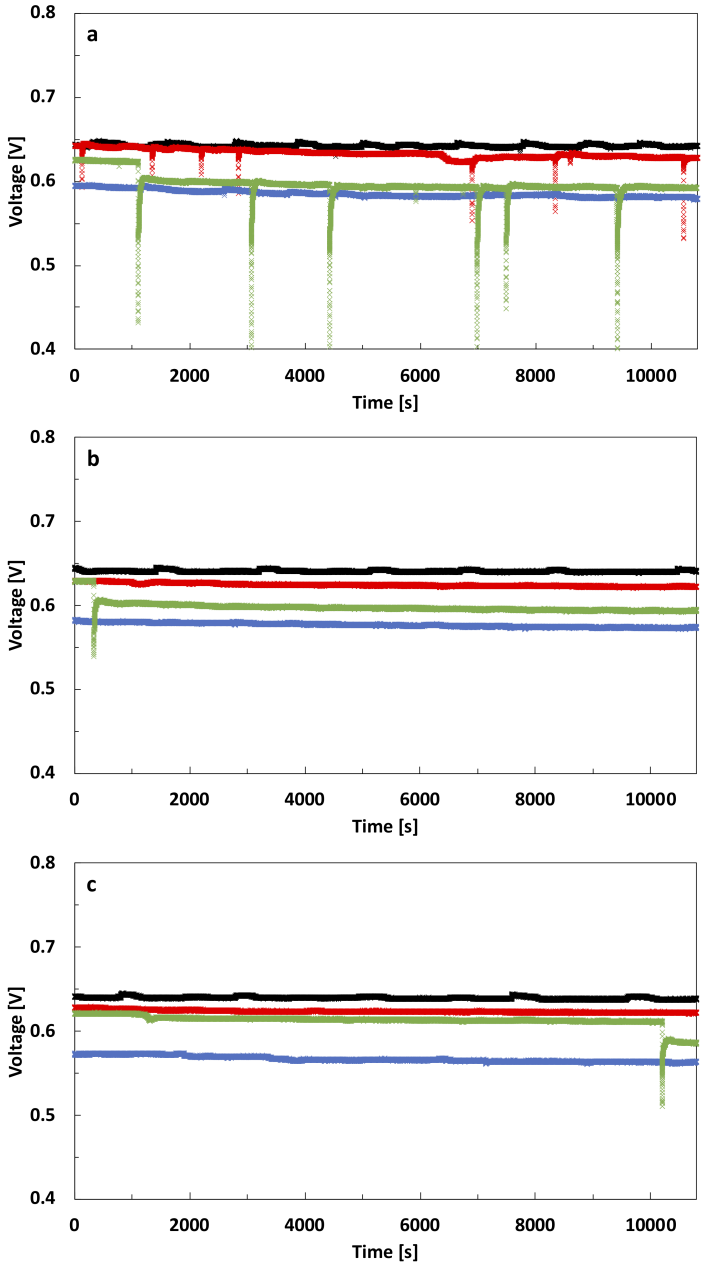

Figure 4.8: Results of hold tests for the serpentine pattern (black), Design 1 (red), Design 2 (green) and Design 3 (blue) at 70% (a), 60% (b), and 50% (c) RH.

Table 4.3: Resistance values for the serpentine pattern (Serp.), the three presented designs (D1, D2, and D3) and the serpentine pattern if the same material as for Design 1 to 3 would be used (Serp.*).

	Serp.	D1	D2	D3	Serp.*
$R_{11}[m\Omega]$	0.027	0.429	0.434	0.473	0.432

capacitances (Fig. 4.7e and f) and Warburg diffusion impedances (Fig. 4.7d) indicate problems, most probably caused by poor water management [185]. Even though a reduction in RH reduces the amount of water transported into the PEMFC, charge transfer resistances increased, and the Warburg diffusion impedance stayed approximately the same. An explanation for this could be that the tests of each design were started at the highest RH. Therefore, water was able to accumulate and stayed inside the cell even during the tests at lower relative humidities, thus further showing that the tree-like designs had problems with water removal.

4.4.5 Comparison of ohmic resistance of the FFPs

In order to evaluate the impact of the resistance of the FFPs alone, simulations on the plates were performed, using COMSOL 5.5. For this, the 3D model created in SOLIDWORKS 2019 were used and meshed by applying the physics-controlled mesh algorithm. The EC physics module was used for the simulations. The ground was set at the face of the FFP which touches the GDL in the PEMFC, and the terminal was set at the opposite surface. Results were computed for currents between 0 A and 30 A to verify for consistency. Because the serpentine FFP, supplied by balticFuelCells, consisted of a different material than the tree-like designs, a fifth simulation was created. Here, the serpentine FFP had the same material than the presented designs. The resistance was calculated by creating a global evaluation of the resistance R_{11}, which is directly provided by COMSOL 5.5, see Table 4.3. Simulation results showed coherent values for different current densities. Due to the lower specific resistance (12 $\mu\Omega$m) of the serpentine FFP, the calculated ohmic resistance is much lower than the tree-like designs, which were machined into Schunk FU4369 graphite (190 $\mu\Omega$m). The resistance of the FFP increased with an increase in scaling factor a_i and a_o, due to the increase in channel width and therefore a reduction in the contact area. However, if the serpentine pattern used the same material than the tree-like designs, it was observed that Design 1 exhibited a smaller resistance, even though the design had two patterns and two plates (inlet and outlet pat-

tern). If the scaling factor would decrease even further, the resistance would decrease too.

By comparing these results with R_1 from the circuit fitting (Fig. 4.7a), it was also observed that the ohmic resistance R_{11} (Table 4.3) of the flow field plate was only a small part of R_1. Therefore it may be deduced that other resistances in the fuel cell decreased in Design 2 as compared to 1 and 3, due to *e.g.* better hydration of the membrane (higher water content inside the fuel cell) or a better contact between the inlet or outlet plate. However, the difference in R_1 should not account for the large disparity between the performances of the different designs.

4.4.6 Comparison to numerical analysis

The next point for discussion is the comparison between the numerical analysis of the width scaling factors of such tree-like FFPs [165]. It was shown earlier that an increase in width scaling factor, in our case a_i and a_o, decreases the viscous dissipation, increasing thereby the efficiency of the FFP. In the study presented in [165], only hydrodynamic pressure losses were included. The experiments showed that a decrease in viscous dissipation in the flow channels of the flow field does not automatically increase the fuel cell performance. This topic is much more complex, as a higher pressure drop also helps with the removal of water [25]. This was observed in the experiments, as Design 1 had the highest performance among the tree-like designs. It is well known, and also shown here, that there is an essential dissipation also by electronic or thermal resistances. This trade-off situation can be handled by *Pareto optimisation* and should be added to future numerical analyses of these patterns. Wechsatol *et al.* [189], for example, showed that the pure 'hydraulic' and 'thermal' flow field designs based upon minimum viscous or thermal dissipation accordingly, produce different optimal patterns for the scaling factors a_i and a_o in the fractal-like systems. The approach based upon minimum entropy production (similar to Eq. 4.3) due to viscous, thermal, electronic dissipation in the FFP and PEMFC allows more accurate minimization of all types of loss in the system.

4.4.7 Influence of channel/land ratio

Another point for discussion is the ratio between channels and land on the flow field. For serpentine patterns, it had been shown that a channel:land ratio around 1 or above shows improved PEMFC performance [27]. Due to the increased pressure drop when this ratio is increased above 1, an optimum can be found, if the total efficiency (including the PEMFC and auxiliary

equipment like pumps) is investigated [26]. For the case of the presented tree-like patterns, a different trend was observed. Design 1 had a lower channel:land ratio at the outlet plate than Design 3 but had a higher power output. Therefore, similar conclusions regarding this ratio known from the serpentine pattern, should not be applied for the tree-like patterns.

4.4.8 Influence of branching generation numbers

The number of branching generation levels also has an impact on the PEMFC performance as shown by Trogadas *et al.* [7]. We used a different approach in counting the branching generation levels, however, if the same one as Trogadas *et al.* was used, we would be between four and five branching generation levels. Therefore, future work could include the design of a pattern with a maximum of eight generations, which should be the optimum according to Trogadas *et al.* [7].

4.5 Conclusions

The PEMFC performance of three tree-like flow fields at the cathode side, with different design rules for channel width, was investigated. The flow field plates consisted of two CNC machined graphite plates; one served as the oxygen inlet distributor, the other one as water outlet collector, allowing for a uniform oxygen distribution over the 25 cm^2 area MEA.

With $j = 9$ generations of branches, a channel length reduction of 50% every second branching generation, and a width scaling factor a_i equal to 0.917 and a_o equal to 0.925, a power density within 11% of the value of a standard serpentine flow field at a RH of 70% was obtained. Results of the hold tests indicated stable cell voltages without any major drops for Design 1 and 3. Water accumulation seemed steady, as no sudden cell voltage drops occurred in the hold tests at lower RH.

More importantly, experiments and calculations documented that it could be possible to increase the PEMFC performance beyond the observed values, by using a GDL with better water management properties and through optimisation of the cell's ohmic resistance of flow field materials. Another possibility to increase the performance is to reduce the width scaling parameter a_i and a_o further. However, machining possibilities need to be found, which are able to machine smaller width scaling factors, a, than the presented ones. A reduction in branching generation levels might also lead to an increase in PEMFC performance.

We further showed that numerical analyses of tree-like patterns need to also account for thermal effects and electric resistance. Lowering the pressure drop (viscous dissipation) alone does not automatically yield higher PEMFC performance. This was seen in the experiments as an increase in width scaling parameter a_{i} and a_{o} did not cause the PEMFC to perform better. Therefore Pareto frontiers should be used in future numerical optimisations.

In the absence of oxygen concentration gradients, impedance spectroscopic data further suggested that the present tree-like flow field has a rate-limiting step in cathode reaction, not present with serpentine flow fields and due to an added resistance for water removal from the electrode due to possible water accumulation. It may also be possible to reduce this resistance by a better tailoring better of the water removal of the whole system.

Conflicts of interest

There are no conflicts to declare.

Acknowledgements

We gratefully acknowledge the support from NTNU in Trondheim and the Research Council of Norway through its Centre of Excellence funding scheme with Project No. 262644 (PoreLab). Furthermore, we thank HySA Systems Competence Centre, University of the Western Cape, South Africa, for their great support, the supply of the graphite sheets and the machining of the presented tree-like flow field plates.

4.A Appendix

Table 4.A.1 shows the current steps done during the performance tests. This was taken from Tsotridis *et al.* [182].

Table 4.A.1: This table shows the different set points during the performance tests and their according dwell and data acquisition times.

Set point no.	Current [A]	Current Density [A/cm^2]	Dwell time [s]	Data acquisition time [s]
1	0	0.00	60	30
2	0.5	0.02	60	30
3	1	0.04	60	30
4	1.5	0.06	60	30
5	2	0.08	60	30
6	2.5	0.10	60	30
7	5	0.20	$\geq$120	30
8	7.5	0.30	$\geq$120	30
9	10	0.40	$\geq$120	30
10	15	0.60	$\geq$120	30
11	20	0.80	$\geq$120	30
12	25	1.00	$\geq$120	30
13	30	1.20	$\geq$120	30
14	35	1.40	$\geq$120	30
15	40	1.60	$\geq$120	30
16	45	1.80	$\geq$120	30
17	40	1.60	$\geq$120	30
18	35	1.40	$\geq$120	30
19	30	1.20	$\geq$120	30
20	25	1.00	$\geq$120	30
21	20	0.80	$\geq$120	30
22	15	0.60	$\geq$120	30
23	10	0.40	$\geq$120	30
24	7.5	0.30	$\geq$120	30
25	5	0.20	$\geq$120	30
26	2.5	0.10	60	30
27	2	0.08	60	30
28	1.5	0.06	60	30
29	1	0.04	60	30
30	0.5	0.02	60	30
31	0	0.00	60	30

Chapter 5

Modelling Electrochemical Cells with Porous Electrodes. The Proton Exchange Membrane Fuel Cell

Marco Sauermoser[1], Giulio Fossati[1], Natalya Kizilova[2,3,1], and Signe Kjelstrup[1]

1. PoreLab, Department of Chemistry,
Norwegian University of Science and Technology, NTNU,
NO-7491 Trondheim, Norway

2. Warsaw University of Technology,
Institute of Aviation and Applied Mechanics,
00-665 Warsaw, Poland

3. Department of Applied Mathematics,
V.N. Karazin Kharkov National University,
61022 Kharkiv, Ukraine

This chapter was published in
ECS Transactions (2019), 92(8):279-292

Abstract

We describe a method to find profiles for the electric potential, the concentration and the temperature across a heterogeneous cell, using the fuel cell as an example. The cell is divided into five layers: the electrolyte and the electrodes are treated as homogeneous layers, while the electrode interface regions are treated as planar Gibbs interfaces. The five sets of equations, one for each layer, are solved to give the three profiles. The model is checked for thermodynamic consistency. This reveals *e.g.* that water is not in equilibrium at the interfaces at high current densities. Also, interface transport properties, like Peltier and Soret effects, are essential for the profiles. The polarization curve at high current densities can be explained, not by diffusion limitations, but by a varying membrane resistance for current densities below 7500 A/m^2. The heat fluxes out of the cell vary largely with the boundary conditions that are imposed.

5.1 Introduction

All physical models must obey the balance equations for mass, momentum and energy. In addition, there are constitutive equations of transport. These have often been a matter of choice, however. Any choice, in order to be thermodynamically consistent, must conform with the entropy balance. This applies to the single control volume, or to the system as a whole. In the description of electrochemical systems with porous electrodes, there is an added difficulty in how to define the variables on a coarse-grained level. Electrochemical systems are heterogeneous. How can we then integrate across their nano- or microporous layers and obtain macro-scale variable profiles? The present work will address a way to define constitutive equations for the membrane-electrode assembly (MEA) of the proton exchange fuel cell and its gas diffusion layers (GDL), in the following called porous transport layer (PTL). The procedure was defined already in the 1970'ies, see [28] and references therein. We shall see how it can benefit transport in porous media. The systematic method enables us to compute simultaneously the temperature-, concentration-, and electric potential profiles, and study their impact on one another in a consistent way. Following the prescription of the theory, non-equilibrium thermodynamics for heterogeneous systems [28, 148, 190], we divide the MEA plus PTL into three quasi-homogeneous (bulk) phases and two interface regions between them. One set of constitutive equations are prescribed for each layer, using the entropy production of the layer. The equations cannot be chosen. The method is illustrated with the proton exchange membrane fuel cell. We want *e.g.* to examine the thermal signature of the fuel cell. It is then not enough to compute the total heat

effect from the overall entropy change of the cell; we also need the local Peltier and Dufour coefficients to compute the local heat effects.

The theory of non-equilibrium thermodynamics, which include these effects, is well established for homogeneous systems, and has since long been used to describe diffusion, thermal diffusion, and concentration distributions across membranes. It is not standardly used to describe electrochemical systems (batteries and fuel cells), however. This has motivated this work. An extension of the theory to heterogeneous systems is available [28], so the aim is now to highlight the advantages of the method through an important application. We shall report on results from a one-dimensional model of a proton exchange fuel cell (PEMFC). We shall determine simultaneous sets of cell profiles for the electric potential, gas and water-concentrations, temperature, and entropy production using the constitutive equations under various boundary conditions The study extends earlier work [28, 148, 190, 191] adding *e.g.* details on all fluxes of the cell under various non-isothermal conditions.

5.2 System description

A PEMFC is sketched in Fig. 5.1. The MEA is sandwiched between two PTL, all held together by flow field plates. We assume now that the flow fields on both sides supply the reacting gases (hydrogen and oxygen) to the MEA, while water returns via a separate or same channel (depending on the type of flow pattern) on the cathode side. Several issues are known to be critical for good cell performance. The hydrogen gas need be humidified to avoid membrane dry-out, since each proton is transported, accompanied by 1-2 water molecules (electro-osmotic drag). A clamping pressure need be defined to have certain contact layer resistances and porosities of the PTL. We consider a one-dimensional transport problem across the layers pictured in Fig. 5.1, with positive fluxes from left to right. The homogeneous phases are considered to be continuous, with a row of control volumes (CVs) after each other, in regions CV1, CV2 and CV3. The electrode interfaces are described in a discrete manner, each interface is represented by a single CV. We deal with possible dual porosity of the electrode region and agglomerated catalyst particles, by creating average variables of the region in terms of Gibbs excess properties [28, 148]. The electrode layers have a finite thickness. The averaging procedure projects all densities of mass, energy or entropy, on to the single control volume, see Fig. 5.2, in essence, an area. The electrode regions are relatively thin, compared to the membrane. We have showed elsewhere [28] how to derive the excess entropy production of such layers or interfaces, giving a basis for descriptions of non-isothermal electrochemical

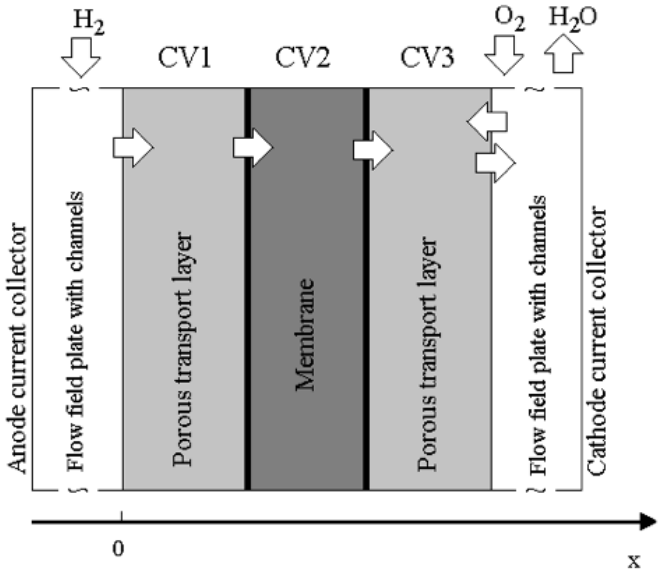

Figure 5.1: Cross-section of the fuel cell core, schematically. The flow fields supply reactants to any membrane location with uniform composition. The gases have access to the nanoporous catalyst (marked by black vertical lines) via nano- and micro-porous layers. CV1, CV2 and CV3 indicate the continuous phases. Each electrocatalytic layer is covered by one CV.

cells. The electrode surface in the description sketched in Fig. 5.2 is an independent thermodynamic system with its own temperature and excess densities, say of platinum. The discrete nature of the interface means that we integrate all gradients over the layer thickness, to a discrete formulation in terms of differences. The constitutive equations obtain a discrete form. This way to treat the electrode layer is at variance with successful continuous models of Bernardi and Verbrugge [192], Broka and Ekdunge [193] and Weber and Newman [194]. The present way differ from the conventional way, not only by coarse-graining the electrode layer into one CV, but also by the type of constitutive equations that are used. We describe below how these follow from the entropy production.

5.3 Theory

5.3.1 The entropy balance

The analysis starts by writing mass-, energy- and entropy balances for each CV, on a continuous or discrete form, depending on the type of CV (not

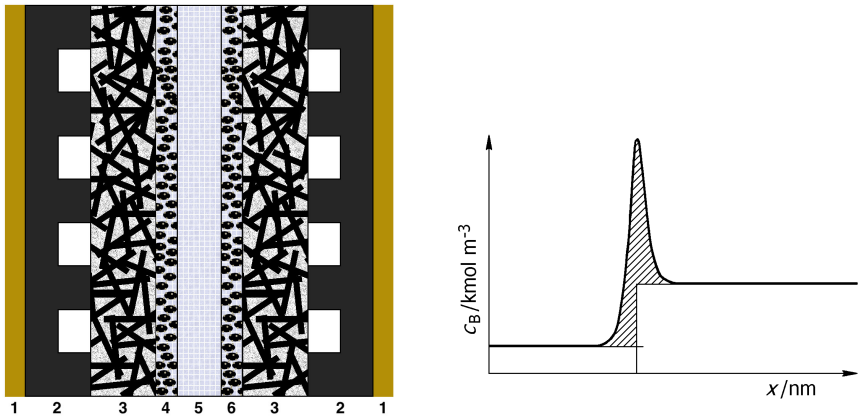

Figure 5.2: Example of construction of surface excess densities (right figure) for the catalytic layer 4 or 6 (left figure). The average density in the interface, say of Pt or Nafion ionomer, is computed from the hatched area under the density variation curve on the right-hand side. The densities of layer 4 become singularities in the description of the layer. Layers 3 and 5 are considered to be homogeneous. The flow field plate and the current collectors are not considered here.

shown here). In the stationary state, the total entropy produced per m^3 control volume, dS_{irr}/dt , is equal to the net entropy flow to the surroundings. For a cross-sectional area of $\Omega = 1$ m^2, we have

$$dS_{irr}/dt = \int \sigma dV = \Omega \left(J_s^{\text{out}} - J_s^{\text{in}} \right) > 0 \tag{5.1}$$

Here σ is the local entropy production in W/(K.m^3) and J_s^{out} and J_s^{in} are the entropy fluxes out of and into the cell. The total entropy production is the integral of the local value over the cell length (x) at constant cross-sectional area. We can find dS_{irr}/dt in two ways: 1) from the right-hand side of the equation, and 2) from the integral. When two numbers are the same, the model is consistent. The entropy production is a product sum of the independent fluxes and forces in the control volume (see refs. [28, 148, 190]). Once the entropy production is derived from the Gibbs equation and the balance equations, the constitutive equations are given (Eqs. 5.2-5.3). The direct link can be used to check if a model is consistent.

5.3.2 Constitutive equations on continuous form

The entropy production of a CV in the polymer membrane gives a flux-force matrix on continuous form. The forces are linear in the fluxes, and the matrix

is originally symmetric. By reshuffling, and introducing transport coefficients [28], we obtain:

$$\begin{aligned}
&[\text{a}] \quad \frac{dT}{dx} = -\frac{1}{\lambda^{\text{m}}} J'_q + \frac{q^{*,\text{m}}}{\lambda^{\text{m}}} \left(J_w - t_w^{\text{m}} \frac{j}{F} \right) + \frac{\pi^{\text{m}}}{\lambda^{\text{m}}} \frac{j}{F} \\
&[\text{b}] \quad \frac{dc_w}{dx} = -\frac{q^{*,\text{m}}}{D_w^{\text{m}} T} \frac{dT}{dx} - \frac{1}{D_w^{\text{m}}} \left[J_w - t_w^{\text{m}} \frac{j}{F} \right] \\
&[\text{c}] \quad \frac{d\phi}{dx} = -\frac{\pi^{\text{m}}}{TF} \frac{dT}{dx} - \frac{t_w^{\text{m}}}{F} \frac{d\mu_w}{dx} - r^{\text{m}} j
\end{aligned} \tag{5.2}$$

Superscripts m and w refer to membrane or water property, respectively. As usual, T is the temperature in K, c is the concentration in mol/m^3, ϕ is the electric potential in V, λ is the thermal conductivity, q^* is the heat of transfer, J is the water flux in mol/s.m^2 , t is the transference number (electro-osmotic drag coefficient), F is Faraday's constant (96500 C/mol), π is the Peltier coefficient, j is the electric current density in A/m^2, μ is the chemical potential and r is the electric resistance. For more specific definitions of all properties, and a discussion of their measurement, see [28, 148, 190].

From Eq. 5.2a, we see that a heat flux across the membrane includes several terms, not only the Fourier term. The water flux is likewise a function not only of j, but also of the temperature gradient. Any net flux of water as well as of the proton flux carries heat in the form of heat of transfer and Peltier heat. The coupled set of constitutive equations have the same formal structure for each volume element, see [28, 148, 190] for details. For the anode and cathode PTL, there are similar matrices with three flux-force relations.

5.3.3 Constitutive equations for the interfaces

The entropy production of the interface has five terms, two for transport of heat and water into the surface, two for transport of heat and water out of the surface, and one term for the electric potential drop across the surface. This gives five constitutive equations, cf. Eq. 5.3 [28, 148, 190]. A similar set can be written for the cathode. Symbols have the same meaning as before. The double superscripts indicate (first) the phase and (second) the adjacent phase. For instance s,m means the surface (subsystem) next to the membrane. Two subscripts, like a,s indicate from phase a to interface s. The full set in Eq. 5.3 is necessary when we want to introduce assumptions. The heat of transfer, for instance may have a small impact on the temperature gradient, but should not be taken out to preserve the symmetry, because it has a

large impact on the heat flux. Otherwise, the model becomes inconsistent. Surface resistances are in general large and cannot be neglected [195]. The gain by going to this level of complication, must be recovered in the outcome: A set of simultaneous variable profiles, consistent with the second law of thermodynamics.

$$
\begin{aligned}
&\text{[a]} \quad \Delta_{\mathrm{a,s}} T = -\frac{1}{\lambda^{\mathrm{s,a}}} \left(J_q'^{\mathrm{a}} - q_w^{*,\mathrm{a}} \left(J_w - t_w \frac{j}{F} \right) - \pi^{\mathrm{a}} \frac{j}{F} \right) \\
&\text{[b]} \quad \Delta_{\mathrm{a,s}} \mu_{w,T} = -q_w^{*,\mathrm{a}} \frac{\Delta T}{T^2} - R_{ww}^{\mathrm{s,a}} \left(J_w - t_w \frac{j}{F} \right) \\
&\text{[c]} \quad \Delta_{\mathrm{s,m}} T = -\frac{1}{\lambda^{\mathrm{s,m}}} \left(J_q'^{\mathrm{a}} - q_{\mathrm{w}}^{*,\mathrm{m}} \left(J_{\mathrm{w}} - t_w \frac{j}{F} \right) - \pi^{\mathrm{m}} \frac{j}{F} \right) \\
&\text{[d]} \quad \Delta_{\mathrm{s,m}} \mu_{w,T} = -q_w^{*,\mathrm{m}} \frac{\Delta T}{T^2} - R_{ww}^{\mathrm{s,m}} \left(J_{\mathrm{w}} - t_w \frac{j}{F} \right) \\
&\text{[e]} \quad \Delta\phi = -\frac{\pi^{\mathrm{a}}}{T^{\mathrm{a}}} \frac{\Delta_{\mathrm{a,s}} T}{F} - \frac{\pi^{\mathrm{m}}}{T^{\mathrm{m}}} \frac{\Delta_{\mathrm{s,a}} T}{F} - t_w \frac{1}{F} \Delta_{\mathrm{a,m}} \mu_{w,T} - r^{\mathrm{s,a}} j
\end{aligned}
\tag{5.3}
$$

The set of equations reflect that the discrete formulation allows accumulation of mass or energy in the surface. The flux into the surface may differ from the flux out of the surface. In the present 1-D model, the fluxes of water and electric charge are constant in the numerical solution procedure. The energy flux is also constant in the steady state, but the heat fluxes are not. The jumps in the heat fluxes at the interface reflect the ability of the system to do electric work, as well as how the energy is dissipated.

5.4 Numerical solution procedure

Five sets of profiles for temperature, composition and potential were determined at stationary state; including three sets for the homogeneous phases, and two interface sets. All computations were done in MATLAB R2018b. The differential equations in the anode and cathode PTL and the membrane were solved by integrating from left to right with the build-in solvers ode45 and ode15s, respectively. The heat flux and water flux in the system were first unknown. So in the first step, the water flux which gave a water activity of 1 at the right side of the membrane, was found using fsolve. The heat flux was then found again using fsolve, trying to minimize the residual ($res = T_{actual} - T_{set}$) at the right side of the cathode PTL. Using this procedure, it was possible to fully control the temperatures at both sides of the fuel cell. The heat flux was adjusted accordingly. The equations for the electrode surfaces, which were modelled as discrete layers, were solved

analytically. The temperature on the right side was found by an iterative process (fsolve), solving the energy balance of the surface.

Another iterative process was needed to find the water concentration on the right-hand side of the cathode surface. The fsolve-routine was again used to find the water molar fraction on the right-hand side of the cathode. This resulted in the set water molar fraction on the right side of the cathode PTL after integrating through the whole layer. To decrease computational time, the results of each iterative process were stored, retrieved for the next set current density and used as new starting value for fsolve. The sets of equations were first solved for a base case with transport properties from the literature [28, 148] see Table 5.1. Two essential assumptions were used: Firstly, we assumed equilibrium for water at both membrane interfaces. Secondly, we assumed that the water activity on the right-hand side of the membrane was 1. This model had a solution for current densities up to 7500 A/m^2. At higher values no solution was found. Numerical solutions were computed for current densities varying in steps of 50 from 50 to 7500 A/m^2. The contributions to the entropy balance were computed for each case. Boundary conditions were chosen as follows: The external temperatures were kept at 340 K in the base case. The pressure at the boundaries was 1 bar. The gases at both inlets (anode and cathode PTL) were always fully saturated with water. The heat and water fluxes were calculated as described in the beginning of this section. The electric potential on the left side of the anode was set to 0 V. An overview of the case studies is given in Table 5.2. We considered a base case followed by a sensitivity analysises of different parameters to see their effect on the various profiles of the fuel cell.

5.5 Results and discussion

The cell performance in terms of various profiles is shown with input from Tables 5.1 and 5.2, in Figs. 5.3-5.9. We present and discuss the base case and conclude that this model is not sufficient at high current densities; it is not thermodynamically consistent. We study the sensitivity of the model for lower current densities, including state-of-the art experimental data. The model can predict local values of the heat flux.

5.5.1 The base case

The simultaneous solution of the model with the basic set of variables (Table 5.1) were documented in part already [28, 148]. The solutions were obtained with the assumption of equilibrium for water at both membrane - electrode interfaces. The results are shown in Figs. 5.3, 5.5. Figure 5.3

Table 5.1: Transport properties for the reference case were taken from [28].

Parameter	Unit	Value
$r^{\mathrm{a}} = r^{\mathrm{c}}$	ohm m	10^{-4}
$r^{\mathrm{s,a}} = r^{\mathrm{s,c}}$	ohm m^2	7.2 x 10^{-6}
λ^{m}	W/Km	0.2
$\lambda^{\mathrm{a}} = \lambda^{\mathrm{c}}$	W/Km	1
$\lambda^{\mathrm{s,a}} = \lambda^{\mathrm{a,c}}$	$\mathrm{W/Km}^2$	1000
$D_{w\mathrm{H}} = D_{\mathrm{ON}}$	m^2/s	5 x 10^{-5}
D^{m}	m^2/s	1.5 x 10^{-10}
j_0	$\mathrm{A/m}^2$	2.5 x 10^{-3}
$q^{*,\mathrm{i}}$	J/mol	$-TS^i$
$t_w^{\mathrm{m}} = t_w^{\mathrm{a,r}} = t_w^{\mathrm{c,l}}$	mol w/mol H^+	1.2
$t_w^{\mathrm{a,PTL}} = t_w^{\mathrm{a,l}}$	mol w/mol H^+	0
$t_w^{\mathrm{c,r}} = t_w^{\mathrm{c,PTL}}$	mol w/mol H^+	1.7

shows that the water concentration decreases from the start of the anode backing down to the membrane. This is expected because water is taken away by electro-osmosis in the membrane; the electro-osmotic drag will often dry the membrane at this location. On the cathode side, however, the water concentration is high. This is where water is produced, and water is transported out of the cell. Water is mostly pulled into the anode, but can be transported out of the anode if the current density becomes very low, 500 $\mathrm{A/m}^2$. This is explained in more detail in connection with Fig. 5.6. The electric potential profiles in Figure 5.3 (bottom) give the power that can be extracted from the cell (the potential difference between the terminals times the current) and therefore also the work that is lost within the cell. The drop in potential on the anode side is due to disappearance of hydrogen. Work is needed to convert hydrogen gas (at high entropy) into protons in the membrane (with low entropy). This is a reversible process, meaning that the drop changes direction, when the electric current is reversed. All three potential profiles across the membrane express reductions in the work output, increasing with the current density. A small part of the reduction (<40 mV) is due to uphill movement of water, cf. Eq. 5.2. The remaining loss is due to resistance loss which varies with membrane water content. The potential rise on the cathode side is the combined effect of the positive Nernst potential minus the overpotential. For the highest computed current density, 7500 $\mathrm{A/m}^2$, we notice that the terminal point on the right-hand side of the PTL becomes negative. This result is contrary to the purpose of

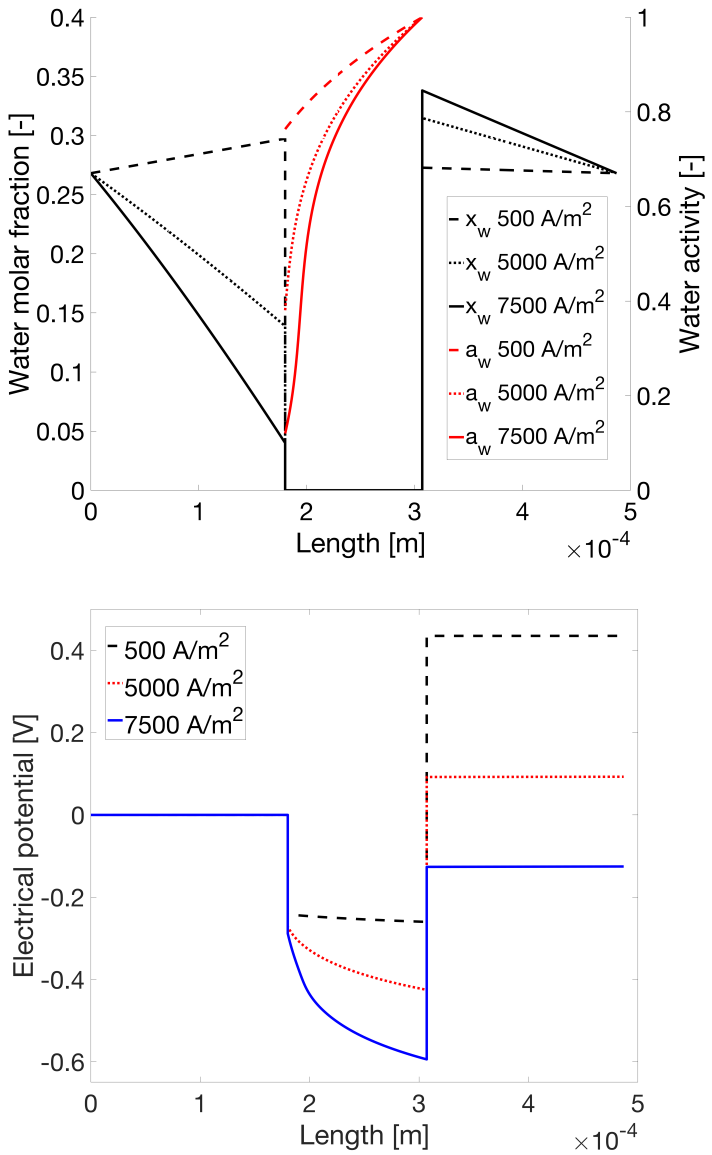

Figure 5.3: On the top, we see the mole fraction profile of water in hydrogen and air, followed by the membrane liquid water activity and the water profile in the cathode. On the bottom is the electric potential profile through the PEMFC. Profiles are shown at current densities (in A/m^2): 500 (dashed), 5000 (dotted) and 7500 (solid). The profiles are continuous in the PTL and the membrane. The electric potential jumps at the electrode interfaces.

Table 5.2: Overview of simulations.

Case / property	Current densities [A/m^2]	Sensitivity study	Quantity of interest
Base case	500, 5000, 7500	-	Molar fraction-, temperature-, electric potential-, and heat flux profiles
Water molar fraction profile	50-7500 in steps of 50	Water flux, J_w	Water activity and molar fraction profile
Temperature profile	50-7500 in steps of 50	Heat production	Peltier heat, heat of transfer, measurable heat contribution
Polarization curve	50-7500 in steps of 50	-	Potential drop at membrane, cathode and total
Overpotential	50-7500 in steps of 50	Exchange current density, j_0	Heat production, potential profile, polarization curve

the fuel cell, and a clear sign that the model becomes insufficient.

The temperature and heat flux profiles that accompany the results in Fig. 5.3 are shown in Fig. 5.5. Details are given in Fig. 5.7. We see, as expected, that the highest temperature is always at the cathode. There is a discontinuity in the heat flux at the electrode interfaces. This is clear from the energy balance and can be associated with the electrochemical reaction. The temperatures at the terminal points are the same, 340 K (cf. Figure 5.5). This choice has a large impact of the local heat fluxes. In the present case, most of the heat escapes the cell on the anode side (there is a negative heat flux at this location). We explain this by the enthalpy of evaporation at the cathode, which is a heat sink, and the heat is given off at condensation on the anode. The heat fluxes out of the cell increase, as expected, with the current density. They have contributions from irreversible and reversible processes; i.e. Fourier type heat conduction, heats of transfer, and Peltier heats.

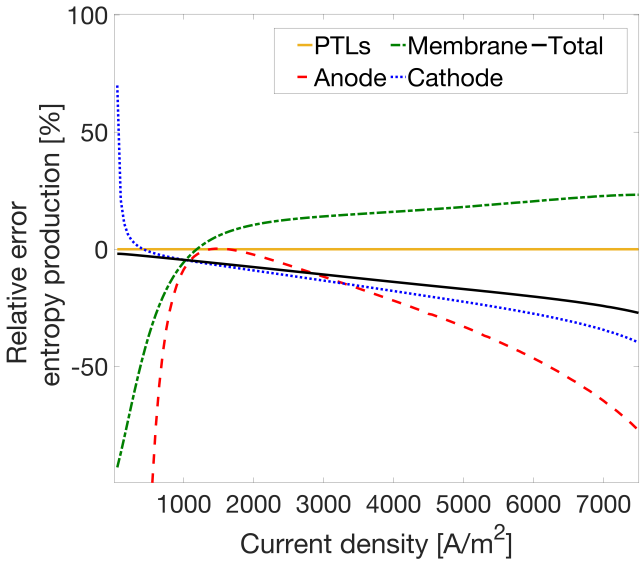

Figure 5.4: The difference between the entropy production calculated from integral over the flux-force products and the entropy balance for various current densities. The deviation in percent is shown for the PTLs (solid unbroken), the membrane (dash-dotted green), the anode (dashed red), the cathode (dotted blue) and the total cell (solid black).

5.5.2 Consistency control

The entropy production was computed and compared to the net entropy flux of each control volume. The results are pictured in Fig. 5.4. For the case in question, the two computations differed by 17% for the total cell for the highest current density. At low current densities the error decreased. The model is a valid thermodynamic model, only when the agreement is perfect. Clearly the assumptions we use, most prominently the assumption of equilibrium for water at the interfaces, is not correct. Rangel and Koper confirms this [195].

This way to actively use a consistency criterion to check on the validity of the model has only seldom been used before [148, 191]. The constitutive equations and the form of the balance equations are normally a choice of the modeler, but non-equilibrium thermodynamics theory directs the choice. The heat flux, can for instance, not be modeled by Fourier's law alone. Non-equilibrium thermodynamics prescribes a coupling of heat and charge transport (Peltier effect) and heat and mass transport (Dufour effect, heat of

transfer). The need for these terms can be tested using the entropy balance. It is essential to invoke not only Peltier effects, but also heats of transfer, since the terms are large.

5.5.3 Sensitivity analysis

The profiles can be understood in terms of the theoretical expressions for each layer. It is useful to distinguish between small and large terms. The computations were run, changing the current density in steps of 50 A/m^2, from 50 to 7500 A/m^2, keeping the boundary values for temperature and humidity on both sides constant (Tables 5.1 and 5.2). The aim was to quantify the contribution of each term contributing to the governing equations, and find the most important phenomena in the various regimes of the fuel cell. This ultimately helps find optimal cell properties. The gradients/differences in our differential equations are intercorrelated. We are interested in how the gradients of one variable is influenced by other gradients.

Concentration profile of water

It is of prior importance to control the water transport in the cell. The molar fractions of the water vapor in the bulk phases were shown in Fig. 5.3. In the anode PTL, where we have a mixture of hydrogen gas and water vapour at 1 bar, there is saturated vapour at the entrance. This defines the water mole fraction at this position, once the temperature is given. The mole fraction profile for water in the membrane was determined, and the Springer correlation was used to find the water activity from the water content (Figure 5.3 top) , see ref. [148], resulting in a non-linear profile for the water activity.

Figure 5.6 explains the water transport in the membrane. Two counteracting phenomena take place, back-diffusion (negative contribution) and electro-osmotic drag (positive contribution), cf. Eq. 5.3. The thermal diffusion term is almost four orders of magnitude smaller than either of the two mentioned. When the electro-osmotic drag is larger than the back-diffusion term, as is mostly the case in Fig. 5.6, a water activity of unity can be maintained at the cathode side of the membrane. The difference between the upper (dotted black) and lower (dash-dotted red) lines is almost constant (solid blue). At low current densities, the water flux (dash-dotted red) becomes negative, meaning that water is transported out of the cell. The vapor at the entrance becomes super-saturated when the water flux is negative, as shown in Fig. 5.6 (top), this allows for the negative flux. In the cathode PTL, water is always transported out of the cell. We neglected all coupling effects in the model, so the gradient can be understood alone from inter-diffusion of water

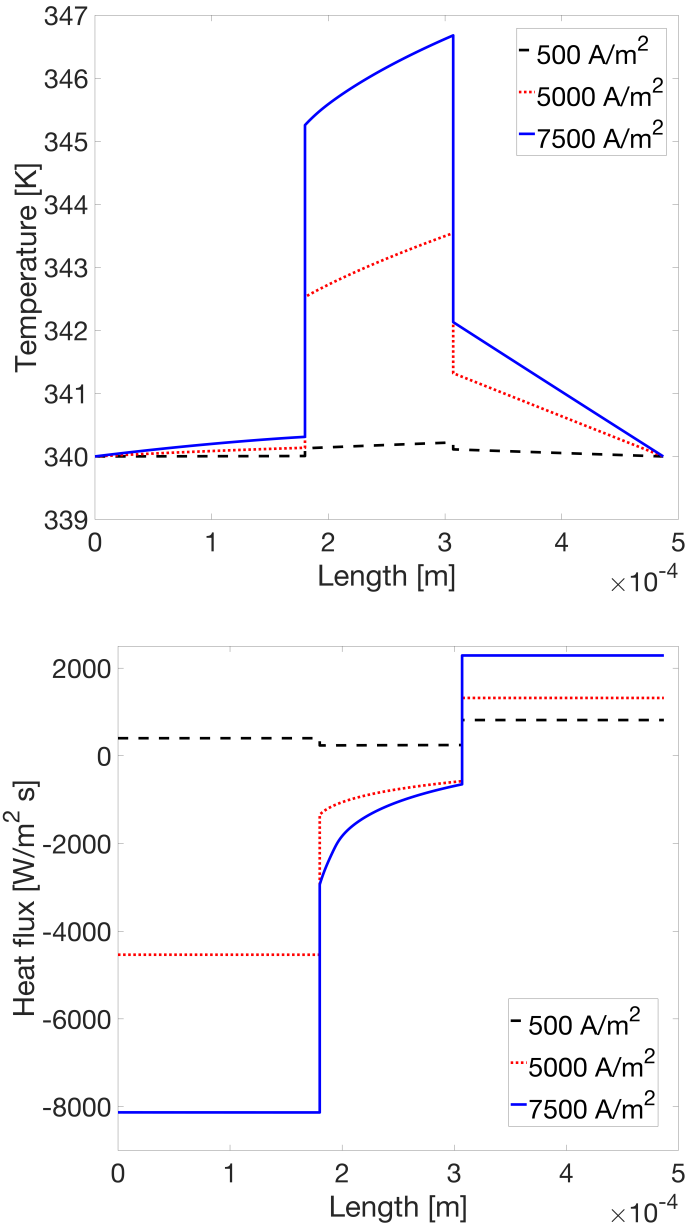

Figure 5.5: The temperature (top) and the heat flux profiles (bottom) through the PEMFC at various current densities (in A/m^2) 500 (dashed black), 5000 (dotted red) and 7500 (solid blue).

vapour and air.

Temperature profiles

The profiles across the membrane in Fig. 5.5, sandwiched between electrode layers at positions around 0.2 and 0.3 mm, are curving. This is due to Joule heat. We also see a discontinuity in the temperature at the electrode interfaces, which can be traced back to Peltier heats and heats of transfer.

Thermal management of the fuel cell is of central importance to cell operation. The factors that have an impact on the temperature profile are therefore of interest. According to theory, there is not only a Fourier type contribution to the heat flux, there are also terms related to electric current (Peltier effect) and mass flux (Dufour effect). The discrepancy between the present and earlier models [194, 196, 197] is due *e.g.* to the value used for the Peltier coefficient. We compare the three contributions to the heat flux in Fig. 5.7.

We have assumed that the vapour present in the anode PTL condenses to a liquid state in the membrane, and oppositely that all liquid water produced at the cathode evaporates. These effects explain the asymmetry in the heat profile. The need for heat for evaporation, on the cathode side, explain the relatively small heat flux our of the cathode. A relatively high membrane thermal conductivity may funnel heat transport to the anode, inside the cell. To see the contributions from the Peltier heat, and the heat transported reversibly with water, we compare these terms to the measurable heat flux in Fig. 5.7. Dashed blue curves are heat transferred reversibly with water, solid red curves are Peltier effects, and the yellow broken line is the total measurable heat flux. The dotted yellow curve gives the combination that determines the temperature gradient.

In the anode PTL, the sum of the three contributions is negative for any current density, resulting in a positive temperature gradient. The slope increases as the current density increases. The contribution of the Peltier heat and the heat of transfer give negative contributions to the measurable heat flux, keeping the temperature profile low. The reversible terms become less significant at higher current densities, meaning that irreversible sources like the Joule heat and the overpotential takes over. In the cathode, likewise, the two reversible contributions have opposite sign, making a smaller total effect, and a small positive heat flux. The straight lines are the signature of terms that are proportional to the current density, i.e. the Peltier term and the Dufour term (the water flux is proportional to the current density).

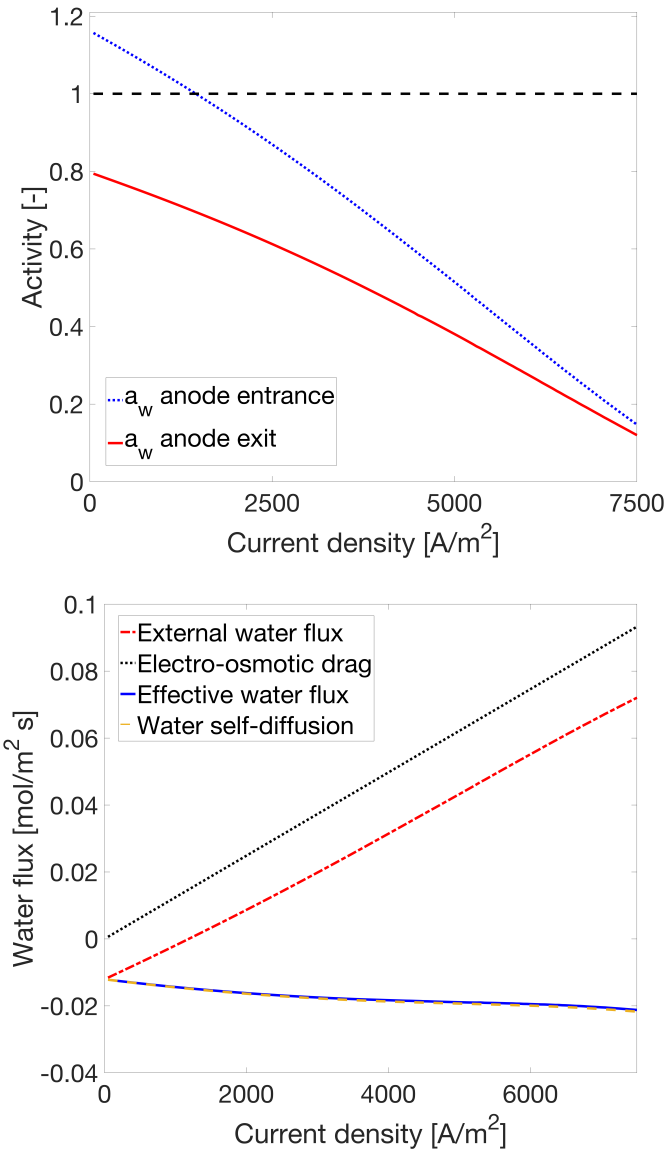

Figure 5.6: The water activity at the anode entrance (dotted blue) and exit (solid red) as a function of current density (top), and the water flux and its contributions (bottom). The dotted black line is the electro-osmotic drag, the dash-dotted red line is the computed net water flux, and the dashed yellow line is the back-diffusion. The solid blue line is the difference is the effective water flux in the cell.

Electric potential profile

The common way to characterize the fuel cell performance is through its polarization curve (the performance or IV curve). The cell voltage is measured and plotted for a certain current density. After performing the computations with different current density values, incrementally increasing it in steps of 50 A/m^2, we used to construct this curve (Figure 5.8).

We can distinguish between the three well known regimes in the polarization curve: an initial drop, a linear part and the final drop for high current densities. All regimes reflect the properties of the model. The voltage becomes negative for high current densities, a sign that the model becomes too simple. Nevertheless, the simple model can be used to point at improvements.

The first regime is due to the activation overpotential at the cathode. This gives a dominating loss, reflected in a non-linear curve at low current densities. It is immediately clear that the formula chosen to compute the overpotential at the cathode has a large impact, see Fig. 5.8 (bottom). Here the Tafel formula was used, following [28] [148].

$$\eta^c = \frac{2RT}{F} \ln \frac{j}{j_0} \tag{5.4}$$

The exchange current density from experiments was given in Table 5.1. By increasing this by a factor 10, the reference polarization curve (black) in Fig. 5.9 (bottom) is lifted by more than 0.1 V (dashed red). State-of-the art values with the Butler-Volmer equation as an alternative, will improve conditions more. We note that a smaller overpotential gives a smaller heat flow out of the cell on the cathode as well as the anode side. It can also be seen that a decrease in the overpotential, significantly decreases the heat fluxes going out of the system (Figure 5.9 top). At an exponent of 1, we even see that the heat flux at the cathode becomes negative, meaning that the heat used for evaporation is sufficient to change the sign of the heat flux there.

At medium current densities, the curve is linear, and the losses that are connected to a constant ohmic resistance. The third region of the curve is commonly connected to mass transfer limitations in the PTLs. However, in our case we are using a current density, giving a sufficient partial pressure of the reactants. Mass transfer is not causing any significant entropy production, cf. Fig. 5.4. Figure 5.8 (bottom) shows that the origin of the non-linear decrease in the polarization curve at high current densities, is due to the

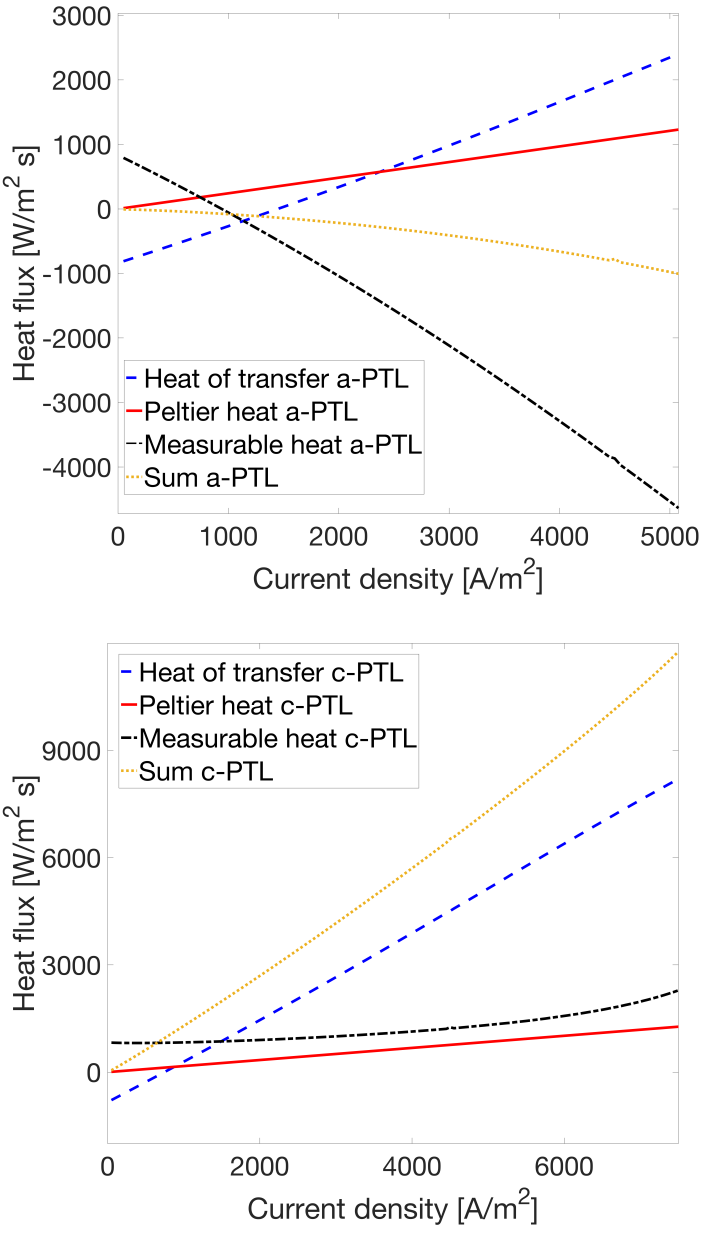

Figure 5.7: Heat flux contributions in the anode PTL (top) and cathode PTL (bottom), showing the heat transferred reversibly with water (dashed blue), the Peltier effects (solid red), the measurable heat (dashed-dotted black) and the total heat flux (dotted yellow).

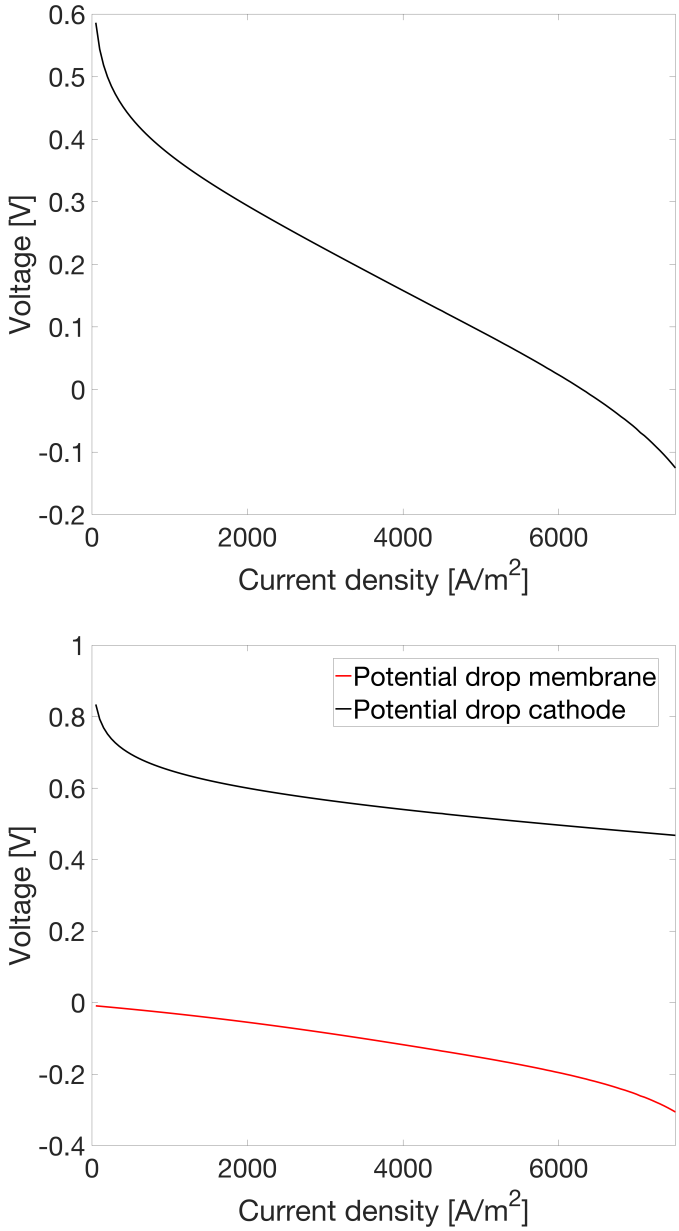

Figure 5.8: The polarization curve (top) and the main contributions to the curve (bottom).

membrane. The electric potential profile varies in a non-linear way across the membrane. Figure 5.3 (bottom) shows that the negative concavity in the membrane is reflected in the polarization curve in Figure 5.8. The electrical resistivity of the membrane is a non-linear function of its water content, which is a function of the water activity [148]. At high current densities, the electro-osmotic drag becomes very important. Back-diffusion does not compensate for the drag, and the water content increases linearly from left to right in the membrane (Fig. 5.3). The non-linear profile of water activity in the membrane follows directly from the correlation between water content and and water activity. In particular, the term containing the derivative of the water content with respect to water activity, $d\lambda/da_w$, in combination with a minimum in the activity function located around a_w=0.35 have an impact. This variation in water activity across the membrane is often neglected in the literature (it is often assumed to be constant). However, the variation in water content has, as we have seen, a big impact on the potential profile. In work to come, we will update the model with experimental results.

5.6 Conclusions

We have presented a general method of analysis suited for electrochemical systems which are composed of layered, porous materials. The method starts with the entropy production of the layer, as defined by non-equilibrium thermodynamics theory. Dynamic boundary conditions are formulated for interacting heat, mass and charge transport in the relatively thin porous electrodes, while the electrolyte and electrode backings are described as continuous media. The method gives a systematic approach to deal with the difficult electrode region, as the model can be tested for thermodynamic consistency.

We have shown for the case of 1D-transport across a fuel cell how the theoretical formulation can be used to systematically improve the physical model by clarifying the role of the assumptions used. For instance, we have seen that the common assumption of equilibrium for water at the electrodes can not be applied, and that the origin of the non-linear region of the polarization curve at high current densities, is the membrane, not the PTLs.

In reality, the transport problems in the fuel cell are at least 2D. Knowledge of how all processes interact can help design. The central problem of water management gives one example: How can we supply sufficient water to the anode to keep the membrane from drying? How can we help the water produced at the cathode to leave the catalyst in a manner not detrimental

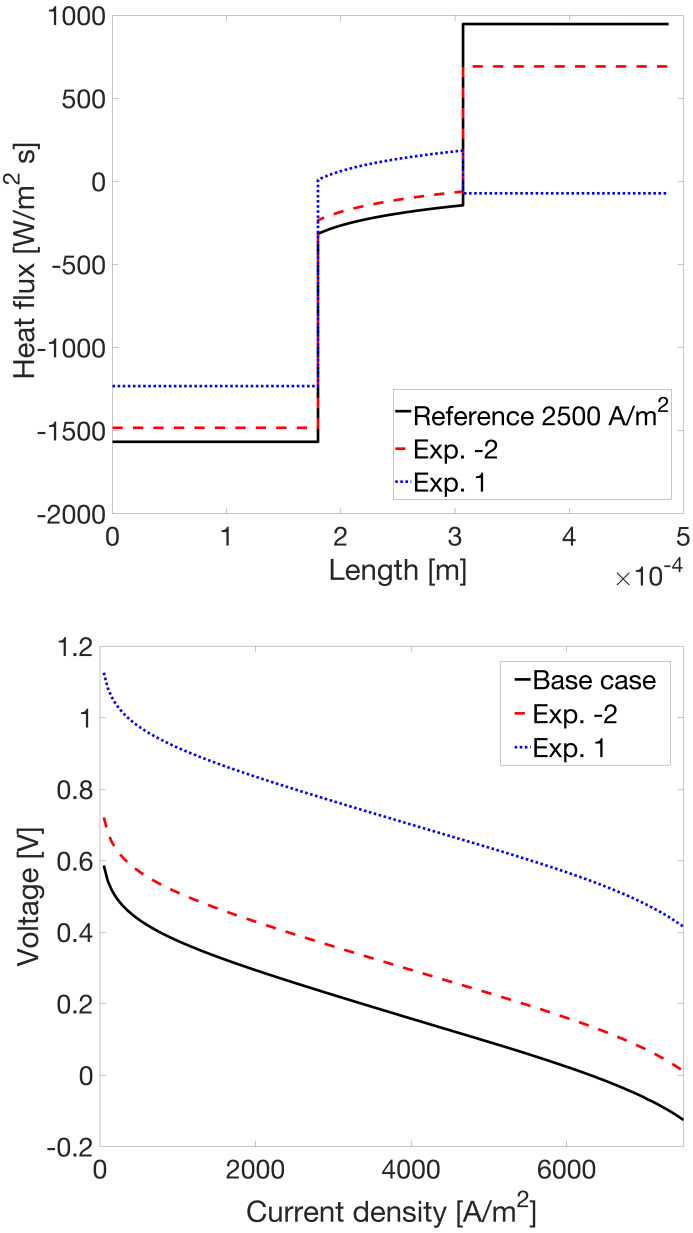

Figure 5.9: Heat flux values across the cell (top) and polarization curve (bottom), showing the base case with $j_0 = 2.5 \text{ x } 10^{-3}$ (solid black), the case where the exponent was changed to -2 (dashed red) and to +1 (dotted blue).

to the overall cell performance. Which heat control will help in this context? With the advent of more detailed experimental results on heat and water fluxes [197, 198], the simple 1D model in this article, can be controlled. With more sophisticated steps included, the model may become a tool for design of auxiliary systems. We have described the construction of a model where all interacting fluxes are included, making a basis for introduction of new experimental results. The method is general and might well be applied for modelling of thermal effects in batteries, say in the Li-ion battery.

Acknowledgments

The authors are grateful to the Research Council of Norway by its Center of Excellence funding scheme, PoreLab project no. 262644.

Chapter 6

The impact of Peltier and Dufour coefficients on heat fluxes and temperature profiles in the polymer electrolyte fuel cells

Marco Sauermoser[1], Signe Kjelstrup[1] and Bruno G. Pollet[2]

1. PoreLab, Department of Chemistry,
Norwegian University of Science and Technology, NTNU,
NO-7491 Trondheim, Norway

2. Department of Energy and Process Engineering,
Norwegian University of Science and Technology, NTNU,
NO-7491 Trondheim, Norway

This chapter was published in
J. Electrochem. Soc. (2020), 167(14):144503

Abstract

We show that the coupling effects in non-equilibrium thermodynamics for heat-, mass- and charge-transport in the polymer electrolyte membrane fuel cell (PEMFC) all give significant contributions to local heat effects. The set of equations was solved by modifying an open-source 1D fuel cell algorithm. The entropy balance was used to check for model consistency. The balance was obeyed within 10% error in all PEMFC layers, except for the cathode backing. The Dufour effect/thermal diffusion and the Peltier/Seebeck coefficient are commonly neglected. Here they are included systematically. The model was used to compute heat fluxes out of the cell. A temperature difference of 5 K between the left and right boundary of the system could change the heat fluxes up to 44%. The Dufour effect, for instance, increases the temperature of both anode and cathode, up to 9 K. The possibility to accurately predict local heat effects can be important for the design of fuel cell stacks, where intermediate cooling is central. This work is based on Paper 1484 presented at the Atlanta, Georgia, Meeting of the Society, October 13-17, 2019.

6.1 Introduction

Electrochemical systems like fuel cells and batteries are becoming increasingly more important to realize a transition to renewable energy systems [199, 200]. Activities to increase system efficiencies are high, and also central for economic competitiveness. A critical issue, say, for fuel cell stacks and lithium batteries alike, is the local heat production inside the cell. This plays an essential role for safety issues [201], durability [202] and auxiliary equipment design (*e.g.* cooling equipment [203]) and therefore also system efficiency. Sufficiently detailed physical models are required to predict the cell behaviour. This paper addresses the issue of local heat production, sources and sinks, in polymer electrolyte membrane fuel cells (PEMFC) in a more complete way than before. A preliminary version of the work was already presented [174]. For a similar analysis of the lithium battery, we refer to [204].

The now dominant ways to model coarse-grained PEMFCs were developed during the last century [192–194]. In particular, there was an effort to define variables for a porous electrode. All physical models must obey the balance equations for mass, momentum and energy. In addition, there are constitutive equations of transport. These have often been a matter of choice, however. In order to be thermodynamically consistent, any choice must conform, not only with the conservation laws but also with the entropy balance. This applies to a control volume, and to the system as a whole. The only theory that

addresses the entropy balance directly is non-equilibrium thermodynamics [28]. The extension of this general theory to heterogeneous systems was made in the 1970s, see [28] and references therein. It is capable of dealing with porous electrodes [148, 190, 193]. The cell is then divided into separate layers, each layer treated as an autonomous subsystem, with an entropy production, σ, assigned to it. Siemer *et al.* [205] and Huerta *et al.* [206] applied non-equilibrium thermodynamics to solid oxide fuel cells as well as PEMFCs.

The theory teaches us about the interaction (coupling) of the various phenomena in a cell layer, such as the electro-osmotic effect, the Soret/Dufour, and Seebeck/Peltier effects in addition to Fourier's, Fick's, and Ohm's law. When we want, *e.g.*, to examine the thermal signature of the PEMFC, it is then not enough to only compute the reversible heat effect from the overall entropy change of the cell [207]. Also, the Peltier, Dufour, or their reciprocal Seebeck and Soret-coefficients are needed to compute the local heat effects. These terms have not, or only partially, been taken into account in earlier models [208, 209]. They are needed when the local variation in temperature, composition and dissipation matters.

The purpose of this work is thus to document in particular how the heat effects in the PEMFC can be modelled and understood using non-equilibrium thermodynamics, extending earlier work [28, 148, 174, 191]. The method will be used to document:

1. A set of simultaneous solutions for profiles of essential variables such as the electric potential, water concentration, and temperature, in addition to water- and heat flux-values across the cell
2. The effect of coupling terms, in particular, the commonly neglected Soret/Dufour and Seebeck/Peltier effects
3. The impact of these effects on the heat and water fluxes in and out of the cell
4. If the model obeys the entropy balance locally as well as globally
5. Properties important to cell design

We will recapitulate the constitutive equations that can be used to solve the profiles mentioned [28]. The system, with its subsystems and excess variables, is first described. The theory for homogeneous layers and porous

electrodes is recapitulated afterwards. The case studies include a Base Case computed using typical data from the literature. The model is implemented in an open-source 1D fuel cell code [210]. The modifications introduced by us are described in the solution procedure. A result presentation and discussion follows.

We shall conclude like Bvumbe *et al.* [207], that it is crucial to model individual and local contributions to flux equations to gain a deeper, more fundamental understanding of the processes in the fuel cell and how they interact.

6.2 System

The PEMFC is sketched in Fig. 6.1. The membrane electrode assembly (MEA) is sandwiched between two porous transport layers (PTL), all held together by flow field plates (FFP). The current collector plate and the FFP are labelled 1 and 2, respectively. The porous transport layers are denoted by 3, the membrane by 5, while the electrocatalytic layers on the anode and cathode are labelled 4 and 6, respectively. Several issues are known to be critical for good cell performance cf. [22]. The fuel gases need to be humidified to avoid membrane dry-out because each proton transported carry along 1-2 water molecules (electro-osmotic drag coefficient) across the membrane. We assume that water exits via the same or a separate flow field and consider one-dimensional transport perpendicular to the layers pictured in Fig. 6.1. There are adiabatic boundaries in the other dimensions. The positive direction of the fluxes is from left to right.

6.2.1 Layer definitions

The reacting gases can enter on both sides via the flow field, and have access to the nanoporous catalyst via nano- and micro-porous layers as described in Fig. 6.1. In spite of knowledge of the finer micro-structure indicated in this figure, we describe three of the fuel cell layers as continuous, homogeneous phases, while the electrode layers will be treated discretely.

The continuous regions, with a row of control volumes (CV) after each other, are indicated in Fig. 6.2 (left) by CV1, CV2 and CV3. In Fig. 6.1, they are represented by layers 3 (CV1 and CV3) and 5 (CV2). The electrocatalytic layers, each covered by one CV, are indicated in this figure by black vertical bars. The electrode interfaces are thus described in a discrete manner. A single CV represents the anode and the cathode catalytic layers. We are then dealing with a possible dual-porosity of the electrode region and agglomerated

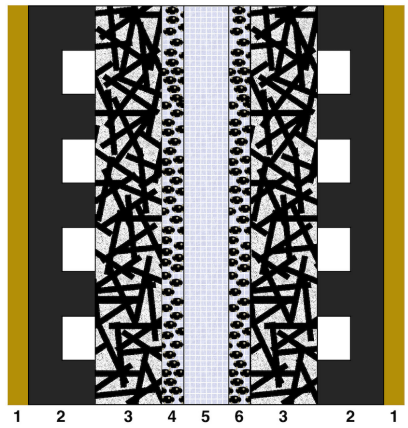

Figure 6.1: Cross-section of the fuel cell core, schematically. The gases in the flow fields (2) have access to the nanoporous catalyst (4 and 6) on both sides of the membrane (5) via the micro-porous layers (3) or porous transport layers (PTL).

catalyst particles, through the use of average variables in the region. The variables are created as Gibbs excess properties [28]. The electrode layers have a finite thickness, but this is integrated out. This averaging procedure projects all densities of mass, energy or entropy, on to a single control volume, see right-hand side of Fig. 6.2, in essence, an area. We can do this since the electrode regions are relatively thin compared to the membrane. The electrode surface in the description sketched in Fig. 6.2, is with this procedure regarded as an independent thermodynamic system with, say, its own temperature and excess density, say of platinum. The constitutive equations obtain a discrete form on this basis.

This way to treat the electrode layer is at variance with successful continuum models of Bernardi and Verbrugge [192], Broka and Ekdunge [193], and Weber and Newman [194]. It is at variance but should describe the same physical phenomena. The presented way differs from the conventional way, not only by the coarse-graining procedure for the electrode layer but also by the type of constitutive equations that are used. It also offers precise access to the entropy production of the layer(s). We describe below how these equations follow from the entropy production.

6.3 Theory

We need the entropy production to be able to define constitutive equations and give below appropriate expressions for all relevant CVs and the electrode

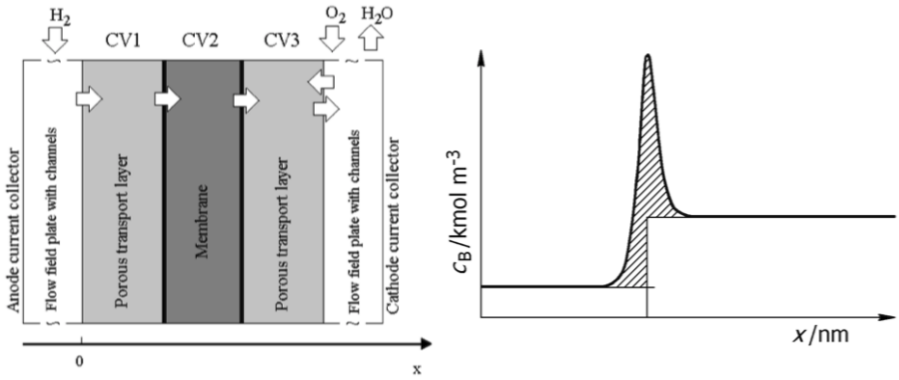

Figure 6.2: PEMFC layer structure (left), with an example of how to construct a surface excess density for the catalytic layer (right). The regions CV1, CV2 and CV3 indicate the continuous phases, of layers 3 and 5 in Fig. 6.1, while the electrocatalytic layers (4 and 6 in Fig. 6.1) are covered by one CV (black vertical bar). The average density in the interface, say of Pt or Nafion ionomer, is computed from the hatched area under the density variation curve on the right-hand side. The densities of layers 4 and 6 become singularities in the description of these layers. The flow fields and the current collectors are not considered here.

surfaces of Fig. 6.2. We are seeking a simultaneous solution of the constitutive equations and the corresponding conservation equations, for all five layers.

6.3.1 The entropy balance

The entropy production is standardly obtained in non-equilibrium thermodynamics by introducing mass- and energy-balances (see below) into Gibbs equation [28].

For a control volume in a homogeneous phase, the entropy produced per m^3 is denoted σ. The total entropy production of the CV, dS_{irr}/dt, in W/K can be obtained in two ways. We can integrate σ across the CV, V. Alternatively, if we consider the system as a black box, we can find the total entropy production as the net entropy flow to the surroundings. For a 1D-system with a cross-sectional area $\Omega = 1$ m^2, we integrate along the $x-$axis. At steady state, the first and second procedures give as entropy balance:

$$\frac{dS_{irr}}{dt} = \int \sigma dV = \Omega \int \sigma dx = \Omega \left(J_s^{\text{out}} - J_s^{\text{in}} \right) > 0 \tag{6.1}$$

Here J_s^{out} and J_s^{in} are the entropy fluxes out of and into the (sub-)system, respectively. We can find the entropy production from the right-hand side of

the equation or from the integral. We can do this for a single layer or the whole cell. When the two numbers are the same, the thermodynamic model in use is consistent. We shall systematically use the entropy balance in this manner to check for consistency of the models we examine. The value will be computed in two ways, and the results will be compared.

The corresponding formula for the porous electrode, treated as a Gibbs surface layer, concerns the excess entropy production. The discrete form of the entropy balance at the surface is here

$$\frac{dS^{\mathrm{s}}_{irr}}{dt} = \Omega\sigma^{s} = \Omega\left(J^{\mathrm{s,out}} - J^{\mathrm{s,in}}\right) > 0 \tag{6.2}$$

Superscript s refers to the surface position. The σ^{s} has the unit W/K m^2 in the discrete description. Once the entropy production is derived, the constitutive equations follow, cf. (Eqs.6.7 to 6.20).

6.3.2 Conservation of mass and energy

The present analysis deals with an adiabatic 1D-fuel cell in steady state. The conservation equations for mass are, therefore, all related to the electric current density j.

$$J_{\mathrm{H_2}} = j/2F \tag{6.3}$$

$$J_{\mathrm{O_2}} = -j/4F \tag{6.4}$$

$$J^{\mathrm{c}}_{w} = J^{\mathrm{a}}_{w} + j/2F \tag{6.5}$$

The symbol J will always be used for a flux in mol/(m^{2}s), while j is the electric current density as measured in the external circuit in A/m^2 and F is Faraday's constant in C/mol. Subscripts indicate components, hydrogen, oxygen, or water (w). Superscripts denote the homogeneous phase we are in, where a indicates the anode PTL, m the membrane and c the cathode PTL.

As we move from left to right across the cell, there is energy conversion by cell internal energy (enthalpy) and entropy into electric energy. The energy flux along the $x-$axis, J_u, is constant in the steady-state. For the three homogeneous phases, it takes the form [28, 148]:

$$J_u = J'^{\mathrm{a}}_{q} + J_{\mathrm{H_2}}H_{\mathrm{H_2}} + J^{\mathrm{a}}_{w}H^{\mathrm{a}}_{w} + j\phi^{\mathrm{a}} \tag{6.6a}$$

$$= J'^{\mathrm{m}}_{q} + J^{\mathrm{m}}_{w}H^{\mathrm{m}}_{w} + j\phi^{\mathrm{m}} \tag{6.6b}$$

$$= J'^{\mathrm{c}}_{q} + J_{\mathrm{O_2}}H_{\mathrm{O_2}} + J^{\mathrm{c}}_{w}H^{\mathrm{c}}_{w} + j\phi^{\mathrm{c}} \tag{6.6c}$$

Subscript q refers to heat, and J'_q is the measurable heat flux, while H_i is the enthalpy of component i. The potential, generated by the fuel cell

reaction, between the terminals is $\phi^{\text{cell}} = \phi^{\text{c,rb}} - \phi^{\text{a,lb}}$, where rb and lb are the right and left system boundaries. The potential drop on the left-hand side (anode) is $\phi^{\text{m,a}} - \phi^{\text{a,m}}$, while at the drop on the right-hand side (cathode) is $\phi^{\text{c,m}} - \phi^{\text{m,c}}$. Superscripts indicate first the phase we are in (first symbol), and next, the neighbouring phase. The enthalpy, as well as the electric potential, are not absolute and needs a reference.

6.3.3 Constitutive equations for homogeneous phases

The entropy production in any control volume is the product sum of the independent fluxes and forces [28, 190]. The entropy production of a CV in the continous form, say, for the polymer membrane is:

$$\sigma = J'_q \nabla \frac{1}{T} - J_w \frac{1}{T} \nabla \mu_{w,T} - j \frac{1}{T} \nabla \phi \tag{6.7}$$

Each term represents dissipation of energy as heat into the surroundings. However, each term is linked to the other terms by linear flux-force relationships. For instance, the electric potential gradient is a function not only of the current density like in Ohm's law but also of the gradient in the inverse temperature and of the chemical potential. The proportionality coefficients are the so-called Onsager coefficients, and these can be directly related to commonly used transport coefficients. We have skipped this derivation, as it can be found in the literature [28, 148]. Only the matrix of Onsager coefficients is symmetric. After introducing the common coefficients, we obtain, *e.g.*, for the membrane:

$$\frac{dT}{dx} = -\frac{1}{\lambda^{\text{m}}} J'_q + \frac{q^{*,\text{m}}}{\lambda^{\text{m}}} \left(J_w - t_w^{\text{m}} \frac{j}{F} \right) + \frac{\pi^{\text{m}}}{\lambda^{\text{m}}} \frac{j}{F} \tag{6.8}$$

$$\frac{dx_w}{dx} = -\frac{q^{*,\text{m}} x_w}{RT^2} \frac{dT}{dx} - \frac{1}{cD_w^{\text{m}}} \left[J_w - t_w^{\text{m}} \frac{j}{F} \right] \tag{6.9}$$

$$\frac{d\phi}{dx} = -\frac{\pi^{\text{m}}}{TF} \frac{dT}{dx} - \frac{t_w^{\text{m}} RT}{F x_w} \frac{dx_w}{dx} - r^{\text{m}} j \tag{6.10}$$

As usual, T is the absolute temperature in K, x_w is the water molar fraction, c is the total concentration in mol/m^3, ϕ is the electric potential in V, λ^{m} is the membrane thermal conductivity in W/m K, $q^{*,\text{m}}$ is the heat of transfer of water in the membrane in J/mol, D_w^{m} is the diffusivity coefficient of water in the membrane in m^2/s, t_w is the transference coefficient of water (the electro-osmotic drag coefficient), π^{m} is the membrane Peltier heat in J, and r^{m} is the membrane electric resistance in Ohm m. To convert the chemical

potential gradient in Eq. 6.7 into the concentration gradient in Eq. 6.9, we used the following thermodynamic expression:

$$\mu_{w,T} = \mu^0_{w,T} + RT \ln\left(\frac{x_w}{x^*_w}\right) \tag{6.11}$$

where $\mu^0_{w,T}$ is the chemical potential at constant temperature and standard conditions, and x^*_w is the water molar fraction at saturation.

The terms that are usually encountered in fuel cell modelling are the terms related to thermal conductivity (Fourier's law), diffusion (Fick's law), electric resistance (Ohm's law) and the electro-osmotic effect, represented by the water transference coefficient

$$t^{\mathrm{i}}_w = \left(\frac{J^{\mathrm{i}}_w}{j/F}\right)_{\Delta\mu_w=0} \tag{6.12}$$

This work has a focus on Seebeck/Peltier and Soret/Dufour effects. The Peltier coefficient of a conductor i expresses the heat reversibly carried by the electric current and is defined by

$$\pi^{\mathrm{i}} = \left(\frac{J'^{,\mathrm{i}}_q}{j/F}\right)_{dT=0} \tag{6.13}$$

The Dufour effect expresses the heat, reversibly carried by mass fluxes (in the absence of electric current), and can be expressed by the heat of transfer. The heat of transfer is defined by

$$q^{*,\mathrm{i}} = \left(\frac{J'^{,\mathrm{i}}_q}{J_w}\right)_{j=0,dT=0} \tag{6.14}$$

The only component free to diffuse is water. The Dufour effect can also be related to the thermal diffusion coefficient. For further details, see [28, 148]. While the Peltier effect is sometimes estimated [194], the Dufour effect has not been included in a systematic analysis as far as we know. It is the purpose of this paper to show that neither of these effects can be neglected. We see from Eq. 6.8 that a temperature gradient arises for several reasons. There is not only a term due to the measurable heat flux but also terms containing the Dufour and Peltier effects. Any net flux of water will carry heat in the form of a heat of transfer, while proton transfer is accompanied by Peltier heat.

The water concentration gradient in Eq. 6.9 is likewise a function of the electric current density, j, and of water flux, J_w, but also of the temperature gradient. The electric work, described by Eq. 6.10, include work done first to move heat against a temperature gradient, and second to move water against its chemical potential gradient. Finally, there is an ohmic potential drop. The work to move water against its chemical potential gradient has been neglected in the literature so far.

We have here given the set for the membrane. Similar coupled sets of constitutive equations apply to the anode and cathode PTL, see [28]. Here, we use J_D, the interdiffusion flux, instead of J_w, because more then one component is present in the PTLs.

$$J_D = \left(\frac{J_w}{x_w} - \frac{J_i}{x_i} \right) x_w \tag{6.15}$$

where i is either hydrogen in the anode PTL or oxygen in the cathode PTL.

6.3.4 Constitutive equations for the electrode surfaces

For the electrode surfaces, the entropy production has in the outset five terms, two for the transport of heat into and out of the surface, one for the transport of water across the surface, one term for the chemical reaction supplied by the gas flux, and one for the electric potential drop across the surface. For the anode side, we obtain:

$$\begin{aligned} \sigma^{\mathrm{s}} = & J_q'^{\mathrm{a,m}} \left(\frac{1}{T^{\mathrm{s}}} - \frac{1}{T^{\mathrm{a,m}}} \right) + J_q'^{\mathrm{m,a}} \left(\frac{1}{T^{\mathrm{m,a}}} - \frac{1}{T^{\mathrm{s}}} \right) \\ & + J_w^{\mathrm{m,a}} \left(-\frac{\mu_w^{\mathrm{m,a}} - \mu_w^{\mathrm{a,m}}}{T^{\mathrm{m,a}}} \right) - j \left[\frac{\phi^{\mathrm{m,a}} - \phi^{\mathrm{a,m}}}{T^{\mathrm{s}}} + \frac{\Delta_n G^{\mathrm{s}}/F}{T^{\mathrm{s}}} \right] \end{aligned} \tag{6.16}$$

The entropy production for the cathode surface is similar. All symbols will then refer accordingly to the cathode.

It is common in literature to assume water equilibrium across the surfaces [211]:

$$\Delta_{\mathrm{a,m}} \mu_w = 0 \quad \text{and} \quad \Delta_{\mathrm{m,c}} \mu_w = 0 \tag{6.17}$$

The assumption will be discussed below. Equation 6.17 removes the water term in the entropy production. We have also assumed equilibrium for adsorption of hydrogen (oxygen) at the anode (cathode) surface. When these conditions are combined with the above, we obtain an entropy production with three terms, and three constitutive equations (Eq. 6.18, 6.19 and 6.20),

for details, see [28, 148, 190]. Two subscripts separated by a comma, as in a,s, mean from phase a to phase s, where a is the anode PTL and m is the membrane and s is the electrode surface. The constitutive equations for the anode become:

$$\Delta_{\mathrm{a,s}}T = -\frac{1}{\lambda^{\mathrm{s,a}}}\left[J_q'^{\mathrm{a,m}} - q^{*,\mathrm{a}}\left(J_w^{\mathrm{a,m}} - t_w^{\mathrm{a}}\frac{j}{F}\right) - \pi^{\mathrm{a}}\frac{j}{F}\right] \tag{6.18}$$

$$\Delta_{\mathrm{s,m}}T = -\frac{1}{\lambda^{\mathrm{s,m}}}\left[J_q'^{\mathrm{m,c}} - q^{*,\mathrm{m}}\left(J_w^{\mathrm{m,c}} - t_w^{\mathrm{m}}\frac{j}{F}\right) + \pi^{\mathrm{m}}\frac{j}{F}\right] \tag{6.19}$$

$$\Delta_{\mathrm{a,m}}\phi_{\mathrm{eff}} = -\frac{\pi^{\mathrm{a}}}{T^{\mathrm{a,m}}}\frac{\Delta_{\mathrm{a,s}}T}{F} - \frac{\pi^{\mathrm{m}}}{T^{\mathrm{m,a}}}\frac{\Delta_{\mathrm{s,m}}T}{F} - r^{\mathrm{s,a}}j \tag{6.20}$$

$\Delta_{\mathrm{a,m}}\phi_{eff}$ is the effective electric potential at the anode, $\Delta_{\mathrm{a,m}}\phi_{eff} = \Delta_{\mathrm{a,m}}\phi + \Delta_n G^{\mathrm{s}}/F$. When $\sigma^{\mathrm{s}} = 0$ (open-circuit potential) all terms are zero. From the last term on the right-hand side in Eq. 6.16, we obtain the Nernst equation. The contributions to the equations are of the same type as described for the membrane. It is an advantage to know the full set of equations, Eqs. 6.16-6.20, when we want to introduce further assumptions. Surface resistances are, in general, substantial and cannot be neglected [195]. The gain by going to this level of complication in the description must be recovered in the outcome. The outcome here is a set of simultaneous variable profiles, consistent with the second law of thermodynamics.

The heat flux into a surface may differ from the heat flux out of the surface, *e.g.*, due to changes in latent heat (see the energy balances in Eq. 6.6). In the present 1-D model, the fluxes of water and electric charge (protons) in the membrane are constant. The energy flux is also constant in the steady-state. This simplifies the numerical solution procedure of the equations presented.

6.4 Case studies

In order to answer the questions raised, we implemented the model described, as shown above. We present that as a Base Case below. In Study 1, we gave the contributions from the Soret/Dufour and Seebeck/Peltier effects to the heat and water fluxes, and the electrode temperature jumps. In Study 2, we described the effect of asymmetric temperature boundary conditions. Experimental data and estimated transport properties, used to solve the equations, are given in Table 6.1. The transport coefficients used in our model are effective coefficients. For the surface, they refer to the whole surface area and are excess properties. For the homogenous layers/the continuous description, we use local coefficients. For instance, the electric resistance is a

Table 6.1: Transport coefficient values used for the Base Case and further studies in this investigation.

Parameter	Unit	Value
r^{m}	ohm m	calculated [31]
$r^{\mathrm{a}} = r^{\mathrm{c}}$	ohm m	2.1×10^{-4} [212]
$r^{\mathrm{s,a}} = r^{\mathrm{s,c}}$	ohm m^2	7.2×10^{-6} [28]
λ^{m}	W/Km	calculated [213]
$\lambda^{\mathrm{a}} = \lambda^{\mathrm{c}}$	W/Km	0.38 [212]
$\lambda^{\mathrm{s,a}}$=$\lambda^{\mathrm{s,m}}$=$\lambda^{\mathrm{s,c}}$	W/Km^2	1000 [28]
$D^{\mathrm{a}}_{w\mathrm{H}_2}$, $D^{\mathrm{c}}_{w\mathrm{O}_2}$, D^{m}_{w}	m^2/s	calculated [31, 214]
l^{a}=l^{c}	m	235×10^{-6} [212]
l^{m}	m	50.8×10^{-6} [215]
j_0	A/m^2	calculated [216]
$q^{*,\mathrm{m}}$	J/mol	-TS_w [28, 217]
t^{m}_w	mol w/mol H+	1.2 [28]
t^{a}_w= t^{c}_w	mol w/mol H+	0 [28]

function of temperature and water content in the membrane, but a constant at the surface or PTL.

6.4.1 Base Case

The Base Case presents all relevant profiles with equilibrium and transport properties as defined in Table 6.1, and below.

6.4.2 Study 1. Peltier and Dufour effects

Coupling terms, like the Soret/Dufour and Seebeck/Peltier effect, in the Base Case were computed, to study the impact of these effects on temperature jumps, heat and water fluxes, as a function of current density.

6.4.3 Study 2. Thermal boundary conditions

In the second study, we investigated the influence of different boundary temperatures compared to the Base Case. The temperatures at both sides varied, as shown in Table 6.3. The main questions were: How does the PEMFC respond to temperatures change on the boundaries? What are the practical implications of the findings?

6.5 Solution procedures

All computations were performed in MATLAB R2019a. The code was based on the published open-source code of Vetter and Schumacher [210]. This utilised the bvp4c solver to solve a multi-point boundary value problem. The differences between our implementation and the code [210] were:

1. Equations presented in the theory replaced the differential equations of Vetter and Schumacher [210].
2. The parameter sweep was done by changing the current density instead of the voltage.
3. Three domains were used for the multi-point boundary value problem instead of five. The domains were the anode PTL, the membrane and the cathode PTL.
4. The equations for the electrodes were solved in the boundary condition function. This was needed in the bvp4c solver and then included in the boundary conditions. With this, it was possible to model the electrodes as surfaces without a spatial discretisation, which is an advantage in our set-up.
5. The Butler-Volmer equation (Eq. 6.21) was solved iteratively with MATLAB's build-in fzero algorithm.

Fig. 6.3 shows the schematic of the numerical solving process of this model. First the boundary conditions and parameters were set. Based on the first current density value, the initial guess was computed. Inside the bvp4c solver, each layer was solved and the boundary conditions between the anode PTL and membrane and the membrane and cathode PTL were computed from the jumps on the electrode surfaces. If the solution converged, the next current density step was chosen and the process of solving the differential equations started again. In the end the solution of all current density steps is extracted and contributions to heat and water flux and to the temperature jumps at the electrodes are calculated. As convergence criteria we set a relative error tolerance of 10^{-4} and an absolute error tolerance of 10^{-6} in the bvp4c solver, which was the reference value in the open-source code from Vetter and Schumacher [210]. The Butler-Volmer equation, used for both electrodes, included a correction from the partial fuel pressure at the electrodes [22]:

$$j = j_0 \left[\exp\left(\frac{\alpha n F \eta}{RT}\right) - \exp\left(\frac{-(1-\alpha) n F \eta}{RT}\right) \right] \tag{6.21}$$

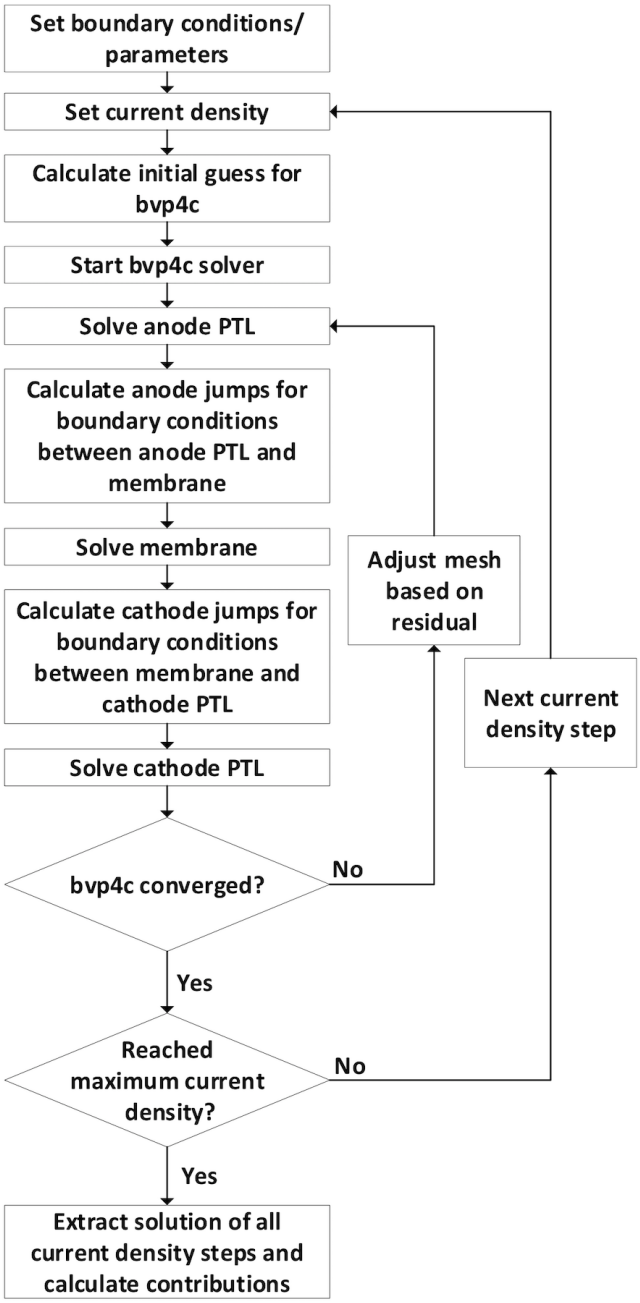

Figure 6.3: Schematic of the numerical solving process of the model.

Here η is the overpotential in V, α is the charge transfer coefficient of the electrode, n is the number of electrons involved in the cell reaction, which was $n = 2$ in our case. α was set to 0.5. The exchange current density j_0 of Eq. 6.21 was adjusted to depend on the ratio of the actual and standard gas pressure at the electrode [216]. j_0 got replaced by either $j_{0,\mathrm{O_2}}$ or $j_{0,\mathrm{H_2}}$ depending on the electrode.

$$j_{0,\mathrm{O_2}} = \mathrm{EPSA^c} j'_{0,\mathrm{O_2}} \left(\frac{p_{\mathrm{O_2}}}{p^0} \right)^{0.001678T} \tag{6.22}$$

$$j_{0,\mathrm{H_2}} = \mathrm{EPSA^a} j'_{0,\mathrm{H_2}} \left(\frac{p_{\mathrm{H_2}}}{p^0} \right)^{0.5} \tag{6.23}$$

Here $j_{0,\mathrm{O_2}}$ and $j_{0,\mathrm{H_2}}$ are the revised equilibrium exchange current densities for oxygen (cathode) and hydrogen (anode) respectively in A/m^2, EPSA is the electrochemical Pt surface area of the cathode or anode in the unit of cm^2 Pt surface per cm^2 electrode geometric area (cm^2/cm^2), $j'_{0,\mathrm{O_2}}$ and $j'_{0,\mathrm{H_2}}$ are the intrinsic exchange current densities in A/m^2 of the cathode and anode, $p_{\mathrm{O_2}}$ and $p_{\mathrm{H_2}}$ are partial pressures of oxygen and hydrogen, respectively, p^0 is the standard pressure in bar, and T is the temperature at the cathode surface. The values for the intrinsic exchange current densities, $j'_{0,\mathrm{O_2}} = 3 \times 10^{-5}$ A/m^2 and $j'_{0,\mathrm{H_2}} = 10$ A/m^2, were taken from [22].

The EPSA was calculated with the following equations [216]:

$$\mathrm{EPSA^c} = 0.02396 T'^2 - 5.958 * T' + 429.3; \tag{6.24}$$

$$\mathrm{EPSA^a} = 0.0009915 * T'^2 - 0.5201 * T' + 55.94; \tag{6.25}$$

where T' is the temperature at the anode or cathode in degrees Celsius.

The boundary conditions of the cell domains are given in Table 6.2 and 6.3, where a denotes the anode PTL, m the membrane, c the cathode PTL, lb the left and rb the right boundary of the PEMFC. The temperature T and water molar fraction x_w had a fixed value on both the left and right boundary of the fuel cell. x_w on the outer boundaries was calculated based from saturation pressure at a given temperature and the set relative humidity [218]. The potential ϕ and entropy production σ were set to zero on the left inlet. The electrode reactions at the interfaces between the different domains, give jumps in the boundary conditions there. We added a term for each variable, calculated from Eqs. 6.18 and 6.20. Using Eq. 6.17 we obtained the water activity at the entrance of the membrane, a_w^{entrance} and the water activity at the entrance of the cathode PTL (left side of cathode

Table 6.2: Boundary conditions of the different domains in the boundary value problem. The superscript's first letter describes the homogeneous layer and the second letter describes the position. This can either be on the left or right side of the layer, indicated by the second letter of the superscript, which denounces the neighbouring phase. Superscripts lb and rb stand for left and right boundary at the inlets of the fuel cell.

	Inlet left | a PTL	a PTL | m
T	$T^{\mathrm{a,lb}} = T^{\mathrm{lb}}$	$T^{\mathrm{m,a}} = T^{\mathrm{a,m}} + \Delta_{\mathrm{a,m}} T$ $J_q'^{\mathrm{m,a}} = J_q'^{\mathrm{a,m}} + \Delta_{\mathrm{a,m}} J_q'$
x_w	$x_w^{\mathrm{a,lb}} = x_w^{\mathrm{lb}}$	$J_w^{\mathrm{m,a}} = J_w^{\mathrm{a,m}} + \Delta_{\mathrm{a,m}} J_w$
ϕ	$\phi^{\mathrm{a,lb}} = 0$	$\phi^{\mathrm{m,a}} = \phi^{\mathrm{a,m}} + \Delta_{\mathrm{a,m}} \phi$
σ	$\sigma^{\mathrm{a,lb}} = 0$	$\sigma^{\mathrm{m,a}} = \sigma^{\mathrm{a,m}} + \Delta_{\mathrm{a,m}} \sigma$
a_w		$a_w^{\mathrm{m,a}} = a_w^{\mathrm{entrance}}$
	m | c PTL	c PTL | Inlet right
T	$T^{\mathrm{c,m}} = T^{\mathrm{m,c}} + \Delta_{\mathrm{m,c}} T$ $J_q'^{\mathrm{c,m}} = J_q'^{\mathrm{m,c}} + \Delta_{\mathrm{m,c}} J_q'$	$T^{\mathrm{c,rb}} = T^{\mathrm{rb}}$
x_w	$x_w^{\mathrm{c,m}} = x_w^{\mathrm{entrance}}$ $J_w^{\mathrm{c,m}} = J_w^{\mathrm{m,c}} + \Delta_{\mathrm{m,c}} J_w$	$x_w^{\mathrm{c,rb}} = x_w^{\mathrm{rb}}$
ϕ	$\phi^{\mathrm{c,m}} = \phi^{\mathrm{m,c}} + \Delta_{\mathrm{m,c}} \phi$	
σ	$\sigma^{\mathrm{c,m}} = \sigma^{\mathrm{m,c}} + \Delta_{\mathrm{m,c}} \sigma$	
a_w		

PTL), x_w^{entrance} in Eq. 6.26 and 6.27. Eq. 6.26 and 6.27 were then used as boundary conditions, see Table 6.2.

$$\ln a_w^{\mathrm{entrance}} = \frac{\mu_w^{\mathrm{m,a}} - H_w^{\mathrm{m,a}}}{R T^{\mathrm{m,a}}} + S_w^{0,\mathrm{m}} + \frac{c_{p,w}^{\mathrm{m}}}{R} \ln\left(\frac{298}{T^{\mathrm{m,a}}}\right) \tag{6.26}$$

where $\mu_w^{\mathrm{m,a}}$ is the chemical potential at the left side of the membrane, which is, due to the equilibrium assumption, $\mu_w^{\mathrm{m,a}} = \mu_w^{\mathrm{a,m}} = H_w^{\mathrm{a,m}} - T^{\mathrm{a,m}} S_w^{\mathrm{a,m}}$, $H_w^{\mathrm{m,a}}$ is the enthalpy of liquid water on the left side in the membrane, $S_w^{0,\mathrm{m}}$ is the standard entropy of liquid water and $c_{p,w}^{\mathrm{m}}$ is the specific heat capacity of liquid water in the membrane.

$$\ln x_w^{\mathrm{entrance}} = \frac{\mu_w^{\mathrm{c,m}} - H_w^{\mathrm{c,m}}}{R T^{\mathrm{c,m}}} + S_w^{0,\mathrm{c}} + \frac{c_{p,w}^{\mathrm{c}}}{R} \ln\left(\frac{298}{T^{\mathrm{c,m}}}\right) \tag{6.27}$$

where $\mu_w^{\mathrm{c,m}}$ is the chemical potential at the left side of the cathode PTL, which is, due to the equilibrium assumption, $\mu_w^{\mathrm{c,m}} = \mu_w^{\mathrm{m,c}} = H_w^{\mathrm{m,c}} - T^{\mathrm{m,c}} S_w^{\mathrm{m,c}}$,

Table 6.3: Temperatures used in the calculations at the fuel cell boundaries where T^{lb} and T^{rb} are the temperatures at the left and right boundaries of the system (inlets) in K used in Study 2.

Case	T^{lb}	T^{rb}
1	350	350
2	335	340
3	340	335
4	340	345
5	345	340

$H_w^{\mathrm{c,m}}$ is the enthalpy of vapour water on the left side in the cathode PTL, $S_w^{0,\mathrm{c}}$ is the standard entropy of vapour water and $c_{p,w}^{\mathrm{c}}$ is the specific heat capacity of vapour water in the cathode PTL. Schroeder's paradox describes that the membrane water content λ_w depends on the state of the neighbouring phase in equilibrium with the membrane. With water vapour in contact with the membrane, as was the case here, the water activity cannot go above 1, and the water content upper limit is (approximately) 14 molecules per membrane ionic site. Therefore we used the data of Weber and Newman [30]. A curve fit was done on the data from Weber and Newman, resulting in Eq 6.28.

$$\lambda_w = 1.07e - 14e^{34.2a_w} + 1.4e^{1.96a_w} \tag{6.28}$$

The numerical solutions were found for current densities between 0 and 14000 $\mathrm{A/m^2}$. These current densities cover the normal range of cell operation. The electric current density was constant through the cell, while the measurable heat flux and the water flux were jumping at the interfaces, due to phase transitions of water and due to the production of water. These fluxes and the resulting profiles were calculated as described below.

The Base Case and Study 1 used boundary temperatures of 340 K and a relative humidity of 70% at both sides of the fuel cell and a constant pressure of 1.013 bar.

The contributions to the water and heat fluxes and the temperature jumps at the electrodes were calculated, using the results of the integration across the whole cell for all current densities. The temperature boundary conditions in Study 2 are given in Table 6.3. Again a pressure of 1.013 bar and a relative humidity of 70% was used.

6.6 Results and discussion

6.6.1 Base Case

The results of the Base Case are plotted in Figures 6.4, 6.5 and 6.6, and discussed in the following.

The polarisation curve

The reference (Base Case) polarisation curve is plotted as a solid black line in Fig. 6.4 (top). Additionally, the power density curves for the different temperatures are shown in Fig. 6.4 (bottom) The curve reproduced results well known from the literature with similar conditions cf. Rahgoshay *et al.* (boundary temperatures of 350 K and a pressure of 1.5 bar) [219]. Yuan *et al.* [220] showed also similar results over the mid-range of current densities; however, a higher relative humidity was used (100%). We saw the initial drop due to the cathode overpotential from the reversible limit value 1.185 V to approximately 0.85 V at 100 A/m^2. Even though air was used on the cathode side and the Butler-Volmer equation was utilised with a partial pressure correction, the voltage drop at high current densities was still linear in the current density. The result did not change by reducing the diffusion coefficient a factor of 10. The other lines, shown in Fig. 6.4, refer to Studies 1 and 2 and are discussed below.

Temperature- and heat flux profile

Generally, we reported higher temperatures/temperature jumps in the fuel cell than known from other authors [194, 210, 219]. Qualitatively, a general rise of a few degrees above the boundary value has been reported. Using our equations, we can identify the cause of the profiles. We first noted that the heat flux, as pictured in Fig. 6.5d, was pointing out of the fuel cell at typical current densities, on both the anode and the cathode side. This is consistent with the fact that fuel cells, especially fuel cell stacks, need to be cooled during operation [22].

The temperature profile, pictured in Fig. 6.5a, showed two interesting facts, a very high temperature at the cathode (349 K as compared to 340 K at the boundaries, and significant temperature jumps at both electrodes, up to 3 and 2 K above the PTL on the anode and cathode side, respectively, at around 8000 A/m^2). The temperature profile had its highest point at the cathode (membrane side). At lower current densities the higher temperature was on the PTL side of the cathode, whereas at higher current densities

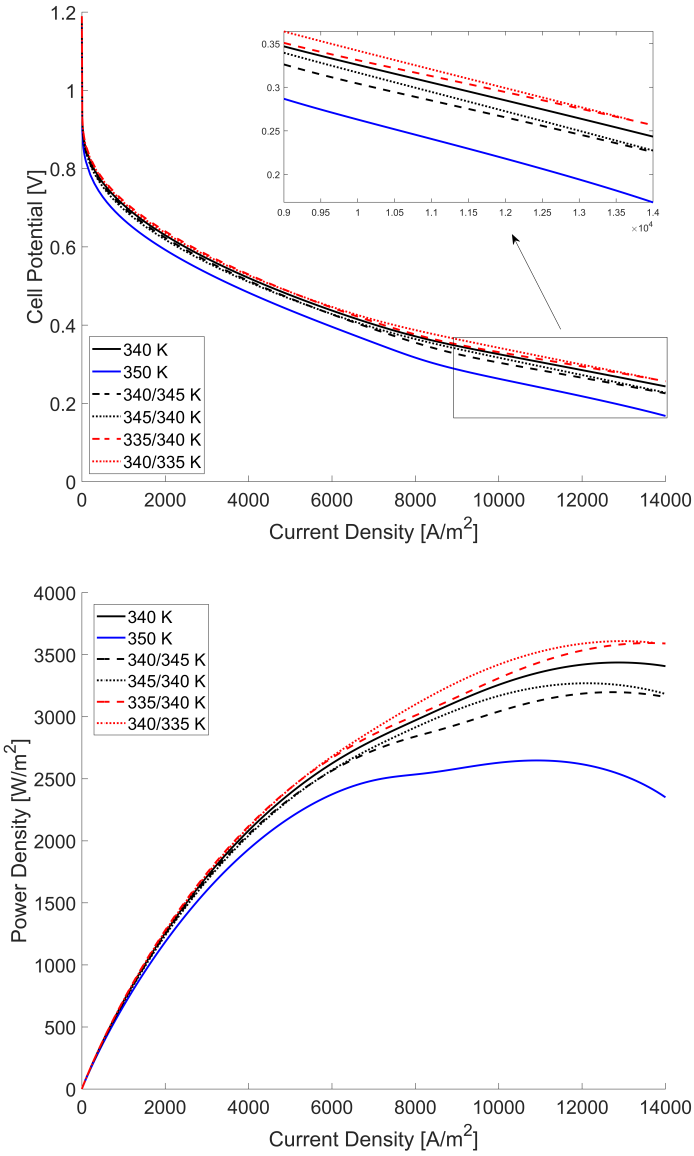

Figure 6.4: IV curves (top) and power density curves (bottom) at 1.013 bar and 70% relative humidity at different temperatures at the outer boundaries of the cell.

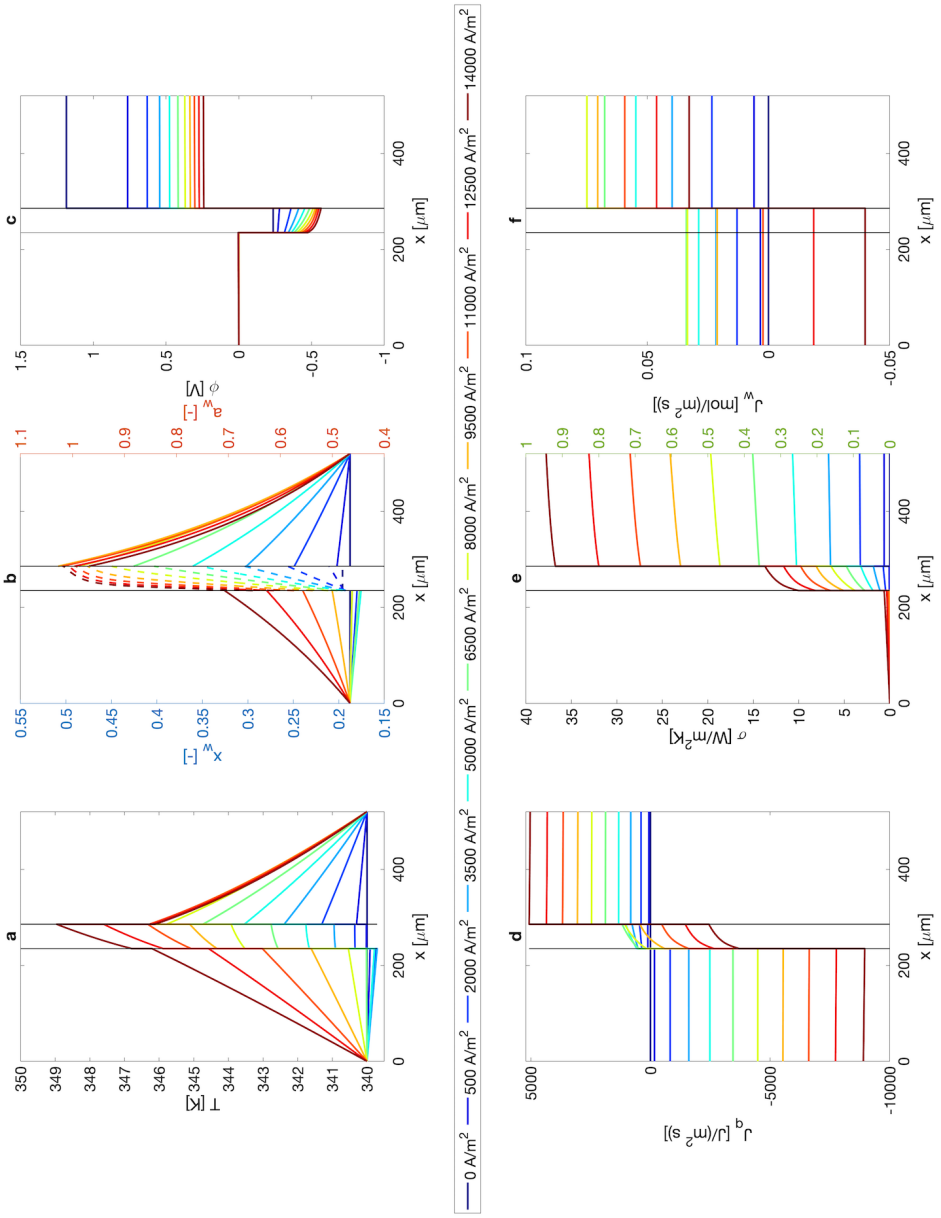

Figure 6.5: Profiles of Base Case at 340 K and 70% relative humidity at both outer boundaries at 1.013 bar constant pressure.(a) Temperature profile in K, (b) water molar fraction and activity profile, (c) potential profile in V, (d) measurable heat flux profile in J/(m^{2}s), (e) entropy production profile in W/(m^{2}K) and (f) water flux profile in mol/(m^{2}s).

the higher temperature was on the membrane side of the cathode. Rowe and Li showed a similar profile, where the highest temperature was at the membrane/cathode interface [221]. However, no jumps at the electrode interfaces were implemented by them.

This could be explained by looking at the heat flux in the membrane, see Fig. 6.5d. At lower current densities, we had a positive heat flux into the membrane, which decreased and became negative at higher current densities. The heat flux had a significant influence on the temperature jump at the anode, which will be discussed further below in connection with Study 1. We shall see the explanation that the coupling terms could lead to higher temperatures and higher jumps.

The obvious reason for the jumps across the electrode surfaces was the energy released by water condensation when water goes from gaseous state in the anode PTL to liquid state in the membrane. This was reflected in the change in enthalpy in the energy balance, *e.g.*, of the anode, cf. Eq. 6.6a and b. Due to the phase transition, this term played a vital role in the energy balance,

$$J_q'^{\mathrm{a}} - J_q'^{\mathrm{m}} + j\phi^{\mathrm{a}} - j\phi^{\mathrm{m}} + J_{\mathrm{H_2}} H_{\mathrm{H_2}} + J_w^{\mathrm{a}} H_w^{\mathrm{a}} - J_w^{\mathrm{m}} H_w^{\mathrm{m}} = 0 \tag{6.29}$$

Vie *et al.* [222] observed a difference of max. 3-4 K between the left and right side of the PTLs for a wide range of current densities with a cell temperature of around 338 K at open cell voltage, but at higher pressure (4.5 bar). Results of our model showed smaller temperature differences in the anode PTL and higher ones in the cathode PTL. Our observation differs from Vie *et al.*'s. This could be linked to different operating conditions such as overall temperature, pressure etc. Furthermore, in a 1D model, heat can only leave in the x-direction, while in reality, heat also leaks to the other sides. The measurements will, therefore, give smaller differences.

Water and water flux profile

The water concentration profile and water flux at the anode and cathode sides as well as in the membrane were well studied in the literature. The results for the cathode PTL fitted well with the ones from Vetter and Schumacher [210]. In the anode PTL, we observed the opposite gradient in the water molar fraction profile for very high current densities. However, the model only accounts for water vapour. The gradient in the water mole fraction varied largely with the current density, see Fig. 6.5b. Water was always transported out of the cathode region, in agreement with the production of water (Eq. 6.5).

The water activity in the membrane did not exceed unity in the model, even at the highest current density, in agreement with the Weber and Newman water isotherm [30] and Schroeder's paradox. We saw at higher current densities that the membrane became more and more saturated with water.

Water was transported from the anode to the cathode for most current densities. At $j = 11000$ A/m^2 there was, however, a sign change in the gradient of the mole fraction (cf. Fig. 6.5b), reflecting a change in the direction of the membrane water flux, see Fig. 6.5f. This information was not visible from Fig. 6.5b alone. It followed from the expression for the water flux. Weber and Newman [194] already showed that high current densities (low voltage in their case) resulted in a negative water vapour flux in the anode PTL. The highest molar fraction was, however, always at the cathode, fitting well with the fact that water was produced there. The profiles in the membrane were non-linear, for various reasons; coupling effects or the dependence of the resistance on temperature.

These points will be further discussed below, where we present the different contributions to the water flux.

Electric potential and entropy production profile

The electric potential profile is shown as a function of current density in Fig. 6.5c. We set the start value to zero on the left side of the anode PTL, and the decline to the anode surface was negligible, even at high current densities, reflecting the small resistance. The anode potential drop at $j \approx 0$ was mainly due to the pressure of the hydrogen gas being different from 1.013 bar. This drop is explained by the entropy of hydrogen at the reaction site. There is also a small anode overpotential, calculated with Eq. 6.21.

Across the membrane, the curves show a decreasing negative slope, due to the membrane resistance and the water saturation. The figure shows a detrimental voltage drop at high current densities despite the resulting high water saturation, Fig. 6.5b. The increase in the potential on the cathode side gives the essential conversion of chemical to electric energy. It is essentially the overpotential (Eq. 6.21), the partial pressure of oxygen, that lowers the potential, increasingly more as the current density increases. Most of these features are well-known from the literature, see *e.g.* [22, 193], apart from the details given for the anode surface, see for instance [210].

The accumulated entropy production reflected to a large degree the potential profile. It grew where the other was reduced. The highest entropy production

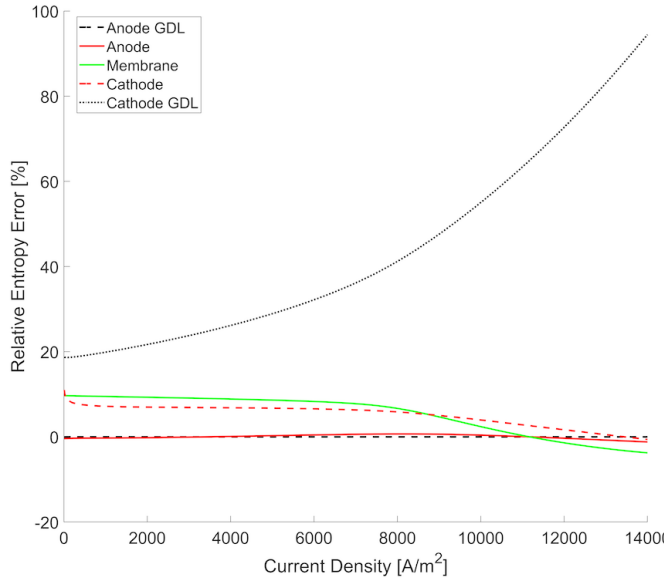

Figure 6.6: Overall relative entropy error of different parts of the system at varying current densities for the Base Case.

was at the cathode. Therefore to minimise the overall entropy production in the system, and make the fuel cell more efficient, one should start to improve the cathode.

The entropy balance and the error in the entropy production, cf. Fig. 6.6, was used to systematically identify errors in the code, during the making of the model program. For instance, a wrong enthalpy value caused an unphysical singularity in the results of a single modelling domain, and could easily be excluded.

The error in the entropy production (Fig. 6.6 was calculated with the help of Eq. 6.1 and 6.2). Fig. 6.6 gives an estimate of how good the assumptions and models are. The error was in general low and decreased with an increase in current density. This showed that there were no major flaws among our assumptions. In particular, the models for the anode and cathode surfaces seems reasonable. The cathode PTL, however, had an ever-increasing error, with a maximum of around 95%. This meant that some assumptions made for the cathode PTL were not reasonable. We suspect that they relate to the water model. Most importantly, we can use the entropy balance to elucidate

the assumptions of water equilibrium across the electrode surfaces, cf. Eq. 6.17. Since the entropy balance is obeyed on both the anode and cathode surfaces (low relative entropy error), the assumption is justified, or the results are consistent with our model.

6.6.2 Study 1

In Study 1 we investigated the contributions to the heat and water flux, such as Soret/Dufour and Seebeck/Peltier effects, in the homogeneous phases and the temperature jumps at the electrodes to see the importance of coupling effects based on the results from the Base Case.

Contributions to the heat flux in the homogeneous phases

The contributions to the measurable heat flux from the Fourier, Peltier and Dufour effects were of interest. The various contributions were computed from the equations shown below, at a temperature of 340 K and 70% relative humidity. Equation 6.30 to 6.32 give the contributions in the different homogenous layers to the overall heat flux J_q' were calculated.

$$J_q'^{\mathrm{a}} = -\lambda^{\mathrm{a}} \frac{dT}{dx} + q^{*,\mathrm{a}} \left(J_D - t_w^{\mathrm{a}} \frac{j}{F} \right) + \pi^{\mathrm{a}} \frac{j}{F} \tag{6.30}$$

$$J_q'^{\mathrm{m}} = -\lambda^{\mathrm{m}} \frac{dT}{dx} + q^{*,\mathrm{m}} \left(J_w - t_w^{\mathrm{m}} \frac{j}{F} \right) + \pi^{\mathrm{m}} \frac{j}{F} \tag{6.31}$$

$$J_q'^{\mathrm{c}} = -\lambda^{\mathrm{c}} \frac{dT}{dx} + q^{*,\mathrm{c}} \left(J_D - t_w^{\mathrm{c}} \frac{j}{F} \right) + \pi^{\mathrm{c}} \frac{j}{F} \tag{6.32}$$

The first term on the right hand side in Equations 6.30 to 6.32 described the Fourier heat contributions to the measurable heat flux J_q'. The second term describes the Dufour contribution, and the last part is the Peltier heat. Results were computed for a location in the middle of a layer. The results were plotted as a function of current density in Fig. 6.7a for the anode PTL, Fig. 6.7b for the membrane and Fig. 6.7c for the cathode PTL. The graphs give a detailed background of the previous figures (cf. Fig. 6.5). The heat flux in each homogeneous phase varied significantly with the current density.

The figures (Fig. 6.7) show that there is no reason to neglect any of the contributions to the overall flux, a priori. The measurable heat flux value is shown by the solid line. We saw that the various effects differ in sign, but in all cases, we obtained a net transport of heat out of the fuel cell, as expected.

In the anode PTL, the heat flux out of the cell was mainly due to Fourier and Dufour effects. In the membrane, the heat flux changed sign. It started with

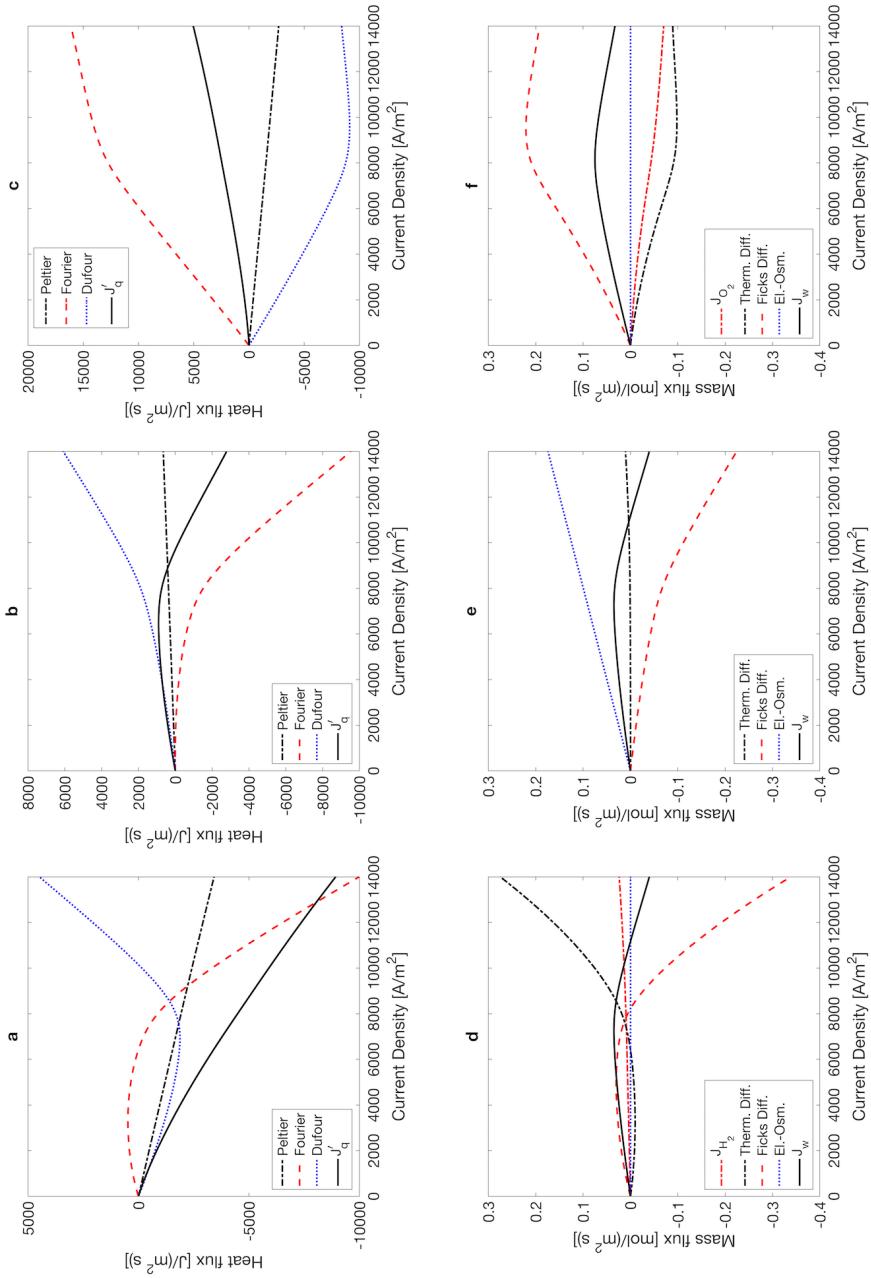

Figure 6.7: Contributions in J/(m^{2}s) to the overall heat flux J_q' in the anode PTL (a), membrane (b) and cathode PTL (c) for different current densities. Contributions in mol/(m^{2}s) to the overall water flux J_w in the anode PTL (d), membrane (e) and cathode PTL (f) for various current densities.

a small positive value, caused by the Peltier term. At around 9700 A/m^2, it became negative. The cathode surface temperature gave then rise to a Fourier term, which again led to a heat loss from the cell also out through the anode PTL. The Peltier heat (or the corresponding entropy flux) was a significant contribution to this in both PTLs.

In the cathode PTL we had a low measurable heat flux, lower than that reported by Vetter and Schumacher [210]. This is probably because we have included the counteracting Dufour-effect, while this was not taken along by Vetter and Schumacher [210]. The last issue applies to all results shown in Figs. 6.7a-c. The Dufour effect is connected to the entropy of water, which is large [217]. These results fit well with the computations form Huerta *et al.* [206], who showed that the Peltier heat has a significant contribution to the heat fluxes in the solid oxide fuel cell.

Contributions to the temperature jumps at the electrode surfaces

In order to compare the different contributions to the temperature jumps at the anode and cathode surfaces, we consider their analytic expressions:

$$\begin{aligned}\Delta_{\mathrm{a,m}}T = &-\frac{1}{\lambda^{\mathrm{s,a}}}\left(J_q'^{\mathrm{a,m}} + J_q'^{\mathrm{m,a}}\right)\\ &+\frac{1}{\lambda^{\mathrm{s,a}}}\left(q^{*,\mathrm{a}}\left(J_w^{\mathrm{a,m}} - t_w^{\mathrm{a}}\frac{j}{F}\right) + q^{*,\mathrm{m}}\left(J_w^{\mathrm{m,a}} - t_w^{\mathrm{m}}\frac{j}{F}\right)\right)\\ &-\frac{j}{\lambda^{\mathrm{s,a}}F}\left(\pi^{\mathrm{a}} + \pi^{\mathrm{m}}\right)\end{aligned} \tag{6.33}$$

$$\begin{aligned}\Delta_{\mathrm{m,c}}T = &-\frac{1}{\lambda^{\mathrm{s,c}}}\left(J_q'^{\mathrm{m,c}} + J_q'^{\mathrm{c,m}}\right)\\ &+\frac{1}{\lambda^{\mathrm{s,c}}}\left(q^{*,\mathrm{m}}\left(J_w^{\mathrm{m,c}} - t_w^{\mathrm{m}}\frac{j}{F}\right) + q^{*,\mathrm{c}}\left(J_w^{\mathrm{c,m}} - t_w^{\mathrm{c}}\frac{j}{F}\right)\right)\\ &-\frac{j}{\lambda^{\mathrm{s,c}}F}\left(\pi^{\mathrm{m}} + \pi^{\mathrm{c}}\right)\end{aligned} \tag{6.34}$$

The temperature jumps in the anode and cathode surfaces are plotted in Fig. 6.8. We identified three terms on the right-hand side in Eq. 6.33 and 6.34:

1. Contributions due to the effective heat flux J_q'.
2. Contributions due to the coupling between heat and mass (Dufour effect).
3. Contributions due to the coupling between heat and charge (Peltier effect).

For both the anode and cathode, the temperature change coming from the Peltier effect was sizable. Furthermore, the temperature jump caused by the Dufour effect, the coupling between the heat and mass flux, was significant. The minimum in the curve could be traced to the variation in the water flux and electro-osmotic drag term $t_w j/F$. The combination of the two terms showed a corresponding maximum in Fig. 6.8 top and bottom. This shows the importance of coupling terms in the set of equations again. For both electrodes, we saw a change in the gradient of the temperature jump and even a sign change in the cathode. This was mainly caused by the sudden change of the contribution from the Dufour effect. The sign change was the reason why the cathode PTL side was the warmer side at low current density at the cathode, as described in the Base Case results discussion above.

Contributions to the water flux in the homogeneous phases

Zaffou *et al.* [223] has pointed out that thermal diffusion needs to be reconsidered in the modelling of fuel cells. Additionally, Kim and Mench [224] measured the thermo-osmotic water flux in the membrane, showing its importance. Our results confirm these finding and show why. The contributions to the overall water flux in the anode PTL, membrane and cathode PTL are described by Eq. 6.35 to 6.37.

$$J_w^{\mathrm{a}} = J_{\mathrm{H_2}} \frac{x_w}{1 - x_w} - D_{w\mathrm{H_2}}^{\mathrm{a}} \frac{q^{*,\mathrm{a}} x_w}{RT^2} \frac{dT}{dx} - D_{w\mathrm{H_2}}^{\mathrm{a}} \frac{dx_w}{dx} + t_w^{\mathrm{a}} \frac{j}{F} \tag{6.35}$$

$$J_w^{\mathrm{m}} = -\frac{q^{*,\mathrm{m}} D_w^{\mathrm{m}} \lambda_w \rho}{RMT^2} \frac{dT}{dx} - \frac{D_w^{\mathrm{m}} \rho}{M} \frac{d\lambda_w}{dx} + t_w^{\mathrm{m}} \frac{j}{F} \tag{6.36}$$

$$J_w^{\mathrm{c}} = J_{\mathrm{O_2}} \frac{x_w}{0.21\,(1 - x_w)} - D_{w\mathrm{O_2}}^{\mathrm{c}} \frac{q^{*,\mathrm{c}} x_w}{RT^2} \frac{dT}{dx} - D_{w\mathrm{O_2}}^{\mathrm{c}} \frac{dx_w}{dx} + t_w^{\mathrm{c}} \frac{j}{F} \tag{6.37}$$

Here, J_w^{m} is the overall water flux in mol/(m^{2}s), λ_w is the water content in the membrane in mole water per mole membrane ionic site, M is the molar mass of the polymer in the membrane in kg/mol and ρ is the membrane dry density in kg/m^3. The first term on the right-hand side, only available in the water flux equation for the anode and cathode PTL, describes the influence of the hydrogen and oxygen flux, introduced by the interdiffusion flux J_D. The second term describes the coupling between mass and heat (thermal diffusion), the third one is the main term given by Fick's law, and the fourth term is the electro-osmotic drag. Fig. 6.7d to f show how each of the contributions changed with the current density.

In the anode (Fig. 6.7d) and cathode PTL (Fig. 6.7e), we saw two counteracting effects again, but this time the effects were Fick's diffusion and

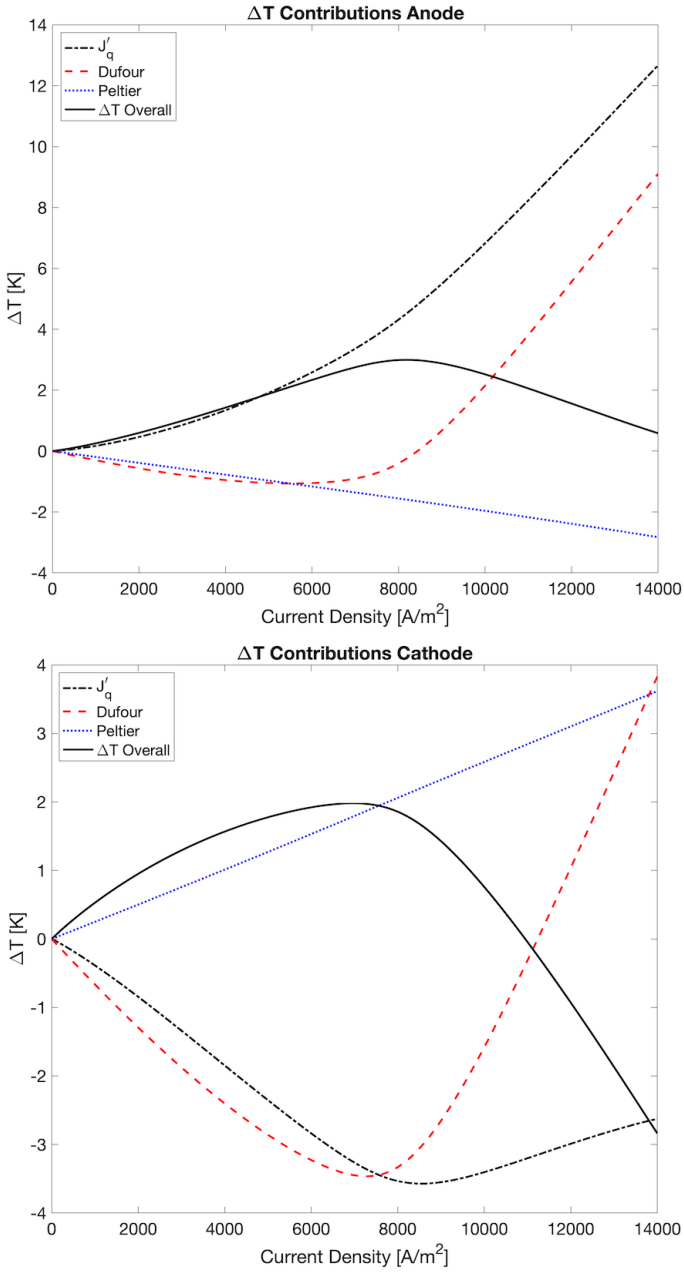

Figure 6.8: Contributions in K to the temperature jump at the anode (top) and cathode (bottom) surface layer for different current densities.

thermal diffusion. This is commonly not discussed in the literature. The role played by oxygen in the cathode was significant. The competition between the diffusion of water and oxygen as given by Eq. 6.15 led to the profile in Fig. 6.5f. For both PTLs, the electro-osmotic drag contribution was zero due to t_w^{a} and t_w^{c} being zero (see Table 6.1).

Temperature gradients can have a significant impact on the water management in the PEMFC. One reason is directly linked to the thermal diffusion in the system. Higher temperature gradients will increase the thermal diffusion. As it is shown in Fig. 6.7f, the contribution of the thermal diffusion decreases the overall water flux in the cathode PTL. If the temperature difference in the cathode PTL would be reduced, the thermal diffusion will reduce too. Therefore, the overall water flux increases, which should help with removal of water. On the other hand, higher temperatures are beneficial to the water management, because more water is evaporating, decreasing the risk of pore blockage and liquid water accumulation. By combining these two points, the best case should be a high, uniform temperature in the cathode PTL.

The biggest contribution to the water flux in the membrane came from the mass-charge coupling term (electro-osmosis). Most of the water transport took place due to charge transfer. At a certain current density, the accumulation of water at the cathode became so high, that back-diffusion set in. This balance of phenomena in the membrane is well documented in the literature [225]. The mass-heat coupling term (thermal diffusion) was smaller. We saw that water moved due to thermal osmosis from the cold to the hot side, as described by Kim and Mench [224], and increased nearly linearly with an increase in current density.

6.6.3 Study 2

In this section, we report results for varying boundary conditions and compare them to the Base Case. We first increased the temperature on both sides from 340 K to 350 K at 70% relative humidity. In the next step, we applied the temperature differences, as given in Table 6.3.

The results are reported in Tables 6.4 to 6.6. The first observation is that the cell potential decreased with decreasing temperature, cf. also Fig. 6.4 and Table 6.5. This is as expected from the thermodynamic relation $F\left(dE/dT\right)_p = \Delta S$. Nevertheless, several experiments have shown [20, 21], that a higher temperature in practice leads to a better performance in term of power output. This may be due to operational conditions, for instance, easier water management. Jang *et al.* [226], however, reported, fuel cell stack

performance increased only till a certain cell temperature. After this, the hydration of the cell decreased, resulting in a performance drop.

All temperature profiles with 350 K at both boundaries gave the same qualitative behaviour, as the Base Case for 340 K (see Table 6.4). The temperature jumps at the electrodes differed only somewhat in magnitude. Nevertheless, interesting details were seen: At the maximum current density, the PTL temperature at the anode was higher, by up to 3 K, than the PTL side temperature of the cathode. Such behaviour has been reported in the literature [222], however the cell temperature was lower (338 K). Also interesting was the negative water flux at the anode, which had a larger absolute value at 340 than at 350 K (comparing the values -0.04 and -0.08 mol/m^{2}s at 14000 A/m^2). Water could obviously leave the cell also by back-diffusion to the anode, if the cathode source term became large enough. Another important observation was that at the maximum current density of 14000 A/m^2, the PTL side of the anode was warmer than the membrane side, which was the opposite to the Base Case but in agreement with observations from Vie *et al.* [222]. The reason for this is the significant impact of the Dufour effect, which led to the sign change of the temperature jump. The water flux, which influences the Dufour effect, had a higher negative magnitude, therefore further reducing the temperature jump. By imposing a temperature difference of 5 K between the boundaries (see Table 6.3 for temperature values), we observed dramatic changes in various locations. When the cathode PTL side was cooled, the temperature jumps became bigger on both electrodes for typical values of the current density (see Table 6.4). We were clearly extracting heat from the cell in the direction of the cathode, and we lowered the temperature peaks. The cooler cathode side introduced an increase in the heat flux out of the cathode and a reduction in the heat flux out of the anode. The results were a more uniform distribution in the cell, smaller entropy production (-0.8% for Case 3 and -1.8% for Case 5). In essence, such knowledge could be used to design and optimise auxiliary cooling systems.

Comparing the results in the IV- and power density curves (Fig. 6.4), with the help of Table 6.5, we can draw the following conclusions: Having a lower temperature at the cathode side gave a better performance than having a decrease on the anode side. Case 4 and 5 had, generally speaking, already a performance increase compared to Case 1 because the temperatures in the system were usually smaller (as discussed at the beginning of this section). Looking at Case 4, the voltage output of the fuel cell increased approximately 12 mV, whereas in Case 5 it increased around 13 mV. Case 2 and 3 increased

Table 6.4: Temperature jumps at the anode and cathode in K as well as absolute temperatures at the membrane side of the anode and cathode at 1000 and 13500 A/m2 for the Base Case and Case 1 to 5 in Study 2.

	1000 A/m^2			
	$\Delta_{\mathrm{a,m}}T$ [K]	$T^{\mathrm{m,a}}$ [K]	$\Delta_{\mathrm{m,c}}T$ [K]	$T^{\mathrm{m,c}}$ [K]
B	0.25	340.10	0.53	340.09
C1	0.32	350.19	0.58	350.18
C2	2.41	342.55	2.70	342.68
C3	-1.87	342.68	-1.60	342.54
C4	2.34	337.51	2.63	337.65
C5	-1.85	337.65	-1.58	337.50
	13500 A/m^2			
	$\Delta_{\mathrm{a,m}}T$ [K]	$T^{\mathrm{m,a}}$ [K]	$\Delta_{\mathrm{m,c}}T$ [K]	$T^{\mathrm{m,c}}$ [K]
B	0.82	346.47	-2.35	348.49
C1	-0.49	358.74	-4.21	361.55
C2	3.59	349.88	0.35	352.10
C3	-2.07	349.14	-5.38	351.20
C4	3.66	343.92	0.61	345.90
C5	-1.99	343.43	-5.08	345.31

the heat in the system, leading to a decrease in cell performance. However, we saw again that a cooler cathode is beneficial (3 mV difference), even more than in Case 4 and 5. To further see the effect of having different temperatures, according to Table 6.3, at the system boundaries, the contributions to the heat fluxes, namely the Dufour effect, the Peltier effect, and the Fourier heat, in the different parts of the system were analysed in the Base Case and Study 2 to 5.

Table 6.6 gives a summary of the changes in the various contributions in different layers of the fuel cell at 13500 A/m^2. This table provides the change in the measurable heat flux J'_q (see fourth table quadrant) at three locations (Anode PTL, Membrane, Cathode PTL), and the change in the contributions from the Peltier term (first table quadrant), Fourier type term (second table quadrant) and Dufour term (third table quadrant). The changes are reported as % difference of the Base Case value. When the temperature difference was

Table 6.5: Potential jumps at the anode and cathode as well as cell potential at 1000 and 13500 A/m2 for the Base Case and Case 1 to 5 in Study 2 in V.

	1000 A/m^2		
	$\Delta_{\mathrm{a,m}}\phi$ [V]	$\Delta_{\mathrm{m,c}}\phi$ [V]	ϕ^{cell} [V]
B	-0.287	1.018	0.707
C1	-0.304	0.994	0.670
C2	-0.288	1.008	0.701
C3	-0.294	1.017	0.696
C4	-0.281	1.019	0.718
C5	-0.286	1.028	0.714
	13500 A/m^2		
	$\Delta_{\mathrm{a,m}}\phi$ [V]	$\Delta_{\mathrm{m,c}}\phi$ [V]	ϕ^{cell} [V]
B	-0.471	0.811	0.254
C1	-0.516	0.764	0.182
C2	-0.474	0.786	0.236
C3	-0.485	0.812	0.239
C4	-0.460	0.810	0.266
C5	-0.470	0.829	0.267

5 K between the left and right-hand side, the contribution of the Peltier heat (Table 6.6 first three columns in the upper table) changes between -2.3% and 2.3%. Case 4 and 5 had an overall reduction of the Peltier effect, due to the generally lower temperatures in the homogenous layer. For Case 2 and 3, it was the opposite. This change was quite small since the Peltier coefficient π only depends on the absolute temperature, which was, compared to the magnitude of the temperature gradient change, insignificant. The Fourier and Dufour contributions differed more significantly with values between 12 and -7% for the first and 31 and -65% for the latter one.

The Fourier heat contribution (Table 6.6 last three columns in the upper table) saw more significant changes compared to the Peltier heat effect, due to its dependence on the temperature gradient instead of the absolute temperature. Between Case 2 and 3 and Case 4 and 5 we observed a difference in sign in the anode PTL and membrane. Case 2 and 3 had higher temperature gradients in those two homogeneous layers, therefore increasing the relative

Table 6.6: Relative change of the overall heat flux J'_q and its contributions in % for the anode PTL, membrane and cathode PTL at 13500 A/m^2 with respect to the Base Case.

	Peltier a PTL	Peltier m	Peltier c PTL	Fourier a PTL	Fourier m	Fourier c PTL
Δ B/C2 [%]	0.1	1	2.1	9.9	11.7	-1.3
Δ B/C3 [%]	2.3	0.8	-0.1	8.5	1.5	-0.8
Δ B/C4 [%]	-2.3	-0.7	0.1	-7.4	-1.5	0.9
Δ B/C5 [%]	0	-0.9	-2.1	-4.4	-6.9	-1.1
	Dufour a PTL	Dufour m	Dufour c PTL	J'_q a PTL	J'_q m	J'_q c PTL
Δ B/C2 [%]	-8.0	-0.4	8.6	13.2	32.4	-28.2
Δ B/C3 [%]	30.9	8.5	-15.5	-10.5	-19.7	17.5
Δ B/C4 [%]	-64.9	-9.9	11.8	8.8	13.7	-26.3
Δ B/C5 [%]	16.1	3.3	-14.6	-15.3	-44.4	16.7

contribution from the Fourier heat effect. For the other two cases, it was the opposite. In the cathode PTL, the temperature gradient was smaller in Case 2 and 4 (where we had a cooler anode) and larger in Case 3 and 5 compared to the Base Case, leading to a reduction and respectively increase in Fourier heat.

The Dufour effect contributions (Table 6.6 first three columns in the lower table) changes in different ways. When the anode side was colder than the cathode side, the contribution decreased in the anode PTL and membrane, whereas for Case 3 and 5 we had the opposite. These observations could be linked to the change in the water flux in these homogenous layers because the heat of transfer coefficient changed only marginal with an increase or decrease of the temperature (5 K temperature difference change q^* for around 1,7%). Having a cooler anode led to a lower water flux directly decreasing the Dufour effect. The same reasoning was also found in the cathode PTL; however, a cooler anode increased the water flux on the cathode side.

As already discussed, imposing a temperature difference at the boundaries of 5 K changed the overall heat flux J'_q significantly (Table 6.6 last three columns in the lower table). Having a cooler anode (Case 2 and 4), increased the heat flux in the anode PTL and membrane and decreased it in the cathode PTL, advanced the asymmetry of it in the fuel cell. A cooler cathode, on the

other hand, achieved the adverse effect and led to a more symmetric heat flux. It also lowered the entropy production in the system.

This detailed comparison of the changes in the contributions to the overall heat fluxes in the fuel cell had not been computed before for the best of our knowledge.

6.6.4 Practical implications

The 1D model presented here, exchanges heat and mass only at the endpoints of the $x-$axis. The other boundaries are adiabatic. This is not so in reality. The temperature profiles, obtained here, could, therefore, be regarded as maximum values when compared to experiments. The model was, nevertheless, an efficient tool for estimation of fluxes in a qualitative and quantitative way, in and out of the cell. Certain FFP patterns exist which can be easily connected to the cell model. These are the bio-inspired tree or fractal-like patterns [7, 10] with uniform flow distribution [165]. These patterns can be subdivided into several subcells with one outlet branch. Therefore they can be connected to our 1D model, for a complete fuel cell system analysis. Thereby, we obtain an efficient cell model, which can be solved with a significant reduction in computation time, but which nevertheless captures the essence of the processes, and can be used for predictions, *i.e.* of local heat and water fluxes, as discussed in Study 1 and 2.

The entropy balance was actively used in the development of the present model to check for model consistency, such as the investigation of the water equilibrium assumption at the electrode surfaces. This is not yet standard procedure but can be recommended especially for validation of thermodynamic properties. A deviation, even a singularity, could immediately be seen in the entropy production error if enthalpy values were wrong.

One of the interesting observations of this model, that may have a practical bearing on PEMFC stack design, is the observation that cathode cooling leads to a higher power density.

6.7 Conclusion

We have presented a non-equilibrium thermodynamic 1D-model of a PEM fuel cell, using a state-of-the-art, open-source code [210] as a starting point. The entropy balance was actively used to check for model consistency. The model added detailed information about coupling effects, such as the Soret/Dufour and Seebeck/Peltier effect, and supplemented in this manner to conventional analyses of the fuel cell.

We have shown that the Dufour effects in the homogeneous layers had the same magnitude, but an opposite sign of the Fourier type contribution to the heat flux. Therefore it must not be neglected. The Peltier effects were also substantial. Coupling terms, additionally, had significant contributions to the effective water flux. By imposing a temperature difference of 5 K between inlets/outlets of the cell, we could significantly alter the magnitude of the heat flux, J_q' (up to 44%). Changes in contributions to the overall heat flux J_q' differed between the anode PTL, membrane and the cathode PTL due to different temperature gradients and water fluxes. An important finding in Study 2 was that a cooler cathode is beneficial to the overall performance of the fuel cell for most current densities and in addition, provided a more uniform heat flux distribution in homogenous layers of the fuel cell. This has to be investigated further in experiments. The presented model included the possibility for phase transition of water only at the electrode surfaces. Future work should allow for condensation/ evaporation also in the PTLs and create an interface with flow field models.

Conflicts of interest

There are no conflicts of interest to declare.

Acknowledgements

We gratefully acknowledge the support from NTNU in Trondheim and the Research Council of Norway through its Centre of Excellence funding scheme with Project No. 262644 (PoreLab).

Chapter 7

Conclusions and future work

The last chapter of this thesis is a global summary of all the conclusions made in the presented chapters. Future steps in the development of the tree-like flow field plates and the NET model of the PEM fuel cell are also described.

7.1 Conclusions

Even though over the years, there has been a focus on developing new flow field designs and on modifying existing ones for PEM fuel cells, the most efficient and optimised flow field pattern has not been found yet. One of the reasons is that the optimisation criteria for such flow fields are relatively complex. Therefore, research efforts should focus on multi-criteria optimisation. One recommendation by us was to use the entropy production approach as (i) it serves as a good objective function for such optimisations, and (ii) it is possible to include all sources of energy dissipation in a multi-physics environment. Moreover, the use of nature-inspired flow field designs is promising and should be combined with the minimum entropy production approach.

One of these nature-inspired flow field designs was the presented tree-like flow field. We showed in Chapter 3 that they provided a uniform distribution of reactants over the active area of the MEA. In this study, the impact of the width scaling factor and channel width on the entropy production was investigated. Scaling factors which were higher than the one given by Murray's law led to lower viscous dissipation due to a reduction in pressure drop along the channels. For that reason, we experimentally analysed the impact of the width scaling factor. Flow field plates consisting of two plates with similar tree-like FF designs, one for the inlet and one for the outlet

pattern, machined in graphite with CNC milling, were compared in various electrochemical tests against serpentine patterns as discussed in Chapter 4. Results showed that the flow field design with a width scaling factor of 0.917 for the inlet and 0.925 for the outlet pattern had a performance which was within 11% (a 0.08 W/cm^2 difference) of the one from the serpentine pattern at a relative humidity of 70%. Increasing the width scaling factor led to a reduction in power density. We argued that the main problems, as clearly indicated by the experiments, originated from water accumulation and the increased resistance of the flow field plates of the new designs compared to the serpentine pattern. Moreover, we found the opposite effect when increasing the width scaling factor, compared to the theoretical analysis in Chapter 3. Therefore, we proposed to use a multi-criteria optimisation, including effects such as electrical or thermal resistances, in addition to the viscous dissipation, for further optimisation of the tree-like flow fields.

The presented NET fuel cell model was useful in indicating that coupling terms such as the Peltier or Dufour effects were detrimental in the modelling process, as those had significant contributions to heat and water fluxes inside the PEM fuel cell. A systematic approach on how to model the PEM fuel cell electrodes as planar Gibbs surfaces was described. The presented models were in 1D. At the same time, processes are at least in 2D in reality. We assumed adiabatic boundaries to the other dimensions. Therefore, fluxes might be higher in 1D than in 2D. However, the presented tree-like flow field plates provided a uniform distribution of the reactant gases. Due to this uniformity, it is possible to link the 1D NET model to the outlet branches since the amount of gasses entering the gas diffusion layer can be precisely calculated.

The consistency check based upon the difference between the entropy balance and entropy production was a useful tool in analysing weaknesses in the made assumptions and the model itself. We concluded that a weakness of the model in Chapter 5 was the assumption of water equilibrium at the PEM fuel cell electrodes. Another one originated from the non-linear part in the polarisation curve, not solely caused by mass-transfer limitations but due to the varying membrane resistance. Results in Chapter 6, however, revealed that the water equilibrium assumption at the electrodes was justified due to the low relative error in entropy production.

The model presented in Chapter 6 was an improvement to the previous one, not only in terms of stability and speed. We showed that the system was susceptible to the temperatures at the system boundaries. Heat fluxes

changed up to 44% if a difference of 5 K was applied between the left and right boundary. An important observation was that a cooler cathode could be beneficial to the overall performance of the fuel cell, and a more uniform heat flux could be observed.

7.2 Future work

Using nature-inspired flow field designs, such as tree-like structures, seems a promising way to increase PEM fuel cell performance. A tool for optimisation can be the minimisation of entropy production. As we have demonstrated, the width scaling factors can have a significant impact on the performance of such a pattern, and Murray's law should not be automatically used for the scaling. In future investigations, the entropy production needs to include additional terms such as thermal and electrical dissipations in addition to the viscous dissipation to correctly predict improvement opportunities for use in PEM fuel cells. One way to accomplish this is by utilising the so-called Pareto frontiers. This tool allows a multiobjective optimisation, showing the best trade-off between the different objectives [227].

The tree-like flow field design, as shown in this thesis, needs to be improved further to be competitive. One way to do this, is to modify the presented designs by either reducing the number of branching generations or the width scaling factor of the inlet and outlet pattern. Another possibility for improvement is to use a different MEA in the PEM fuel cell to counteract the water removal problems, for example, by using a GDL with better hydrophobic properties.

As the next step, in terms of improving the NET model for the PEM fuel cell, liquid water needs to be included in the modelling process. Doing so can enable a better prediction of water problems within the PEM fuel cell which then can be linked to the optimisation of the tree-like FFP. Another step could be to change the model domain from 1- to 2- or 3-D. However, this will also increase the complexity and computational costs of the model. If a FFP like the presented tree-like pattern (Chapter 3 and 4) is used, the FFP can be subdivided into smaller representative elementary volumes (REV), as gas distribution is uniform. The REV needs to include one branch of the inlet and one of the outlet pattern. This should help in reducing the computational time because only a small part of the active area of the PEM fuel cell needs to be simulated. As the NET model is derived from a general set of equations, as shown in Chapter 1, it can also be used to analyse other electrochemical systems, such as batteries and supercapacitors.

List of symbols

α	Branching angle [-]
α	Charge transfer coefficient of the electrode [-]
α	Phase angle [-]
α_i	Phase angle of element i [-]
Δp	Total pressure drop [Pa]
$\Delta p_{j,i}$	Pressure drop in branch i at generation level j [Pa]
$\Delta_n G^{\mathrm{s}}$	Reaction Gibbs energy of neutral surface components [J/mol]
$\Delta_{\mathrm{a,m}}\phi_{eff}$	Effective electric potential at the anode [V]
$\dot{W}$	Viscous dissipation [W/K]
η	Overpotential [V]
η^{c}	Cathode overpotential [V]
η_{II}	Second law efficiceny [-]
$\frac{dS_{irr}}{dt}$	Total entropy production [W/K]
γ	Diameter scaling coefficient [-]
λ	Thermal conductivity [W/(K m)]
λ^{a}	Thermal conductivity of the anode PTL [W/(K m)]
λ^{c}	Thermal conductivity of the cathode PTL [W/(K m)]
λ^{m}	Thermal conductivity of the membrane [W/(K m)]
$\lambda^{\mathrm{s,a}}$	Thermal conductivity of the anode on the anode PTL side [W/(K m^2)]

$\lambda^{\mathrm{s,c}}$ Thermal conductivity of the cathode on the cathode PTL side [W/(K m^2)]

$\lambda^{\mathrm{s,m}}$ Thermal conductivity of the anode on the membrane side [W/(K m^2)]

$\lambda^{\mathrm{s,i}}$ Thermal conductivity at the surface on the inlet side [W/(K m^2)]

$\lambda^{\mathrm{s,o}}$ Thermal conductivity at the surface on the outlet side [W/(K m^2)]

λ_w Water content in the membrane [mol water/mol membrane ionic site]

$\left(\frac{dS^*_{irr}}{dt}\right)_{j,i}$ Total specific entropy production of branch i at generation level j [W/K]

$\left(\frac{dS^*_{irr}}{dt}\right)_{j}$ Total specific entropy production of all branches at generation level j [W/K]

$\left(\frac{dS_{irr}}{dt}\right)_{j,i}$ Total entropy production of branch i at generation level j [W/K]

$\left(\frac{dS_{irr}}{dt}\right)_{j}$ Total entropy production of all branches at generation level j [W/K]

$\mathbf{v}$ Barycentric velocity [m/s]

$\mathrm{EPSA}^{\mathrm{a}}$ Electrochemical Pt surface area of the anode [cm^2/cm^2]

$\mathrm{EPSA}^{\mathrm{c}}$ Electrochemical Pt surface area of the cathode [cm^2/cm^2]

μ Dynamic viscosity [Pa s]

$\mu_{\mathrm{H}_2,T}$ Chemical potential of hydrogen at constant temperature [J/mol]

$\mu_{j,T}$ Chemical potential of component j at constant temperature [J/mol]

$\mu_{k,T}$ Chemical potential of component k at constant temperature [J/mol]

$\mu_{w,T}$ Chemical potential of water at constant temperature [J/mol]

$\mu^0_{w,T}$ Chemical potential of water at constant temperature and standard conditions [J/mol]

$\mu^{\mathrm{a,m}}_{w,T}$ Chemical potential of water at constant temperature in the anode PTL on the membrane side [J/mol]

$\mu_{w,T}^{\mathrm{c,m}}$ Chemical potential of water at constant temperature in the cathode PTL on the membrane side [J/mol]

$\mu_{w,T}^{\mathrm{m,a}}$ Chemical potential of water at constant temperature in the membrane on the anode PTL side [J/mol]

$\mu_{w,T}^{\mathrm{m,c}}$ Chemical potential of water at constant temperature in the membrane on the cathode PTL side [J/mol]

Ω Cross-sectional area [m^2]

ω Angular frequency [s^{-1}]

ϕ Electric potential [V]

$\phi^{\mathrm{a,lb}}$ Electric potential in the anode PTL on the left system boundary side [V]

$\phi^{\mathrm{a,m}}$ Electric potential on the left side of the anode [V]

ϕ^{a} Electric potential in the anode PTL [V]

$\phi^{\mathrm{c,m}}$ Electric potential on the right side of the cathode [V]

ϕ^{cell} Electric potential of the PEMFC [V]

ϕ^{c} Electric potential in the cathode PTL [V]

ϕ^{i} Electric potential at the inlet side of the surface [V]

$\phi^{\mathrm{m,a}}$ Electric potential on the right side of the anode [V]

$\phi^{\mathrm{m,c}}$ Electric potential on the left side of the cathode [V]

ϕ^{m} Electric potential in the membrane PTL [V]

ϕ^{o} Electric potential at the outlet side of the surface [V]

Π Viscous stress tensor [Pa]

π Peltier coefficient [J]

π^{a} Peltier coefficient in the anode PTL [J]

π^{c} Peltier coefficient in the cathode PTL [J]

π^{i} Peltier coefficient on the inlet side of the surface [J]

π^{m} Peltier coefficient in the membrane [J]

π^{o} Peltier coefficient on the outlet side of the surface [J]

ρ Membrane dry density [kg/m^3]

σ Entropy production [W/(K m^3)]

$\sigma^{\mathrm{a,lb}}$ Entropy production in the anode PTL on the left system boundary side [W/(K m^3)]

$\sigma^{\mathrm{a,m}}$ Entropy production in the anode PTL on the membrane side [W/(K m^3)]

$\sigma^{\mathrm{c,m}}$ Entropy production in the cathode PTL on the membrane side [W/(K m^3)]

$\sigma^{\mathrm{m,a}}$ Entropy production in the membrane on the anode PTL side [W/(K m^3)]

$\sigma^{\mathrm{m,c}}$ Entropy production in the membrane on the cathode PTL side [W/(K m^3)]

σ^{s} Entropy production of a surface [W/(K m^2)]

τ_d Time constant [s]

θ Ratio between maximum and minimum volumetric flow rate [-]

a Self-similar scaling factor [-]

a Width scaling factor [-]

a_w Water activity in the membrane [-]

a_w^{entrance} Water activity in the membrane on the anode PTL side [-]

$a_w^{\mathrm{m,a}}$ Water activity in the membrane on the anode PTL side [-]

a_{i} Width scaling factor on the inlet plate [-]

a_{o} Width scaling factor on the outlet plate [-]

AR Aspect ratio [-]

B Rib width [m]

b Self-similar scaling factor [-]

b_j Rib width at generation level j [m]

c Total concentration [mol/m^3]

C^p Pseudo capacitance [F]

C_i^p Pseudo capacitance of element i [F]

c_w Partial molar concentration of water [mol/m^3]

$c_{p,w}^{\mathrm{c}}$ Specific heat capacity of vapour water [J/(K mol)]

$c_{p,w}^{\mathrm{m}}$ Specific heat capacity of liquid water [J/(K mol)]

D Channel depth [m]

D Diffusivity coefficient of gas [m^2/s]

d Pore diamater ditribution [m]

D^{m} Diffusivity coefficient in the membrane [m^2/s]

d_0 Diameter of parent branch [m]

D_h Hydraulic diameter [m]

d_j Diameter at generation level j [m]

D_w^{m} Diffusivity coefficient of water in the membrane [m^2/s]

$d_{0,\mathrm{i}}$ Channel depth at generation level 0 on the inlet plate [m]

$d_{0,\mathrm{o}}$ Channel depth at generation level 0 on the outlet plate [m]

D_{ON} Diffusivity coefficient of oxygen in nitrogen [m^2/s]

D_{ij} Concentration corrected diffusivity coefficient of component i in component j [mol/(m s)]

$d_{j,i}$ Diameter of branch i at generation level j [m]

$D_{w\mathrm{H_2}}^{\mathrm{a}}$ Diffusivity coefficient of water in hydrogen in the anode PTL [m^2/s]

$D_{w\mathrm{O_2}}^{\mathrm{c}}$ Diffusivity coefficient of water in oxygen in the cathode PTL [m^2/s]

D_w Diffusivity coefficient of water in the membrane [m^2/s]

F Farraday's constant[C/mol]

H_k^{i} Molar enthalpy of component k on the inlet side of the surface [J/mol]

H_k^{o} Molar enthalpy of component k on the outlet side of the surface [J/mol]

$H_w^{\mathrm{a,m}}$ Molar enthalpy of water in the anode PTL on the membrane side [J/mol]

H_w^{a} Molar enthalpy of water in the anode PTL [J/mol]

$H_w^{\mathrm{c,m}}$ Molar enthalpy of water in the cathode PTL on the membrane side [J/mol]

H_w^{c} Molar enthalpy of water in the cathode PTL [J/mol]

$H_w^{\mathrm{m,a}}$ Molar enthalpy of water in the membrane on the anode PTL side [J/mol]

$H_w^{\mathrm{m,c}}$ Molar enthalpy of water in the membrane on the cathode PTL side [J/mol]

H_w^{m} Molar enthalpy of water in the membrane [J/mol]

$H_{\mathrm{H_2}}$ Molar enthalpy of hydrogen [J/mol]

$H_{\mathrm{O_2}}$ Molar enthalpy of oxygen [J/mol]

$h_{j,i}$ Channel height of branch i at generation level j [m]

j Charge flux / current density [A/m^2]

j Generation level [-]

j Imaginary unit [-]

j_0 Exchange current density [A/m^2]

J_D Interdiffusion flux [mol/(m^{2}s)]

j_f Generation level number of last generation [-]

J_i Flux of transport phenomena i

J_j Mass flux of component j [mol/(m^{2}s)]

J_k^{i} Molar flux of component k on the inlet side of the surface [mol/(m^{2}s)]

J_k^{o} Molar flux of component k on the outlet side of the surface [mol/(m^{2}s)]

$J_q'^{\mathrm{a,m}}$ Measurable heat flux in the anode PTL on the membrane side [J/(m^{2}s)]

$J_q'^{\mathrm{a}}$ Measurable heat flux in the anode PTL [J/(m^{2}s)]

$J_q'^{\mathrm{c,m}}$ Measurable heat flux in the cathode PTL on the membrane side [J/(m^{2}s)]

$J_q'^{\mathrm{c}}$ Measurable heat flux in the cathode PTL [J/(m^{2}s)]

$J_q'^{\mathrm{i}}$ Measurable heat flux on the inlet side of the surface [J/(m^{2}s)]

$J_q'^{\mathrm{m,a}}$ Measurable heat flux in the membrane on the anode PTL side [J/(m^{2}s)]

$J_q'^{\mathrm{m,c}}$ Measurable heat flux in the membrane on the cathode PTL side [J/(m^{2}s)]

$J_q'^{\mathrm{m}}$ Measurable heat flux in the membrane [J/(m^{2}s)]

$J_q'^{\mathrm{o}}$ Measurable heat flux on the outlet side of the surface [J/(m^{2}s)]

J_q' Measurable heat flux[J/(m^{2}s)]

J_s^{in} Entropy flux into the (sub-)system [W/(K m^2)]

J_s^{out} Entropy flux out of the (sub-)system [W/(K m^2)]

$J_s^{\mathrm{s,in}}$ Entropy flux into the surface [W/(K m^2)]

$J_s^{\mathrm{s,out}}$ Entropy flux out of the surface [W/(K m^2)]

J_u Energy flux [J/(m^{2}s)]

J_w Water flux [mol/(m^{2}s)]

$J_w^{\mathrm{a,m}}$ Water flux in the anode PTL on the membrane side [mol/(m^{2}s)]

J_w^{a} Water flux in the anode PTL [mol/(m^{2}s)]

$J_w^{\mathrm{c,m}}$ Water flux in the cathode PTL on the membrane side [mol/(m^{2}s)]

J_w^{c} Water flux in the cathode PTL [mol/(m^{2}s)]

J_w^{i} Water flux on the inlet side of the surface [mol/(m^{2}s)]

$J_w^{\mathrm{m,a}}$ Water flux in the membrane on the anode PTL side [mol/(m^{2}s)]

$J_w^{\mathrm{m,c}}$ Water flux in the membrane on the cathode PTL side [mol/(m^{2}s)]

J_w^{m} Water flux in the membrane [mol/(m^{2}s)]

J_w^{o} Water flux on the outlet side of the surface [mol/(m^{2}s)]

$j_{0,\mathrm{H_2}}$ Revised exchange current density at the anode [A/m^2]

$j'_{0,\mathrm{H_2}}$ Intrinsic exchange current density at the anode [A/m^2]

$j_{0,\mathrm{O_2}}$ Revised exchange current density at the cathode [A/m^2]

$j'_{0,\mathrm{O_2}}$ Intrinsic exchange current density at the cathode [A/m^2]

$J_{\mathrm{H_2}}$ Hydrogen flux [mol/(m^{2}s)]

$J_{\mathrm{O_2}}$ Oxygen flux [mol/(m^{2}s)]

$j_{max,\mathrm{i}}$ Maximum generation level number on the inlet plate [-]

$j_{max,\mathrm{o}}$ Maximum generation level number on the outlet plate [-]

k Length scaling factor [-]

k Number of daughter elements [-]

L Channel length [m]

L Characteristic length [m]

l^{a} Anode PTL length [m]

l^{c} Cathode PTL length [m]

l^{m} Membrane length [m]

l_0 Channel length at generation level 0 [m]

L_j Channel length at generation level j [m]

L_j Length at generation level j [m]

l_{ij} Transport coefficient between phenomena i and j

L_{ik} Onsager conductivity coefficient between phenomena i and k

$l_{j,i}$ Channel length of branch i at generation level j [m]

M Molar mass of the polymer in the membrane [kg/mol]

m Number of independent fluxes in the system [-]

N Number of outlets [-]

n Number of daughter branches [-]

n Number of electrons involved in the cell reaction [-]

N^{i} Number of components on the inlet side of the surface [-]

N^{o} Number of components on the outlet side of the surface [-]

N_j Number of branches at generation level j [-]

p Pressure [Pa]

p^0 Standard pressure [bar]

p_w Partial pressure of water [atm]

p_w^* Standard pressure of water [atm]

$p_{\mathrm{H_2}}$ Partial pressure of hydrogen [bar]

$p_{\mathrm{O_2}}$ Partial pressure of oxygen [bar]

Pe Peclet number [-]

Q Volumetric flow rate [$\mathrm{m^3/s}$]

q Flow non-uniformity [-]

q^* Heat of transfer [J/mol]

$q^{*,\mathrm{a}}$ Heat of transfer in the anode PTL [J/mol]

$q^{*,\mathrm{c}}$ Heat of transfer in the cathode PTL [J/mol]

$q^{*,\mathrm{i}}$ Heat of transfer in the homogenous layer i [J/mol]

$q^{*,\mathrm{m}}$ Heat of transfer in the membrane [J/mol]

Q_0 Volumetric flow rate at generation level 0 [$\mathrm{m^3/s}$]

Q_i Time constant of element i [$\mathrm{F\ cm^2\ s^{\alpha-1}}$]

Q_j Volumetric flow rate at generation level j [$\mathrm{m^3/s}$]

Q_{avr} Average volumetric flow rate [$\mathrm{m^3/s}$]

$Q_{j,i}$ Volumetric flow rate in branch i at generation level j [m^3/s]

Q_{max} Maximum volumetric flow rate [m^3/s]

Q_{min} Minimum volumetric flow rate [m^3/s]

R Gas constant [J/(K mol)]

r Electric resistance [Ohm m]

r^{a} Electric resistance of the anode PTL [Ohm m]

r^{c} Electric resistance of the cathode PTL [Ohm m]

r^{m} Electric resistance of the membrane [Ohm m]

$r^{s,a}$ Electric resistance of the anode on the anode PTL side [Ohm m^2]

$r^{s,c}$ Electric resistance of the cathode on the cathode PTL side [Ohm m^2]

r^{s} Electric resistance of the surface [Ohm m^2]

R_1 Ohmic resistance [Ohm]

R_2 Charge transfer resistance on the anode [Ohm]

R_3 Charge transfer resistance on the cathode [Ohm]

R_d Diffusion resistance [Ohm]

R_{11} Ohmic resistance of a flow field plate [Ohm]

Re Reynolds number [-]

S^{i} Molar entropy of water in the homogeneous layer i [J/(K mol)]

$S_w^{0,c}$ Standard entropy of vapour water [J/(K mol)]

$S_w^{0,m}$ Standard entropy of liquid water [J/(K mol)]

$S_w^{a,m}$ Molar entropy of water in the anode PTL on the membrane side [J/(K mol)]

$S_w^{m,c}$ Molar entropy of water in the membrane on the cathode PTL side [J/(K mol)]

T Temperature [K]

$T^{\mathrm{a,lb}}$ Temperature in the anode PTL on the left system boundary side [K]

$T^{\mathrm{a,m}}$ Temperature in the anode PTL on the membrane side [K]

$T^{\mathrm{c,m}}$ Temperature in the cathode PTL on the membrane side [K]

$T^{\mathrm{c,rb}}$ Temperature in the cathode PTL on the right system boundary side [K]

T^{lb} Temperature at the left system boundary [K]

$T^{\mathrm{m,a}}$ Temperature in the membrane on the anode PTL side [K]

$T^{\mathrm{m,c}}$ Temperature in the membrane on the cathode PTL side [K]

T^{rb} Temperature at the right system boundary [K]

T^{s} Temperature at the surface [K]

T' Temperature [$^{\circ}C$]

T_0 Temperature of the surroundings [K]

t_w Transference coefficient of water [-]

$t_w^{\mathrm{a,l}}$ Transference coefficient of water at the anode left-hand side [-]

$t_w^{\mathrm{a,PTL}}$ Transference coefficient of water on the PTL side of the anode [-]

$t_w^{\mathrm{a,r}}$ Transference coefficient of water at the anode right-hand side [-]

t_w^{a} Transference coefficient of water in the anode PTL [-]

$t_w^{\mathrm{c,l}}$ Transference coefficient of water at the cathode left-hand side [-]

$t_w^{\mathrm{c,PTL}}$ Transference coefficient of water on the PTL side of the cathode [-]

$t_w^{\mathrm{c,r}}$ Transference coefficient of water at the cathode right-hand side [-]

t_w^{c} Transference coefficient of water in the cathode PTL [-]

t_w^{i} Transference coefficient of water on the inlet side of the surface [-]

t_w^{m} Transference coefficient of water in the membrane [-]

t_w^{o} Transference coefficient of water on the outlet side of the surface [-]

V Volume [m^3]

v Gas velocity [m/s]

v_0 Inlet gas velocity [m/s]

$V_{j,i}$ Volume of branch i at generation level j [m^3]

$V_{spherical,i,j}$ Spherical volume around branch i at generation level j [m^3]

W Channel width [m]

w Work [W]

w_0 Channel width at generation level 0 [m]

w_j Channel width at generation level j [m]

$w_{0,\mathrm{i}}$ Channel width at generation level 0 on the inlet plate [m]

$w_{0,\mathrm{o}}$ Channel width at generation level 0 on the outlet plate [m]

w_{ideal} Ideal work [W]

$w_{j,\mathrm{i}}$ Channel width at generation level j on the inlet plate [m]

$w_{j,\mathrm{o}}$ Channel width at generation level j on the outlet plate [m]

$w_{j,i}$ Channel width of branch i at generation level j [m]

w_{lost} Lost work [W]

x Through-plane coordinate [m]

X_i Driving force of transport phenomena i

x_i Molar fraction of component i [-]

x_w Molar fraction of water [-]

x_w^* Molar fraction of water at saturation [-]

$x_w^{\mathrm{a,lb}}$ Molar fraction of water in the anode PTL on the left system boundary side [-]

$x_w^{\mathrm{c,m}}$ Molar fraction of water in the cathode PTL on membrane side [-]

$x_w^{\mathrm{c,rb}}$ Molar fraction of water in the cathode PTL on the right system boundary side [-]

x_w^{entrance} Molar fraction of water in the cathode PTL on the membrane side [-]

x_w^{lb} Molar fraction of water at the left system boundary [-]

x_w^{rb} Molar fraction of water at the right system boundary [-]

Z_d Warburg diffusion impedance [Ohm]

Bibliography

[1] European Commission, "Green Paper - A 2030 framework for climate and energy policies," *COM(2013) 169 final*, pp. 1–16, 2013.

[2] Norwegian Ministry of Transport, "Norway is electric." `https://www.regjeringen.no/en/topics/transport-and-communications/veg/faktaartikler-vei-og-ts/norway-is-electric/id2677481/`, 2019. Accessed: September 22, 2020.

[3] US Department of Energy, "2018 Cost Projections of PEM Fuel Cell Systems for automobiles and Medium-Duty Vehicles." `www.energy.gov`, 2018. Accessed: January 31, 2020.

[4] New Energy and Industrial Technology Development Organization, "NEDO's Technology Development Roadmap for Fuel Cells and Hydrogen." `https://www.nedo.go.jp/library/battery_hydrogen.html`, 2017. Accessed: January 31, 2020.

[5] B. G. Pollet, S. S. Kocha, and I. Staffell, "Current status of automotive fuel cells for sustainable transport," *Current Opinion in Electrochemistry*, vol. 16, pp. 90–95, 2019.

[6] P. J. Hamilton and B. G. Pollet, "Polymer electrolyte membrane fuel cell (PEMFC) flow field plate: Design, materials and characterisation," *Fuel Cells*, vol. 10, no. 4, pp. 489–509, 2010.

[7] P. Trogadas, J. I. S. Cho, T. P. Neville, J. Marquis, B. Wu, D. J. L. Brett, and M.-O. Coppens, "A lung-inspired approach to scalable and robust fuel cell design," *Energy and Environmental Science*, vol. 11, no. 1, pp. 136–143, 2018.

[8] V. Bethapudi, J. Hack, P. Trogadas, J. Cho, L. Rasha, G. Hinds, P. Shearing, D. Brett, and M.-O. Coppens, "A lung-inspired printed circuit board polymer electrolyte fuel cell," *Energy Conversion and Management*, vol. 202, p. 112198, 2019.

[9] R. Roshandel, F. Arbabi, and G. K. Moghaddam, "Simulation of an innovative flow-field design based on a bio inspired pattern for PEM fuel cells," *Renewable Energy*, vol. 41, pp. 86–95, 2012.

[10] J. I. S. Cho, T. P. Neville, P. Trogadas, Q. Meyer, Y. Wu, R. Ziesche, P. Boillat, M. Cochet, V. Manzi-Orezzoli, P. Shearing, D. J. L. Brett, and M.-O. Coppens, "Visualization of liquid water in a lung-inspired flow-field based polymer electrolyte membrane fuel cell via neutron radiography," *Energy*, vol. 170, pp. 14–21, 2019.

[11] C. E. Damián Ascencio, A. Hernández Guerrero, J. A. Escobar Vargas, C. Rubio-Arana, and F. Elizalde Blancas F., "Three-Dimensional Numerical Prediction of Current Density for a Constructal Theory-Based Flow Field Pattern," in *Proceedings of the ASME 2007 International Mechanical Engineering Congress and Exposition. Volume 6: Energy Systems: Analysis, Thermodynamics and Sustainability*, pp. 627–635, 2007.

[12] T. Chen, Y. Xiao, and T. Chen, "The Impact on PEMFC of Bionic Flow Field with a Different Branch," *Energy Procedia*, vol. 28, pp. 134–139, 2012.

[13] S. Kjelstrup, M.-O. Coppens, J. G. Pharoah, and P. Pfeifer, "Nature-Inspired Energy- and Material-Efficient Design of a Polymer Electrolyte Membrane Fuel Cell," *Energy & Fuels*, vol. 24, no. 9, pp. 5097–5108, 2010.

[14] A. Zlotorowicz, K. Jayasayee, P. I. Dahl, M. S. Thomassen, and S. Kjelstrup, "Tailored porosities of the cathode layer for improved polymer electrolyte fuel cell performance," *Journal of Power Sources*, vol. 287, pp. 472–477, 2015.

[15] S. Gheorghiu, S. Kjelstrup, P. Pfeifer, and M.-O. Coppens, "Is the lung an optimal gas exchanger?," in *Fractals in Biology and Medicine* (G. A. Losa, D. Merlini, T. F. Nonnenmacher, and E. R. Weibel, eds.), pp. 31–42, Birkhäuser, 2005.

[16] E. Magnanelli, Ø. Wilhelmsen, M. Acquarone, L. P. Folkow, and S. Kjelstrup, "The Nasal Geometry of the Reindeer Gives Energy-Efficient Respiration," *Journal of Non-Equilibrium Thermodynamics*, vol. 42, no. 1, pp. 59–78, 2017.

[17] E. Magnanelli, S. B. B. Solberg, and S. Kjelstrup, "Nature-inspired geometrical design of a chemical reactor," *Chemical Engineering Research and Design*, vol. 152, pp. 20–29, 2019.

[18] M.-O. Coppens, "A nature-inspired approach to reactor and catalysis engineering," *Current Opinion in Chemical Engineering*, vol. 1, no. 3, pp. 281–289, 2012.

[19] K.-S. Choi, H.-M. Kim, and S.-M. Moon, "Numerical studies on the geometrical characterization of serpentine flow-field for efficient PEMFC," *International Journal of Hydrogen Energy*, vol. 36, no. 2, pp. 1613–1627, 2011.

[20] Q. Yan, H. Toghiani, and H. Causey, "Steady state and dynamic performance of proton exchange membrane fuel cells (PEMFCs) under various operating conditions and load changes," *Journal of Power Sources*, vol. 161, no. 1, pp. 492 – 502, 2006.

[21] M. Amirinejad, S. Rowshanzamir, and M. H. Eikani, "Effects of operating parameters on performance of a proton exchange membrane fuel cell," *Journal of Power Sources*, vol. 161, no. 2, pp. 872 – 875, 2006.

[22] R. O'Hayre, S.-W. Cha, W. Colella, and F. B. Prinz, *Fuel Cell Fundamentals*. Hoboken, USA: John Wiley & Sons, Inc, 2016.

[23] A. El-kharouf and B. G. Pollet, "Gas Diffusion Media and Their Degradation," in *Polymer Electrolyte Fuel Cell Degradation*, pp. 215–247, Boston, USA: Academic Press, 2012.

[24] P. Deevanhxay, T. Sasabe, S. Tsushima, and S. Hirai, "Effect of liquid water distribution in gas diffusion media with and without microporous layer on PEM fuel cell performance," *Electrochemistry Communications*, vol. 34, pp. 239–241, 2013.

[25] A. Arvay, J. French, J. C. Wang, X. H. Peng, and A. M. Kannan, "Nature inspired flow field designs for proton exchange membrane fuel cell," *International Journal of Hydrogen Energy*, vol. 38, no. 9, pp. 3717 – 3726, 2013.

[26] M. Z. Chowdhury, O. Genc, and S. Toros, "Numerical optimization of channel to land width ratio for PEM fuel cell," *International Journal of Hydrogen Energy*, vol. 43, no. 23, pp. 10798–10809, 2018.

[27] A. Kumar and R. G. Reddy, "Effect of channel dimensions and shape in the flow-field distributor on the performance of polymer electrolyte membrane fuel cells," *Journal of Power Sources*, vol. 113, no. 1, pp. 11–18, 2003.

[28] S. Kjelstrup and D. Bedeaux, *Non-equilibrium Thermodynamics Of Heterogeneous Systems.*, vol. 16 of *Series on Advances in Statistical Mechanics*. London, UK: World Scientific, 2. ed., 2008.

[29] S. Kjelstrup, D. Bedeaux, E. Johannessen, and J. Gross, *Non-equilibrium thermodynamics for engineers*. Singapore: World Scientific, 2. ed., 2017.

[30] A. Z. Weber and J. Newman, "Modeling Transport in Polymer-Electrolyte Fuel Cells," *Chem. Rev.*, vol. 104, no. 10, pp. 4679–4726, 2004.

[31] T. E. Springer, T. A. Zawodzinski, and S. Gottesfeld, "Polymer Electrolyte Fuel Cell Model," *Journal of The Electrochemical Society*, vol. 138, no. 8, pp. 2334–2342, 1991.

[32] D. Bedeaux, A. M. Albano, and P. Mazur, "Boundary conditions and non-equilibrium thermodynamics," *Physica A: Statistical Mechanics and its Applications*, vol. 82, no. 3, pp. 438–462, 1976.

[33] A. M. Albano and D. Bedeaux, "Non-equilibrium electrothermodynamics of polarizable multicomponent fluids with an interface," *Physica A: Statistical Mechanics and its Applications*, vol. 147, no. 1, pp. 407–435, 1987.

[34] S. Kjelstrup and E. Magnanelli, "Efficiency in the process industry: Three thermodynamic tools for better resource use," *Trends in Food Science & Technology*, vol. 104, pp. 84–90, 2020.

[35] M.-O. Coppens, C. Xuereb, and V. Gerbaud, eds., "Natur-Inspired Chemical Engineering [Special Issue]," *Chemical Engineering Research and Design*, 2018.

[36] A. S. Perera and M.-O. Coppens, "Re-designing materials for biomedical applications: from biomimicry to nature-inspired chemical engineering," *Philosophical Transactions of the Royal Society A: Mathematical, Physical and Engineering Sciences*, vol. 377, no. 2138, p. 20180268, 2019.

[37] C. J. Cleveland and C. Morris, *Handbook of Energy: Chronologies, Top Ten lists, and Word Clouds*, vol. 2. Boston, USA: Elsevier, 1. ed., 2014.

[38] A. Hermann, T. Chaudhuri, and P. Spagnol, "Bipolar plates for PEM fuel cells: A review," *International Journal of Hydrogen Energy*, vol. 30, no. 12, pp. 1297–1302, 2005.

[39] V. Skákalová, P. Kotrusz, M. Jergel, T. Susi, A. Mittelberger, V. Vretenár, P. Šiffalovič, J. Kotakoski, J. C. Meyer, and M. Hulman, "Chemical Oxidation of Graphite: Evolution of the Structure and Properties," *The Journal of Physical Chemistry C*, vol. 122, no. 1, pp. 929–935, 2018.

[40] H. Li, Y. Tang, Z. Wang, Z. Shi, S. Wu, D. Song, J. Zhang, K. Fatih, J. Zhang, H. Wang, Z. Liu, R. Abouatallah, and A. Mazza, "A review of water flooding issues in the proton exchange membrane fuel cell," *Journal of Power Sources*, vol. 178, no. 1, pp. 103–117, 2008.

[41] N. Yousfi-Steiner, P. Moçotéguy, D. Candusso, D. Hissel, A. Hernandez, and A. Aslanides, "A review on PEM voltage degradation associated with water management: Impacts, influent factors and characterization," *Journal of Power Sources*, vol. 183, no. 1, pp. 260–274, 2008.

[42] F. Barbir, *PEM fuel cells: theory and practice*. London, UK: Academic Press, 2013.

[43] T. Ous and C. Arcoumanis, "Degradation aspects of water formation and transport in Proton Exchange Membrane Fuel Cell: A review," *Journal of Power Sources*, vol. 240, pp. 558–582, 2013.

[44] I. S. Hussaini and C.-Y. Wang, "Visualization and quantification of cathode channel flooding in PEM fuel cells," *Journal of Power Sources*, vol. 187, no. 2, pp. 444–451, 2009.

[45] P. Pei, Y. Li, H. Xu, and Z. Wu, "A review on water fault diagnosis of PEMFC associated with the pressure drop," *Applied Energy*, vol. 173, pp. 366–385, 2016.

[46] M. Ji and Z. Wei, "A Review of Water Management in Polymer Electrolyte Membrane Fuel Cells," *Energies*, vol. 2, pp. 1057–1106, 2009.

[47] EG&G Technical Services Inc., *Fuel Cell Handbook*. Morgantown, USA: US Department of Energy, Office of Fossil Energy, National Energy Technology Laboratory, 5. ed., 2000.

[48] X. Li and I. Sabir, "Review of bipolar plates in PEM fuel cells: Flow-field designs," *International Journal of Hydrogen Energy*, vol. 30, no. 4, pp. 359–371, 2005.

[49] H. Kahraman and M. F. Orhan, "Flow field bipolar plates in a proton exchange membrane fuel cell: Analysis & modeling," *Energy Conversion and Management*, vol. 133, pp. 363–384, 2017.

[50] T. Suzuki, A. Iiyama, N. Kubo, N. Saito, K. Shinohara, S. Shimotori, Y. Sugawara, and K. Yamada, "(Invited) Toward the Future Fuel Cell -Challenge for 2040-," *ECS Transactions*, vol. 92, no. 8, pp. 3–7, 2019.

[51] Fuel Cells and Hydrogen 2 Joint Undertaking FCH 2 JU, "Addendum to the Multi-Annual Work Plan 2014-2020." `https://www.fch.europa.eu/sites/default/files/MAWP%20final%20version_endorsed%20GB%2015062018%20%28ID%203712421%29.pdf`, 2018. Accessed: January 31, 2020.

[52] Strategy Advisory Committee of the Technology Roadmap for Energy Saving and New Energy Vehicles, "Hydrogen Fuel Cell Vehicle Technology Roadmap." `http://www.sae-china.org/download/1896/Hydrogen+Fuel+Cell+Vehicle+Technology+Roadmap+%E6%B0%A2%E7%87%83%E6%96%99%E7%94%B5%E6%B1%A0%E6%B1%BD%E8%BD%A6%E6%8A%80%E6%9C%AF%E8%B7%AF%E7%BA%BF%E5%9B%BE.pdf`, 2016. Accessed: January 31, 2020.

[53] C. S. Gittleman, A. Kongkanand, D. Masten, and W. Gu, "Materials research and development focus areas for low cost automotive proton-exchange membrane fuel cells," *Current Opinion in Electrochemistry*, vol. 18, pp. 81–89, 2019.

[54] Y. Wang, D. F. Ruiz Diaz, K. S. Chen, Z. Wang, and X. C. Adroher, "Materials, technological status, and fundamentals of PEM fuel cells - A review," *Materials Today*, vol. 32, pp. 178–203, 2020.

[55] A. S. Aricò, P. Cretì, V. Baglio, E. Modica, and V. Antonucci, "Influence of flow field design on the performance of a direct methanol fuel cell," *Journal of Power Sources*, vol. 91, no. 2, pp. 202–209, 2000.

[56] F. K. Swanepoel, M. J. Case, and H. C. v. Z. Pienaar, *Design of a Unitised Regenerative Fuel Cell System for Remote Telecommunications Applications*. Vaal University of Technology, Vanderbijlpark, 2005.

[57] G.-B. Jung, A. Su, C.-H. Tu, Y.-T. Lin, F.-B. Weng, and S.-H. Chan, "Effects of cathode flow fields on direct methanol fuel cell-simulation study," *Journal of Power Sources*, vol. 171, no. 1, pp. 212–217, 2007.

[58] S. Maharudrayya, S. Jayanti, and A. P. Deshpande, "Pressure drop and flow distribution in multiple parallel-channel configurations used in proton-exchange membrane fuel cell stacks," *Journal of Power Sources*, vol. 157, no. 1, pp. 358–367, 2006.

[59] P. van Tonder and H. Pienaar, "Bipolar plates and flow field topologies for the regenerative fuel cell," in *IEEE Africon '11*, pp. 1–5, 2011.

[60] F. Arbabi, R. Roshandel, and G. Karimi Moghaddam, "Numerical modeling of an innovative bipolar plate design based on the leaf venation patterns for PEM fuel cells," *International Journal of Engineering*, vol. 25, no. 3, pp. 177–186, 2012.

[61] A. P. Manso, F. F. Marzo, J. Barranco, X. Garikano, and M. Garmendia Mujika, "Influence of geometric parameters of the flow fields on the performance of a PEM fuel cell. A review," *International Journal of Hydrogen Energy*, vol. 37, no. 20, pp. 15256–15287, 2012.

[62] T. Sousa, M. Mamlouk, K. Scott, and C. M. Rangel, "Three Dimensional Model of a High Temperature PEMFC. Study of the Flow Field Effect on Performance," *Fuel Cells*, vol. 12, no. 4, pp. 566–576, 2012.

[63] Y. Song, C. Zhang, C.-Y. Ling, M. Han, R.-Y. Yong, D. Sun, and J. Chen, "Review on current research of materials, fabrication and application for bipolar plate in proton exchange membrane fuel cell," *International Journal of Hydrogen Energy*, vol. 45, no. 54, pp. 29832–29847, 2019.

[64] R. Taccani and N. Zuliani, "Effect of flow field design on performances of high temperature PEM fuel cells: Experimental analysis," *International Journal of Hydrogen Energy*, vol. 36, no. 16, pp. 10282–10287, 2011.

[65] N. F. Asri, T. Husaini, A. B. Sulong, E. H. Majlan, and W. R. W. Daud, "Coating of stainless steel and titanium bipolar plates for anticorrosion in PEMFC: A review," *International Journal of Hydrogen Energy*, vol. 42, no. 14, pp. 9135 – 9148, 2017.

[66] H.-C. Chiu, J.-H. Jang, W.-M. Yan, H.-Y. Li, and C.-C. Liao, "A three-dimensional modeling of transport phenomena of proton exchange

membrane fuel cells with various flow fields," *Applied Energy*, vol. 96, pp. 359–370, 2012.

[67] J.-Y. Jang, C.-H. Cheng, W.-T. Liao, Y.-X. Huang, and Y.-C. Tsai, "Experimental and numerical study of proton exchange membrane fuel cell with spiral flow channels," *Applied Energy*, vol. 99, pp. 67–79, 2012.

[68] D. Spernjak, A. K. Prasad, and S. G. Advani, "In situ comparison of water content and dynamics in parallel, single-serpentine, and interdigitated flow fields of polymer electrolyte membrane fuel cells," *Journal of Power Sources*, vol. 195, no. 11, pp. 3553–3568, 2010.

[69] P. T. Nguyen, T. Berning, and N. Djilali, "Computational model of a PEM fuel cell with serpentine gas flow channels," *Journal of Power Sources*, vol. 130, no. 1, pp. 149–157, 2004.

[70] J. Park and X. Li, "An experimental and numerical investigation on the cross flow through gas diffusion layer in a PEM fuel cell with a serpentine flow channel," *Journal of Power Sources*, vol. 163, no. 2, pp. 853–863, 2007.

[71] D. H. Jeon, S. Greenway, S. Shimpalee, and J. W. Van Zee, "The effect of serpentine flow-field designs on PEM fuel cell performance," *International Journal of Hydrogen Energy*, vol. 33, no. 3, pp. 1052–1066, 2008.

[72] P. V. Suresh, S. Jayanti, A. P. Deshpande, and P. Haridoss, "An improved serpentine flow field with enhanced cross-flow for fuel cell applications," *International Journal of Hydrogen Energy*, vol. 36, no. 10, pp. 6067–6072, 2011.

[73] C.-Y. Wang, "Fundamental Models for Fuel Cell Engineering," *Chemical Reviews*, vol. 104, no. 10, pp. 4727–4766, 2004.

[74] X. Li, I. Sabir, and J. Park, "A flow channel design procedure for PEM fuel cells with effective water removal," *Journal of Power Sources*, vol. 163, no. 2, pp. 933–942, 2007.

[75] Y. Zhang, P. Zhang, Z. Yuan, H. He, Y. Zhao, and X. Liu, "A tapered serpentine flow field for the anode of micro direct methanol fuel cells," *Journal of Power Sources*, vol. 196, no. 6, pp. 3255–3259, 2011.

[76] Y.-C. Park, P. Chippar, S.-K. Kim, S. Lim, D.-H. Jung, H. Ju, and D.-H. Peck, "Effects of serpentine flow-field designs with different channel and rib widths on the performance of a direct methanol fuel cell," *Journal of Power Sources*, vol. 205, pp. 32–47, 2012.

[77] A. Ozden, M. Ercelik, D. Ouellette, C. O. Colpan, H. Ganjehsarabi, and F. Hamdullahpur, "Designing, modeling and performance investigation of bio-inspired flow field based DMFCs," *International Journal of Hydrogen Energy*, vol. 42, no. 33, pp. 21546–21558, 2017.

[78] D. Ouellette, A. Ozden, M. Ercelik, C. O. Colpan, H. Ganjehsarabi, X. Li, and F. Hamdullahpur, "Assessment of different bio-inspired flow fields for direct methanol fuel cells through 3D modeling and experimental studies," *International Journal of Hydrogen Energy*, vol. 43, no. 2, pp. 1152–1170, 2018.

[79] J. H. Nam, K.-J. Lee, S. Sohn, and C.-J. Kim, "Multi-pass serpentine flow-fields to enhance under-rib convection in polymer electrolyte membrane fuel cells: Design and geometrical characterization," *Journal of Power Sources*, vol. 188, no. 1, pp. 14–23, 2009.

[80] K. Tüber, A. Oedegaard, M. Hermann, and C. Hebling, "Investigation of fractal flow-fields in portable proton exchange membrane and direct methanol fuel cells," *Journal of Power Sources*, vol. 131, no. 1, pp. 175–181, 2004.

[81] J. P. Kloess, X. Wang, J. Liu, Z. Shi, and L. Guessous, "Investigation of bio-inspired flow channel designs for bipolar plates in proton exchange membrane fuel cells," *Journal of Power Sources*, vol. 188, no. 1, pp. 132–140, 2009.

[82] P. Martins Belchor, M. M. Camargo Forte, and D. E. Ortiz Suman Carpenter, "Parallel serpentine-baffle flow field design for water management in a proton exchange membrane fuel cell," *International Journal of Hydrogen Energy*, vol. 37, no. 16, pp. 11904–11911, 2012.

[83] X.-D. Wang, Y.-Y. Duan, W.-M. Yan, D.-J. Lee, A. Su, and P.-H. Chi, "Channel aspect ratio effect for serpentine proton exchange membrane fuel cell: Role of sub-rib convection," *Journal of Power Sources*, vol. 193, no. 2, pp. 684–690, 2009.

[84] S. Shimpalee, S. Greenway, and J. W. Van Zee, "The impact of channel path length on PEMFC flow-field design," *Journal of Power Sources*, vol. 160, no. 1, pp. 398–406, 2006.

[85] H. Kahraman, C. Haşimoğlu, I. Çevik, and A. Murcak, "A different flow field design approach for performance improvement of a PEMFC," *Acta Physica Polonica A*, vol. 131, no. 3, pp. 484–486, 2017.

[86] W. Li, Q. Zhang, C. Wang, X. Yan, S. Shen, G. Xia, F. Zhu, and J. Zhang, "Experimental and numerical analysis of a three-dimensional flow field for PEMFCs," *Applied Energy*, vol. 195, pp. 278–288, 2017.

[87] A. Pollegri and P. M. Spaziante, *Bipolar Separator for Electrochemical Cells and Method of Preparation Thereof*. Washington, DC: U.S. Patent and Trademark Office: U.S. Patent No. 4197178, 1980.

[88] E. Hontañón, M. J. Escudero, C. Bautista, P. L. García-Ybarra, and L. Daza, "Optimisation of flow-field in polymer electrolyte membrane fuel cells using computational fluid dynamics techniques," *Journal of Power Sources*, vol. 86, no. 1, pp. 363–368, 2000.

[89] J. Lobato, P. Cañizares, M. A. Rodrigo, F. J. Pinar, E. Mena, and D. Úbeda, "Three-dimensional model of a 50cm^2 high temperature PEM fuel cell. Study of the flow channel geometry influence," *International Journal of Hydrogen Energy*, vol. 35, no. 11, pp. 5510–5520, 2010.

[90] X.-D. Wang, Y.-Y. Duan, W.-M. Yan, and X.-F. Peng, "Effects of flow channel geometry on cell performance for PEM fuel cells with parallel and interdigitated flow fields," *Electrochimica Acta*, vol. 53, no. 16, pp. 5334–5343, 2008.

[91] S. G. Kandlikar, Z. Lu, W. E. Domigan, A. D. White, and M. W. Benedict, "Measurement of flow maldistribution in parallel channels and its application to ex-situ and in-situ experiments in PEMFC water management studies," *International Journal of Heat and Mass Transfer*, vol. 52, no. 7, pp. 1741–1752, 2009.

[92] V. B. Oliveira, C. M. Rangel, and A. Pinto, "Effect of anode and cathode flow field design on the performance of a direct methanol fuel cell," *Chemical Engineering Journal*, vol. 157, no. 1, pp. 174–180, 2010.

[93] Y. Lu and R. G. Reddy, "Effect of flow fields on the performance of micro-direct methanol fuel cells," *International Journal of Hydrogen Energy*, vol. 36, no. 1, pp. 822–829, 2011.

[94] B. H. Lim, E. H. Majlan, W. R. W. Daud, M. I. Rosli, and T. Husaini, "Numerical analysis of modified parallel flow field designs for fuel cells,"

International Journal of Hydrogen Energy, vol. 42, no. 14, pp. 9210–9218, 2017.

[95] M. Sajid Hossain, B. Shabani, and C. P. Cheung, "Enhanced gas flow uniformity across parallel channel cathode flow field of Proton Exchange Membrane fuel cells," *International Journal of Hydrogen Energy*, vol. 42, no. 8, pp. 5272–5283, 2017.

[96] M. Ashrafi, H. Kanani, and M. Shams, "Numerical and experimental study of two-phase flow uniformity in channels of parallel PEM fuel cells with modified Z-type flow-fields," *Energy*, vol. 147, pp. 317 – 328, 2018.

[97] J. Lobato, P. Cañizares, M. A. Rodrigo, F. J. Pinar, and D. Úbeda, "Study of flow channel geometry using current distribution measurement in a high temperature polymer electrolyte membrane fuel cell," *Journal of Power Sources*, vol. 196, no. 9, pp. 4209–4217, 2011.

[98] N. Guo, M. C. Leu, and U. O. Koylu, "Network based optimization model for pin-type flow field of polymer electrolyte membrane fuel cell," *International Journal of Hydrogen Energy*, vol. 38, no. 16, pp. 6750–6761, 2013.

[99] S.-S. Hsieh and Y.-J. Huang, "Measurements of current and water distribution for a micro-PEM fuel cell with different flow fields," *Journal of Power Sources*, vol. 183, no. 1, pp. 193–204, 2008.

[100] N. Guo, M. C. Leu, and M. Wu, "Bio-inspired design of bipolar plate flow fields for polymer electrolyte membrane fuel cells," in *Proceedings of international SFF Symposium*, pp. 607–623, Missouri University of Science and Technology, 2011.

[101] W. Dong-Hui, Y. Lin-Zhi, P. Zhong-Yu, L. Cong-Da, L. Gang, and L. Qiao-Hui, "A novel intersectant flow field of metal bipolar plate for proton exchange membrane fuel cell," *International Journal of Energy Research*, vol. 41, no. 14, pp. 2184–2193, 2017.

[102] W. Dong-Hui, Y. Lin-Zhi, P. Zhong-Yu, L. Cong-Da, L. Gang, and L. Qiao-Hui, "Performance investigation of proton exchange membrane fuel cell with intersectant flow field," *International Journal of Heat and Mass Transfer*, vol. 121, pp. 775–787, 2018.

[103] G. Hu, J. Fan, S. Chen, Y. Liu, and K. Cen, "Three-dimensional numerical analysis of proton exchange membrane fuel cells (PEMFCs)

with conventional and interdigitated flow fields," *Journal of Power Sources*, vol. 136, no. 1, pp. 1–9, 2004.

[104] G. Zhang, L. Guo, B. Ma, and H. Liu, "Comparison of current distributions in proton exchange membrane fuel cells with interdigitated and serpentine flow fields," *Journal of Power Sources*, vol. 188, no. 1, pp. 213–219, 2009.

[105] A. Arvay, J. French, and A. M. Kannan, "Modeling and Simulation of Biologically Inspired Flow Field Designs for Proton Exchange Membrane Fuel Cells," *The Open Electrochemistry Journal*, vol. 6, no. 1, pp. 1–9, 2015.

[106] A. D. Santamaria, J. Bachman, and J. W. Park, "Design strategy for a polymer electrolyte membrane fuel cell flow-field capable of switching between parallel and interdigitated configurations," *International Journal of Hydrogen Energy*, vol. 38, no. 14, pp. 5807–5812, 2013.

[107] S. Y. Hwang, H.-I. Joh, M. A. Scibioh, S.-Y. Lee, S.-K. Kim, T. G. Lee, and H. Y. Ha, "Impact of cathode channel depth on performance of direct methanol fuel cells," *Journal of Power Sources*, vol. 183, no. 1, pp. 226–231, 2008.

[108] M. A. R. Sadiq Al-Baghdadi, "Three-dimensional computational fluid dynamics model of a tubular-shaped PEM fuel cell," *Renewable Energy*, vol. 33, no. 6, pp. 1334–1345, 2008.

[109] X.-D. Wang, W.-M. Yan, Y.-Y. Duan, F.-B. Weng, G.-B. Jung, and C.-Y. Lee, "Numerical study on channel size effect for proton exchange membrane fuel cell with serpentine flow field," *Energy Conversion and Management*, vol. 51, no. 5, pp. 959–968, 2010.

[110] P. Wawdee, S. Limtrakul, T. Vatanatham, and M. W. Fowler, "Water transport in a PEM fuel cell with slanted channel flow field plates," *International Journal of Hydrogen Energy*, vol. 40, no. 9, pp. 3739–3748, 2015.

[111] S. Chen, X. Zhang, and H. Liu, "Effect of pressure difference between adjacent channels in an adjustable flow field in PEM fuel cells," *International Journal of Hydrogen Energy*, vol. 42, no. 7, pp. 4667–4672, 2017.

[112] T. Berning, D. M. Lu, and N. Djilali, "Three-dimensional computational analysis of transport phenomena in a PEM fuel cell," *Journal of Power Sources*, vol. 106, no. 1, pp. 284–294, 2002.

[113] C. Wang, Q. Zhang, S. Shen, X. Yan, F. Zhu, X. Cheng, and J. Zhang, "The respective effect of under-rib convection and pressure drop of flow fields on the performance of PEM fuel cells," *Scientific Reports*, vol. 7, no. 1, p. 43447, 2017.

[114] S. Kreesaeng, B. Chalermsinsuwan, and P. Piumsomboon, "Effect of Channel Designs on Open-Cathode PEM Fuel Cell Performance: A Computational Study," *Energy Procedia*, vol. 79, pp. 733–745, 2015.

[115] S. Shimpalee and J. W. Van Zee, "Numerical studies on rib & channel dimension of flow-field on PEMFC performance," *International Journal of Hydrogen Energy*, vol. 32, no. 7, pp. 842–856, 2007.

[116] S. G. Goebel, "Impact of land width and channel span on fuel cell performance," *Journal of Power Sources*, vol. 196, no. 18, pp. 7550–7554, 2011.

[117] G. Inoue, Y. Matsukuma, and M. Minemoto, "Effect of gas channel depth on current density distribution of polymer electrolyte fuel cell by numerical analysis including gas flow through gas diffusion layer," *Journal of Power Sources*, vol. 157, no. 1, pp. 136–152, 2006.

[118] H. C. Liu, W. M. Yan, C. Y. Soong, F. Chen, and H. S. Chu, "Reactant gas transport and cell performance of proton exchange membrane fuel cells with tapered flow field design," *Journal of Power Sources*, vol. 158, no. 1, pp. 78–87, 2006.

[119] E. Alizadeh, S. Rahgoshay, M. Rahimi-Esbo, M. Khorshidian, and S. Saadat, "A novel cooling flow field design for polymer electrolyte membrane fuel cell stack," *International Journal of Hydrogen Energy*, vol. 41, no. 20, pp. 8525 – 8532, 2016.

[120] X. Zhang, A. Higier, X. Zhang, and H. Liu, "Experimental Studies of Effect of Land Width in PEM Fuel Cells with Serpentine Flow Field and Carbon Cloth," *Energies*, vol. 12, no. 3, 2019.

[121] A. Mohammadi-Ahmar, B. Osanloo, A. Solati, and J. Ghasemi, "Performance improvement of the circular tubular PEMFC by using different architectures and number of layers," *Energy Conversion and Management*, vol. 128, pp. 238–249, 2016.

[122] I. Khazaee and M. Ghazikhani, "Performance improvement of proton exchange membrane fuel cell by using annular shaped geometry," *Journal of Power Sources*, vol. 196, no. 5, pp. 2661–2668, 2011.

[123] L. Sun, P. H. Oosthuizen, and K. B. McAuley, "A numerical study of channel-to-channel flow cross-over through the gas diffusion layer in a PEM-fuel-cell flow system using a serpentine channel with a trapezoidal cross-sectional shape," *International Journal of Thermal Sciences*, vol. 45, no. 10, pp. 1021–1026, 2006.

[124] J. P. Owejan, T. A. Trabold, D. L. Jacobson, M. Arif, and S. G. Kandlikar, "Effects of flow field and diffusion layer properties on water accumulation in a PEM fuel cell," *International Journal of Hydrogen Energy*, vol. 32, no. 17, pp. 4489–4502, 2007.

[125] X. Zeng, Y. Ge, J. Shen, L. Zeng, Z. Liu, and W. Liu, "The optimization of channels for a proton exchange membrane fuel cell applying genetic algorithm," *International Journal of Heat and Mass Transfer*, vol. 105, pp. 81–89, 2017.

[126] N. Bunmark, S. Limtrakul, M. W. Fowler, T. Vatanatham, and J. Gostick, "Assisted water management in a PEMFC with a modified flow field and its effect on performance," *International Journal of Hydrogen Energy*, vol. 35, no. 13, pp. 6887–6896, 2010.

[127] R. Boddu, U. K. Marupakula, B. Summers, and P. Majumdar, "Development of bipolar plates with different flow channel configurations for fuel cells," *Journal of Power Sources*, vol. 189, no. 2, pp. 1083–1092, 2009.

[128] Y. M. Ferng, A. Su, and S.-M. Lu, "Experiment and simulation investigations for effects of flow channel patterns on the PEMFC performance," *International Journal of Energy Research*, vol. 32, no. 1, pp. 12–23, 2008.

[129] Y. M. Ferng and A. Su, "A three-dimensional full-cell CFD model used to investigate the effects of different flow channel designs on PEMFC performance," *International Journal of Hydrogen Energy*, vol. 32, no. 17, pp. 4466–4476, 2007.

[130] X.-D. Wang, Y.-X. Huang, C.-H. Cheng, J.-Y. Jang, D.-J. Lee, W.-M. Yan, and A. Su, "An inverse geometry design problem for optimization of single serpentine flow field of PEM fuel cell," *International Journal of Hydrogen Energy*, vol. 35, no. 9, pp. 4247–4257, 2010.

[131] Y. Tang, W. Yuan, M. Pan, and Z. Wan, "Feasibility study of porous copper fiber sintered felt: A novel porous flow field in proton exchange membrane fuel cells," *International Journal of Hydrogen Energy*, vol. 35, no. 18, pp. 9661–9677, 2010.

[132] Z. Saghali and J. Mahmoudimehr, "Superiority of a novel conic tubular PEM fuel cell over the conventional cylindrical one," *International Journal of Hydrogen Energy*, vol. 42, no. 48, pp. 28865–28882, 2017.

[133] S. Cano-Andrade, A. Hernandez-Guerrero, M. R. von Spakovsky, C. E. Damian-Ascencio, and J. C. Rubio-Arana, "Current density and polarization curves for radial flow field patterns applied to PEMFCs (Proton Exchange Membrane Fuel Cells)," *Energy*, vol. 35, no. 2, pp. 920–927, 2010.

[134] B. R. Friess and M. Hoorfar, "Development of a novel radial cathode flow field for PEMFC," *International Journal of Hydrogen Energy*, vol. 37, no. 9, pp. 7719–7729, 2012.

[135] D. Juárez-Robles, A. Hernández-Guerrero, C. E. Damián-Ascencio, and C. Rubio-Arana, "Three Dimensional Analysis of a PEM Fuel Cell With the Shape of a Fermat Spiral for the Flow Channel Configuration," in *Proceedings of the ASME 2008 International Mechanical Engineering Congress and Exposition, Vol. 8, Energy Systems: Analysis, Thermodynamics and Sustainability; Sustainable Products and Processes*, pp. 711–720, 2008.

[136] I. Perez-Raya, A. Hernandez-Guerrero, F. Elizalde-Blancas, D. Juarez-Robles, and L. Almanza-Huerta, "3D Analysis of a New Radial Channel for PEMFCs and Comparison With a Traditional Channeled System," in *ASME 2010 International Mechanical Engineering Congress and Exposition, Vol. 5, Energy Systems Analysis, Thermodynamics and Sustainability; NanoEngineering for Energy; Engineering to Address Climate Change, Parts A and B*, pp. 899–908, 2010.

[137] V. Gurau, F. Barbir, and J. K. Neutzler, *Fuel Cell Collector Plates With Improved Mass Transfer Channels*. Washington, DC: U.S. Patent and Trademark Office: US Patent No. 6551736, 2003.

[138] Y. Tabe, T. Nasu, S. Morioka, and T. Chikahisa, "Performance characteristics and internal phenomena of polymer electrolyte membrane fuel cell with porous flow field," *Journal of Power Sources*, vol. 238, pp. 21–28, 2013.

[139] M. Kozakai, K. Date, Y. Tabe, and T. Chikahisa, "Improving gas diffusivity with bi-porous flow-field in polymer electrolyte membrane fuel cells," *International Journal of Hydrogen Energy*, vol. 41, no. 30, pp. 13180–13189, 2016.

[140] A. Kumar and R. G. Reddy, "Modeling of polymer electrolyte membrane fuel cell with metal foam in the flow-field of the bipolar/end plates," *Journal of Power Sources*, vol. 114, no. 1, pp. 54–62, 2003.

[141] R. K. Mallick, S. B. Thombre, and N. K. Shrivastava, "Vapor feed direct methanol fuel cells (DMFCs): A review," *Renewable and Sustainable Energy Reviews*, vol. 56, pp. 51–74, 2016.

[142] W. Yuan, Z. Yan, Z. Tan, A. Wang, Z. Li, and Y. Tang, "Anode optimization based on gradient porous control medium for passive liquid-feed direct methanol fuel cells," *Renewable Energy*, vol. 89, pp. 71–79, 2016.

[143] J. Wang, "Theory and practice of flow field designs for fuel cell scaling-up: A critical review," *Applied Energy*, vol. 157, pp. 640–663, 2015.

[144] H. Liu and P. Li, "Maintaining equal operating conditions for all cells in a fuel cell stack using an external flow distributor," *International Journal of Hydrogen Energy*, vol. 38, no. 9, pp. 3757–3766, 2013.

[145] L. Luo and D. Tondeur, "Optimal distribution of viscous dissipation in a multi-scale branched fluid distributor," *International Journal of Thermal Sciences*, vol. 44, no. 12, pp. 1131–1141, 2005.

[146] Z. Fan, X. Zhou, L. Luo, and W. Yuan, "Experimental investigation of the flow distribution of a 2-dimensional constructal distributor," *Experimental Thermal and Fluid Science*, vol. 33, no. 1, pp. 77–83, 2008.

[147] B. Ramos-Alvarado, A. Hernandez-Guerrero, F. Elizalde-Blancas, and M. W. Ellis, "Constructal flow distributor as a bipolar plate for proton exchange membrane fuel cells," *International Journal of Hydrogen Energy*, vol. 36, no. 20, pp. 12965–12976, 2011.

[148] S. Kjelstrup and A. Røsjorde, "Local and total entropy production and heat and water fluxes in a one-dimensional polymer electrolyte fuel cell," *The Journal of Physical Chemistry B*, vol. 109, no. 18, pp. 9020–9033, 2005.

[149] D. Lorenzini-Gutierrez, A. Hernandez-Guerrero, B. Ramos-Alvarado, I. Perez-Raya, and A. Alatorre-Ordaz, "Performance analysis of a proton exchange membrane fuel cell using tree-shaped designs for flow distribution," *International Journal of Hydrogen Energy*, vol. 38, no. 34, pp. 14750–14763, 2013.

[150] L. Wang, Y. Fan, and L. Luo, "Lattice Boltzmann method for shape optimization of fluid distributor," *Computers & Fluids*, vol. 94, pp. 49–57, 2014.

[151] S. M. Senn and D. Poulikakos, "Tree network channels as fluid distributors constructing double-staircase polymer electrolyte fuel cells," *Journal of Applied Physics*, vol. 96, no. 1, pp. 842–852, 2004.

[152] N. Guo, M. C. Leu, and U. O. Koylu, "Bio-inspired flow field designs for polymer electrolyte membrane fuel cells," *International Journal of Hydrogen Energy*, vol. 39, no. 36, pp. 21185–21195, 2014.

[153] C. D. Murray, "The Physiological Principle of Minimum Work. I. The Vascular System and the Cost of Blood Volume," *Proceedings of the National Academy of Sciences*, vol. 12, no. 3, pp. 207–214, 1926.

[154] A. Bejan, *Shape and Structure, from Engineering to Nature*. Cambridge, UK: Cambridge University Press, 2000.

[155] N. Kizilova, "Computational Approach to Optimal Transport Network Construction in Biomechanics," in *Computational Science and Its Applications - ICCSA 2004* (A. Laganá, M. L. Gavrilova, V. Kumar, Y. Mun, C. J. K. Tan, and O. Gervasi, eds.), pp. 476–485, Springer Berlin Heidelberg, 2004.

[156] N. Kizilova, "Long-distance liquid transport in plants," *Proceedings of the Estonian Academy of Sciences*, vol. 57, no. 3, pp. 179–203, 2008.

[157] C. D. Murray, "The physiological principle of minimum work applied to the angle of branching of arteries.," *Journal of General Physiology*, vol. 9, no. 6, pp. 835–841, 1926.

[158] H. B. M. Uylings, "Optimization of diameters and bifurcation angles in lung and vascular tree structures," *Bulletin of Mathematical Biology*, vol. 39, no. 5, pp. 509–520, 1977.

[159] R. W. Barber and D. R. Emerson, "Optimal design of microfluidic networks using biologically inspired principles," *Microfluidics and Nanofluidics*, vol. 4, no. 3, pp. 179–191, 2008.

[160] N. Kizilova, M. Hamadiche, and M. Gad-El-Hak, "Mathematical models of biofluid flows in compliant ducts," *Archives of Mechanics*, vol. 64, no. 1, pp. 65–94, 2012.

[161] V. Cherevko and N. Kizilova, "Complex Flows of Immiscible Microfluids and Nanofluids with Velocity Slip Boundary Conditions," in *Nanophysics, Nanomaterials, Interface Studies, and Applications* (O. Fesenko and L. Yatsenko, eds.), pp. 207–228, Springer International Publishing, 2017.

[162] C. Hou, S. Gheorghiu, M.-O. Coppens, V. H. Huxley, and P. Pfeifer, "Gas Diffusion through the Fractal Landscape of the Lung: How Deep Does Oxygen Enter the Alveolar System?," in *Fractals in Biology and Medicine* (G. A. Losa, D. Merlini, T. F. Nonnenmacher, and E. R. Weibel, eds.), pp. 17–30, Birkhäuser, 2005.

[163] J. M. Currie, *Biomimetic design applied to the redesign of a PEM fuel cell flow field.* PhD thesis, University of Toronto, Toronto, Canada, 2010.

[164] H. Morikawa, H. Kikuchi, and N. Saito, "Development and Advances of a V-Flow FC Stack for FCX Clarity," *SAE International Journal of Engines*, vol. 2, no. 1, pp. 955–959, 2009.

[165] M. Sauermoser, S. Kjelstrup, N. Kizilova, B. G. Pollet, and E. G. Flekkøy, "Seeking minimum entropy production for a tree-like flowfield in a fuel cell," *Physical Chemistry Chemical Physics*, vol. 22, no. 13, pp. 6993–7003, 2020.

[166] C. Spiegel, *Designing and building fuel cells.* New York, USA: McGraw-Hill, 1. ed., 2007.

[167] H. W. Wu, "A review of recent development: Transport and performance modeling of PEM fuel cells," *Applied Energy*, vol. 165, pp. 81–106, 2016.

[168] H. Liu, P. Li, D. Juarez-Robles, K. Wang, and A. Hernandez-Guerrero, "Experimental Study and Comparison of Various Designs of Gas Flow Fields to PEM Fuel Cells and Cell Stack Performance," *Frontiers in Energy Research*, vol. 2, p. 2, 2014.

[169] T. Monsaf, B. M. Hocine, S. Youcef, and M. Abdallah, "Unsteady three-dimensional numerical study of mass transfer in PEM fuel cell with

spiral flow field," *International Journal of Hydrogen Energy*, vol. 42, no. 2, pp. 1237–1251, 2017.

[170] O. Burheim, P. J. Vie, S. Møller-Holst, J. Pharoah, and S. Kjelstrup, "A calorimetric analysis of a polymer electrolyte fuel cell and the production of h2o2 at the cathode," *Electrochimica Acta*, vol. 55, no. 3, pp. 935 – 942, 2010.

[171] M. LaBarbera, "Principles of design of fluid transport systems in zoology," *Science*, vol. 249, no. 4972, pp. 992–1000, 1990.

[172] C. D. Murray, "The physiological principle of minimum work. ii. oxygen exchange in capillaries," *Proceedings of the National Academy of Sciences*, vol. 12, no. 5, pp. 299–304, 1926.

[173] F. M. White, *Fluid Mechanics*. New York, USA: McGraw-Hill, 7. ed., 2011.

[174] M. Sauermoser, G. Fossati, N. Kizilova, and S. Kjelstrup, "(invited) modelling electrochemical cells with porous electrodes. the proton exchange membrane fuel cell," *Electrochemical Society Transactions*, vol. 92, pp. 279–292, 2019.

[175] A. Su, Y. C. , and F. B. Weng, "The impact of flow field pattern on concentration and performance in pemfc," *International Journal of Energy Research*, vol. 29, no. 5, pp. 409–425, 2005.

[176] B. J. West, G. B., Brown and J. H. and Enquist, "General Model for the Origin of Allometric Scaling Laws in Biology.," *Science*, vol. 276, no. 5309, pp. 122–126, 1997.

[177] M. Sauermoser, N. Kizilova, B. G. Pollet, and S. Kjelstrup, "Flow Field Patterns for Proton Exchange Membrane Fuel Cells," *Frontiers in Energy Research*, vol. 8, p. 13, 2020.

[178] A. Taniguchi, T. Akita, K. Yasuda, and Y. Miyazaki, "Analysis of electrocatalyst degradation in PEMFC caused by cell reversal during fuel starvation," *Journal of Power Sources*, vol. 130, pp. 42–49, 2004.

[179] Synnogy Ltd, "The UK Fuel Cell Industry: A Capabilities Guide 2003." `https://www.lowcvp.org.uk/assets/reports/Fuel_Cell_UK_CapabilityGuide_100903.pdf`, 2003. Accessed: 18.08.2020.

[180] R. Behrou, A. Pizzolato, and A. Forner-Cuenca, "Topology optimization as a powerful tool to design advanced PEMFCs flow fields," *International Journal of Heat and Mass Transfer*, vol. 135, pp. 72–92, 2019.

[181] J. Duhn, A. Jensen, S. Wedel, and C. Wix, "Optimization of a new flow design for solid oxide cells using computational fluid dynamics modelling," *Journal of Power Sources*, vol. 336, pp. 261–271, 2016.

[182] G. Tsotridis, A. Pilenga, G. D. Marco, and T. Malkow, "EU harmonised test protocols for PEMFC MEA testing in single cell configuration for automotive applications; JRC Science for Policy report," *EUR 27632 EN*, 2015.

[183] A. M. Dhirde, N. V. Dale, H. Salehfar, M. D. Mann, and T. Han, "Equivalent Electric Circuit Modeling and Performance Analysis of a PEM Fuel Cell Stack Using Impedance Spectroscopy," *IEEE Transactions on Energy Conversion*, vol. 25, no. 3, pp. 778–786, 2010.

[184] J.-L. Dellis, "Zfit." `https://www.mathworks.com/matlabcentral/fileexchange/19460-zfit`, 2020. Accessed: 18.08.2020.

[185] N. Fouquet, C. Doulet, C. Nouillant, G. Dauphin-Tanguy, and B. Ould-Bouamama, "Model based PEM fuel cell state-of-health monitoring via ac impedance measurements," *Journal of Power Sources*, vol. 159, no. 2, pp. 905 – 913, 2006.

[186] X.-Z. Yuan, C. Song, H. Wang, and J. Zhang, "Electrochemical Impedance Spectroscopy in PEM Fuel Cells: Fundamentals and Applications," ch. EIS Equivalent Circuits, pp. 139–192, London, UK: Springer, 2010.

[187] M. Pérez-Page and V. Pérez-Herranz, "Study of the electrochemical behaviour of a 300 W PEM fuel cell stack by Electrochemical Impedance Spectroscopy," *International Journal of Hydrogen Energy*, vol. 39, no. 8, pp. 4009–4015, 2014.

[188] A. Jayakumar, S. P. Sethu, M. Ramos, J. Robertson, and A. Al-Jumaily, "A technical review on gas diffusion, mechanism and medium of PEM fuel cell," *Ionics*, vol. 21, no. 1, pp. 1–18, 2015.

[189] W. Wechsatol, S. Lorente, and A. Bejan, "Tree-shaped flow structures: are both thermal-resistance and flow-resistance minimisations necessary?," *International Journal of Exergy*, vol. 1, no. 1, pp. 2–17, 2004.

[190] S. Kjelstrup and D. Bedeaux, "Thermodynamics of Electrochemical Systems," in *Springer Handbook of Electrochemical Energy* (C. Breitkopf and K. Swider-Lyons, eds.), Springer Handbooks, ch. 4, pp. 69–93, Berlin, Heidelberg, Germany: Springer, 2017.

[191] J. C. Garcia Navarro, "Modeling a Proton Exchange Membrane Fuel Cell using Non-Equilibrium Thermodynamics: A Second Law analysis of assumptions and parameters," Master's thesis, Faculty of Applied Science, TU Delft, Delft, Netherlands, 2014.

[192] D. M. Bernardi and M. W. Verbrugge, "Mathematical model of a gas diffusion electrode bonded to a polymer electrolyte," *AIChE Journal*, vol. 37, no. 8, pp. 1151–1163, 1991.

[193] K. Broka and P. Ekdunge, "Modelling the pem fuel cell cathode," *Journal of Applied Electrochemistry*, vol. 27, no. 3, pp. 281–289, 1997.

[194] A. Z. Weber and J. Newman, "Coupled Thermal and Water Management in Polymer Electrolyte Fuel Cells," *Journal of The Electrochemical Society*, vol. 153, no. 12, pp. A2205–A2214, 2006.

[195] A. L. Rangel-Cárdenas and G. J. M. Koper, "Transport in Proton Exchange Membranes for Fuel Cell Applications-A Systematic Non-Equilibrium Approach," *Materials*, vol. 10, no. 6, p. 576, 2017.

[196] M. J. Lampinen and M. Fomino, "Analysis of free energy and entropy changes for half-cell reactions," *Journal of The Electrochemical Society*, vol. 140, no. 12, pp. 3537–3546, 1993.

[197] J. Ramousse, O. Lottin, S. Didierjean, and D. Maillet, "Heat sources in proton exchange membrane (pem) fuel cells," *Journal of Power Sources*, vol. 192, no. 2, pp. 435 – 441, 2009.

[198] M. Cochet, A. Forner-Cuenca, V. Manzi, M. Siegwart, D. Scheuble, and P. Boillat, "Novel concept for evaporative cooling of fuel cells: an experimental study based on neutron imaging," *Fuel Cells*, vol. 18, no. 5, pp. 619–626, 2018.

[199] T. S. Uyar and D. Beşikci, "Integration of hydrogen energy systems into renewable energy systems for better design of 100% renewable energy communities," *International Journal of Hydrogen Energy*, vol. 42, no. 4, pp. 2453–2456, 2017.

[200] J. Wang, H. Wang, and Y. Fan, "Techno-Economic Challenges of Fuel Cell Commercialization," *Engineering*, vol. 4, no. 3, pp. 352 – 360, 2018.

[201] P. Rodatz, F. Büchi, C. Onder, and L. Guzzella, "Operational aspects of a large PEFC stack under practical conditions," *Journal of Power Sources*, vol. 128, no. 2, pp. 208 – 217, 2004.

[202] J. Wu, X. Z. Yuan, J. J. Martin, H. Wang, J. Zhang, J. Shen, S. Wu, and W. Merida, "A review of PEM fuel cell durability: Degradation mechanisms and mitigation strategies," *Journal of Power Sources*, vol. 184, no. 1, pp. 104 – 119, 2008.

[203] Y. Saygili, I. Eroglu, and S. Kincal, "Model based temperature controller development for water cooled PEM fuel cell systems," *International Journal of Hydrogen Energy*, vol. 40, no. 1, pp. 615 – 622, 2015.

[204] A. F. Gunnarshaug, S. Kjelstrup, D. Bedeaux, F. Richter, and O. S. Burheim, "The reversible heat effects at lithium iron phosphate- and graphite electrodes," *Electrochimica Acta*, vol. 337, p. 135567, 2020.

[205] M. Siemer, T. Marquardt, G. V. Huerta, and S. Kabelac, "Local entropy production rates in a polymer electrolyte membrane fuel cell," *Journal of Non-Equilibrium Thermodynamics*, vol. 42, no. 1, pp. 1–30, 2017.

[206] G. V. Huerta, V. Flasbart, T. Marquardt, P. Radici, and S. Kabelac, "Impact of multi-causal transport mechanisms in an electrolyte supported planar SOFC with (ZrO2)x-1(Y2O3)x electrolyte," *Entropy*, vol. 20, no. 6, pp. 1–19, 2018.

[207] T. J. Bvumbe, P. Bujlo, I. Tolj, K. Mouton, G. Swart, S. Pasupathi, and B. G. Pollet, "Review on management, mechanisms and modelling of thermal processes in PEMFC," *Hydrogen and Fuel Cells*, vol. 1, pp. 1–20, 2016.

[208] Y. Zong, B. Zhou, and A. Sobiesiak, "Water and thermal management in a single PEM fuel cell with non-uniform stack temperature," *Journal of Power Sources*, vol. 161, no. 1, pp. 143 – 159, 2006.

[209] A. Kulikovsky, "Heat transport in a PEFC: Exact solutions and a novel method for measuring thermal conductivities of the catalyst layers and membrane," *Electrochemistry Communications*, vol. 9, no. 1, pp. 6 – 12, 2007.

[210] R. Vetter and J. O. Schumacher, "Free open reference implementation of a two-phase PEM fuel cell model," *Computer Physics Communications*, vol. 234, pp. 223 – 234, 2019.

[211] H. Meng, "A three-dimensional PEM fuel cell model with consistent treatment of water transport in MEA," *Journal of Power Sources*, vol. 162, no. 1, pp. 426–435, 2006.

[212] R. Schweiss, S. Hofmeister, C. Meiser, D. Dan, A. Baumann, T. Kuster, N. Haak, S. Bacher, and G. Korus, "Powering up fuel cells - Our gas diffusion layer," *SGL CARBON GmbH*, 2019.

[213] O. Burheim, P. J. S. Vie, J. G. Pharoah, and S. Kjelstrup, "Ex situ measurements of through-plane thermal conductivities in a polymer electrolyte fuel cell," *Journal of Power Sources*, vol. 195, no. 1, pp. 249–256, 2010.

[214] R. B. Bird, W. E. Stewart, and E. N. Lightfoot, *Transport phenomena*. New York, USA: Wiley, revised 2. ed., 2007.

[215] W. Grot, "Appendix C - Solution Cast Nafion Film," in *Fluorinated Ionomers*, PDL Handbook Series, pp. 251 – 257, Oxford, UK: William Andrew Publishing, 2. ed., 2011.

[216] C. Song, Y. Tang, J. L. Zhang, J. Zhang, H. Wang, J. Shen, S. McDermid, J. Li, and P. Kozak, "PEM fuel cell reaction kinetics in the temperature range of 23-120°C," *Electrochimica Acta*, vol. 52, no. 7, pp. 2552 – 2561, 2007.

[217] A. F. Gunnarshaug, S. Kjelstrup, and D. Bedeaux, "The heat of transfer and the Peltier coefficient of electrolytes," *Chemical Physics Letters: X*, vol. 5, p. 100040, 2020.

[218] B. E. Poling, J. M. Prausnitz, and J. P. O'Connell, *The properties of gases and liquids*. New York, USA: McGraw-Hill, 5. ed., 2001.

[219] S. M. Rahgoshay, A. A. Ranjbar, A. Ramiar, and E. Alizadeh, "Thermal investigation of a PEM fuel cell with cooling flow field," *Energy*, vol. 134, pp. 61 – 73, 2017.

[220] W. Yuan, Y. Tang, M. Pan, Z. Li, and B. Tang, "Model prediction of effects of operating parameters on proton exchange membrane fuel cell performance," *Renewable Energy*, vol. 35, no. 3, pp. 656 – 666, 2010.

[221] A. Rowe and X. Li, "Mathematical modeling of proton exchange membrane fuel cells," *Journal of Power Sources*, vol. 102, no. 1, pp. 82 – 96, 2001.

[222] P. J. Vie and S. Kjelstrup, "Thermal conductivities from temperature profiles in the polymer electrolyte fuel cell," *Electrochimica Acta*, vol. 49, no. 7, pp. 1069 – 1077, 2004.

[223] R. Zaffou, J. Yi, R. Kunz, and J. Fenton, "Effects of Temperature Difference on Water Management in PEMFCs," *ECS Transactions*, vol. 1, no. 6, pp. 429–438, 2006.

[224] S. Kim and M. Mench, "Investigation of temperature-driven water transport in polymer electrolyte fuel cell: Thermo-osmosis in membranes," *Journal of Membrane Science*, vol. 328, no. 1, pp. 113 – 120, 2009.

[225] Q. Yan, H. Toghiani, and J. Wu, "Investigation of water transport through membrane in a PEM fuel cell by water balance experiments," *Journal of Power Sources*, vol. 158, no. 1, pp. 316 – 325, 2006.

[226] J.-H. Jang, H.-C. Chiu, W.-M. Yan, and W.-L. Sun, "Effects of operating conditions on the performances of individual cell and stack of PEM fuel cell," *Journal of Power Sources*, vol. 180, no. 1, pp. 476 – 483, 2008.

[227] E. Goodarzi, M. Ziaei, and E. Z. Hosseinipour, *Introduction to Optimization Analysis in Hydrosystem Engineering*, ch. Multiobjective Optimization, pp. 111–147. Cham, Switzerland: Springer, 2014.

ISBN 978-82-326-5749-0 (printed ver.)
ISBN 978-82-326-4752-1 (electronic ver.)
ISSN 1503-8181 (printed ver.)
ISSN 2703-8084 (online ver.)

NTNU

Norwegian University of
Science and Technology